SPECTROSCOPIC MODE IDENTIFICATION IN A SAMPLE OF NON-RADIALLY PULSATING STARS

A thesis submitted in partial fulfilment of the requirements for the Degree of

Doctor of Philosophy in Astronomy

at the University of Canterbury

by D. J. Wright

University of Canterbury

2008

Table of Contents

List of Figures

Abstract

This thesis has analysed spectroscopic data for three stars in detail, the β Cephei star V2052 Ophiuchus, the γ Doradus star QW Puppis and the γ Doradus candidate star HD139095. Twelve other candidate γ Doradus stars have had their $V_{rot}\sin i$, binary status and, where possible, the presence of line profile variation determined.

A new technique utilising scaled delta functions has been developed to allow the extraction of a single, high S/N line profile from a high resolution and large wavelength range spectrum. This procedure has performed well in the γ Doradus stars examined.

The application of the new mode identification technique, the Fourier Parameter Fit method, to the three stars examined in detail has been very successful. For each of the three stars constraints have been placed on the degree (l) and the azimuthal order (m) of the non-radial pulsation modes detected.

Chapter 1
Introduction

A detailed knowledge of a star's pulsations can be used to constrain parameters describing the interior structure and evolution of the star. This is called asteroseismology which, as its name suggests, works on principles similar to that of seismology which uses earthquakes to study the internal structure of the Earth. The process of asteroseismology matches detailed models of a star's pulsational behaviour to observations of that star.

Asteroseismology has had many successes. It has been used to deduce the core composition for, and crystalline structure of, white dwarfs (Kanaan et al. 2005) and the non-linear internal rotational behaviour of a β Cephei star (Aerts et al. 2003; Dupret et al. 2004). It has placed tight constraints on the mass, temperature, radii and metallicity of many stars (Handler et al. 2003; Mazumdar et al. 2006; Rodríguez et al. 2006; Casas et al. 2006; Briquet et al. 2007; Lenz et al. 2008)**.**

Stars which pulsate can be found in many different parts of the Hertzsprung-Russell diagram, representing a vast array of different stellar conditions. Of particular use to astronomers are stars which demonstrate multiple pulsational modes since these provide more constraints on the models.

The stellar pulsations referred to can be either radial, where the entire surface of the star has the same radius which increases and decreases throughout the pulsation, or non-radial, where there are travelling waves propagating around the stellar surface in a spherically harmonic pattern. Radial pulsation waves propagate through the entire star so they can only provide information on the mean density. Non-radial pulsation (NRP) waves propagate only in certain regions of the stellar interior, so they can yield specific information about the layers in which they propagate. To obtain the most information from a non-radial pulsation mode, the spherical harmonic quantum numbers l and m must be determined. The process of deriving these parameters is called mode identification and is the focus of this thesis.

1.1 Non-radial pulsation

Three parameters describe the mode of a NRP. The quantum parameter l is called the degree of the mode and is the number of nodal lines in the pulsation. The parameter m is called the order and is the number of nodal lines that cross the pulsational axis poles, which are usually also the rotational axis poles. The third parameter is the number of radial nodes n. Figure 1-1 shows examples of the appearance of some l=3 modes with different m values. Values of n are not visible. Note that l =0 is a radial pulsation.

These stellar oscillations can be observed both photometrically, as brightness variations, and spectroscopically, as spectral line profile variations (LPVs). The NRP causes brightness variation across the stellar surface as the travelling waves lead to photospheric temperature changes. This brightness variation can be observed photometrically. The travelling waves also cause Doppler shifting

of surface elements due to the velocity field of the stellar atmosphere. This leads to periodic line profile variations.

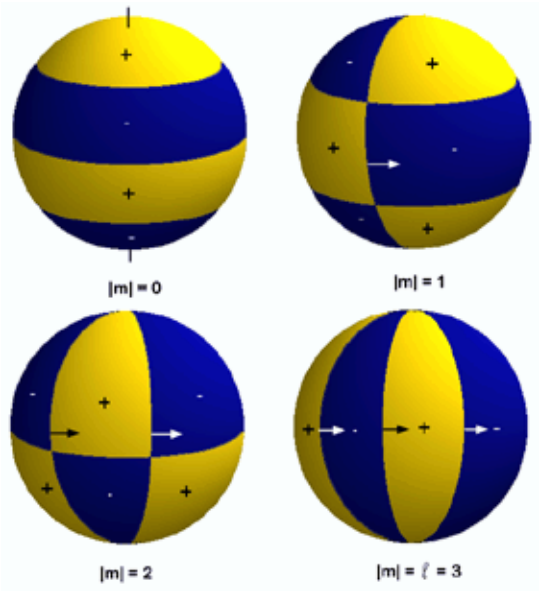

Figure 1-1: An example of four *l*=3 spherically harmonic non-radial pulsations (from Zima 2005).

Multi-colour photometric time series observations can uniquely identify the degree, *l*, of a pulsation mode using a method defined by Heynderickx et al. (1994) and improved by Dupret et al. (2003). In some cases multi-colour photometry can determine the ratio of the bolometric flux variation to the radial displacement, which is sensitive to stellar convection and can help in the selection of the convective model (Daszynska-Daszkiewicz et al. 2003).

High-resolution time series spectroscopy can uniquely identify the order, *m,* of the pulsation mode and constrain the degree, *l.* Hence this is complementary to photometric time series data. There are multiple techniques used in spectroscopic mode identification, with the most common methods being:

- a direct comparison of synthetic and observed line profiles (Mantegazza et al. 2000; Balona 2003);
- an analysis of the moments of the observed spectral line profile (Balona 1986; Aerts et al. 1992; Briquet and Aerts 2003);
- Doppler imaging of the stellar surface (Berdyugina et al. 2003);
- an analysis of the phase and amplitude across the line profile (Schrijvers and Telting 1999; Zima 2006).

This thesis focuses on spectroscopic mode identification with particular use of the most recently developed analysis method, the Fourier parameter fit (FPF) method (Zima 2006), which models the phase and amplitude across the line profile.

1.2 Synthesizing non-radial pulsations

Stars are large self-gravitating bodies that emit large amounts of energy created in their core by nuclear fusion. The energy created in the core can be transported to the surface of the star via radiative or convective means. The turbulent motion in the convective regions, as well as rotation and magnetic effects, can cause instabilities in the star allowing stable oscillations.

If a star is modelled initially as a spherically symmetric object in hydrostatic equilibrium, without rotation or a magnetic field, then each part of the star can be described by the spherical coordinates r, θ and φ, where r is the radius, θ is the angle from the pole (between 0 and π) and φ is the azimuthal angle or the angle around the equator (between 0 and 2π). The movement of a mass element is described by the Lagrangian displacement vector ξ (ξ_r , ξ_θ, ξ_φ). This vector changes the pressure, density and the gravitational potential as a

function of r, θ and φ, and time. Linear, adiabatic perturbation of these parameters can be described by the following equations (see Zima 2005):

Poisson's equation:

$$\nabla^2\Phi' = 4\pi G\rho' ; \tag{1.1}$$

Equation of motion:

$$\rho_0 \frac{d^2\xi}{dt^2} = -\rho_0\nabla\Phi' - \rho'\nabla\Phi_0 - \nabla P' ; \tag{1.2}$$

Equation of continuity:

$$\rho' + \xi\cdot\nabla\rho_0 + \rho_0\nabla\cdot\xi = 0 ; \tag{1.3}$$

Condition for adiabacity

$$P' + \xi\cdot\nabla P_0 = \frac{P_0}{\rho_0}\gamma_{ad}\left(\rho' + \xi\cdot\nabla\rho_0\right), \tag{1.4}$$

where P', ρ', and Φ are the Eulerian perturbations, G is the gravitational constant and γ_{ad} is the adiabatic coefficient. This set of differential equations is solved by assuming that r, θ and φ depend on $Y_l^m(\theta, \varphi)\, e^{i\omega t}$, where $Y_l^m(\theta, \varphi)$ depends on the aforementioned spherical degree l and order m, ω is the angular pulsational frequency and t is the time. The spherical harmonic can be written as

$$Y_{\lambda}^{m}(\theta,\phi) \equiv N_{\lambda}^{m} P_{\lambda}^{|m|}(\cos\theta) e^{im\phi} \tag{1.5}$$

where $P_l^{|m|}$ is the associated Legendre polynomial of degree l and azimuthal order m given by

$$P_{\lambda}^{|m|}(x) \equiv \frac{(-1)^m}{2^{\lambda}\lambda!}\left(1-x^2\right)^{\frac{m}{2}} \frac{d^{\lambda+m}}{dx^{\lambda+m}}\left(x^2-1\right)^{\lambda} \tag{1.6}$$

and

$$N_{\lambda}^{m} = (-1)^{\frac{m+|m|}{2}} \sqrt{\frac{(2\lambda+1)}{4\pi}\frac{(\lambda-|m|)!}{(\lambda+|m|)!}} \tag{1.7}$$

is the normalisation constant (equations and descriptions have been taken from Zima (2005).

For each value of l there can be (2 l +1) values of m such that – l< m< l . Modes with m=0 are called axisymmetric or zonal and modes with |m|= l are called sectoral modes. All other values of m are called tesseral modes. Axisymmetric modes are standing waves since they do not propagate around the rotational axis. Various conventions for m are used in the literature. A positive value for m can be assigned to either prograde or retrograde motion, where prograde motion is in the direction of rotation and retrograde is the opposite. The convention used in this thesis is that of the FPF software, that positive values of m denote retrograde motion, which results in a lower observed frequency in the observer's frame of reference.

The effects of NRP on the spectral line profile depend on the pulsation's quantum numbers. Some examples of theoretical line profile variations (LPVs) for different modes are shown in Figure 1-2. These profiles have been generated using the FPF software (Zima 2006). No temperature effects are considered and no differentiation between *p*- or *g*-modes is made. All of the modes shown are generated using an inclination of 45^{o}. In Figure 1-2 different representations of the variable line profile are introduced. The stacked plot of line profiles has been generated by displacing the true sequence to show the temporal variability. The 2-D colour-mapped surface plot is created by subtracting the mean line profile from each individual line profile, and plotting the residuals as a single row in grayscale representation.

From Figure 1-2 it is clear that for axisymmetric (m=0) modes fixed parts of the profiles appear to pulse up and down (red to blue in the colour-mapped plot). For the case of tesseral and sectoral modes ($|m|>0$) of moderate to high degree ($l>2$), the line profile shows moving 'bumps' from the blue side to the red side of the line for $m>0$ (or red to blue for $m<0$). These statements are true for inclinations greater than approximately 10^{o}. At smaller inclinations there can be more complex patterns observed in the residuals because of a significant contribution from the 'far side' of the star (the visible region of the star on the further side of the rotational axis).

1.3 Non radially pulsating variables

There are many varieties of non-radially pulsating stars, including the main sequence γ Doradus, δ Scuti, β Cephei and SPB stars, the evolved subdwarf B

and subdwarf O stars and the different classes of pulsating white dwarf (DAVs, DBVs, DOVs and the PG 1159 stars).

The primary mechanism causing the NRP observed in many stars, such as the β Cephei and δ Scuti stars, is the κ mechanism, a modulation of the radiative energy transport in the star's envelope (Gautschy and Saio 1995). Recently a flux-blocking mechanism has been defined to explain the NRP observed in γ Doradus stars (Guzik et al. 2000).

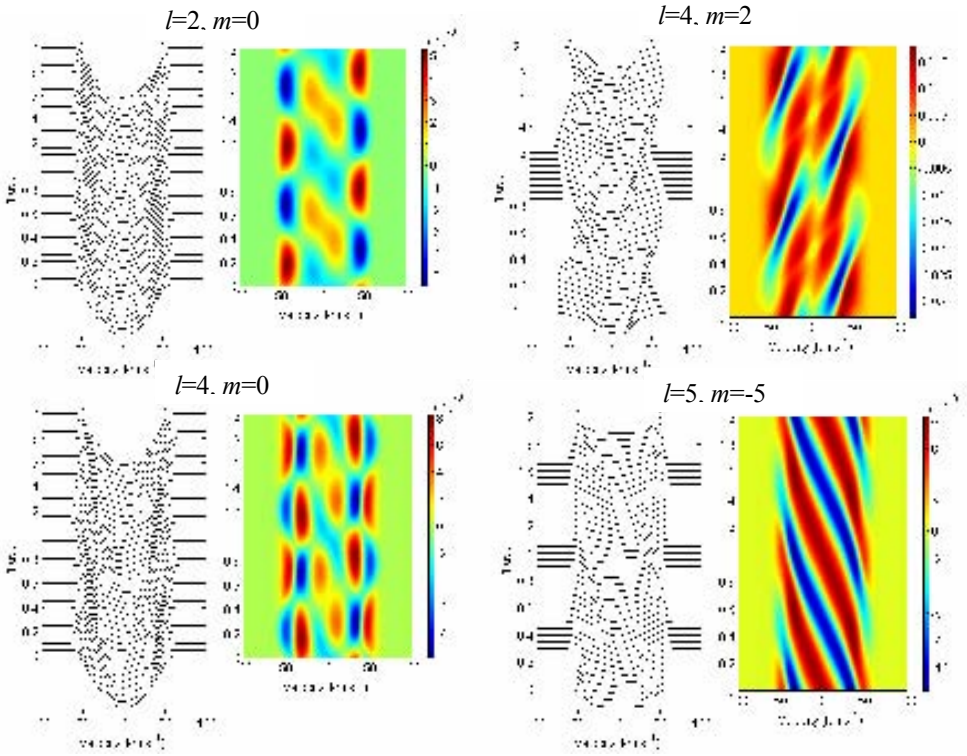

Figure 1-2: Examples of synthetic line profile variations caused by non-radial pulsations. For each mode the line profiles are shown in a stacked plot and the difference from the mean is plotted as a 2-D colour mapped surface. The values of the colours are shown on the right. The modes are: *l*=2, *m*=0 (top left); *l*=4, *m*=2 (top right); *l*=4, *m*=0 (bottom left); *l*=5, *m*=-5 (bottom right). These profiles were produced using the LIPS code provided as part of the FPF software package (Zima 2006).

NRPs are grouped into *p*- and *g*-mode pulsation, where the dominant restoring force of the pulsation is either *pressure* or *gravity* respectively. In the high

frequency domain the main restoring force is pressure and these *p*-modes are trapped in regions of the stellar envelope. They tend to have a large radial component in their displacement. The *g*-modes occur in the deeper regions of the star at lower frequencies and they have a larger horizontal component to their displacement than *p*-modes. It should be noted that in evolved objects the basic description above is no longer valid as the two frequency domains can overlap and modes of a mixed nature can occur i.e. *g*-mode characteristics in the deep layers and *p*-mode characteristics in the outer layers.

Some non-radially pulsating stars have been well studied. For example, pulsating white dwarf asteroseismology is very advanced with approximately 150 pulsating white dwarf stars known and many of them with multiple, uniquely identified, pulsation modes. This has permitted measurements of composition and even understanding of the mode selection mechanism, as well as very precise values of the mass and luminosity. Conversely, the γ Dor stars are a new group of variable star that has only recently been defined (Kaye et al. 1999), and asteroseismology has only just begun to be applied to these stars.

In this thesis, one β Cephei star and two γ Doradus stars are investigated in detail. A basic description of both these types of pulsator is given below.

β Cephei stars are B0-B3 III-V type stars that show pulsation with periodicities around 3-8 cd^{-1}. They are massive stars with M_{star}~7-20M_{sun} and pulsate in low order (*n*) *p*- and *g*-modes. The pulsations are driven by the κ mechanism activated by the metallic line opacity enhancements that occur at a temperature of ~200,000 K (Gautschy and Saio 1995). As a group they are well defined

and asterosiesmology has been successful in several stars (Aerts et al. 2003; Aerts et al. 2004; Aerts et al. 2004).

γ Doradus stars, identified as a group only in the late 1990s (Kaye et al. 1999), lie at the red edge of the classical instability strip and show 0.3-3 cd^{-1} *g*-mode pulsations (Guzik et al. 2000). Evolutionary models show both main-sequence (MS) and post-MS stars fall into the convective-blocking instability strip that is believed best to describe their pulsations (Guzik et al. 2000). Theoretically they could also show *p*-mode pulsations such as those observed in δ Scuti stars, driven by the κ mechanism, since these two groups overlap on the Hertzsprung-Russell diagram. A star with both *p*- and *g*-mode pulsations would allow further restrictions to be placed on the pulsation modelling and hence a better determination of their internal characteristics could be achieved. Investigating these stars is appealing due to their multi-*g*-mode oscillations, the possibility of finding *p*-modes as well and the early stage of characterisation of the stars as a group.

1.4 Mode identification

Spectroscopic identification of the pulsation mode requires the precise determination of the frequencies present in the data. Because of the presence of close frequency multiplets in many of the non-radially pulsating stars, the required frequency resolution is only achieved with a very long timebase of observations.

In the case of the β Cephei stars, this kind of dataset can be obtained with a number of dedicated observing runs over a substantial time (> 6 months). This can be achieved with a high resolution spectrograph at a single site because

one full night's observations will sample the entire phase of a typical β Cephei frequency at least once. To resolve multiple frequencies it is necessary to have a longer continuous dataset. Thus many of the detailed β Cephei investigations have used multi-site data.

For γ Dor stars it is almost essential to have multiple sites monitoring the same star with high resolution spectroscopic instruments. The typical frequency range for these objects is such that it is very unlikely that the complete phase of a pulsation can be sampled in a single night. Hence continuous monitoring from multiple sites for extended periods (long observation runs of greater than 1week) are required to obtain the quality of data necessary for asteroseismological analysis. This type of observational campaign is extremely difficult to organise and relies on small telescopes where dedicated access for such studies can be obtained. This further limits the data quality because of the lower signal-to-noise (S/N) data that will be obtained on smaller telescopes.

1.5 Thesis outline

This thesis is organised as follows:

In Chapter 2 the observations, instrumentation and the reduction process used in this thesis are outlined. This includes a description of the process involved in homogenising the spectroscopic datasets from two observatories.

Chapter 3 gives a theoretical simulation of how to determine an average spectral line profile for an observation using a cross-correlation method. The approach is to broaden rotationally a Gaussian line profile which is then

replicated many times at random wavelengths to simulate a stellar spectrum. Photon noise, various spectral line densities, continuum fitting errors and rest wavelength errors are simulated. Multiple methods of determining the spectral line profile are then compared with the initially-created rotationally-broadened Gaussian to determine which method best recovers the line profile. A large number of trials are run for a statistical examination of the results.

In Chapter 4 the various methods used to analyse the stellar spectra are explained. This includes the method used to determine if line profile variations are present in a star, the measurement of the equivalent width and radial velocity of a line profile, the measurement of the projected rotational velocity of a star and the pulsational mode identification.

Chapter 5 is an analysis of the 89 spectroscopic observations of the β Cephei star V2052 Ophiuchus. The observations were obtained at the Mount John University Observatory (MJUO). First, the best approach to spectral line analysis for this star is discussed. Then, investigations of the frequencies present in the equivalent width, radial velocity and minimum intensity measurements, as well as the pixel-by-pixel variations is carried out. A mode identification is then attempted for the non-radial oscillation frequencies present in the observations.

Chapter 6 is an analysis of the 179 observations obtained of the γ Dor candidate star QW Puppis. The spectra were obtained at two observatories, the South African Astronomical Observatory (SAAO) and MJUO. For this object two methods of defining the spectral line profile are investigated based on results from Chapter 3. Investigations of the frequencies present in the equivalent width and radial velocity measurements, as well as the pixel-by-pixel variations, is carried out for both line profile datasets. A mode

identification is then attempted for the frequencies determined to be caused by NRP for each dataset.

An analysis of the 57 observations obtained at SAAO of the γ Dor star HD139095 is contained in Chapter 7. An investigation of the frequencies present in the data, similar to that carried out for QW Puppis, is completed, followed by an attempted mode identification for the NRP frequencies detected.

Chapter 8 is an overview of twelve other γ Dor candidate stars for which only a few observations were obtained. The possible presence of LPVs is discussed and a measurement of the projected rotational velocity is made for each star.

Chapter 9 is a summary of all of the significant conclusions from the thesis and some direction for future work in this exciting area of stellar astrophysics.

Chapter 2
Spectroscopic Observations and Data Reduction

2.1 Spectroscopic observations

The data sets analysed in this thesis consisted of observations obtained from either the 1.0m McLellan telescope at Mount John University Observatory (MJUO) or the 1.9m telescope at the South African Astronomical Observatory (SAAO). At MJUO the High Efficiency and Resolution Canterbury University Large Échelle Spectrograph (HERCULES, Hearnshaw et al. 2003) was used. The Grating Instrument for Radiation Analysis with a Fibre Fed Échelle (GIRAFFE, a copy of the MUSICOS spectrograph, Baudrand and Bohm 1992) spectrograph was used at SAAO.

To observe effectively stellar non-radial pulsations (NRPs), the integration time of an exposure must be sufficient to give good signal-to-noise (S/N). For this thesis a S/N > 100 for wavelengths >4500Å was selected as a requirement. The exposure time must also not be too large a fraction of the pulsation period. This is because sampling large fractions of the pulsation period would smear out the deformation of the line profile. For this thesis it was decided not to have an integration time longer than 1/20 of the typical pulsation period of an

object. This limit means that any star that has typical periods < 20 times the integration time necessary for at least 100 S/N are not considered good targets for our instruments.

2.1.1 Star selection

The HERCULES spectrograph at MJUO was the main instrument available for use during this investigation so star selection was based on this instrumentation. A number of star types exhibit NRPs, for example: β Cephei, δ Scuti, ZZ Ceti, Subdwarf B and γ Doradus variables. γ Doradus variables were selected for study in this thesis for the reasons outlined below.

The ZZ Ceti and Subdwarf B stars are faint (~13th magnitude) and beyond the observable limit of HERCULES, hence they are not considered for investigation. The δ Scuti variables have a large number of modes. This means that long multi-site campaigns are necessary to identify as many of the frequencies present as possible so that they can be accounted for in the behaviour of the spectral line profile. They also commonly have pulsation periods < 2hrs which means only the bright targets can be well sampled with sufficient S/N. These requirements, combined with the relatively well-studied state of these stars lead to the conclusion that they were also to be excluded from selection. The β Cephei stars are currently being investigated by a well organised group of researchers. (Aerts et al. 2004; Aerts et al. 2003; Dupret et al. 2004). They are taking a systematic approach to understanding these stars, so β Cephei stars were also eliminated as targets for a multi-site campaign. However, some observations of V2052 Oph, a β Cephei star, were analysed in this thesis to demonstrate the effectivness of our analysis techniques. These were observed as part of a multi-site campaign organised by Conny Aerts. The

observations of the β Cephei star V2052 Oph were obtained during a multi-site campaign focussed on ν Eri (Aerts et al. 2004). V2052 Oph was the secondary target of the campaign. The observations were taken at MJUO with HERCULES.

Based on the remaining NRP star types it was decided that γ Dor variables would be the most appropriate for a multi-site campaign. These objects have typical periods from 8-80 hrs allowing up to 30 minute exposure times. This means that γ Dor stars as faint as V ~8 can be observed while meeting the S/N requirement. A number of candidate γ Dor variables were also observed at MJUO to contribute to increasing the numbers in this relatively small class of variable star. The candidates were observed only at MJUO and only a few observations were obtained for most of them.

The objects selected for study were obtained from the list of candidate γ Dor stars in Appendix A (Handler 1999; Henry and Fekel 2003). The targets observed were selected from this list based on the following criteria

- observable when telescope time was allocated;
- V brighter than 8^{th} magnitude;
- declination less than 0^{o}, i.e. south of the equator.

The main multi-site campaign target chosen was QW Puppis. It was selected because it was bright and available for observation during the allocated campaign period. It also had a previous photometric study (Poretti et al. 1997) in which four frequencies were identified. The secondary target for the campaign was HD 139095, which was chosen because it was observable in the latter half of the night when QW Pup was no longer observable.

2.2 Spectroscopic instrumentation details

The HERCULES (at MJUO) and GIRAFFE (at SAAO) spectrographs used different detector systems described below.

2.2.1 Series 200 CCD at MJUO

Many of the observations used in this thesis were made with a Series 200 SITe CCD camera. It is a 1024 x 1024 pixel detector with 24μm x 24μm sized pixels. A full well is ~300,000 electrons and it has a maximum ADU readout of 65,535. The camera was used with a gain of 0.82 ADU/electron and has a base level noise of 2.59 electrons. The wavelength range observed was 4500Å - 7050Å with gaps in each order because of the size of the detector.

2.2.2 CCD on GIRAFFE at SAAO

The detector on the SAAO GIRAFFE spectrograph was a SAAO TEK6 CCD camera. This was a Tektronix 1024 x 1024 detector with 24μm x 24μm sized pixels. The image was read out through two amplifiers. The top amplifier had a gain of 0.833 ADU/electron with a readout noise of 6.7 electrons; the bottom amplifier had a gain of 0.926 ADU/electron with a readout noise of 6.1 electrons. The wavelength range observed was 4300Å - 6800Å.

2.3 Data reduction

There are a number of steps involved in reducing the spectroscopic data before any analysis can be done. Data obtained from different observatories were reduced using the local data reduction package. At MJUO this reduction package was the HERCULES Reduction Software Package (HRSP) (Skuljan

2004) and at SAAO the reduction software was XSPEC2. Each package completes the reduction in a number of similar steps: order detection, flat-fielding, wavelength-calibration and normalisation to produce 1-dimensional spectra.

2.3.1 HRSP

HRSP (Skuljan 2004) is a set of standard reduction procedures configured specifically for the HERCULES spectrograph. It begins by identifying the precise absolute position of the observed images in the much larger HERCULES echellogram by comparing a thorium-argon calibration image (hereafter ThAr) to a reference image (see Figure 2-1). Then the bias, computed from an overscan strip on the image, is subtracted from all frames. Next it locates the order positions using a smooth field image, extracts the smooth field and normalises it for calibrating the stellar image. Each spectral order is extracted from the image and is divided by the smooth field. The ThAr images taken before and after the stellar spectrum are compared to calculate any shift in pixel position and the result is linearly interpolated to correspond with the time of the stellar image's observation. Wavelength calibration is computed from a two-dimensional polynomial fit to a large number of calibration lines taken from the two ThAr images. Finally the observational stellar data orders are extracted and rebinned to a linear wavelength scale.

2.3.2 XSPEC2

The SAAO reduction software XSPEC2 follows many similar steps to HRSP. Order detection for each stellar image is done using a smooth field image and the smooth field for each order is determined. The stellar orders are extracted and divided by the smooth field. A number of ThAr images taken throughout

the night are examined for the positions of the ThAr lines. From these positions a wavelength calibration solution is determined. The relative pixel positions of each of the ThAr lines versus time are plotted and a polynomial is fitted to the positions interactively. The timing of each observation is projected onto this polynomial fit to determine the position of the wavelength solution on the extracted observation image. The images are extracted to give a one dimensional spectrum for each order.

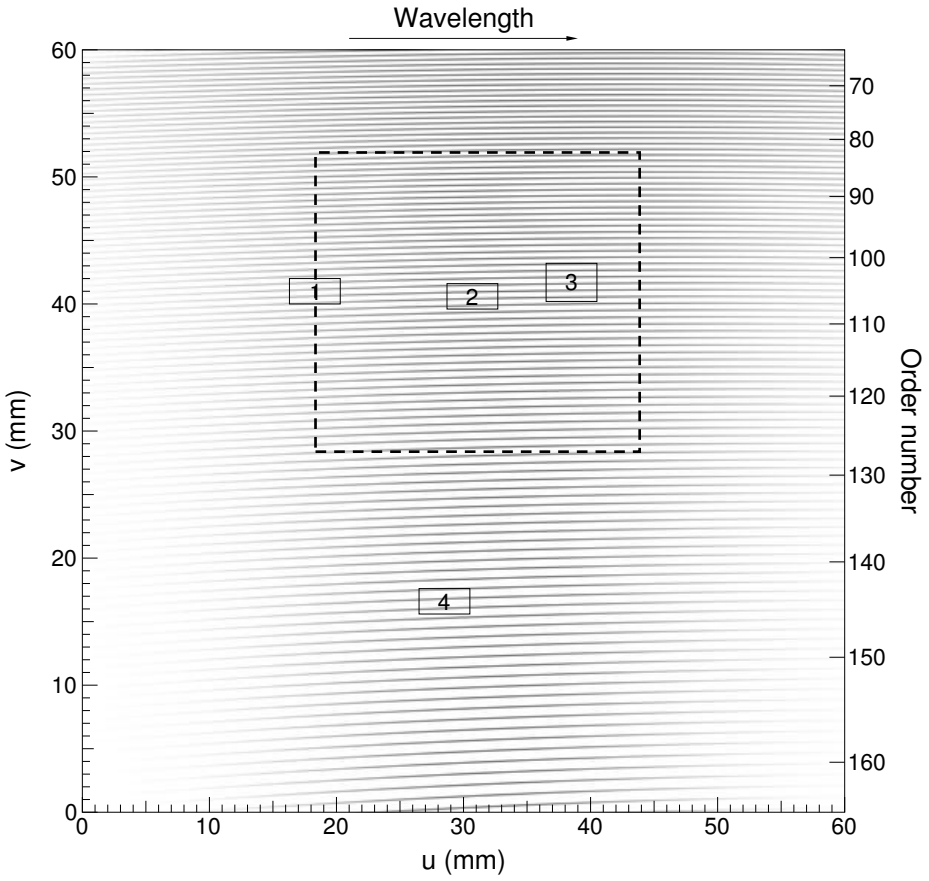

Figure 2-1: Position of images obtained with the Series 200 CCD camera in the full echellogram of HERCULES. The boxed numbers are the centres of the different CCD positions. The dashed box is the approximate position of the image obtained with the Series 200 CCD camera centred on position 2.

2.4 Final spectrum preparation

There is some additional processing of the data before analysis can begin. This processing involves normalisation of the spectra via continuum fitting and then removing the instrumental profile.

2.4.1 Continuum fitting

Continuum fitting or continuum normalisation is the process of fitting the data in each order so that the continuum level in the stellar spectrum is always unity. Any process in which the data is altered manually can introduce uncertain results. It is easy for the observer to inflict changes on the data that reflect their expectations. In a situation where many observations of the same star are available, an inspection of the mean spectrum after continuum fitting can be indicative of whether (on average) the continuum was fitted well. The easiest way of removing any possibility of forcing the data to match preconceptions is to remove the observer's input and automate the continuum fitting routine.

2.4.1.1 Automated continuum fitting

The automated continuum-fitting routine deals with each spectral order individually. It uses a fifth-order-least-squares polynomial fit to each spectrum then examines the residuals of the fit and removes any data points from the original pre-fit spectrum that fall outside two standard deviations from the mean of the residuals. A new fifth-order fit is then applied to the remaining data in the pre-fit spectrum. This procedure is then repeated again removing any data outside two standard deviations from the mean of the residuals. In the third, fourth and fifth repeats of the procedure, data points are removed that

fall below minus one times the standard deviation of the residuals, so that real spectral lines do not influence the position of the continuum. The final fifth-order polynomial fit to the remaining data from the pre-fit spectrum is used as the continuum fit. The original spectrum before removal of any data is divided by this continuum fit.

This routine (CONTBYRESID, see Appendix B) was extensively tested before use on any object but was known to have difficulties only in the case of a very broad-lined star on a spectral order with many lines (see Figure 2-2 for two examples of automated continuum fitting). To check that the automated continuum fitting routine had made a reasonable estimate of the continuum position, one of the highest S/N spectra for each object was manually continuum fitted for all orders using the routine outlined below. The mean automatically continuum fitted spectrum was then compared with this. If they were similar for each order, then the automated continuum fitting was considered to have been successful and the automatically continuum fitted spectrum was used for analysis. If only specific orders had difficulties, then those orders were manually continuum fitted.

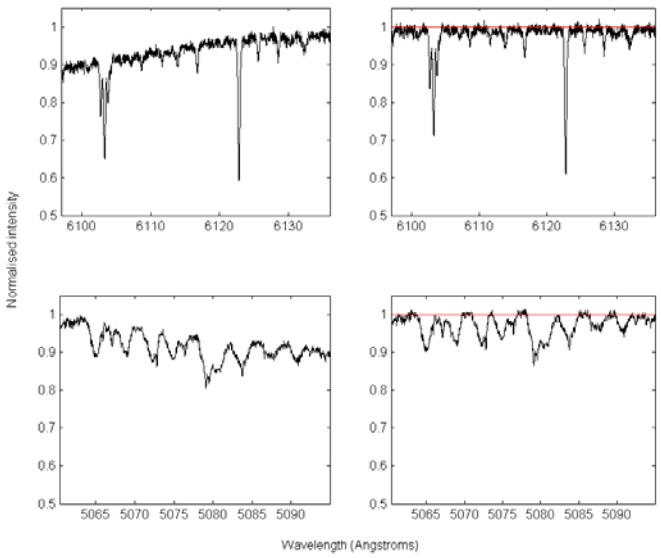

Figure 2-2: Automated continuum fitting examples. On the left are two pre-continuum fitted spectral orders of different stars: Top – HD17310, Bottom – QW Puppis. On the right are the data after automated continuum fitting. The top and bottom examples demonstrate an easy sharp lined star and a more difficult broad lined star respectively.

2.4.1.2 *M*

anual continuum fitting

Manual continuum fitting requires the observer to define, for a minimum of six points, where the continuum level is for each order being fitted. Using cubic spline interpolation, a line is fitted through the chosen points and this is taken as the continuum fit. The spectral order is then divided by the fitted line. Figure 2-3 displays an example where manual continuum fitting was necessary. This is implemented in the code SPLINECONTFIT, see Appendix B.

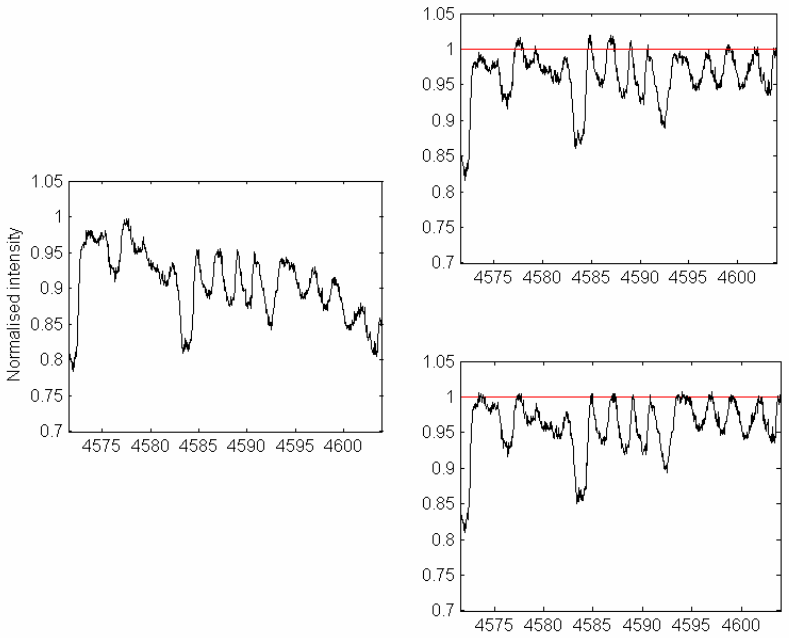

Figure 2-3: On the left is the pre-continuum fitted spectral order 124 of QW Puppis. On the right are: (top) the data after automated continuum fitting, (bottom) the data after manual continuum fitting. The two sets of continuum fitted data do not agree well. In this case every order 124 of the observations of QW Puppis was manually continuum fitted.

2.4.2 Removing the instrumental profile

When examining individual spectral lines obtained with different instruments it is necessary to eliminate the effects of each spectrograph's instrumental profile. Having done this means the data can be considered to contain only information relating to the star observed, allowing data from the different instruments to be compared directly.

In the case where observations are taken using only one instrument it is not necessary to remove the instrumental profile as long as this is taken into consideration for any analysis of the line profile. This is because, while the

instrumental profile of a given spectrograph will change from night to night, the changes are small and are not worth removal due to the possible errors introduced by removing the instrumental profile. This is particularly the case for the HERCULES spectrograph, which is known to be very stable.

For the multi-site campaign data it was necessary to remove the instrumental profile from both the SAAO and MJUO observations to allow them to be compared directly.

The procedure outlined in pages 243-250 of Gray (1992) was followed. The steps are explained in the following paragraphs.

The observed spectrum obtained from the spectrograph D(λ) can be considered to be the stellar spectrum F(λ) convolved with the instrumental profile I(λ), namely

$$D(\lambda) = I(\lambda) * F(\lambda) . \tag{2.1}$$

In Fourier space the convolution can be considered as a multiplication. So where d(σ), i(σ) and f(σ) are the respective Fourier transforms of D(λ), I(λ) and F(λ) we have

$$d(\sigma) = i(\sigma) f(\sigma) . \tag{2.2}$$

Were it a simple case, the effects of the instrumental profile could be removed easily using

$$f(\sigma) = \frac{d(\sigma)}{i(\sigma)} .$$

(2.3)

However noise complicates this process by increasing the amplitudes in the high frequency region where the instrumental profile is small. The effect is that the inverse transform of f(σ) obtained from a direct division of d(σ) by i(σ) results in a stellar spectrum primarily composed of noise. To counter the effects of noise on the reconstruction of our stellar spectrum we use the Fourier noise filter described by Gray (1992) φ(σ). This results in the situation

$$f_2(\sigma) = \frac{d(\sigma)\varphi(\sigma)}{i(\sigma)}.$$

(2.4)

The difference between $f_2(\sigma)$ and f(σ) is due to the error introduced by the filtering process. The choice of the filter is key to the reconstruction process where 'the optimum filter minimizes the square of the errors between the true transform and the restored-filtered transform.' (Gray 1992). Gray (1992) describes a reasonable filter

$$\varphi(\sigma) = \frac{1}{1 + (B/A)^2 10^{2\alpha_0^2\sigma^2}},$$

(2.5)

where *B* describes the noise level defined for this thesis as the mean Fourier amplitude of d(σ) over the range 2.5-5.0Å^{-1}. *A* is the zero ordinate of d(σ) and α_0 is selected by examining the Fourier transform of a least-squares Gaussian fit to d(σ), see Figure 2-4 and Figure 12.10 of Gray (1992). A Gaussian of the form

$$G = a \cdot e^{\left(\frac{2\sqrt{\ln 2}(\lambda - b)}{FWHM}\right)^2} \tag{2.6}$$

is used for the fitting, where *a* is the depth of the fit to the line, *b* is the position in Angstroms of the centre of the fit to the line, λ is the vector of wavelengths that describe the line and *FWHM* is the full width at half maximum of the fit to the line.

Following Gray (1992) an inspection of Figure 2-4 implies a value of $\alpha_0 = 1.4$ would be suitable value for filtering the line profile shown. Upon examination of a large number of profiles filtered using $\alpha_0 = 1.4$, it was felt that this level of filtering may be too heavy and the resulting filtered profiles may have had some real signal removed. To ensure that the filtering process was not removing signal a slightly lower value for α_0 was chosen than that which would have been selected based on Gray (1992). For example, in Figure 2-4 the value $\alpha_0=1.2$ was selected rather than $\alpha_0=1.4$. A α_0 value was selected for each star by inspection of a few Fourier transforms of Gaussian fits to line profiles such as that shown Figure 2-4.

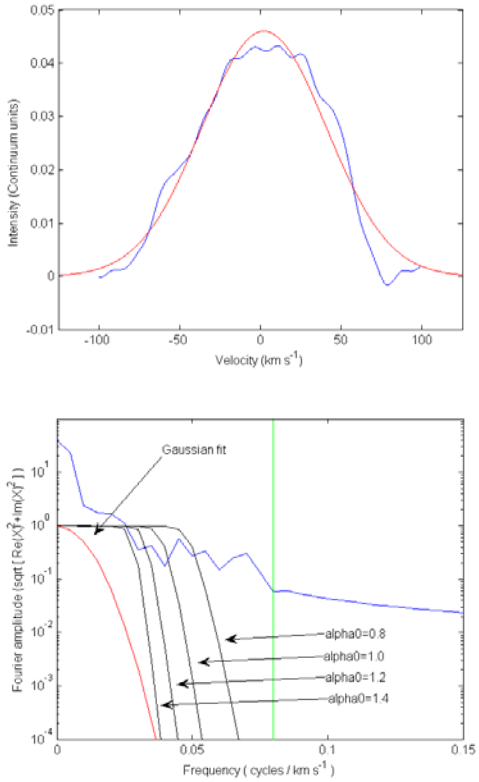

Figure 2-4: Top: An observed line profile of QW Puppis (blue) and the least squares Gaussian fit (red). Bottom: The Fourier transform of the line profile (blue) and the fitted Gaussian (red) and a selection of filters for various α_0 values (black).

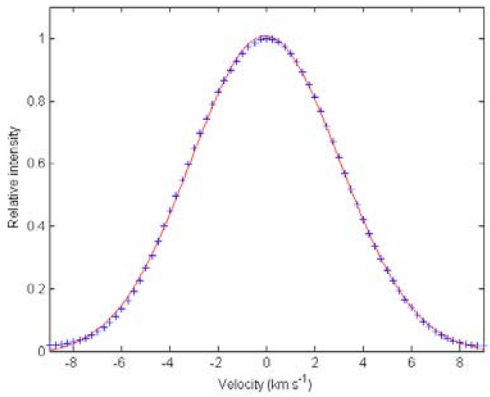

Figure 2-5: The cross-correlation function resulting from combining 8 thorium lines (blue pluses) and the Gaussian fit to the data (red). The FWHM from the fit is used for defining the spectrograph response function.

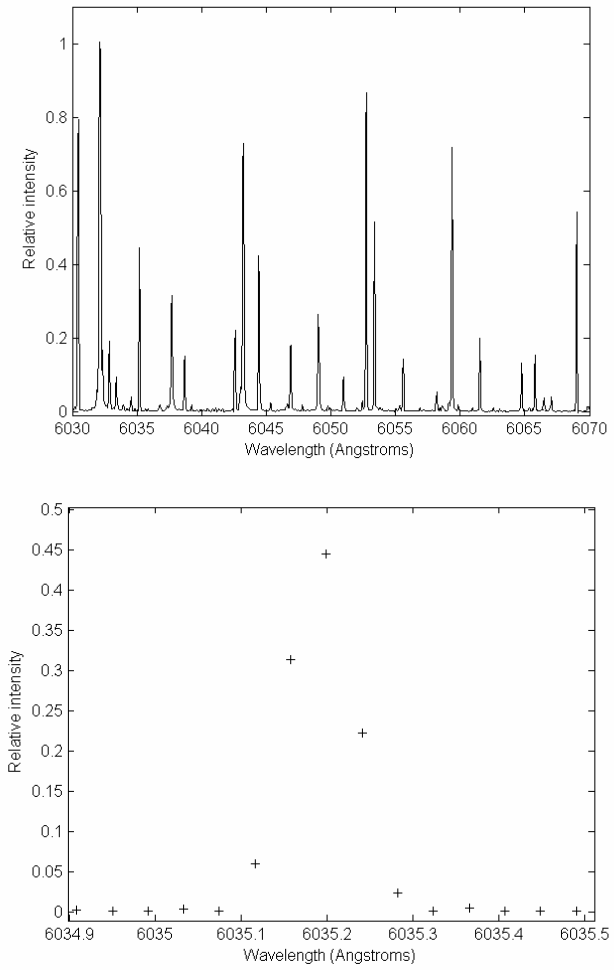

Figure 2-6: Top: A section of a thorium-argon wavelength calibration spectrum from the HERCULES spectrograph using the Spectral instruments 200 series camera. Bottom: A single thorium line taken from the above section of spectrum. The single line is not well sampled.

Once the filter is defined then the instrumental profile must be determined. The instrumental profile can be obtained from a thorium line taken from one of the wavelength calibration observations (see Figure 2-6, top panel). The instrumental profile was approximated by a Gaussian of the same form as in

Equation 2.6. Since a single thorium line is poorly sampled (see Figure 2-6, bottom panel), a cross-correlation technique, is used to combine the information from eight thorium lines resulting in Figure 2-5. The cross-correlation function is much better defined than the single thorium line and the FWHM of the instrumental profile is taken from the Gaussian fit to this cross-correlation function.

Chapter 3
Determination of the stellar line profile

Successful spectroscopic mode identification relies on high S/N data that is well sampled in time. The analysis requires only a single line profile. In a stellar spectrum that covers a large wavelength range, such as the ones obtained for this thesis, it is possible to combine data from different spectral lines to get a single, much higher S/N spectral line profile. In order to get the most out of the data available, an investigation into the best method of extracting a line profile from an échelle spectrum was carried out.

3.1 Methods of determining the spectral line profile

There were five methods of line profile determination examined for this thesis and these are summarised below

Single line profile: A single good line profile available in a spectrum is used for analysis. The properties required for the line profile are: unblended, isolated to allow good continuum fitting; strong so as to be well defined; and known to be sensitive to the presence of non-radial pulsations. An example of this analysis is the use of the Si III 4553Å line in Section 5.2 of this thesis. In this case the other lines in the Si III triplet were not available to be combined

with the Si III 4553Å line. The Si III 4553Å line is known to be insensitive to temperature changes (Aerts et al. 2004; De Ridder et al. 2002), so its line profile variations (LPVs) are due to the projected velocity field from the NRP.

Added line profile: A few line profiles, satisfying the requirements for the single line profile, can be added together if they have been shown to vary similarly in their phase and amplitudes for both the equivalent widths (as a fractional change) and velocities. The addition in velocity space gives increased S/N compared to a single line profile. An example of this is in the spectroscopic analysis of FG Vir (Zima 2005) where four Fe I lines were added together for analysis.

Cross-correlation with a mean or synthetic spectrum: A spectrum of an object can be cross-correlated with the mean spectrum of all observations of that object or with a synthetic spectrum. This produces a profile which can be examined for velocity variations to determine frequencies present in the original spectrum (Mantegazza and Poretti 2002). The amplitudes of the frequencies should be determined from the original profiles because those extracted from the cross-correlation function (hereafter CCF) profile will be of smaller amplitude. This is because of the broadening effect that occurs when a mean or synthetic spectrum is used as a template (pg 100, Zima 2005). This method requires that there are sufficient observations for a good mean spectrum, or that a synthetic spectrum can be well fitted to a significant portion of the spectrum. This method is fast and easy to implement and it produces a very high S/N profile. The drawback to this method is that the resulting CCF can not be considered directly representative of line profiles in the spectrum of the star. Consequently, this method is not investigated further in this thesis.

Cross-correlation with delta functions positioned at the rest wavelengths of the lines present in the spectrum: This is used to obtain a profile which represents all the lines with delta functions in the template. It does not introduce broadening so the extracted profile can be compared with an individual line profile. The extracted profile can be expected to have the same amplitudes and phases as those lines in the template. This procedure also requires that all the lines considered are varying in phase and with similar amplitudes for both the equivalent width and velocity measures. This method does allow for easy inclusion of lines though if any line in a blend is used then all lines in that blend should be included. This method is also easy to implement. It requires rest wavelengths for a significant proportion of the lines in the region used for the cross-correlation, which are available in synthetic spectra line lists.

Cross-correlation with delta functions positioned at the rest wavelengths of the lines present in the spectrum and scaled to the depths of the lines that they are positioned to represent: This is an attempt to improve the CCF obtained using the method above by weighting the function in favour of the stronger lines. It has all the requirements of the method above. It was included to examine whether it produces a more representative profile to that in the spectrum than the unit-sized delta functions.

3.2 Simulations of line profile recovery

A number of stellar spectra were simulated to determine which method produces the profile that best represents the real stellar line profile. Only the methods that result in a profile similar to the real stellar profile were

considered: the single profile, added profile, unit delta-function CCF method (hereafter unit CCF) and scaled delta-function CCF method (hereafter scaled CCF). The extracted line profile was then compared to the real stellar profile used to produce the synthetic spectrum and a measure was made of their similarity.

The simulated spectrum was produced using a program TESTPROFILERECOVERY (see Appendix B) written in MATLAB. The code takes a single line profile as its input and randomly places a specified number of copies throughout a supplied range of 'wavelengths' (see Figure 3-1). The original line is first normalised and the copies are randomly scaled to cover a range of depths up to a maximum that is specified as an input to the program. Line blending is simplified to the linear addition of line intensities. A template of the spectrum is generated with delta functions positioned at the centre of the lines used for the cross-correlation. Both unit and scaled delta function templates are made. The spectrum and the templates are cross-correlated using the MATLAB function XCORR for the unbiased estimate of the CCF

$$CCF_{xy}(m) = \begin{cases} \sum_{n=0}^{N-m-1} \frac{1}{N-|m|} x_{n+m} y_n^* & m \geq 0 \\ CCF_{yx}^*(m) & m < 0 \end{cases}, \tag{3.1}$$

where x and y are two same-length vectors describing the profiles and m is the shift of the vectors relative to each other. A negative shift results in the reversed conjugate of the calculation compared to the case of a positive shift.

A 'best line' is selected from the simulated spectrum by attributing each line with a 'goodness' value defined as

$$goodness = dist^2 \cdot depth \tag{3.2}$$

where *dist* is the distance from the line to the nearest line and *depth* is the depth of the line. In this way isolated lines are preferred over deep lines. In most cases this selects one of the best lines in the synthesised spectrum for testing.

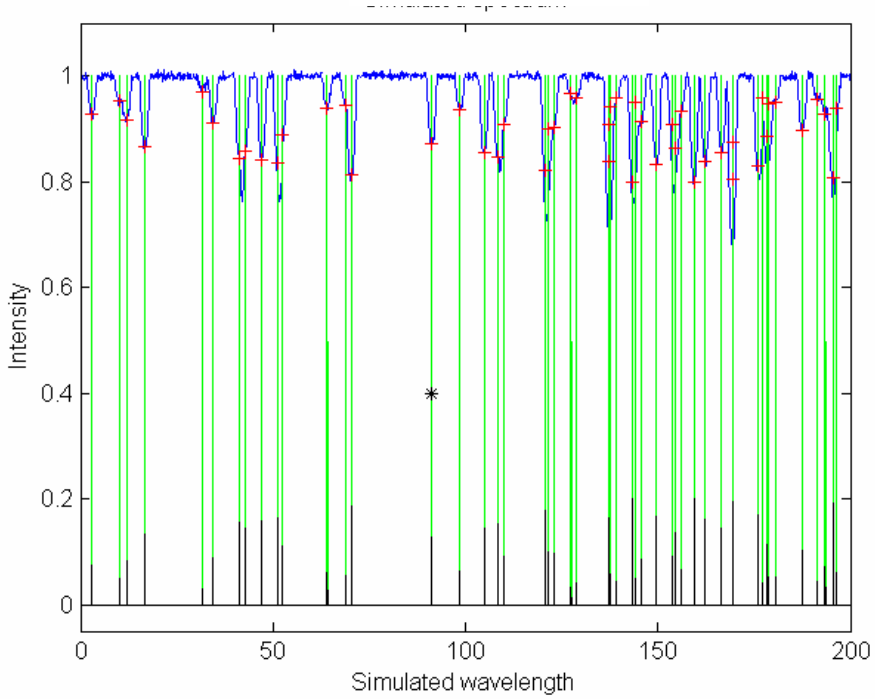

Figure 3-1: Example of simulated spectrum for the cross-correlation of the unit delta function template (green) and scaled delta function template (black) with a simulated spectrum (blue). The red crosses indicate the depths and positions of the lines. The black asterisk shows the 'best line' used for comparison with the CCFs. The input line profile is a Gaussian with a FWHM of 0.2 broadened using the Gray (1992) broadening function to $V_{rot}\sin i$ =60 km s^{-1}.

To more fairly compare the best line with the CCFs, the best line profile is smoothed using the same algorithm outlined in Section 2.4.2 which uses the Fourier filtering method of Gray (1992).

Next a comparison is made between the 'best line' selected from the simulated spectrum and the real spectral line profile, and the unit and scaled cross-correlation functions with the real spectral line profile using a defined similarity statistic *t*. The numerical representation *t,* or how similar a CCF or 'best line' is to the inputted line, was defined as

$$t = \frac{\sum_{i=1}^{n} \sqrt{\left(CCF_i - x_i\right)^2}}{n}, \tag{3.3}$$

where *x* is the inputted line profile and *n* is the number of bins in the CCF and the input line profile. This is simply the mean-root-squared difference between the profiles. A value of zero would indicate a perfect match. To give some insight into the sensitivity of *t*, Figure 3-2 shows a plot of the real spectral line profile, the best line, unit CCF and scaled CCF line profiles for a typical simulation of a $V_{rot}\sin i$ =60 km s^{-1} line profile. The *t* statistic for each line extracted is given at the top of the figure.

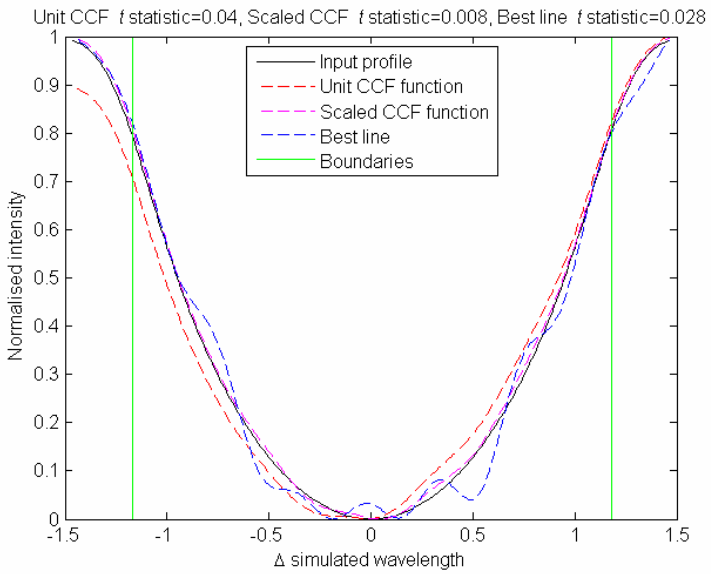

Figure 3-2: Examples of the input line profile (black), the unit delta function CCF line profile (red dashed), the scaled delta function CCF line profile (magenta dashed) and the best line extracted profile (blue dashed). The green lines mark the boundaries for the calculation of *t* which is set to 0.8 of the height of the input profile. $t < 0.03$ is treated as a reasonable estimate of the input line profile, $t < 0.02$ is a good estimate of the input line profile, $t < 0.01$ is an excellent estimate of the input line profile.

There are a number of parameters defining each simulated spectrum.

Number of lines *nlines*: This is simply the number of lines in the simulated spectrum that are used for the cross-correlation.

Line density ρ: This is the number of lines *nlines* divided by the wavelength range of the simulation λ_{range}.

$$\rho = \frac{nlines}{\lambda_{range}}$$

Blending parameter η: If a single line is well described (defined to 0.99 of its height from its base) over a wavelength range of λ_{line} then η is the line density

ρ multiplied by λ_{line}. It is a ratio of the size in Å that would be needed to describe all the lines in the spectrum, if they were all unblended and side by side, divided by the actual range (in Å) of the synthesised spectrum. An increase in the blending parameter means an increase in the amount of line blending occurring in the spectrum.

Noise: This is the standard deviation of the normally distributed noise added to the simulated spectrum. The selections ranged from 0 to 0.1.

Continuum error amplitude *cerramp*: This is the combined amplitude of two low frequency sinusoids added to the synthesised spectrum to simulate continuum fitting errors.

The standard deviation of the delta function displacement *dispstd*: The standard deviation of the normally distributed displacement in bins applied to the delta function template.

The maximum depth of the lines *depth*: The line depths used were randomly generated for each line between 0.02 and *depth*.

Additionally the program can simulate noise by adding randomly generated, normally distributed noise that can be scaled to produce any S/N. It simulates continuum fitting errors that, due to the random nature of the positioning of the lines, are simply simulated by the addition of two randomly generated low frequency sine waves whose amplitudes add to a supplied value (*cerramp*) to the final intensity spectrum. Increasing *cerramp* increases the simulated continuum fitting error. It also simulates rest wavelength errors by randomly

displacing (with a normal distribution) the positions of the template spectrum's delta functions (*dispstd*).

3.2.1 Results of the simulations

3.2.1.1 Basic simulations

The three profiles (best line, unit CCF and scaled CCF) were compared with the input line profile and the *t* statistic was determined. A grid of parameter values were tested with each parameter set run 300 times to get a good sample of the line profile recovery for each method and for each parameter set. In these trials no continuum fitting errors or displacement of the delta functions were used. The parameter ranges tested were:

input profile = Broadened Gaussian with a pre-broadening FWHM of 0.33

$V_{rot} \sin i$ = [5 10 20 60 100] km s^{-1}

λ_{range} = [50 100 200]

nlines = [25 50 100 200 400]

noise = [0.01 0.03 0.05]

dispstd = 0 pixels

cerramp = 0

depth = [0.1 0.2 0.3]

These values were chosen to resemble the range of γ Dor spectra obtained during observing.

To display the results of the simulations, "box and whisker" graphs are used. In Figure 3-3 there is an example of a typical distribution of *t* values and how

that distribution is represented as a “box and whisker” plot. The “box” displays the interquartile range and the median (red line). The 95% confidence interval for the median is marked by the notches in the side of the box (too small to be seen in Figure 3-3, but more obvious in Figure 3-4). The “whiskers” in each plot extend out to a maximum of twice the interquartile range (twice the size of the box). Values outside the “whiskers” are considered outliers and the percentage of data that are outliers is displayed in brackets (to the nearest whole percent) in the x-axis label for each “box and whisker” plot.

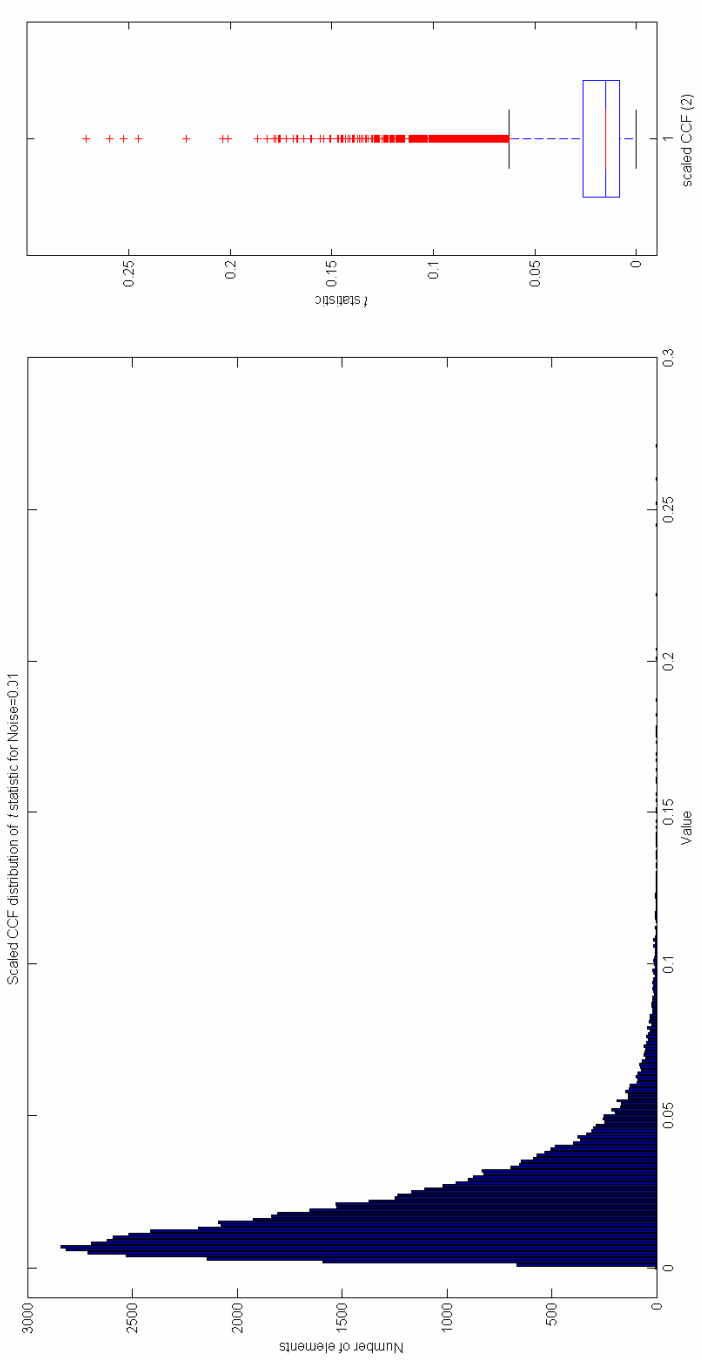

Figure 3-3: A typical distribution of t values for a trial grid of parameters (bottom) and its representation as a box and whisker graph (top). The number in brackets in the x-axis label on the right is the percentage of data falling outside the whiskers, represented as red +'s in the plot.

In Figure 3-4 the *t* statistic is grouped according to the noise value added to the data. All of the *t* statistic data that falls into a given category, in this case each noise value, is plotted as a box and whisker graph for each profile. The number of *t* values represented by each box and whisker plot is listed in the caption. Figure 3-4 shows that in the case of a small amount of noise (*noise*=0.01) a single line profile does an excellent job of estimating the input profile. Some of the single line data for low noise gives poor fits because some very high blending parameter trials (low spectrum size, high line numbers) are included. However, the median for all the low noise trials is still very low. Not surprisingly the single line profile shows considerable dependence on the noise level in the data. In contrast both of the CCF methods show little dependence on the noise level of the data. This is to be expected since they combine information over a lot of positions which average out the noise introduced. The scaled delta function CCF method performs slightly, but significantly, better in this and all other cases relative to the unit delta function CCF method.

In Figure 3-5 the best line shows increasingly worse profile recovery for $V_{rot}\sin i \geq 20$ km s^{-1}. The large outlier percentage is again the high blending parameter trials. Interestingly line recovery for the CCF methods improves very slightly for $V_{rot}\sin i$ =10 - 20 km s^{-1} over 5 km s^{-1}. For higher values of $V_{rot}\sin i$ >60 kms^{-1} the recovery begins to deteriorate.

Figure 3-6 shows the dependence on line depth for profile recovery. As expected, the single line shows a strong dependence, with increasing line depth producing better profile recovery. The CCF methods are surprisingly insensitive to the depth of the lines with only a small improvement in profile recovery with increasing line depth.

Figure 3-7 and Figure 3-8 demonstrate the trends for increasing number of lines in the synthesis and increasing the spectrum size of the synthesis. They show opposite trends from each other due to the fact that each parameter is tested over the range of all the other parameters, so increasing the number of lines effectively increases the blending parameter of the trials as the spectrum size tested remains the same for each box and whisker plot. The same is true for the increasing spectrum size where only the blending parameter is decreasing.

These figures clearly show that the single line is very sensitive to the blending parameter, with profile recovery good at low blending and very poor at high blending. The CCF methods also recover the profile better at lower densities, but have a much lower dependence on the blending parameter.

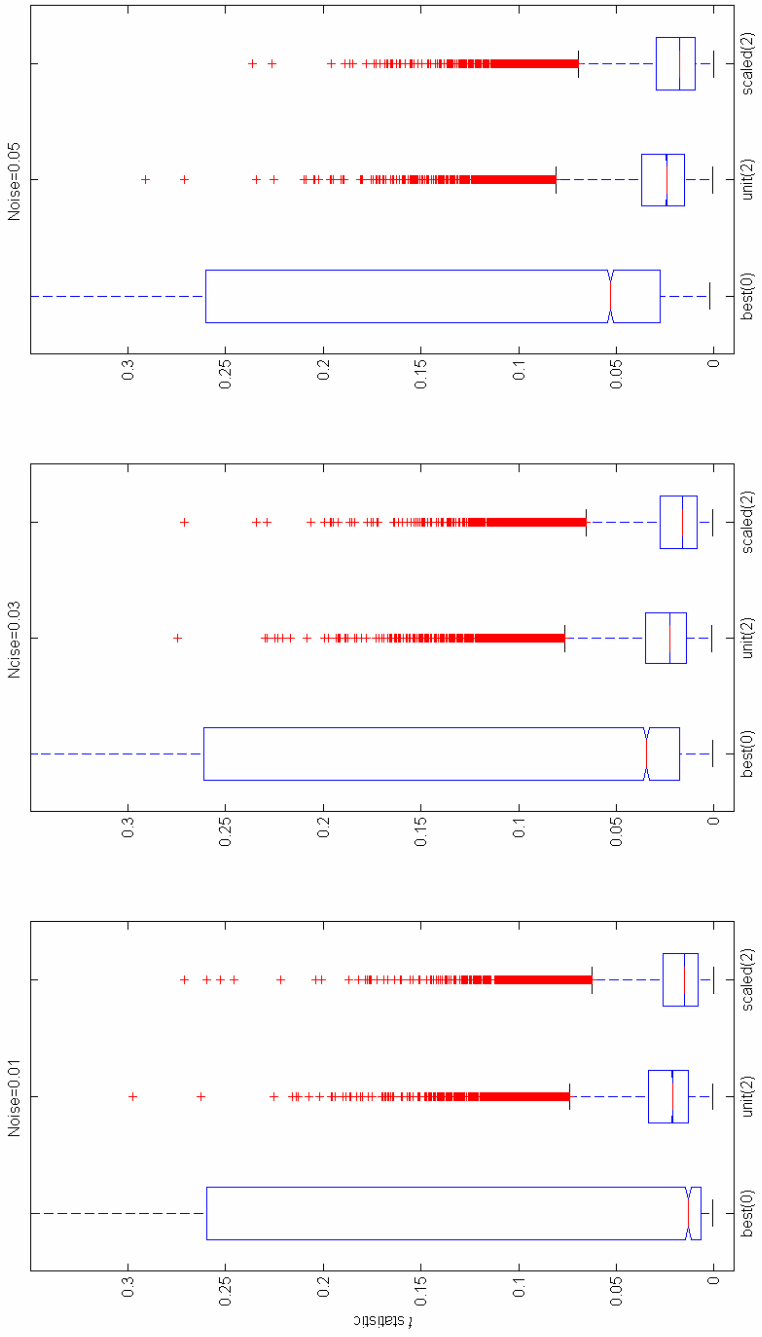

Figure 3-4: Box and whisker plots showing the dependence of the best line, unit CCF and scaled CCF methods on the spectrum noise. Each "box and whisker" plot represents 67 500 trials.

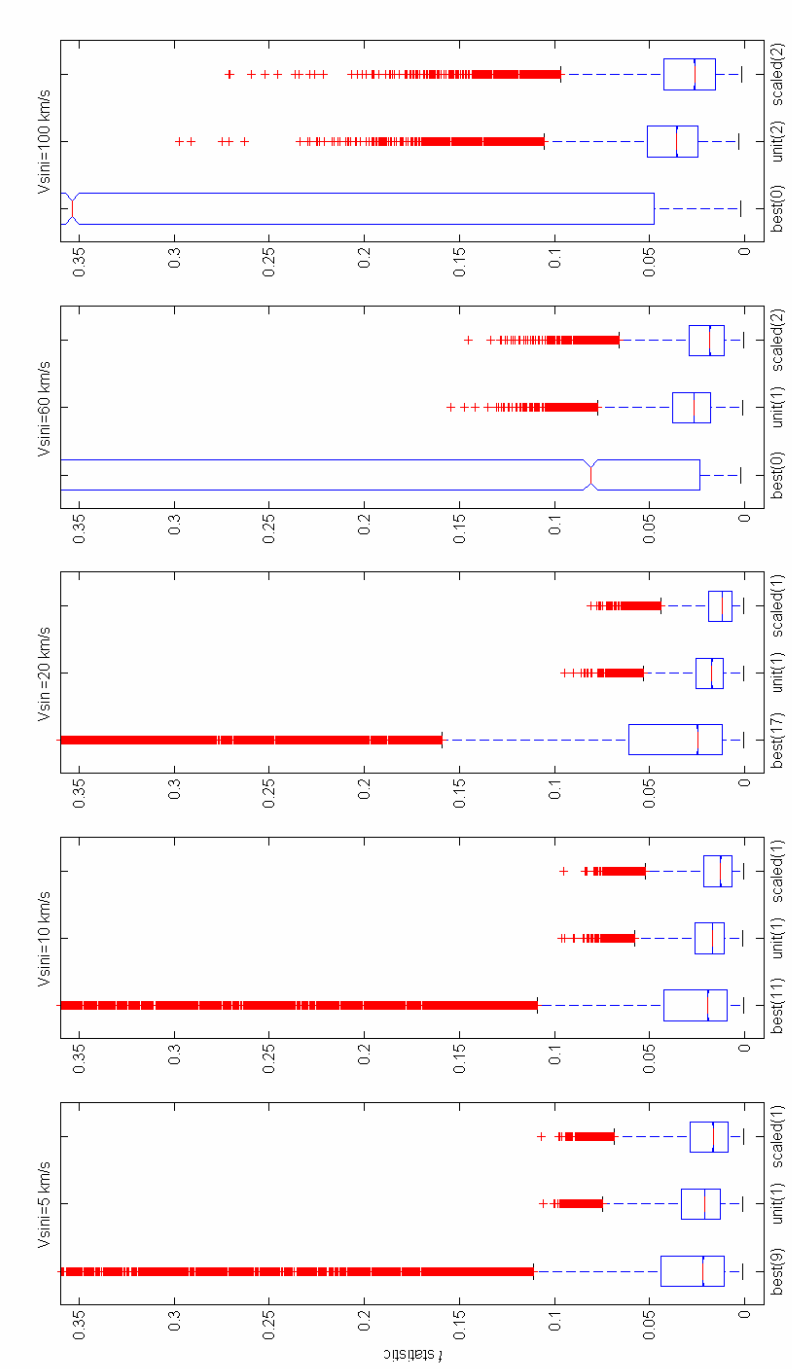

Figure 3-5: Box and whisker plots showing the dependence of the best line, unit CCF and scaled CCF methods on the $V_{rot}\sin i$ of the line. Each "box and whisker" plot represents 40 500 trials.

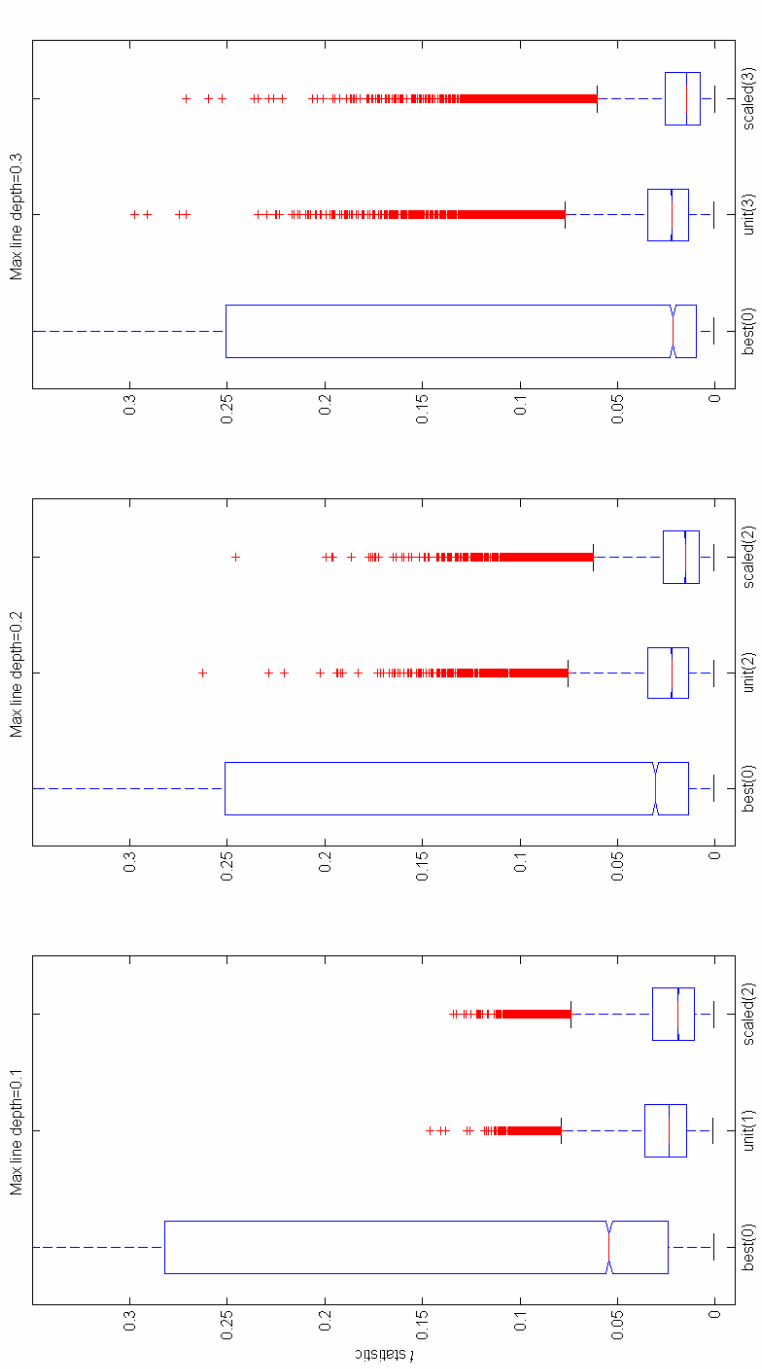

Figure 3-6: Box and whisker plots showing the dependence of the best line, unit CCF and scaled CCF methods on the maximum line depth. Each "box and whisker" plot represents 67 500 trials.

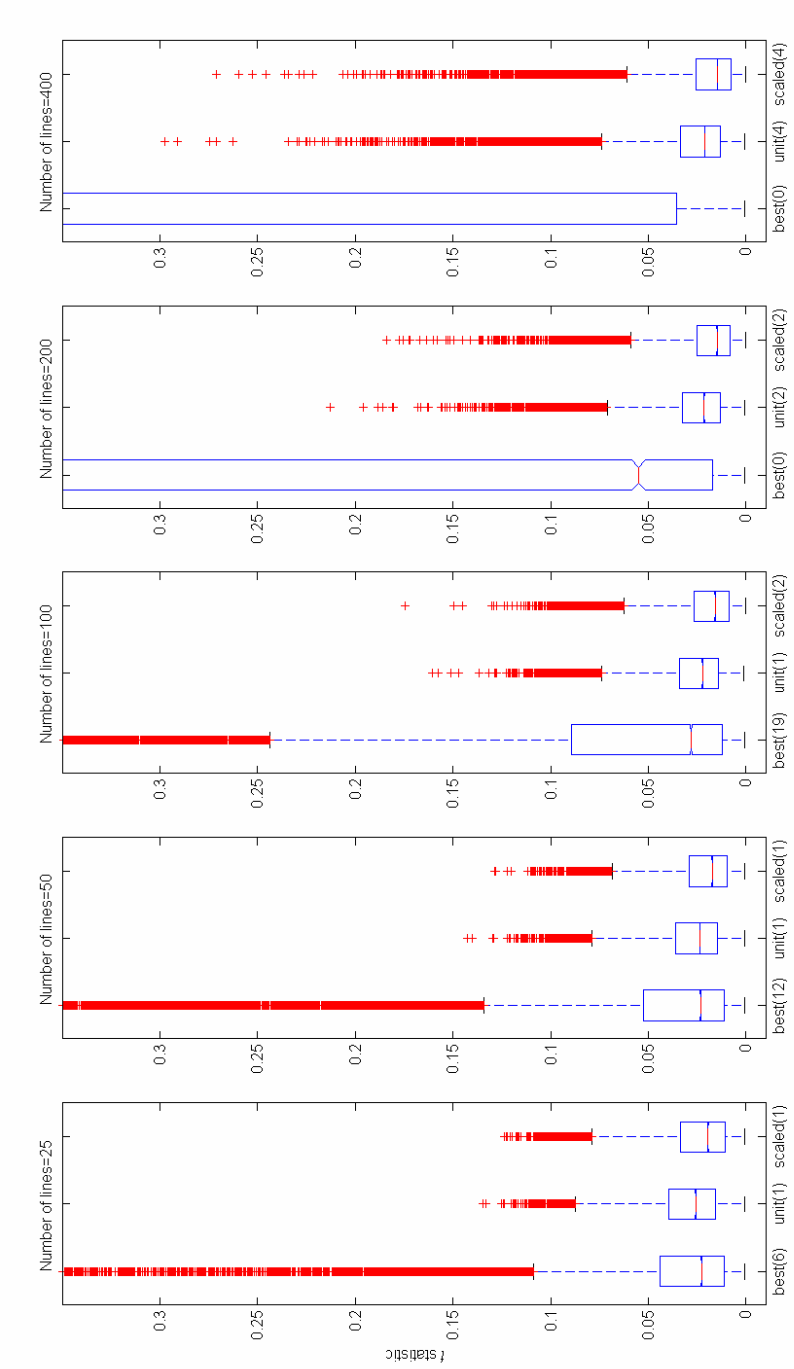

Figure 3-7: Box and whisker plots showing the dependence of the best line, unit CCF and scaled CCF methods on the number of lines in the synthetic spectrum. Each "box and whisker" plot represents 40 500 trials.

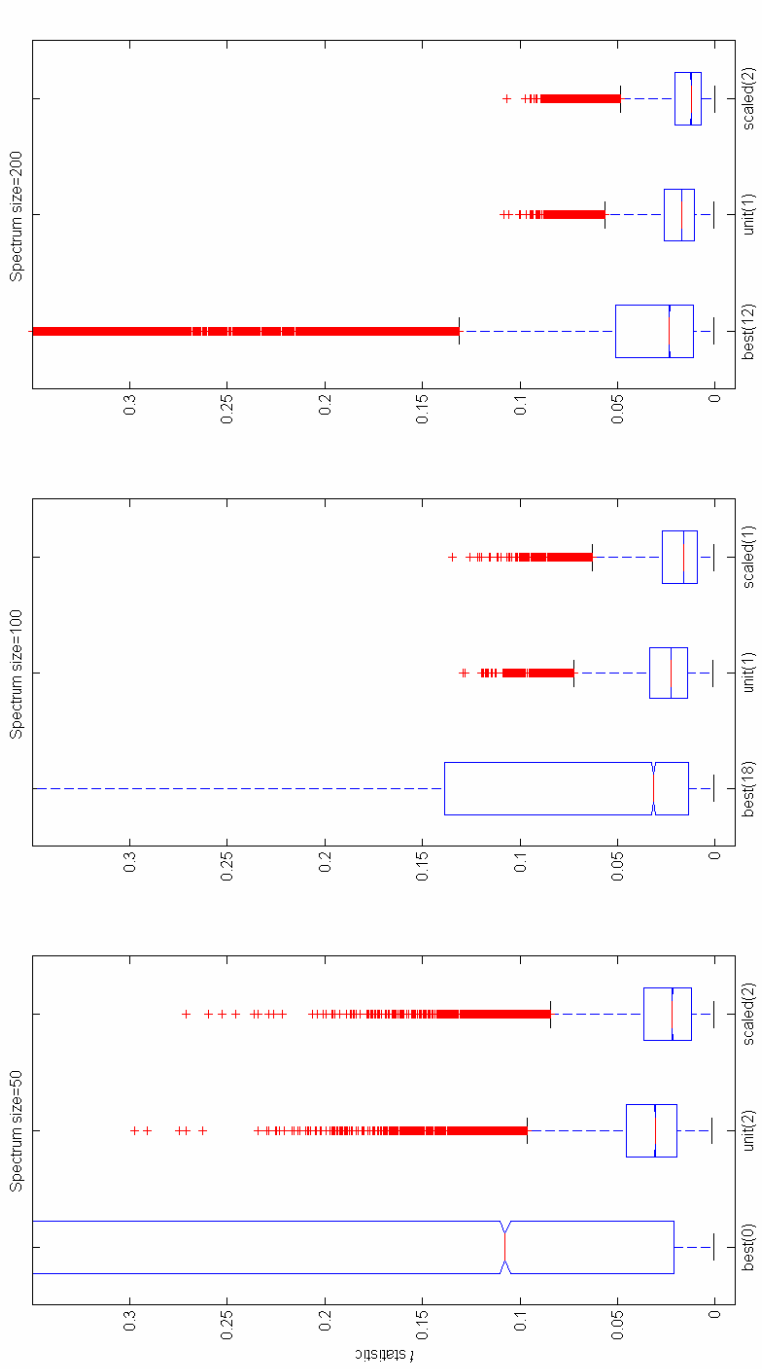

Figure 3-8: Box and whisker plots showing the dependence of the best line, unit CCF and scaled CCF methods on the size of the synthetic spectrum. Each "box and whisker" plot represents 67 500 trials.

3.2.1.2 Effects of continuum and rest wavelength errors

To investigate the dependence of line recovery on continuum fitting errors and normally distributed errors in the rest wavelengths of lines, another set of trial parameters was run. This time the range for the parameters already tested was smaller to reduce computation time. The ranges tested were:

Input profile = Broadened Gaussian with a width parameter of 0.2
$V_{rot}sin$ i = [20 60] km s^{-1}
λ_{range} = [100 200]
nlines = [25 50 100 200]
noise = [0.01 0.03]
cerramp = [0.01 0.03 0.05 0.10]
dispstd = [1 3 5] pixels
depth = 0.2

The values other than *cerramp* and *dispstd* were again chosen to closely reflect the observations obtained of γ Dor stars.

In Figure 3-9 it can be seen that the single line is very slightly affected by the increasing continuum fitting error. The CCF methods are again relatively independent due to the averaging over a number of line profiles.

Figure 3-10 shows the dependence of the methods on the rest wavelength error. The single line *t* results are not considered very relevant in this situation as the line profile is simply red or blue shifted by the wavelength error. This would result in an incorrect mean radial velocity but would have no effect on the recovery of distortions of the line profile. The CCFs show a very small

dependence on the rest wavelength error. The increasing error broadens the resulting CCF making for worse profile recovery. It would also smear out any distortions of the line profile due to summing different parts of each profile for a given delta function.

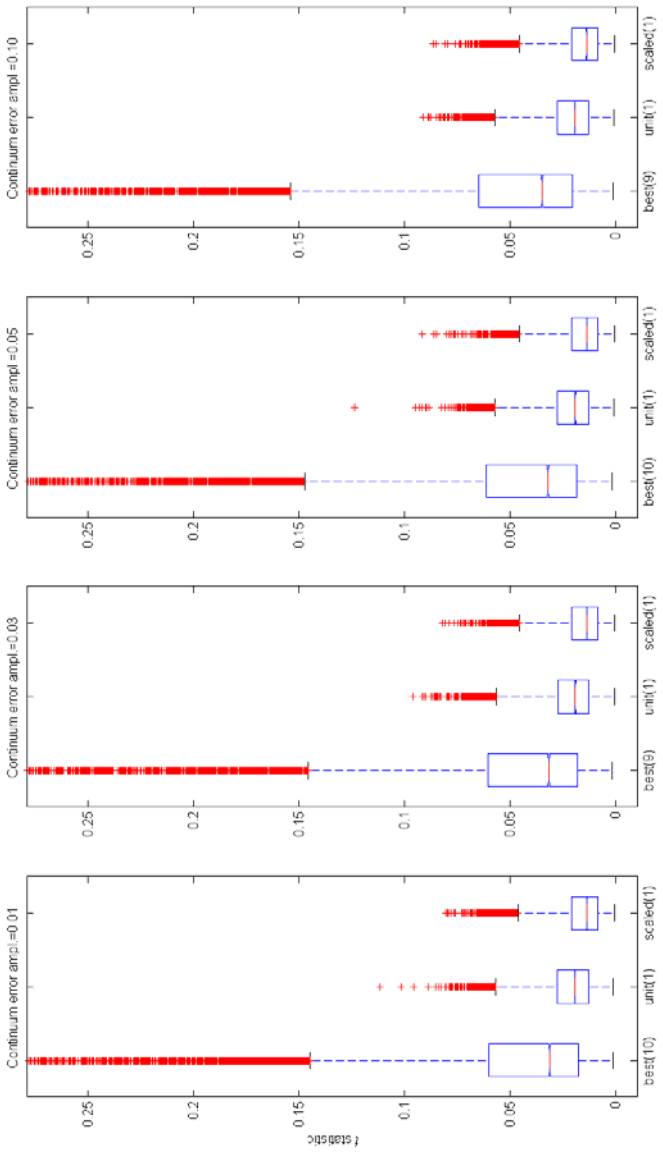

Figure 3-9: Box and whisker plots showing the dependence of the best line, unit CCF and scaled CCF methods on the continuum error amplitude. Each "box and whisker" plot represents 28 800 trials.

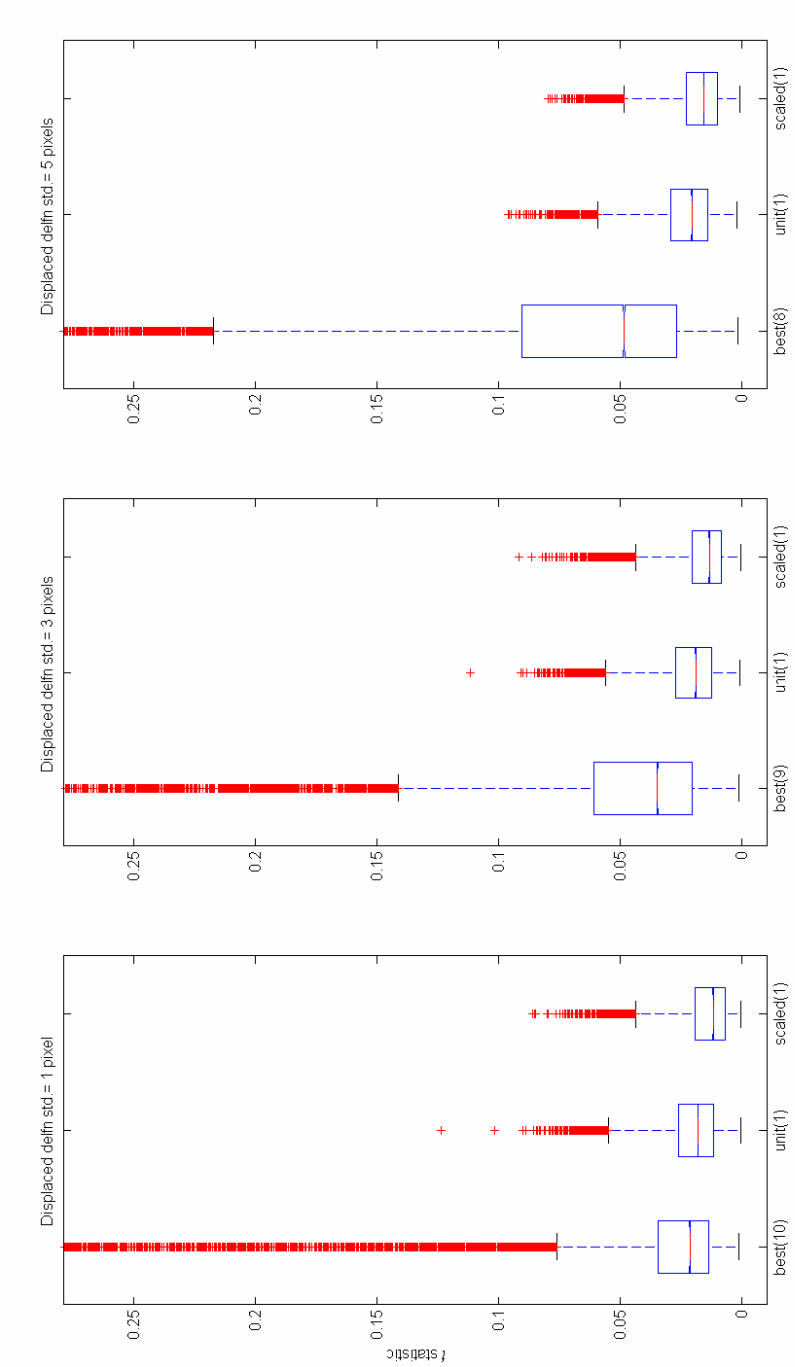

Figure 3-10: Box and whisker plots showing the dependence of the best line, unit CCF and scaled CCF methods on the standard deviation of the delta function displacement. Each "box and whisker" plot represents 38 400 trials.

The results of every test indicate that the scaled delta function CCF is significantly better at determining the input profile than the unit delta function CCF. In the case of very low noise (*noise* ≤ 0.01) and medium to low $V_{rot}\sin i$ ($V_{rot}\sin i \leq 20$ km s^{-1}) the single line method can be as good as the scaled method for determining the line profile.

It is concluded from these tests that, of the methods considered, the best tool for line profile determination from a spectrum is the scaled delta function CCF.

3.2.2 Application of the scaled delta function CCF

There are a number of assumptions made in the above trials that must be discussed before the scaled CCF method can be applied to real data. The method assumes that: a template with appropriately scaled delta functions can be produced for each object for which this method is used; that lines at different wavelengths have the same shape; and that lines from different species or with different excitation potentials exhibit the same pulsational deformation. Some of these assumptions are known to be incorrect given certain conditions, so it remains to examine over what range of situations the scaled CCF method can be applied. Each of these assumptions is discussed in this section.

To produce a scaled delta function template for each object to be examined based on the spectra obtained can be a difficult task. Each stars mean spectrum needs to be reasonably well fitted using spectrum synthesis software over the entire wavelength range of the template. Once the spectrum is reasonably well

fitted the wavelength and depth for each line in the synthesised spectrum can be obtained.

In the case of the γ Dor candidates examined in this thesis the same template was used for all the scaled CCF analyses. This was considered sufficient because when appropriate broadening levels were applied to the synthesised spectrum a reasonable match to each of the γ Dor stars was obtained.

To further improve the synthetic spectrum's match to each individual star's spectrum would have involved abundance changes which would be a very long and difficult task over the large wavelength range 4500-7200Å. The template was created using a synthetic spectrum of a solar abundance star with stellar parameters Teff = 7000 K, log g = 4.0, [Fe/H] = 0.0 (solar) and microturbulence = 2.0 km s^{-1}. The synthesis software was MOOG (Sneden 1973) using a Kurucz stellar model. The spectrum was matched to the observed mean spectrum of HD17310. This star was used because it was a low $V_{rot}\sin i$ star, and hence had less line blending, and had been observed with the Series 600 CCD at MJUO on HERCULES, so its spectra covered the full wavelength range being used. The output obtained from MOOG was the synthetic spectrum using the SYNTH driver and equivalent widths for each line using the EWFIND driver.

To determine each line's depth in the entire synthetic spectrum, a Gaussian was fitted via a least-squares method to a number of isolated lines in the unbroadened synthetic spectrum. A linear relationship was used to approximate the synthetic line depth vs. synthetic line equivalent width relationship and so a delta function table of wavelengths and depths was created. The delta function depths were then scaled to closely match the

spectrum of HD17310. Only delta functions with a depth greater than 0.073 in the unbroadened synthetic spectrum were included in the delta function template because these lines were the weakest lines just visible in the spectra of the observed low $V_{rot}\sin i$ stars. The regions with hydrogen lines or telluric lines were not included in the delta function template. For the MJUO observations with the Series 200 CCD the delta function template did not include lines that fell in the inter-order gaps or at the very edge of the orders. The complete list of wavelength species and depth is available in Appendix C.

Different wavelength regions will have lines of different species and excitation potentials but these are discussed separately. The same line species with the same excitation potential but from a different wavelength region may have different line shape. This is due to line broadening mechanisms which come from velocity distributions such as thermal broadening, micro- and macro-turbulence and rotational broadening. The combined effects of these velocity distributions are approximately the same for each line, ignoring saturated spectral lines, hence lines are of similar shape in velocity space but not in wavelength space. To manage this, the scaled CCF is applied after transforming the observation into logarithmic space by taking the natural logarithm of the wavelength values (Skuljan et al. 1999; Skuljan et al. 2000).

The rotational broadening curve of Gray (1992) demonstrates that rotational broadening has a wavelength dependence that is not easily solved by combining the lines in logarithmic space. To examine whether it is theoretically reasonable to combine lines from different wavelength regions, using the broadening curve of Gray (1992), line profile changes for lines of different wavelength were examined (see Figure 3-11).

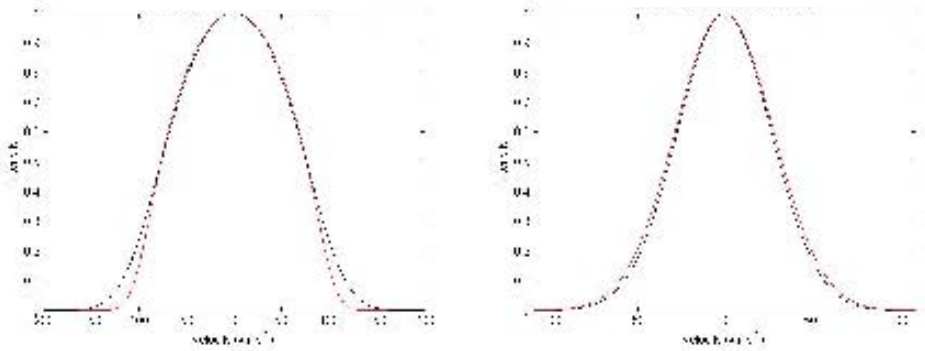

Figure 3-11: Theoretical inverted line profiles demonstrating the behaviour of rotational broadening on different wavelengths. Left: $V_{rot}\sin i$ = 100 km s^{-1}, line profiles for wavelengths 4000Å and 8000Å show significant differences in the wings of the line profile. Right: $V_{rot}\sin i$ = 10 km s^{-1}, line profiles for wavelengths 4000Å and 8000Å show small differences.

Figure 3-11 indicates that a high $V_{rot}\sin i$ star's lines will change shape with increasing wavelength in the wings of the profile. The examples in Figure 3-11 are for wavelengths that are outside the extremes of the delta function template but give an indication of the maximum change that can be expected in the line profile. The method used to synthesise the line profile is not always particularly good at the wings of the profile because of the use of a Gaussian to approximate what is actually a Voigt profile. This approximation is also made in the FPF method, the primary method of mode identification in this thesis (see Section 4.2.3.4). For this reason only the core of the line profile is used in the detailed analyses of the stars investigated in this thesis. Because the wavelength dependence of the rotational broadening primarily affects the wings of the line profile it is not considered in the analysis of the CCFs obtained in this thesis.

The scaled CCF is only useful for determining variations in a line profile if all the lines included in the delta function are varying in a similar way. For γ Dor stars the line formation region is at a similar depth for all of the metal lines that are included in the scaled CCF. The lines can, however, behave quite differently to temperature and gravity variations caused by a non-radial pulsation (NRP). It is difficult to simulate which lines will vary similarly as was shown by Zima (2005, pgs 95-130).

In order to justify the use of the scaled CCF in detecting variations in the line profile due to NRP in γ Dor stars, the QW Pup data set is examined in Section 6.3 using both the scaled CCF line profiles and a combined line profile using four of the strongest lines in the spectrum. From these results it is concluded that it is valid to use the scaled CCF to obtain a line profile that is considered representative of each individual line profile.

This method is not valid for the β Cephei star V2052 Oph as at least one of the strong spectral lines (Si III 4553Å) is known to vary differently from other strong lines (He I 4713Å) (Neiner et al. 2003). This is very likely the case for other β Cephei stars also.

3.3 Future work on line profile recovery

To understand better the dependencies of the scaled CCF, simulations involving a random error in the depth of the delta functions should be run. To test whether there is a minimum depth for a line to be beneficial to the CCF, and so therefore included in the template, a series of trials could be run that examine the CCF with the inclusion of all lines, versus the CCF that only

includes lines with a specified minimum depth. It is expected that for high $V_{rot}\sin i$ objects there will be a decrease in the S/N ratio of the CCF if weak lines are included. Ultimately the simulations should be taken to a stage where a synthetic line profile distorted by a NRP mode (and eventually multiple NRP modes) can be used as the input line profile and a time series of scaled CCFs can be examined for mode identification.

Observationally a study of the frequencies and modes detected in the scaled CCFs of a star's dataset that has already been used in frequency determination and mode analysis. Such a dataset is available for the δ Scuti star FG Vir (Zima 2005; Wright 2003).

Chapter 4
Stellar analysis methods

Having described and justified the processes applied to determine the stellar line profile, the analysis of this data can now be explained.

This thesis is focused on two different parts of analysis of non-radial pulsators: identification and verification of an object's status and pulsation mode analysis. The first part was a set of programs designed to determine whether line profile variations (LPVs) were present in the star's spectral lines, and to deduce the projected rotational velocity of the star. The second part involved determining the frequencies of the LPVs in the three stars V2052 Oph, QW Puppis and HD139095 for which there was a reasonable number of observations available. Then, by examining the different frequencies of profile variation, determine which were caused by non-radial pulsations (NRPs) and what the mode of those NRPs were.

First the basic determination of LPVs and the measurement of $V_{rot}\sin i$ are discussed. This is followed by the methods of frequency analysis and mode identification used on the data of V2052 Oph, QW Puppis and HD139095.

4.1 Identification of object status

Before a successful spectroscopic observational campaign can begin on a target that target must be confirmed as a line profile varying non-radial pulsator. Since good mode identification requires high S/N and good phase coverage through the pulsation, candidate selection is very important for a campaign. To aid in good candidate selection for upcoming campaigns, a number of γ Doradus candidate objects were examined for LPVs and their $V_{rot}\sin i$ was measured using two techniques outlined in Section 4.1.2.

4.1.1 Line profile variations

Each object was investigated for LPVs by examining the variations in their scaled cross-correlation function (CCF) profiles. The scaled CCF profiles are high S/N since they combine information from many spectral lines. Because of this, a small deviation in the scaled CCF is considered significant. The conclusion as to whether an object was demonstrating LPVs was based on the mean of the standard deviation across the profile. Each pixel in the scaled CCFs has a standard deviation. The mean value for all of the pixels in the CCF profile was used as the discriminator between the presence, or not, of LPVs. In this way a conclusion can be made even when only two observations are available. To determine the boundary for the presence of LPVs, the mean standard deviation across the profile for the two γ Dor stars known to show LPVs and for which many observations were available, QW Puppis and HD139095, were measured. They had mean standard deviations of 0.0042 and 0.0025 respectively. By further examining the mean standard deviation across the profile for small subsets of the observations of both stars, a cautious value of 0.0015 was decided upon as the lower limit for the presence of LPVs. This value is likely to fall on the conservative side and claim that there are not

LPVs present in observations where there may be LPVs. This seemed the practical approach so as not to mislead an observer into thinking that a candidate γ Dor star was a better campaign target than it really was.

4.1.2 $V_{rot}sin$ i

The value of $V_{rot}\sin i$ for each object's line profile was determined by considering the results of two methods: direct broadened profile fitting and Fourier profile comparison.

4.1.2.1 Direct profile fitting

In the direct fitting method, the $V_{rot}\sin i$ of the star is determined by the least-squares fitting of the convolution of a Gaussian profile with the broadening function of Gray (1992). This was implemented as

$$G = \frac{2(1-\varepsilon)\sqrt{1-\left(\lambda \cdot c/\left(\lambda_0 \cdot V_{rot}\sin i\right)\right)^2} + \frac{\pi \cdot \varepsilon}{2}\left[1-\left(\lambda \cdot c/\left(\lambda_0 \cdot V_{rot}\sin i\right)\right)^2\right]}{\frac{\pi \cdot \lambda \cdot V_{rot}\sin i}{c}\left(1-\frac{\varepsilon}{3}\right)} \tag{4.1}$$

And the full profile is represented by

$$e^{\left(\frac{\lambda}{w}\right)^2} * G \qquad for \quad G > 0 \tag{4.2}$$

In these expressions G is the broadening curve, ε is the limb-darkening coefficient, λ is the linear vector of wavelengths that describe the line profile, c is the speed of light, λ_0 is the rest wavelength of the line, $V_{rot}\sin i$ is the projected rotational velocity and w is the width parameter of the Gaussian and

* represents convolution. See the MATLAB codes VSINIDIRECTFIT and VSINIFITTINGFN in Appendix B for more details.

The resulting line is fixed to the same depth as the input line profile. The broadening function requires a wavelength as an input, the rest wavelength is used for an individual line profile and for a scaled CCF the centre wavelength of the region used to create it is used. The free parameters fitted are the width of the Gaussian and the $V_{rot}\sin i$ of the broadening function. In this way, the Gaussian can represent the spectrograph's response function and the broadening of the star's line by broadening mechanisms or if the instrumental profile has been removed it will only represent the line broadening mechanisms. Because there is no optimisation of any vertical shift the continuum fitting is very important. Only the core of the line profile is used for the fit because the true line broadening is better represented by a Voigt profile than a Gaussian which has a different shape in the line wings. The core of a given line profile is generally defined by the deeper part of the profile up to 80% of its height. This method is appropriate for use over any realistic range of $V_{rot}\sin i$ values (0 km s^{-1}<$V_{rot}\sin i$ <500 km s^{-1}). The errors for this method are estimated based on a visual inspection of the fit to the profile.

4.1.2.2 Fourier profile comparison

This method uses the Fourier transform of a synthetic line profile of $V_{rot}\sin i$ = 20 km s^{-1} and compares it with the Fourier transform of the line profile to be measured. This method is effective for lines with $V_{rot}\sin i$ > 15 km s^{-1} depending on the noise level in the line profile. To explain this Figure 4-1 shows the resulting Fourier transform of two broadened Gaussians with $V_{rot}\sin i$ =5 and 15 km s^{-1}. The broadened profiles have had noise added to them to simulate S/N=80. The broader the profile the lower the frequency of the first

minima on the abscissa, which is the only measurement necessary to make. Since the noise in the Fourier domain is limited to the higher frequencies, the broader profiles $V_{rot}\sin i$ can be more easily measured because the noise is not present in the area of the measurement. In Figure 4-1 the lower $V_{rot}\sin i$ line profile's first minima cannot be determined because of the noise. The broader line profile's minima can be measured as it is distinct from the noise.

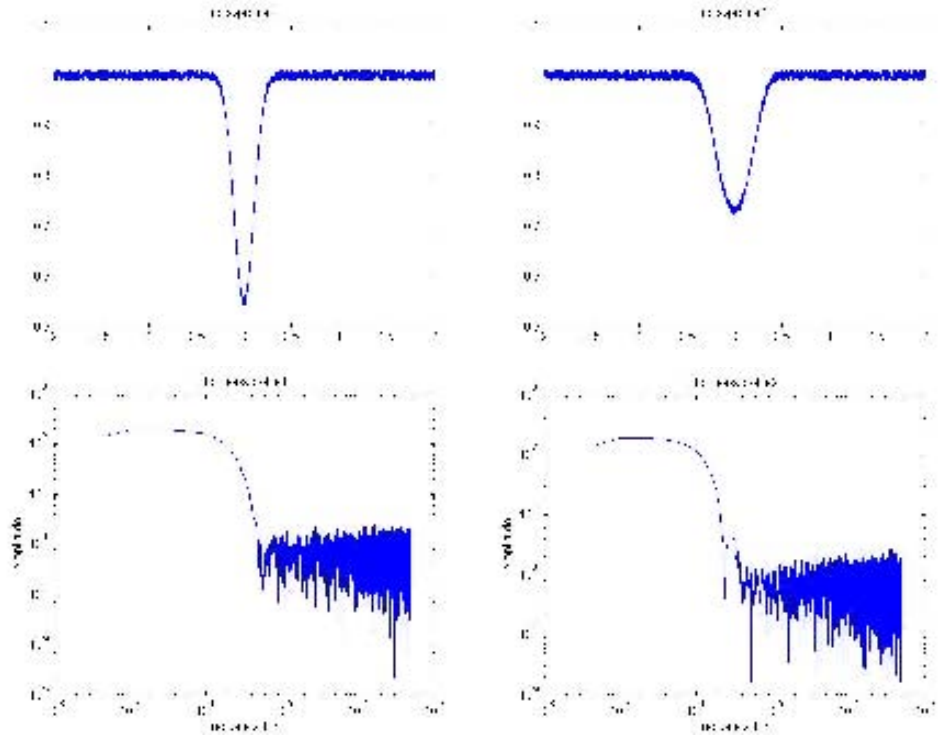

Figure 4-1: Top: Synthetic spectra with Vsin *i* = 5 km s^{-1} (left) and Vsin *i* = 15 km s^{-1} (right) with noise added to simulate 80 S/N. Bottom: Log-log plots of the Fourier transforms of the synthetic spectra.

To determine the value of $V_{rot}\sin i$ for a line profile the ratio of the positions of the first minimum on the abscissa between an observed and a theoretical profile is examined. By multiplying this ratio by the $V_{rot}\sin i$ of the theoretical profile the $V_{rot}\sin i$ of the observed line is obtained. This can be put as

$$V_{rot}\sin i_{OBSERVED} = \frac{position_{THEORY}}{position_{OBSERVED}} \cdot V_{rot}\sin i_{THEORY} \tag{4.3}$$

where the $position_{THEORY}$ and the $position_{OBSERVED}$ are the positions of the first minima along the abscissa for the theoretical and observed lines respectively.

For example the subplots in Figure 4-2 show the normalised Fourier transform of the mean scaled CCF of the γ Dor star HD139095 (black) and the normalised Fourier transform of a theoretical profile of $V_{rot}\sin i$ =20 km s^{-1} (red). The positions of the first minima are marked with a vertical green line. By multiplying the ratio of the two positions by 20 km s^{-1} the value of $V_{rot}\sin i$ for HD139095 can be measured to be 64.5 km s^{-1}. In each of the subplots the value of the full width at half maximum (FWHM) of the theoretical line's Gaussian that was broadened is changed. This shows how the position of the first minima is not affected by the FWHM of the Gaussian in the theoretical profile, nor is it likely to be sensitive to the Voigt intrinsic profile of the scaled CCF, especially if only the core of the profile is used for the measurement. The uncertainty in the determined $V_{rot}\sin i$ value is estimated based on the number of observations contributing to the profile and a visual inspection of the symmetry of the profile. This can be argued since a large number of observations means that the average profile will be similar to the rotationally broadened profile for the star without deviations due to the pulsations. This

measurement is implemented in the code FOURVSINIMEASURE (see Appendix B).

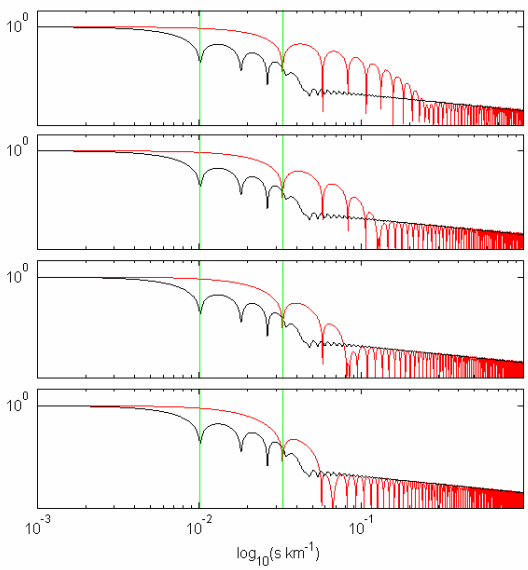

Figure 4-2: Example applications of the Fourier method using different values for the FWHM of the intrinsic Gaussian. Each application has the Fourier transform of the mean scaled CCF for all HD139095 SAAO observations (black) and the Fourier transform of the synthetic line profile made from a broadened Gaussian (red). From the top down the value of the FWHM of the intrinsic Gaussian is 5, 10, 15 and 20 km s^{-1} respectively. The $V_{rot}\sin i$ of the synthetic line is kept constant at 20 km s^{-1}. Each application gave the same value of $V_{rot}\sin i$ = 64.5 km s^{-1}.

4.1.3 Binaries

Single-lined (SB1) and double-lined (SB2) spectroscopic binaries are also commonly encountered in the γ Doradus population. The SB2s are readily identified if observed at any time other than the crossover point in their radial velocity curve as the two components will generally be easily identifiable. A SB1 will show a relatively large velocity shift of the whole spectral line or CCF as time passes. The $V_{rot}\sin i$ of each spectroscopically-visible component was determined from observations where the spectral lines were observed

separated. None of the binary stars analysed had sufficient data for determination of the orbit. For this reason it was not possible to determine whether LPVs was present in either of the components since the spectral lines have large velocity shifts with time and are often affected by the other component's spectral lines.

4.2 Detailed analysis and mode identification

4.2.1 Equivalent width and velocity measurements

In NRP, equivalent width variations are indicative of temperature and brightness changes occurring in the stellar atmosphere. In such cases, the variations should occur at the pulsation frequencies present in the star. Hence, each star's line profiles are examined for equivalent width variation and the resulting frequencies and amplitudes are discussed with regard to possible temperature and brightness changes occurring in the star.

For low to moderate degree (l<5) modes the LPVs can be detected as velocity variations using the following definition of radial velocity as the line centroid from Aerts (2004)

$$V_{rad} = \frac{\sum_{i=1}^{n}(1-I_i)(x_i - x_0)\Delta x_i}{\sum_{i=1}^{n}(1-I_i)\Delta x_i}, \tag{4.4}$$

where I_i is the normalised flux measured at wavelength pixel λ_i and $\Delta x_i = x_i - x_{i-1}$ where x_i is the velocity corresponding to pixel λ_i with respect to the laboratory wavelength λ_0. Because this measurement is made over the whole spectral line it is integrating across the entire stellar surface. For this reason it is similar to

photometry which can only detect lower degree modes due to the geometrical cancellation effects present in higher degree modes.

The line profiles of each star were examined for velocity variations by using a fixed range for $[x_i , x_n]$.

The equivalent width and velocity measurements frequency content was determined by following a typical prewhitening procedure:

1. examine highest peaks in Fourier transform of the data;
2. select the highest peak that is not caused by clumping due to the data sampling;
3. remove the frequency by subtracting a least-squares fit to the data;
4. examine highest peaks in Fourier transform of the residual data;
5. select the highest peak that is not caused by clumping due to the data sampling;
6. remove all of the selected frequencies simultaneously by subtracting a multi-frequency least-squares fit to the original data (the data before removal of any frequencies);
7. repeat steps 4-6 until no more significant frequencies remain.

Significant frequencies are defined as those with S/N > 4, where the S/N is determined locally around each peak in question.

The frequencies obtained using this procedure were compared with those found using the pixel-by-pixel frequency analysis method outlined in the next section. If the frequencies determined for the equivalent width matched those found in the pixel-by-pixel frequency analysis then they were treated as if

caused by temperature and brightness variations. This was considered during the Fourier parameter fit (FPF) mode identification process.

If the frequencies determined for the velocities matched those found in the pixel-by-pixel frequency analysis then they were caused by low degree modes and this was used to restrict the *l* and *m* search range for the FPF process.

4.2.2 Pixel-by-pixel frequency analysis

Correct frequency identification is a vital part of analysis of a NRP star. The incorrect identification of a frequency would give incorrect Fourier parameters (amplitude and phase across the profile) which are used in the interpretation of the frequency. This could result in an incorrect mode identification or, more likely, no way of determining the mode of pulsation of the frequency.

The frequency identification method used for this thesis was based on extracting the frequencies which were clearly demonstrating NRP-like behaviour, such as the pulsing expected for m=0 pulsation modes or the moving bumps expected for other modes. To do this, a 2-dimensional Fourier transform technique was used, called the pixel-by-pixel frequency analysis method (refpixbypix). This method examined the Fourier transform of each pixel's variation in time. In this way, once a frequency was selected it was possible to observe in what part of the line profile a given pulsation frequency was occurring.

To select the NRP frequencies present in the data, a 2-dimensional plot was made of the line profiles phased to the peaks in the mean Fourier spectrum

across the profile, these are referred to as phased surface plots. The highest peak frequency that showed NRP-like variation in its phased surface plot was selected. If no peaks were found that demonstrated NRP-like behaviour, then the highest peak frequency was selected. Once the frequency was identified, a least squares fit was made to each velocity bin and was removed from the data. . This process then continued in the same way as that outlined in the previous section as a prewhitening procedure. During the frequency removal the phase and amplitude of the least-squares fit for each velocity bin was determined. This provided the phase and amplitude across the profile which were later used in the mode identification. The errors on the phase and amplitude across the profile are based on the residual of the final multi-frequency fit to the data.

The pixel-by-pixel frequency analysis method is appropriate for lines of moderate to high $V_{rot}\sin i$ where the variation in the line profile is spread over a relatively large wavelength range and therefore a large number of pixels. The method is more sensitive to higher degree l than frequencies extracted from the velocity measurements of a line profile.

Once a frequency extraction was complete, the frequency list was examined for combination frequencies using the program CHECKFREQLISTFORCOMBOS (see Appendix B)**.** This program checked a supplied list of frequencies to see if any members could be made from twice another member or from the addition of two other members. It also checked for 1 cd^{-1} aliases of the combinations. The frequencies are identified as combinations or harmonics if they fall within 0.05 cd^{-1} of the expected value for the combination or harmonic frequency.

An example of the two dimensional Fourier transform is shown in Figure 4-3. It is clear in this figure that the peak frequency shown in the mean spectrum

has large amplitude in the ranges [-80, -25] km s^{-1} and [0, 70] km s^{-1} but has very little amplitude in the [-25, 0] km s^{-1} range. The phased surface plot and the amplitude and phase across the profile for the 7.149 cd^{-1} frequency are shown in Figure 4-4.

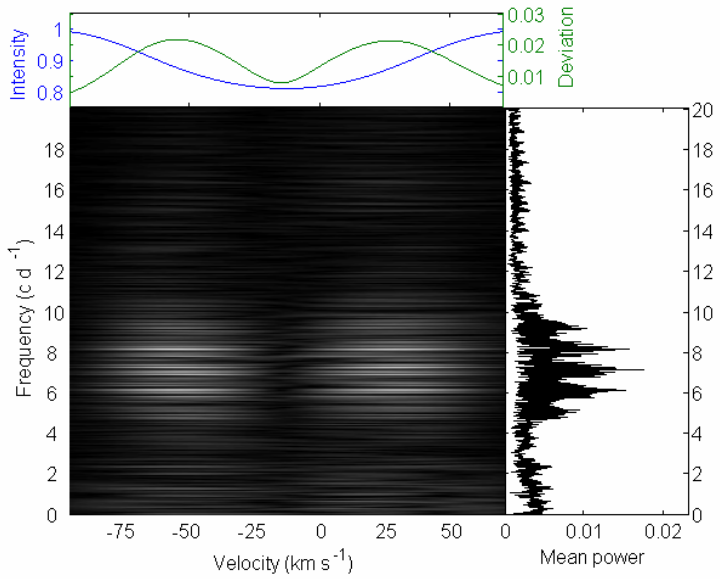

Figure 4-3: The V2052 Oph He I 4713Å line's pixel-by-pixel frequency analysis. The mean frequency spectrum is shown on the right and the mean line profile and the standard deviation across the profile are shown at the top. The peak of the mean frequency spectrum is 7.149 cd^{-1}. It is clear from the grayscale plot that the variation has no amplitude in the centre of the profile at that frequency.

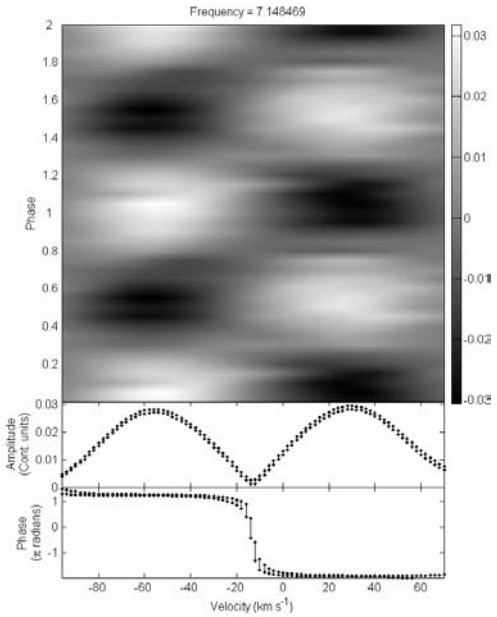

Figure 4-4: Phased surface plot of the V2052 Oph He I 4713Å line's 7.149 cd^{-1} frequency and the determined amplitude and phase across the profile.

The phase and amplitude across the profile of the NRP-like frequencies obtained using this pixel-by-pixel frequency analysis technique were then examined to determine the mode of the oscillation.

4.2.3 Spectroscopic mode identification methods

Correct identification of both *l* and *m* for a number of modes in a star is vital for asteroseismology to be performed. Since it is not possible to make velocity measurements of different parts of a star, as it is for the sun, indirect methods using the light from the entire disk of the star have been developed.

There are a number of different methods available for spectroscopic mode identification in multi-periodic NRP stars. Each technique has limitations

which restrict the use of the method on some stars. The methods investigated for use in this thesis were:

- The moments of the line profile method (Balona 1986a; Balona 1986b; Balona 1987; Briquet and Aerts 2003)
- The intensity period search method (IPS method) (Gies and Kullavanijaya 1988; Schrijvers et al. 1997; Telting and Schrijvers 1997a; Telting and Schrijvers 1997b; Schrijvers and Telting 1999)
- The pixel-by-pixel method (Mantegazza 2000)
- The Fourier parameter fit method (FPF method) (Zima 2006; Zima et al. 2006)

Discussion of each of these methods follows.

4.2.3.1 Moments method

This method originated with Balona (1986a) and utilises the variation of the moments of a line's profile with time. The modes are identified by the minimisation of a discriminant calculated from an evaluation of the similarity between measured and theoretical amplitudes of the frequencies present in the moments. At the time, this drastically reduced the computation time required for the identification of modes because it did not require a model of the entire line profile, only its moments.

Briquet & Aerts (2003) improved the moment method by adapting it to rotating objects. They improved multimode fits by simultaneously fitting the amplitudes of the pulsation frequencies and coupled frequencies and they showed that only the first three moments are required to describe the line profile well enough for mode identification. The first three moments of the

profile are the barycentre of the line (the velocity of the line), the variance across the line and the line skewness respectively. The zeroth moment of the line profile is the equivalent width.

The moment method is particularly sensitive to axisymmetric modes which become apparent quickly upon application of the method, as any axisymmetric modes will have no amplitude in the even moments. It is applicable to slow rotators ($V_{rot}\sin i < 30$ km s^{-1}) for modes $l \leq 6$. It is a comparatively quick method and so is generally calculated over an evenly spaced grid defined over the parameters l, m, v_p , i, $V_{rot}\sin i$, and σ. Where v_p is the pulsational velocity, i is the inclination of the rotational axis and σ is the intrinsic width of the line before any broadening due to rotation, pulsation etc.

In general, a number of solutions will fit the data well for each mode. At this point there is no way to determine between them based on the moments as there is no significance available for any of the parameters. To further distinguish between the solutions, one can now produce synthetic line profiles for each of the best few solutions leaving a single mode or, at worst, a few modes, as possible matches to the data.

In practice, the moment method was not applicable to the stars studied in detail in this thesis due to the high rotation in the objects.

4.2.3.2 The intensity period search (IPS) method

Gies & Kullavanijaya (1988) describe a method for determining the phase change across the line profile. This takes the phase information from a Fourier transform of the variation of each data bin at an identified period. The total

phase change across the line ($\Delta\Psi_0$) was stated as a measure of the *m* value of the mode using the relation $\Delta\Psi_0 = \pi m$. Later Merryfield (1993) showed that $\Delta\Psi_0$ is an indicator of *l* rather than *m* and Schrijvers (1997) proved $\Delta\Psi_1$, the phase change across the line at the first harmonic frequency, to be related to *m*. Over four papers (Schrijvers et al. 1997; Telting and Schrijvers 1997a; Telting and Schrijvers 1997b; Schrijvers and Telting 1999) they develop and test the IPS method.

This method takes into account the velocity field from a slowly rotating NRP star considering local temperature and brightness effects on the line profile including equivalent width changes. *p*- and *g*-modes are defined by their horizontal to vertical velocity ratios (*k* values), both are considered in the Monte Carlo simulations. The conclusion of their simulations was that there are linear relationships between the phase across the profile at the pulsation frequency and *l* and the phase across the profile at the first harmonic frequency and *m*.

The work resulted in many empirical relations for different circumstances. For example, the relationships for NRP caused solely by the velocity field effects and neglecting temperature and brightness effects are:

$$\lambda \approx 0.1 + 1.09\left|\Delta\Psi_0\right|/\pi \tag{4.5}$$

$$m \approx -1.33 + 0.54\left|\Delta\Psi_1\right|/\pi \tag{4.6}$$

The application of these relations is quite simple. Though to identify *m* there must be significant amplitude detected at the first harmonic frequency which requires a very high quality data set.

4.2.3.3 The pixel-by-pixel method

The pixel-by-pixel method of mode identification utilises the amplitude and the phase across the profile determined for a pulsation frequency to generate a number of mean subtracted profiles evenly distributed across one pulsation cycle. These phased profiles are treated as mono-mode pulsation profiles and are compared with synthetic profiles. A deviation parameter based on the weighted difference between the observed and synthetic profiles is calculated and minimised over a grid of parameters. It allows the determination of *l*, *m*, the pulsation amplitude, inclination and $V_{rot}\sin i$. This method was recently improved upon by the development of the Fourier parameter fit method.

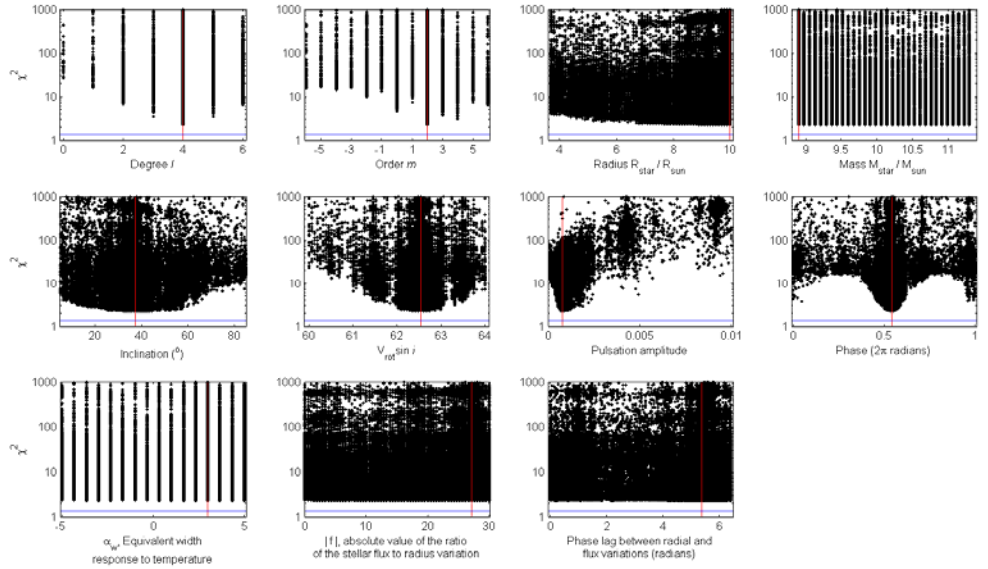

Figure 4-5: χ^2 optimisations for various pulsational, stellar and line specific parameters for the 6.827 cd^{-1} frequency in the He I 4713Å line.

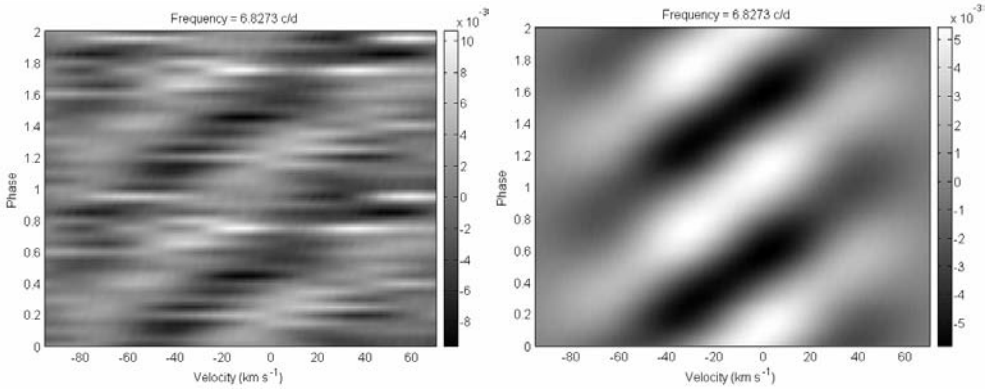

Figure 4-6: Observed mean-subtracted profiles for the He I 4713Å line phased to the 6.827 cd^{-1} frequency (left). Theoretical mean-subtracted profiles produced from the best fit parameters (right).

4.2.3.4 The Fourier parameter fit method (FPF method)

The Fourier parameter fit (FPF) method of Zima (2006) uses stellar pulsation models to compare theoretical zero point profiles and amplitude and phase across the profiles simultaneously for each determined pulsational frequency. The errors in the data are determined from the residual variation in the prewhitened spectra and the goodness of the fit is measured with a χ^2 test. The best fit is determined by supplying a range of pulsational parameters to examine. Because there are often many variables involved, the fit is optimised using a genetic algorithm. In principle, this method has no limit to the range of *l* and *m* that can be identified and is particularly good for constraining *m*.

For this thesis, the interpretation of the FPF results used a plot of the different stellar parameters tested versus reduced χ^2 (see Figure 4-5) to determine the range of *l* and *m* that produce the lowest χ^2 values. Based on how pronounced the minimum is on each χ^2 subplot, the range and uncertainty in the parameters is estimated e.g. in Figure 4-5 the inclination has a large uncertainty because the minimum is not very pronounced whereas the phase of the pulsation frequency has a small uncertainty because the minimum is pronounced.

If the optimum fit is sufficiently good (i.e. reduced $\chi^2<3$) a comparison of theoretical profiles produced from the best fit parameters to the phased surface plot of the observations is made (see Figure 4-6). This is a final check on the validity of the values obtained from the optimisation.

Chapter 5
V2052 Ophiuchi

V2052 Oph is a B1-2 IV-V star classified as a β Cephei variable. Jerzykiewicz (1972) determined a 3h 21min (7.164 cd^{-1}) variation in its light output which has now been thoroughly examined spectroscopically and photometrically (Pike 1974; Morton and Hansen 1974; Perryman et al. 1997; Heynderickx 1992) and has been determined to be an $l = 0$ single radial mode (Cugier et al. 1994; Heynderickx et al. 1994; Neiner et al. 2003).

Neiner et al. (2003) (hereafter N03) have completed the only detailed spectroscopic examination of this object. They obtained 41 International Ultraviolet Explorer (IUE) spectra and 113 Musicos spectropolarimetric measurements (518 individual spectra) of V2052 Oph and were able to identify a rotation period of 3.638833±0.000003 d (0.2748 cd^{-1}) using the equivalent width variations of C IV, Si IV, N V and Al III lines. They also identified two frequencies believed to correspond to radial (7.145 cd^{-1}, previously identified) and nonradial (6.82 cd^{-1}) pulsation (NRP). They were able to obtain a $V_{rot}\sin i$ =63±2 km s^{-1} using the Fourier $V_{rot}\sin i$ method (outlined in Section 4.1.2, this thesis) and the stellar parameters T_{eff} = 25200±1100 K, log g =4.2±0.11 using non-local thermal equilibrium model atmospheres calculated with TLUSTY (Hubeny and Lanz 1995). Further, using the evolutionary tracks of Schaller (1992) and an extinction $E(B\text{-}V)$ = 0.30

(Papaj et al. 1991) they obtain $M = 10.1\pm0.6\ M_{sun}$, $R = 4.1\pm0.2\ R_{sun}$ and $d = 290\pm50$ pc, which agrees with the Hipparcos parallax measurement of 254^{+83}_{-50} pc. Combining all of this information they give values for inclination $i = 71\pm10^{o}$ and equatorial rotational velocity $V_{rot} = 63$ km s^{-1}. Examining the variability of He I and Si III lines they were able to agree with the previous identification of the 7.145 cd^{-1} frequency as $l = 0$, based on the phase and power (amplitude^2) across the profiles and observe a much weaker oscillation at 6.82 cd^{-1} identified as $l = 3$ or 4 also based on the phase and power across the profile. Also observed in the spectroscopy was a frequency (0.54 cd^{-1}) believed to correspond to twice the rotational frequency (0.2748 cd^{-1}). Surprisingly, this frequency had a higher amplitude than the rotational frequency. The spectropolarimetric measurements allowed the examination of the magnetic field which was determined to be a weak varying longitudinal field in phase with the rotational period. V2052 Oph was then modelled with an oblique rotator dipole model where the axis of the dipole and the axis of rotation do not coincide (see Figure 5-1). This model is known to show modulation of wind sensitive UV lines and longitudinal magnetic field variation with the rotation frequency as is seen in V2052 Oph. The angle between the rotational axis and the magnetic axis was determined to be $\beta = 35\pm18^{o}$. The pulsation axis is thought to be aligned with the magnetic axis based on the modulation of the amplitude of the 7.145 cd^{-1} frequency with the rotation period.

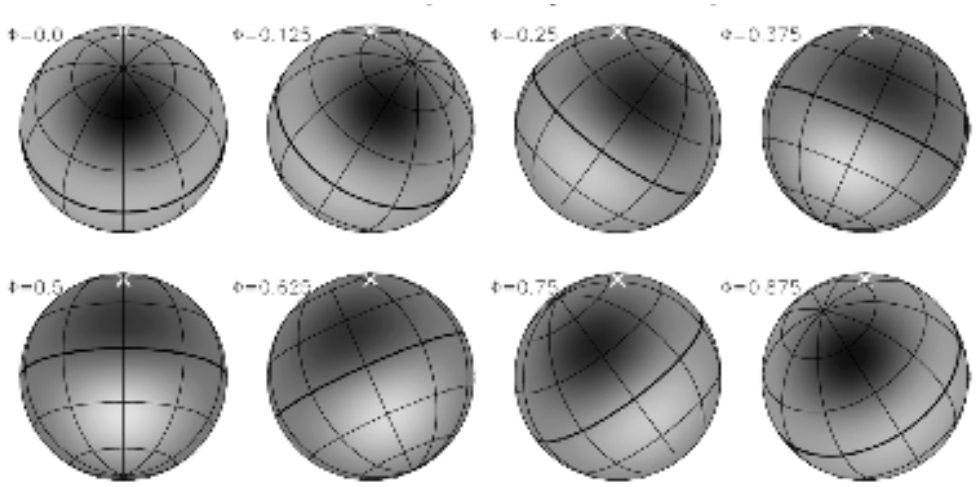

Figure 5-1: Figure 16 of Neiner et al. (2003). This figure indicates the relative contribution of the magnetic dipole in the stellar model to the measured longitudinal magnetic field at different rotational phases. Black corresponds to positive field values and white to negative field values. This explains how an offset magnetic axis relative to the rotational axis can allow the measurement of the rotational frequency. The rotational axis is marked with a white x and the black lines are a grid of magnetic longitudes and latitudes.

5.1 Observations

Eighty nine spectroscopic observations were obtained of V2052 Oph with the HERCULES spectrograph on the 1m McLellan telescope at MJUO during 29th May – 7th July 2004. This implies a theoretical frequency resolution of 0.038 cd^{-1} using 1.5/T where T is the time span of the observations (Loumos and Deeming 1978). The integration time was 10 min giving S/N~200. To have a well defined frequency, as little of a pulsation cycle should be sampled as possible in a single observation, whilst still getting the required S/N. This is to avoid smearing out of the changes in the line profile. By defining one tenth of a pulsation cycle as the limit to be sampled in an observation to maintain a well defined pulsation frequency, the upper limit for well defined frequencies can be stated as 14.4 cd^{-1}. These observations were contributing to a multi-site campaign organised by Conny Aerts with ν Eridani as the primary target.

Details of the MJUO observations are outlined in Table 5-1. The observations covered the range 4500 - 7000Å with some inter-order gaps. The observations used the 100 micron fibre optic cable for a resolution of R≈40000.

5.2 Line profile variations

The lines Si III 4553Å, He I 4713Å and He I 5876Å were selected for analysis. These were the only strong lines present in our wavelength region. N03 had observed the Si III line to vary such that its minimum intensity (the bottom of the line profile) was out of phase with the He I lines minimum intensities. The Si III line is known to be temperature insensitive and is a favourite line for β Cephei star type analysis (De Ridder et al. 2002; Aerts et al. 2004). Figure 5-2 shows the Si III 4553Å line variation and the deviation from the mean after reduction and continuum fitting.

Table 5-1: Observations by the author of V2052 Oph with the HERCULES spectrograph on the 1m McLellan telescope at MJUO.

Date	**Heliocentric Julian date**	**# of spectra**
29-05-2004	2453154	18
02-06-2004	2453158	6
03-06-2004	2453159	3
04-06-2004	2453160	1
06-06-2004	2453162	9
07-06-2004	2453163	12
04-07-2004	2453190	18
05-07-2004	2453191	18
07-07-2004	2453193	4

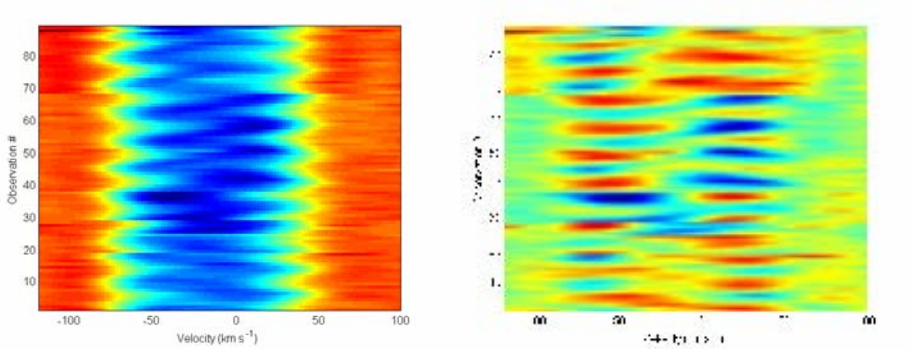

Figure 5-2: The Si III 4553Å line variation (left) and the deviation from the mean profile (right) after reduction and continuum fitting. Red is higher values, blue is lower values. The discontinuities are caused by gaps from the end of a night to the start of the next observing night.

The strong variation observed in the line profile is due to the 7.145 cd^{-1} frequency identified in N03.

5.3 Equivalent width, radial velocity and minimum intensity measurements

As there were only a few strong lines in the spectrum and the Si III 4553Å line had been shown to vary differently to the He I lines, the technique of cross-correlation for increased S/N profiles and precision frequency determination outlined in Section 4.2 was not appropriate. This is because the strong lines varying differently would contribute to the cross-correlation function in opposing ways, thereby making any variation more difficult to detect, particularly in a spectrum with only a few significant lines.

As a result, the equivalent widths and radial velocities of each of the spectral lines were determined using the methods outlined in Section 4.2. The three

lines were initially measured over two different ranges to determine if significant variation was occurring in the wings of the line profiles (see Figure 5-3 for an example of the different ranges used). This was done because our primary method for mode identification, the Fourier parameter fit (FPF) method, does not deal well with the line wings where the lines profile deviates from a rotationally broadened Gaussian. The two ranges of velocities included in the analysis differed for each line since the mean velocities for each of the lines did not agree with each other (see Figure 5-5 and Figure 5-6 for examples of velocities for each line). For the He I 5876Å line this is probably an effect of blending since this line is a close triplet with one component stronger than the others.

The equivalent width and velocity variations observed for the He I 5876Å line for each of the velocity ranges are shown in Figure 5-4 and a single night's variation in Figure 5-5. There appears to be variation in both the equivalent widths and the velocities for each of the lines.

No significant differences were found for the different velocity ranges inspected for each line. A small and expected increase in the scatter was observed for the equivalent width of the larger velocity region when compared to the core only region. A slightly smaller amplitude of variation was observed for the core only part of the He I 5875Å line. As a result, all further investigation of this star focussed solely on the variations observed in the core region of the three lines.

In Figure 5-5 and Figure 5-6 it is shown that the equivalent width variations of the Si III 4553Å line are not similar to the He I lines. This is expected because

of the very different temperature response of the Si III line compared to the He I lines.

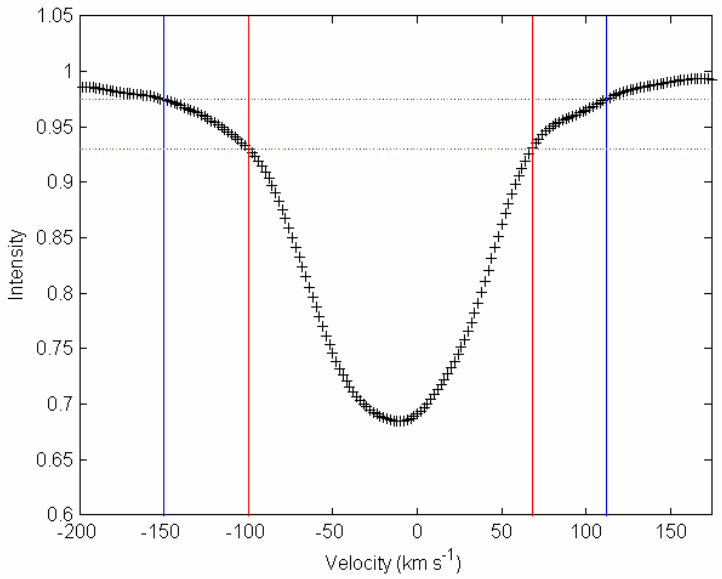

Figure 5-3: He I 5876Å line regions chosen for analysis. One region encompasses the line core only (red) the other includes the lines wings (blue). Dotted lines indicate the constant intensity in the selection.

Also in Figure 5-5 and Figure 5-6 the velocities of each line clearly show strong variation which corresponds with the well known 7.145 cd^{-1} frequency. Each of the three lines appears to be varying in phase for this frequency.

The minimum intensity of each line profile for every observation was determined for comparison with the results of N03. The minimum intensity for each observed line profile was determined by fitting a parabola to the lowest point and its surrounding ten pixels (i.e. the minimum±5 pixels).

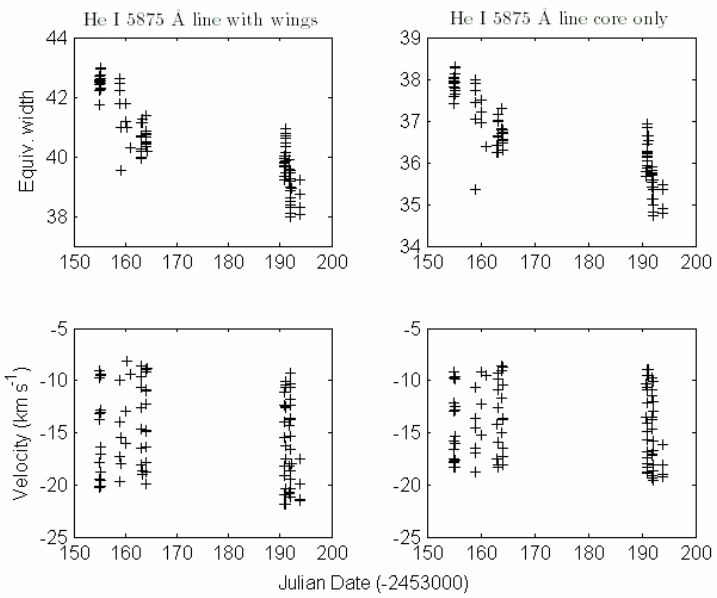

Figure 5-4: All equivalent width (top row) and velocity (bottom row) measurements for the He I 5876Å line. The figures on the left are for the entire line while the figures on the right are for the line core only.

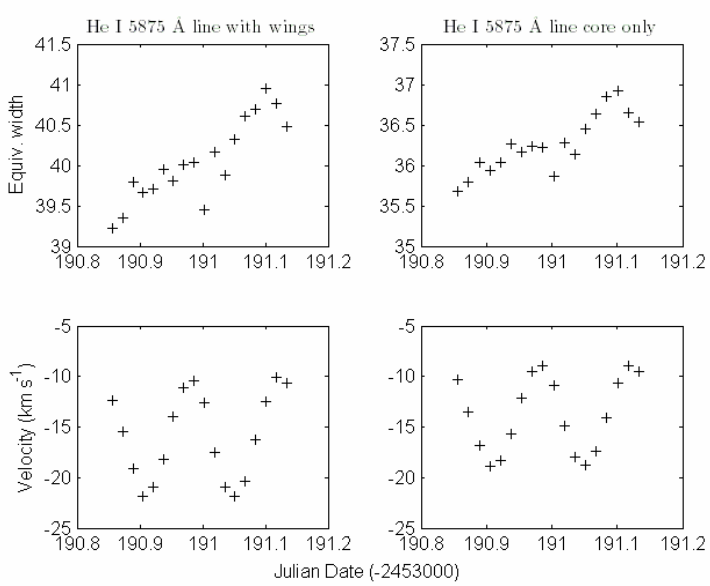

Figure 5-5: A smaller region of Figure 5-4 showing a single night's variations of the He I 5876Å line. Note the different amplitudes of the velocity variations for the different line regions.

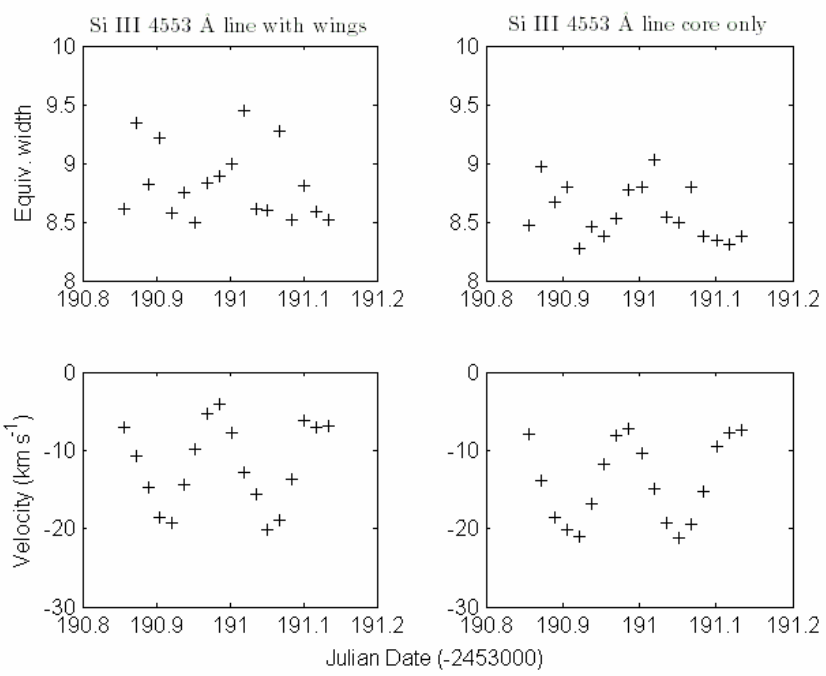

Figure 5-6: A single nights variations of the Si III 4553Å line. Note the increased scatter for the equivalent width variations for the larger line region and the different variation in the equivalent widths when compared to the He I lines.

In Figure 5-7 it is clear there is periodic variation in the minimum intensity of each of the lines and that the Si III 4553Å line is varying differently to the He I lines as noted by N03. The clear variation in each of the He I lines in Figure 5-7 appears to be in phase with, and of similar frequency to, the strong variations observed in the velocity measurements, but upon further investigation carried out in Section 5.4 it is clear that this variation is actually the 6.82 cd^{-1} frequency that was identified by N03 as a non-radial mode. This makes sense because the 7.145 cd^{-1} frequency has little or no amplitude at each line's centre.

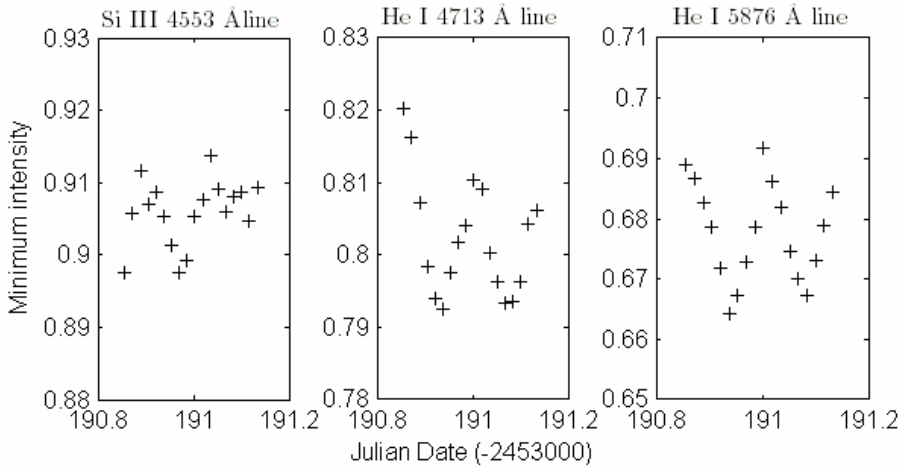

Figure 5-7: The variation of the minimum intensity of the lines examined. Note that the Si III line's variation is out of phase relative to that of the He I lines.

5.4 Frequency analysis

To determine the frequencies present in the variations of the equivalent width, velocity and minimum intensity an examination of the Fourier transform for non-evenly spaced data is made using the PERIOD04 software (Lenz and Breger 2004).

The frequency analysis proceeded in the manner outlined in Section 4.2. The sequential frequency extraction of the equivalent width variation for the Si III 4553Å line is shown in Figure 5-8 where the 0.296 cd^{-1} and 0.607 cd^{-1} frequencies are expected to be associated with the rotational frequency and the peak at 7.145 cd^{-1} is the previously known frequency. The final extracted frequency, 2.956 cd^{-1}, does not coincide with any known frequency and does not appear in any other frequency extraction of this data, so the frequency extraction ends here. The forced frequency extraction in Figure 5-9 does not appear as good a fit as the sequential extraction of frequencies and results in much higher residuals (see Table 5-2).

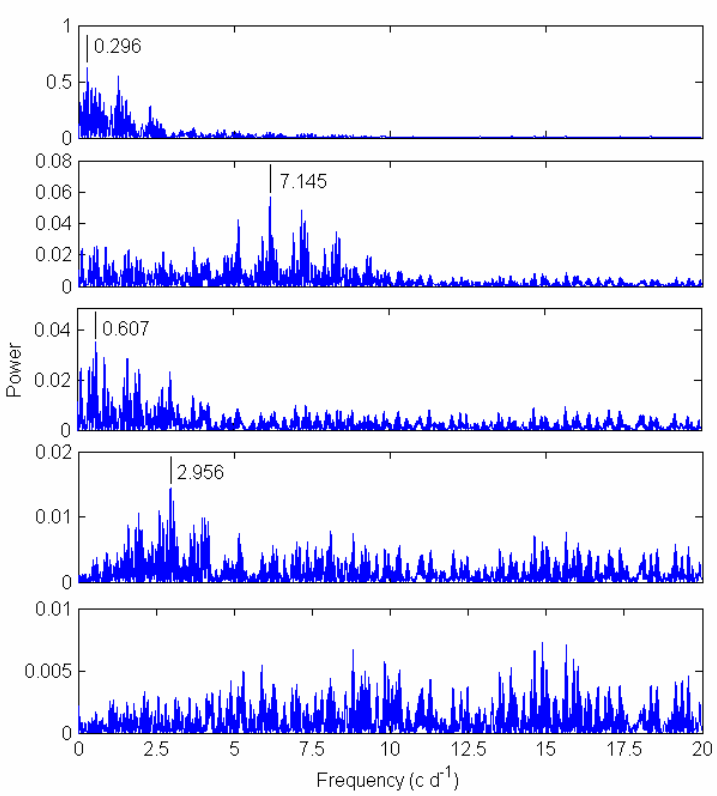

Figure 5-8: Frequency extraction for Si III 4553Å lines equivalent width variations. The final frequency extracted (2.956 cd^{-1}) does not agree with any found in other lines or previous work on this object. It is there to demonstrate that frequency extraction can continue but does not significantly decrease the residuals to the fit (see Table 5-2).

Figure 5-10 shows the frequency extraction of the equivalent width variation for the He I 4713Å line. The notable difference from the Si III line is the lack of the 7.145 cd^{-1} frequency.

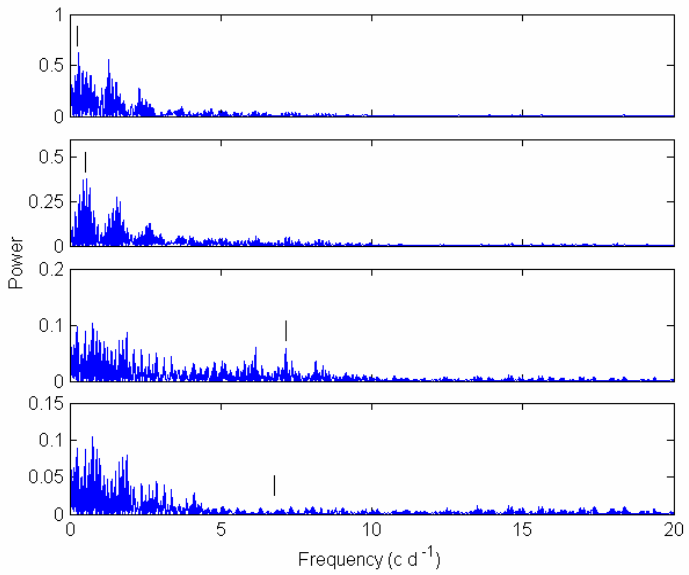

Figure 5-9: Forced extraction of the 0.2748 cd^{-1}, 0.54 cd^{-1}, 7.145 cd^{-1} and 6.82 cd^{-1} frequencies for the equivalent width variation of the Si III 4553Å line. The values extracted are marked with a vertical black line in the figure.

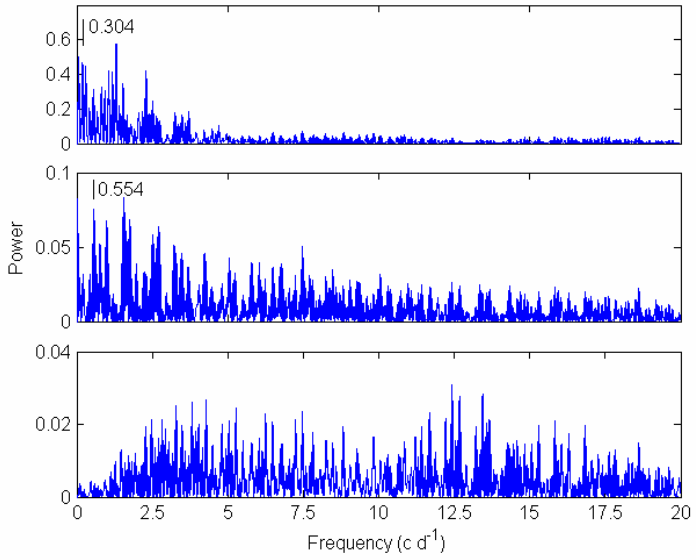

Figure 5-10: Frequency extraction for He I 4713Å lines equivalent width variations. Notably lacking is the presence of the 7.145 cd^{-1} frequency.

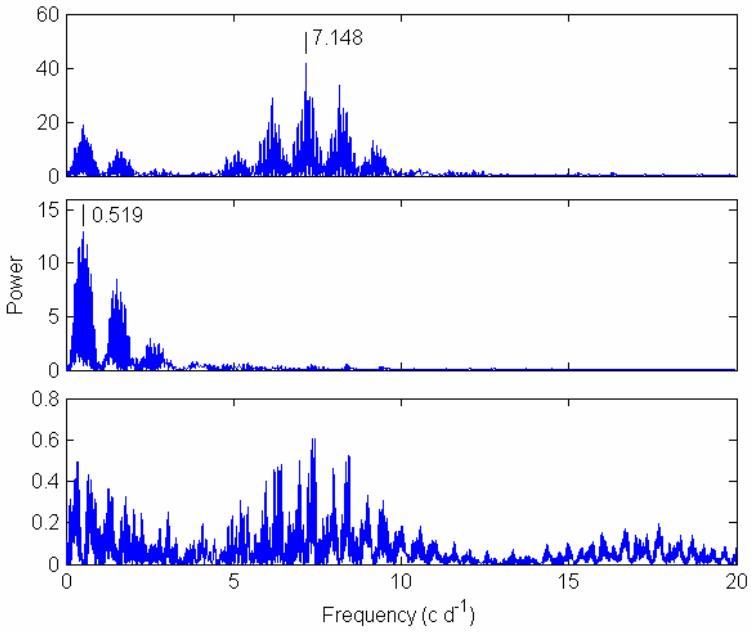

Figure 5-11: The extracted frequencies for the velocity variations for the Si III 4553Å line.

In the Fourier transforms of the velocity variations (Figure 5-11 and Figure 5-12) we find the 7.145 cd^{-1} frequency is present and dominant in each of the lines examined. After extraction of this frequency the rotational frequencies around 0.27 cd^{-1} and 0.54 cd^{-1} can be detected. There is significant power left in the Fourier transforms of all of the residuals in the 5 – 10 cd^{-1} region though the 6.82 cd^{-1} frequency is not specifically detected in any of the velocity variations. See Appendix D for the frequency analysis figures of the He I 5876Å equivalent width and velocity variations.

The minimum intensity of the lines demonstrates very different behaviour to the velocity variations. In examining Figure 5-13, the Si III line's minimum intensity variations, we note the distinct lack of the 7.145 cd^{-1} frequency which

is so dominant in other frequency detection methods. This is not surprising given the nature of the variations of the 7.145 cd^{-1} frequency. The deviations in the line profile reduce to zero in the line centre for each of the three lines examined which is typical for an axisymmetric mode (m=0) as has been previously determined for this oscillation. It is noted, however, that N03 do mention detecting the 7.145 cd^{-1} frequency in their minimum intensity measurements. In Figure 5-13 the minimum intensity variations of the Si III 4553Å line has its strongest frequency at 0.296 cd^{-1} which is associated with the rotation of V2052 Oph. The next most powerful frequency is 6.376 cd^{-1}, an unexpected frequency that does not coincide with any other extracted frequencies from the other methods, or other lines examined. The third extracted frequency 6.828 cd^{-1} is associated with the non-radial mode identified by N03. In the He I 5875Å lines minimum intensity frequency spectrum (Figure 5-14) the strongest frequency is 6. 824 cd^{-1} with the $2f_{rot}$ frequency extracted second. After the removal of those two frequencies there appears to be significant frequencies present left in the data though attempts at extracting the frequencies did not turn up any that agree with other lines or methods of frequency determination.

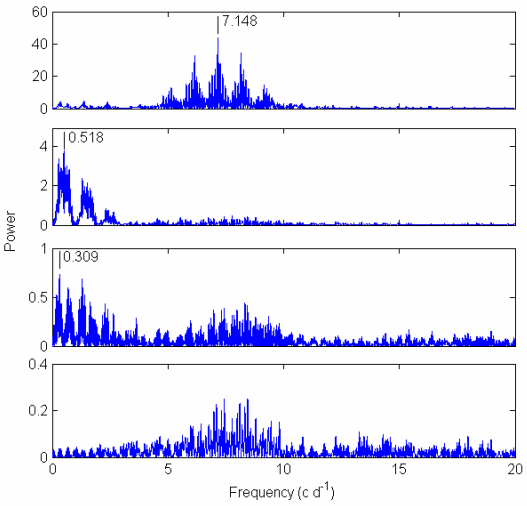

Figure 5-12: The frequencies for the velocity variations of the He I 4713Å line.

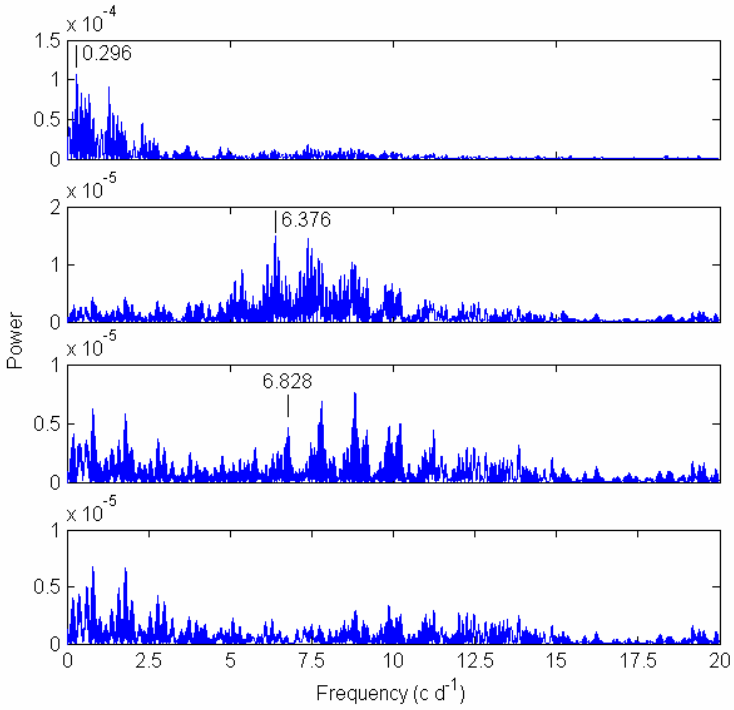

Figure 5-13: Frequencies extracted from the minimum intensity variations of the Si III 4553Å line. 6.376 cd^{-1} is not a frequency used in further analysis. It is extracted here to demonstrate that the 6.828 cd^{-1} frequency is present in the Si III line data.

Along with the Fourier transform of the line profiles' equivalent width, velocity and minimum intensity variations it is possible to examine the Fourier transform of each pixels variation in time to determine in what part of the line profile a given pulsation frequency is occurring (referred to as the pixel-by-pixel frequency analysis method in this text, Section 4.1.1). The pixel-by-pixel frequency analysis method is appropriate for lines of moderate to high $V_{rot}\sin i$ where the variation in the line profile is spread over a relatively large wavelength range and therefore a large number of pixels. The method is more sensitive to higher degree l than frequencies extracted from the velocity measurements of a line profile (Zima 2005). Also note that significant

frequencies detected in the minimum intensity of line variations should also be present in pixel-by-pixel frequency spectra.

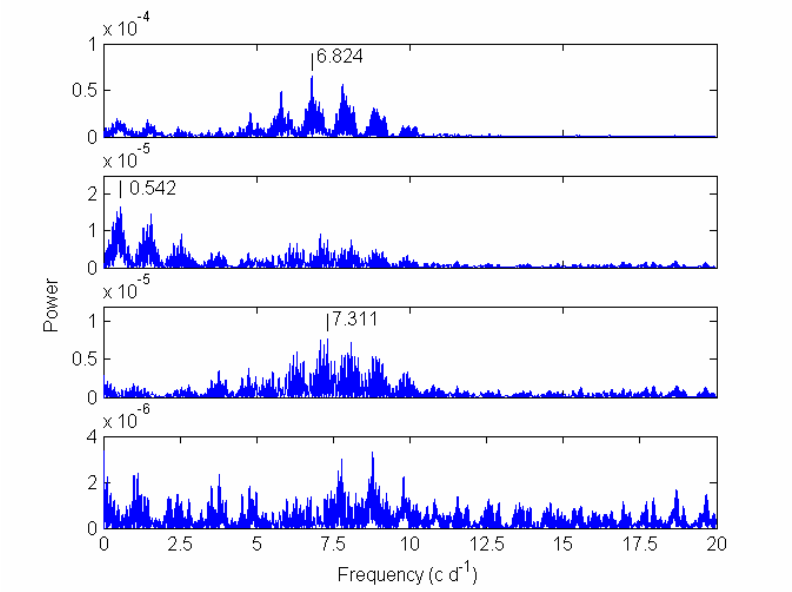

Figure 5-14: Frequencies extracted from the minimum intensity variations of the He I 5875Å line.

It was clear from the frequency analysis outlined so far that the frequencies determined from our data set were unable to match the precision of previous work. As a result of this, in the further frequency analysis any frequency clearly associated with a previously determined frequency will be extracted using the most precise value available from prior studies. The association was determined using the theoretical frequency resolution of 0.038 cd^{-1} as an indicator of the uncertainty of a frequency value and from an examination of the two dimensional phased diagrams (e.g. Figure 5-16).

The pixel-by-pixel frequency analysis method was carried out for the three lines being investigated. This was done using the programs SPEC_DEVAVE SPEC_FOURIERW and SPEC_PERIODW obtained as part of the FPF software.

Figure 5-15 to Figure 5-21 show the Fourier transform of the pixel variations in time for the He I 4713Å line and the extraction of the well determined frequencies from previous studies (see Appendix D for the pixel-by-pixel analysis of the Si III 4553Å and He I 5876Å lines). For Figure 5-15 the deviations caused by f_1 are clearly visible in the left side and right side of the line profiles frequency spectra, whilst it shows no amplitude in the centre of the line.

Figure 5-16 is referred to as a phased surface plot. It is a two dimensional phased diagram created by subtracting the mean profile from each observation, then phasing the resulting profiles to the frequency 7.148 cd^{-1} (f_1). The zero phase point is at Julian date 2,400,000 by multiplying each observation time (minus 2,400,000) by the frequency and ignoring any numbers left of the decimal point. The resulting profiles are then grouped into phase bins of 0.05 and the mean profile of each phase bin is determined. Each point in a phase bin's profile is represented by a grayscale colour and the phased profiles are interpolated between the pixels to produce a smoother surface that more clearly shows the variations. A phase bin in which no observations fall will be represented by an all zeros profile.

In Figure 5-16 clear side-to-side movement can be seen occurring with increasing phase due to frequency f_1.

In Figure 5-17 after extraction of the 7.148 cd^{-1} frequency, there are poorly defined low frequency peaks visible in our mean frequency spectrum. In Figure 5-17 and Figure 5-19 we extract f_{rot} and $2f_{rot}$. These frequencies are associated with the rotation of V2052 OPH so no further analysis is done with

these frequencies in this work. After extraction of the rotation frequencies there is a clear peak in Figure 5-21 around 6.82 cd^{-1} which demonstrates variation in the centre of the line profile, indicating a $m \neq 0$ mode. Figure 5-23 shows the very clear NRP occurring at the 6.82 cd^{-1} frequency. When the 6.82 cd^{-1} frequency was removed from the line profile variations Figure 5-23 is obtained which has a noisy mean frequency spectrum. At this point the lines (particularly the He I lines) show appreciable amplitudes in the 6-10 day region and a possible frequency at around 14.3 cd^{-1} ($2f_1$). Further frequencies are not extracted due to the poor precision of the values and lack of agreement for the different lines. It seems likely that more variation is present in the line profiles of V2052 OPH though the limited data set does not allow determination of there frequencies.

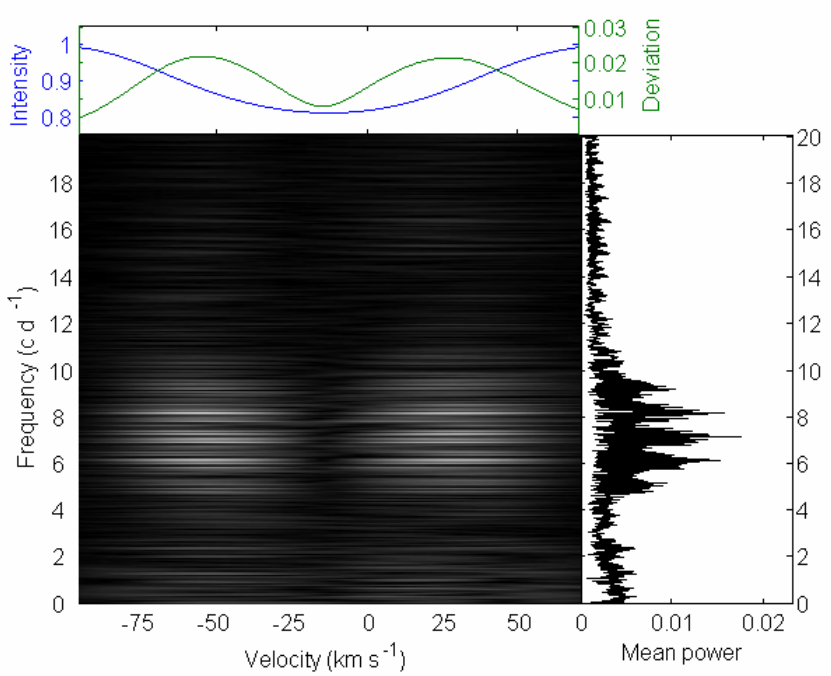

Figure 5-15: He I 4713Å line pixel-by-pixel frequency analysis method. This is the line profile data before the removal of any frequencies. The peak of the mean frequency spectrum is 7.149 cd^{-1} so the well determined pulsation frequency of Heynderickx (1994) is used f_1 = 7.148 cd^{-1} for removal.

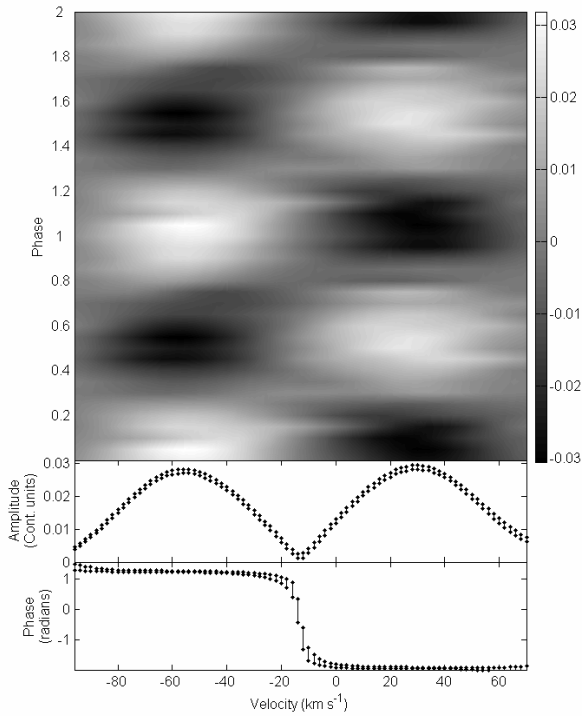

Figure 5-16: Phased surface plot of the 7.148 cd^{-1} frequency and the determined amplitude and phase across the profile.

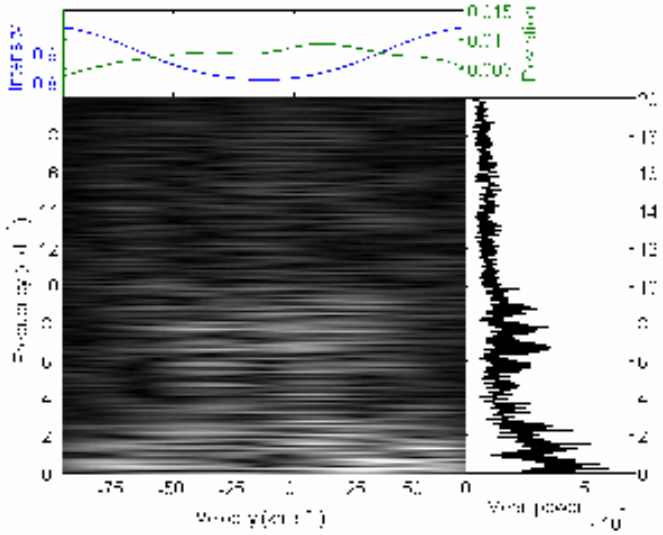

Figure 5-17: He I 4713Å line after extraction of the 7.148 cd^{-1} frequency. The peak in the mean frequency spectrum is 0.2998 cd^{-1} so the well determined rotation frequency from N03 is removed next f_{rot} = 0.2748 cd^{-1}.

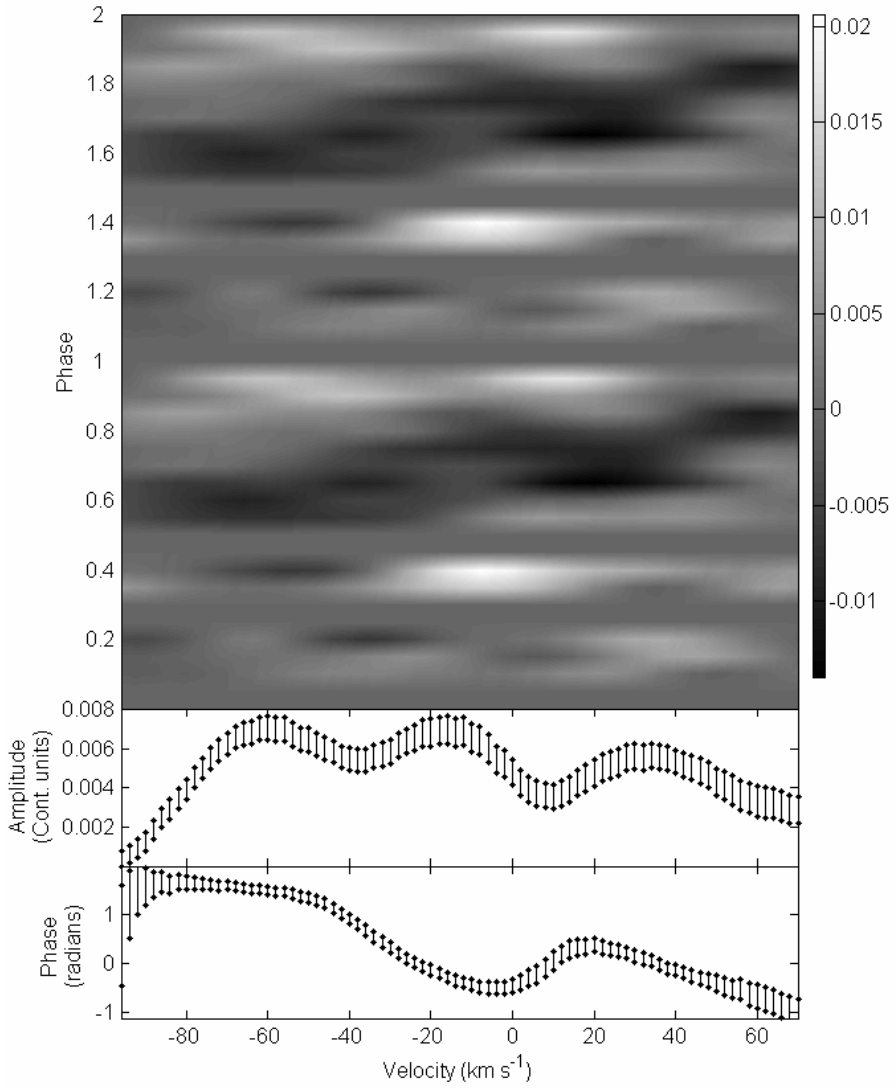

Figure 5-18: Phased surface plot of the 0.2748 cd^{-1} frequency and the determined amplitude and phase across the profile.

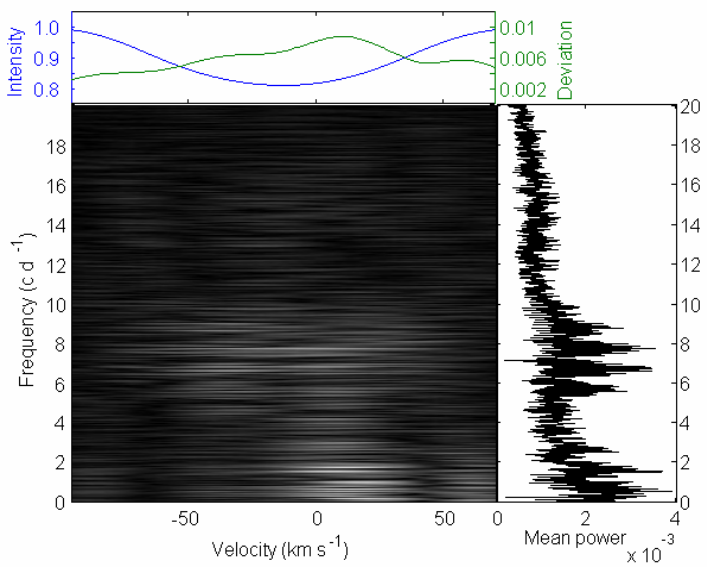

Figure 5-19: He I 4713Å line after extraction of f_1 and f_{rot}. The peak in the mean frequency spectrum is 0.5791 cd^{-1} so next 2 f_{rot} is removed ($2f_{rot}$ = 0.5496 cd^{-1}).

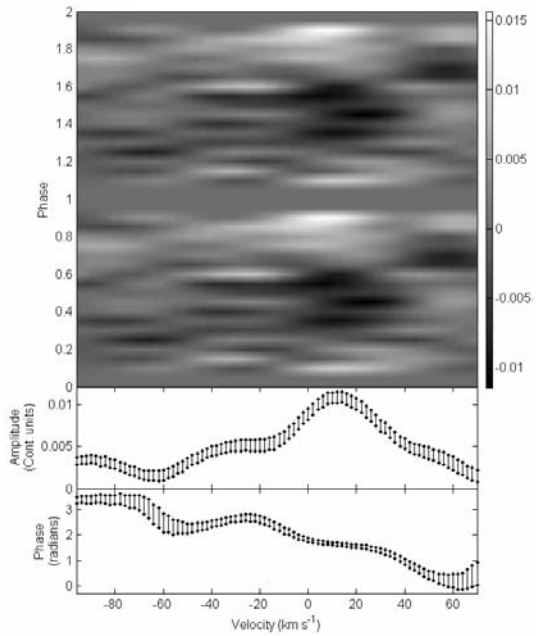

Figure 5-20: Phased surface plot of the 0.5791 cd^{-1} frequency and the determined amplitude and phase across the profile.

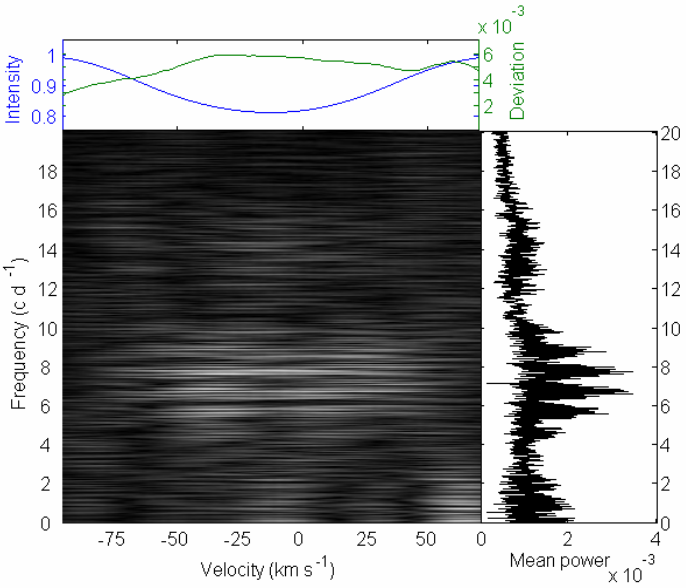

Figure 5-21: He I 4713Å line after extraction of f_1, f_{rot} and $2f_{rot}$. The peak in the mean frequency spectrum is 6.609 cd^{-1} so the next extracted frequency is f_4 = 6.827 cd^{-1} which is the nearest corresponding peak to N03s 6.82 cd^{-1} frequency.

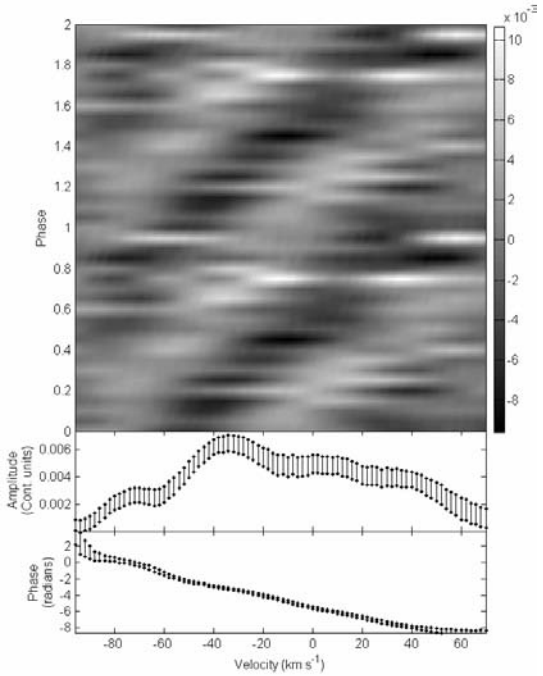

Figure 5-22: Phased surface plot of the 6.827 cd^{-1} frequency and the determined amplitude and phase across the profile.

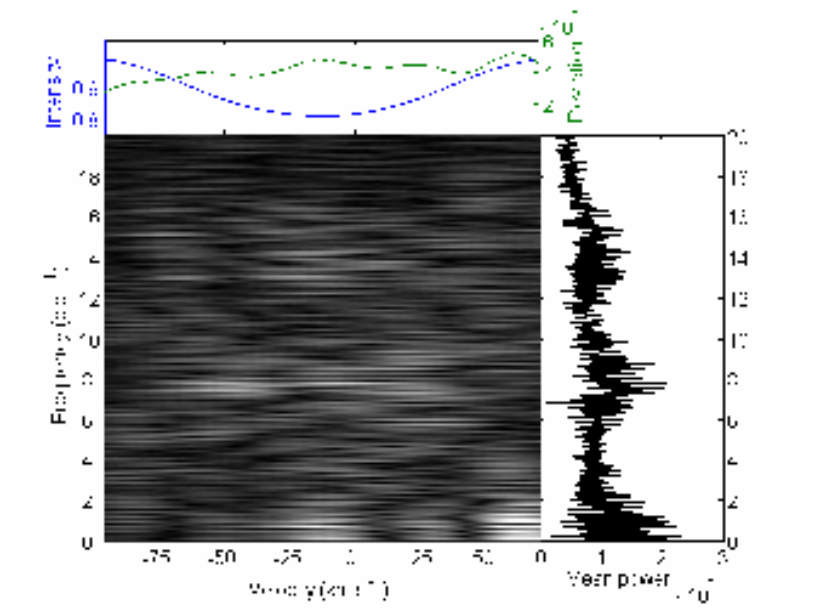

Figure 5-23: He I 4713Å line after extraction of f_1, f_{rot} and $2f_{rot}$ and f_4. The peak in the mean frequency spectrum is 0.2588 cd^{-1}, as this is not a recurring frequency no further frequencies are extracted.

The results from an extraction of the peak frequencies detected can be seen in Table 5-2 (missing figures are available in Appendix D). The four consistently detected frequencies are f_1=7.147±0.005 cd^{-1}, f_2=f_{rot}=0.29±0.03 cd^{-1}, f_3=2f_{rot}=0.54±0.03 cd^{-1}and f_4=6.81±0.02 cd^{-1}. They can all be associated with frequencies identified by N03.

N03 obtained the 0.2748 cd^{-1} frequency from a number of IUE observations examining the equivalent width variations of a number of lines which are associated with stellar winds, this led them to conclude the frequency is the rotation frequency. It is assumed that this is correct and those frequencies extracted from this data set are not analysed further as possible NRPs.

Table 5-2: The extracted frequencies and amplitudes for the different lines analysed and methods used. Amplitudes for the pixel-by-pixel method are calculated from the integral of the amplitude across the profile.

Method/Data	**Si I 4553Å**		**He I 4713Å**		**He I 5876Å**	
	Freq (cd^{-1})	Amp (km s^{-1})	Freq (cd^{-1})	Amp (km s^{-1})	Freq (cd^{-1})	Amp (km s^{-1})
Eq width	0.2963	0.655	0.3042	0.759	0.5798	1.23
	7.145	0.252	0.5541	0.605	0.2957	0.775
	0.6074	0.346	12.43	0.180	4.300	0.354
	2.956	0.146			6.417	0.336
Velocities	7.148	5.29	7.148	6.85	7.148	4.72
	0.519	2.82	0.518	0.907	0.5547	0.484
	7.340	1.83	0.309	1.89	6.187	0.472
Min intens	0.2963	0.00921	6.789	0.00642	6.824	0.00851
	6.376	0.00382	0.2693	0.00605	0.5425	0.00343
	6.828	0.00222	0.5496	0.00414	7.311	0.00299
Pixel-by-pixel	7.148	1.33	7.148	2.99	7.147	3.86
	6.828	0.436	0.2748	0.821	6.825	0.765
	0.5176	1.09	0.5496	0.843	0.5535	0.962
	0.2658	0.483	6.827	0.617	0.2628	0.760

Heynderickx (1992) determine a 7.148 cd^{-1} frequency from photometry. Heynderickx et al. (1994) and N03 attribute the 7.148 cd^{-1} frequency to a radial oscillation (l=0). For Heynderickx (1992) and Heynderickx et al. (1994)

this is based on photometric amplitudes of the variation in different passbands. N03s conclusion is based on a basic examination of amplitude and phase variations across the line profile.

N03 also conclude the 6.82 cd^{-1} frequency is l=3 or 4, determined from the phase change across the profile at this frequency.

It is clear from the summary in Table 5-2 that few frequencies can be precisely extracted from the available data. This is because there are only 89 observations in the sample which was taken over just a two month period. Three of the four frequencies are, however, quite well determined in previous studies of this object. For further investigation, the data values for these three frequencies are taken from previous work to be f_1 = 7.148 cd^{-1}, f_{rot} = 0.2748 cd^{-1} and $2f_{rot}$ = 0.5496 cd^{-1}.

For the 6.81±0.02 cd^{-1} frequency also detected by N03 there is no frequency given more precisely than those obtained from our data set. As a result, the peak frequency in the range of 6.81±0.02 cd^{-1} is taken for each line determined from the mean spectrum in the pixel-by-pixel frequency analysis after removal of the three aforementioned frequencies.

At this point some basic information about the two pulsations m parameters can be obtained. For f_1 it is likely that m=0, based on the variations observed in Figure 5-16. f_4 appears to be a m>0 mode, based on the red to blue movement observed in Figure 5-22.

There is significant power at frequencies ranging from 6-10 cd^{-1} in the Fourier transform of the residuals after extraction for all frequency determination

methods. It seems highly likely that there is more unresolved variation present in this data.

Although it is believed that the four frequencies adopted do not entirely explain the variations observed in the line profiles, no other frequencies can be reliably obtained from the lines investigated. As reasonable precision is required to be able to confidently extract a frequency, it seemed sensible to leave any other variations present in the line profile and have them considered in the uncertainty of the frequencies that are extracted.

5.5 $V_{rot}sin$ i measurements

When few observations are available, the direct fitting and Fourier transform methods of $V_{rot}\sin i$ determination outlined in Section 3.1.1 are used as a best estimate. In the case of V2052 Oph, we have many observations, and can therefore solve for $V_{rot}\sin i$ as part of the optimisation in the application of the FPF method. In doing so this will take into account broadening factors, such as pulsational broadening, that the direct fitting and Fourier transform methods simplify to an intrinsic Gaussian line. It was useful to have a starting point and estimated uncertainty for our optimisation, this was done using the direct fitting and Fourier transform methods, the results for each line are outlined in Table 5-3, shown in Figure 5-24 and Figure 5-25 are the results for the He I 4713Å line (see Appendix D for the other lines).

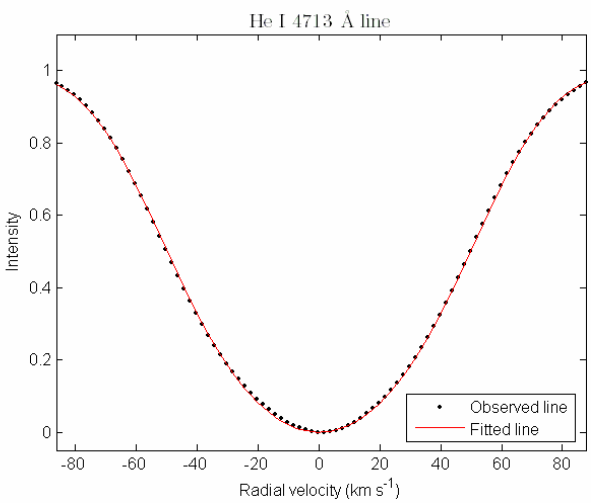

Figure 5-24: Direct fitting technique best fit to the He I 4713Å line gives $V_{rot}\sin i$ =63.1±2.0 km s^{-1}.

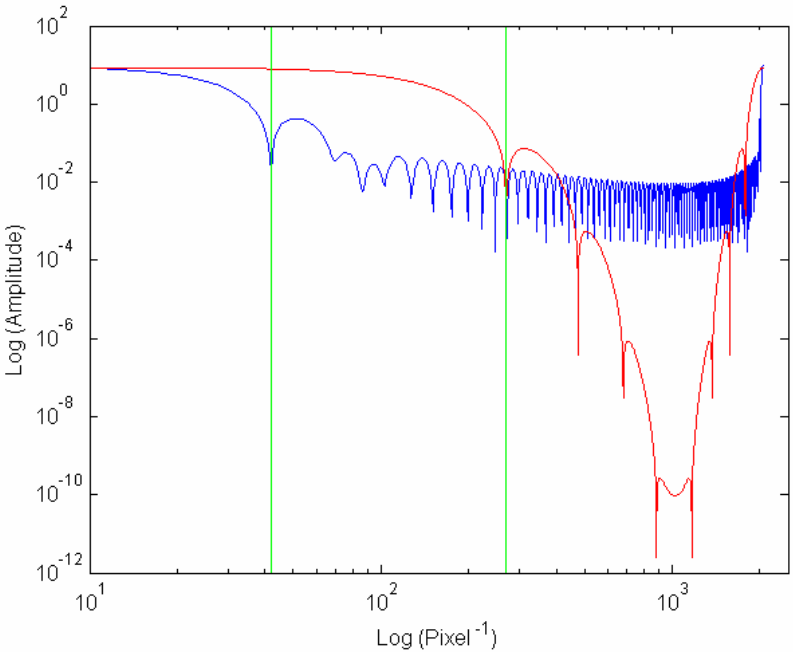

Figure 5-25: log-log plot of the Fourier transform of the He I 4713Å line (blue) and a Gaussian broadened to $V_{rot}\sin i$ = 10 km s^{-1} with the broadening curve of Gray (1992) (red). The green lines indicate the positions of the first minima. The ratio of the first minima along the abscissa (*10 km s^{-1}) gives the $V_{rot}\sin i$ of the line. The result is $V_{rot}\sin i$ = 64.0±4.0 km s^{-1}.

Table 5-3: Summary of $V_{rot}\sin i$ fits for the mean line profiles.

	Direct fit $V_{rot}\sin i$ (km s^{-1})	**Fourier method $V_{rot}\sin i$ (km s^{-1})**
Si III 4553Å	65.3±3.0	65.6±3.0
He I 4713Å	63.1±1.0	64.0±3.0
He I 5876Å	68.8±1.0	64.9±3.0

The Si III 4553Å line has a larger uncertainty as it was difficult to fit the deepest part of the line in the direct fit (see Appendix D for figure). The results from Table 5-3 agree well and a range of $V_{rot}\sin i = 64\pm4$ km s^{-1} was used for the FPF optimisation.

5.6 Mode identification

The two spectroscopic mode identification methods appropriate to apply to V2052 Oph are the intensity period search (IPS) method and the Fourier parameter fit (FPF) method. The results for these techniques are outlined in the following two sections.

5.6.1 Intensity period search (IPS) method

As explained in Section 4.2.3.2 the intensity period search (IPS) method derives relationships between the degree *l* and the azimuthal order *m* of a non-radial pulsation and the measured change in phase across the profile for a pulsation frequency and its first harmonic. In Telting and Schrijvers (1997) and Schrijvers and Telting (1999) a number of relationships are given linking

the phase change across the profile ($\Delta\Psi_0$) and l and $\Delta\Psi_1$ and m for different conditions. The relation chosen for this data is

$$\lambda \approx 0.089 + 1.096 \cdot \left|\Delta\Psi_0\right| / \pi \, . \tag{5.1}$$

This relation is based on detectable modes that are caused primarily by the NRP velocity field.

For the observations of V2052 Oph the first harmonic was not observed for either of the pulsational frequencies detected. Hence the m relation is not used for this data set.

From Figure 5-16 and Figure 5-22 $\Delta\Psi_0$ (7.148 cd^{-1}) = 3.2±0.2 and $\Delta\Psi_0$ (6.827 cd^{-1}) = 12.0±0.5. These values give $l \approx 1.21$ for the f_1 frequency and $l \approx 4.28$ for the f_2 frequency. The stated error for l is ±1 so formally the results are l = 1±1 and l = 4±1 for the f_1 and f_2 frequencies respectively. The result of l = 1±1 for f_1 agrees with the previous determinations of l = 0 from photometric amplitude ratios (Heynderickx et al. 1994) and from phase and power across the spectral line diagrams (N03). The l = 4±1 for f_4 agrees with N03's l = 3 or 4 which was also based on an analysis of the phase and power (amplitude ^{2}) across the spectral line.

5.6.2 Fourier parameter fit (FPF) method

Each of the 3 lines was investigated using the FPF method. A number of stellar parameters must be given as input for the application of the FPF method although most are able to be optimised given a range of possible values. The

parameters used as inputs are based on the model of N03 and the $V_{rot}\sin i$ measurements from the previous section, they are summarised in Table 5-4. Some of the ranges of certain parameters differ between the frequencies to allow an investigation of the local minima of that parameter. The ranges for the amplitude, phase, the equivalent width response to temperature of the line, the ratio of the flux to radius variation and the phase lag between the radial and flux variations were kept broad as no prior knowledge of these variable existed.

When applying the FPF method, all identified frequencies must be removed from the variations in each line profile using a simultaneous least squares fit. This was done during the pixel-by-pixel frequency analysis. This supplies the zero point line profile and the phase and amplitude across the profile for each frequency (e.g. Figure 5-16). These three datasets (zero point, amplitude and phase) are the 'Fourier parameters' that are fitted for each frequency. The residuals after subtraction of the identified frequencies are used to compute the uncertainties in each bin and a χ^2 measure is made for each set of input parameters.

All the variables are then optimised over a specified range using a genetic algorithm which simultaneously solves for each of the variables. A genetic algorithm is used because the very large parameter space to be covered would take too long to investigate using a complete grid. In this case, the variables being optimised are the mass, the radius, the $V_{rot}\sin i$, the inclination, the equivalent width and intrinsic (pre-broadened) width of the line profile, the quadratic limb-darkening parameters, the amplitude of the pulsation as a fraction of the stellar radius, the phase of radial displacement, the Doppler velocity of the line profile, the equivalent width response to temperature of the

line, the ratio of the flux to radius variation and the phase lag between the radial and flux variations. All of these parameters are shown over their optimised range in Figure 5-26, though only a few of them are sensitive to changes.

Table 5-4: FPF parameters used for each of the frequencies. These parameters were optimised over the range given. The format is [start, finish] (step).

Variable	**7.148 cd^{-1} [range] (step)**	**6.827 cd^{-1} [range] (step)**
Degree *l*	[0, 2] (1)	[0, 8] (1)
Azimuthal order *m*	[-2, 2] (1)	[-8, 8] (1)
Radius (R_{star}/R_{sun})	[3.7, 4.5] (0.1)R_{sun}	[3.7, 10] (0.1)R_{sun}
Mass (M_{star}/M_{sun})	[8.9, 11.3] (0.1) M_{sun}	[8.9, 11.3] (0.1) M_{sun}
Inclination (^{o})	[5^o, 85^o] (1^o)	[5^o, 85^o] (1^o)
$V_{rot}\sin i$ (km s^{-1})	[60, 68] (0.1)	[60, 64] (0.1)
Amplitude (fraction of radius)	[0.0001, 0.01] (0.0001)	[0.0001, 0.01] (0.0001)
Phase	[0, 1] (0.01)	[0, 1] (0.01)
α_w equivalent width response to temperature	[-10, 10] (1)	[-5, 5] (1)
$\|f\|$ flux to radius ratio	[0, 30] (1)	[0, 30] (1)
Phase lag between radial and flux variations	[0, 1] (0.01)	[0, 1] (0.01)

Some parameters were refined in a preliminary optimisation in which only the zero point line profile was fitted and only those variables which have significant influence on the zero point line profile were fitted. This allowed the variables to be quite well determined for the full scale optimisation, decreasing the time for the algorithm to converge.

The results from the FPF method for f_1 in the He I 4713Å line are shown in Figure 5-26 to Figure 5-29. The results for the other lines (He I 5876Å and Si III 4553Å) are quite similar; the graphs can be seen in Appendix D. In Figure 5-26 are the graphs of l, m, stellar radius and mass, inclination, $V_{rot}\sin i$, pulsation amplitude and phase, α_w the spectral lines equivalent width response to temperature, the ratio of flux to radius variation, and phase lag between radial and flux variations all versus the χ^2 statistic. In each graph, each point is a tested model. The minimum value for each graph is 3.004, at the best fit position. The 95% confidence limit for the reduced χ^2 for this data is 1.16 which is not reached by any model. It is clear there are very different dependencies for the different parameters. For example the stellar mass and radius are very poorly defined in this fit, whereas the pulsation amplitude and phase are well defined with a relatively clear peak. The optimised parameters are specified in Table 5-5. The 95% confidence limit may not have been obtained but there are limits that can be placed on the parameters based on an examination of Figure 5-26 to Figure 5-29. The two most important parameters for this thesis are the degree l and azimuthal order m. That f_1 is an axisymmetric mode ($m = 0$) is very clear from the Figure 5-26, though it is not so clear which of l=0, 1 or 2 is the correct degree of the pulsation. Previous work have unambiguously identified l=0 (radial pulsation) for this mode which is plausible for our results given the small differences in the χ^2 values for the different l.

In Figure 5-27 the best fit to the zero point profile and the amplitude and phase across the profile is shown. In Figure 5-28 and Figure 5-29 two different ways of examining the differences between the synthetic and the observed line profile variations (after subtraction of the mean profile) are shown. Figure

5-28 uses the phased surface plot of the two sets of data while Figure 5-29 looks at the individual residuals for each profile.

In Table 5-5 the parameters for the best three fits are given since they have similar χ^2 values. Note that some of the differences between the fits are insignificant because of the very weak dependence of some variables e.g. mass. It can be seen from these results that an l =0,1 or 2 mode can be a good fit to the variations observed for f_1. Previous work has suggested l =0 and m =0 which agrees with our result of l =1±1 and m =0.

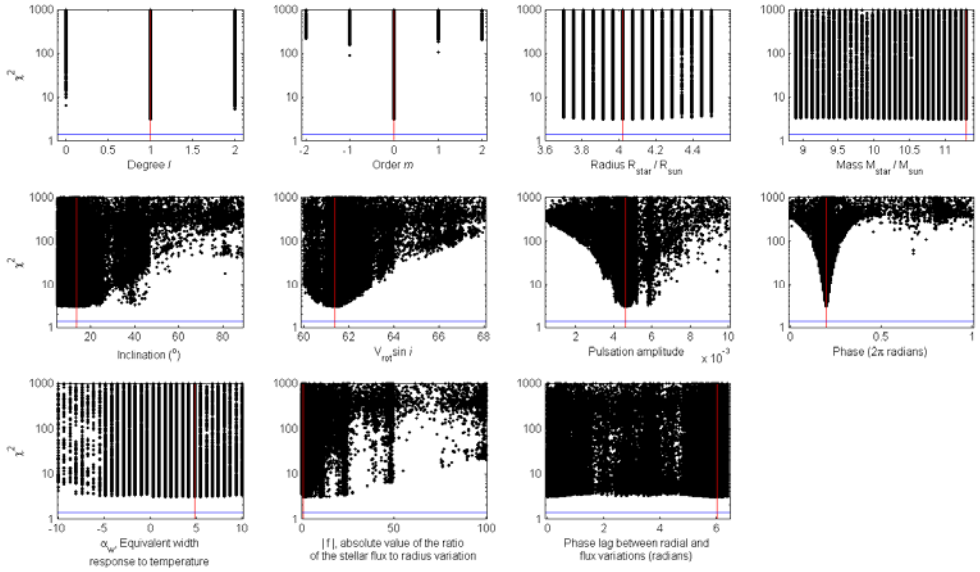

Figure 5-26: χ^2 optimisations for various pulsational, stellar and line specific parameters for f_1 in the He I 4713Å line. The red line in each sub-plot indicates the position of the minimum χ^2 and the blue line indicates the 95% confidence level of 1.16.

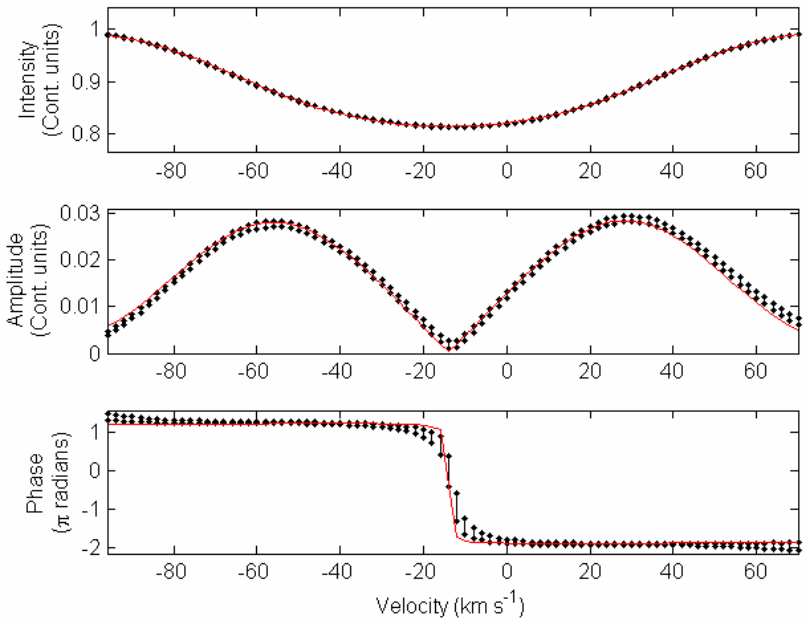

Figure 5-27: Best fit to the zero point profile and amplitude and phase across the profile for f_1 in the He I 4713Å line. The fit is a l=1 m=0 non-radial pulsation.

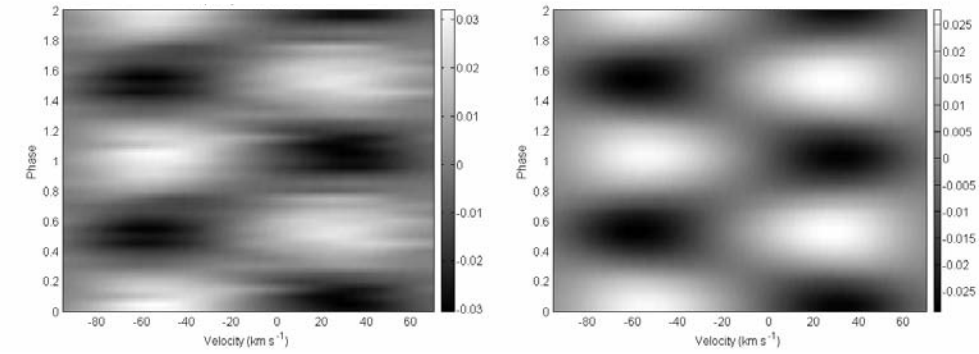

Figure 5-28: Observed profile residuals after subtraction of the mean profile for the He I 4713Å line phased to f_1 (left). Theoretical profiles produced with the LIPS program based on the best fit parameters (right).

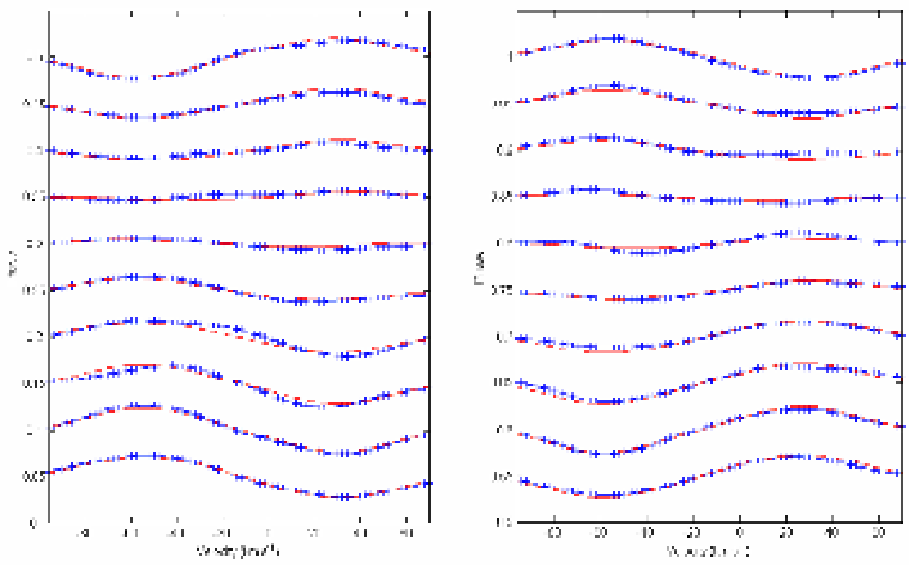

Figure 5-29: Observed profile residuals after subtraction of the mean profile for the He I 4713Å line phased to f_1 and separated vertically and arranged on to a phase axis (blue pluses). Theoretical profiles produced with the LIPS program based on the best fit parameters (red lines). The size of the deviations in continuum units can be estimated from the colour bars in Figure 5-28.

Table 5-5: The parameters of the three best fits to the frequency 7.145 cd^{-1} (f_1)

Variable	***l*=1 *m*=0**	***l*=2 *m*=0**	***l*=0 *m*=0**
χ^2	3.004	5.202	6.318
Radius (R_{star}/R_{sun})	4.02	3.70	4.23
Mass (M_{star}/M_{sun})	11.3	11.3	8.9
Inclination (^{o})	13.60	14.26	19.55
$V_{rot}\sin i$ (km s^{-1})	61.4	61.4	61.6
Amplitude (fraction of radius)	0.0046	0.0046	0.0064
Phase	0.197	0.197	0.197
α_w equivalent width response to temperature	4.84	2.26	2.26
$\|f\|$ flux to radius ratio	0.787	1.57	1.57
Phase lag between radial and flux variations	0.96	0.71	0.945

The results for f_4 are shown in Figure 5-30 through to Figure 5-33. The results are similar to those for f_1 in that many of the parameters are not very sensitive with poorly defined minima or no minima at all. The 95% confidence level is not reached for any model though there are indications that it is a l=4±2 m=2±2 mode. After an examination of the best fits for different l and m combinations the l=4, m=2 model was selected as the best. Based on the fitted parameters for this pulsation mode Figure 5-32 and Figure 5-33 were created. The match to the data in these figures is quite good.

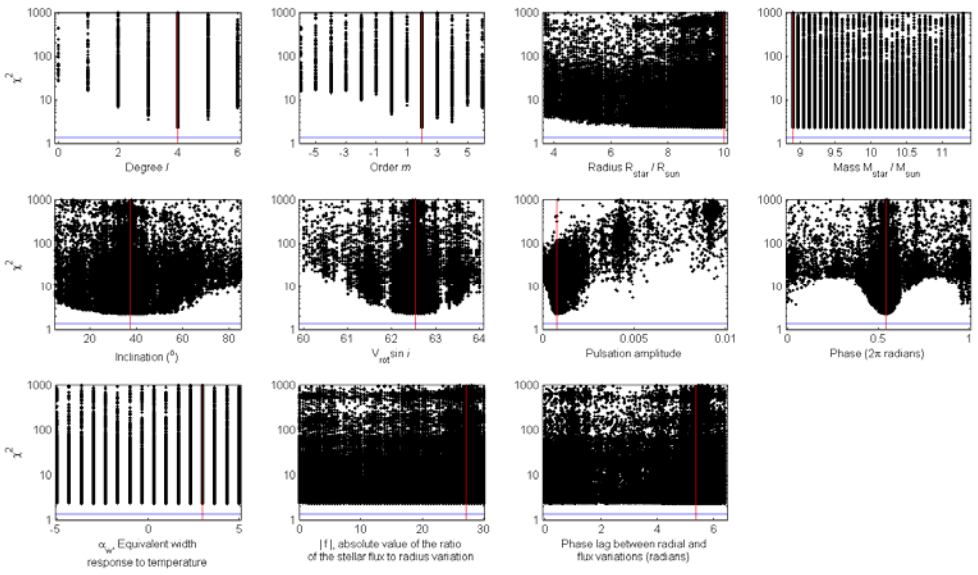

Figure 5-30: χ^2 optimisations for various pulsational, stellar and line specific parameters for f_4 in the He I 4713Å line

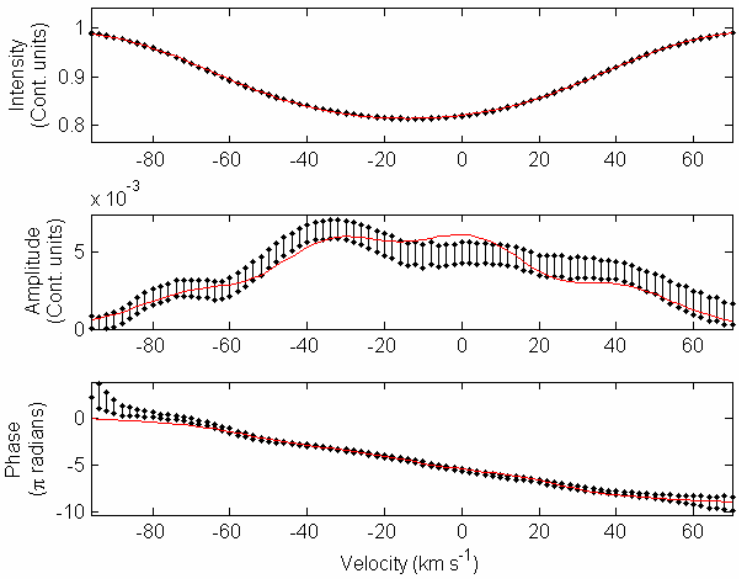

Figure 5-31: Best fit to the zero point profile and amplitude and phase across the profile for f_4 in the He I 4713Å line. The fit is a l=4 m=2 non-radial pulsation.

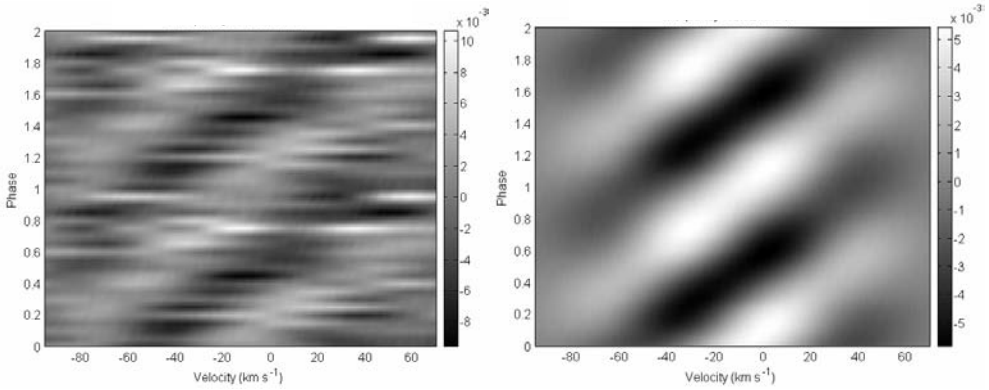

Figure 5-32: The same as Figure 5-28 but f_1 has been removed via least squares fitting to the observed profiles and the residuals have been phased to f_4.

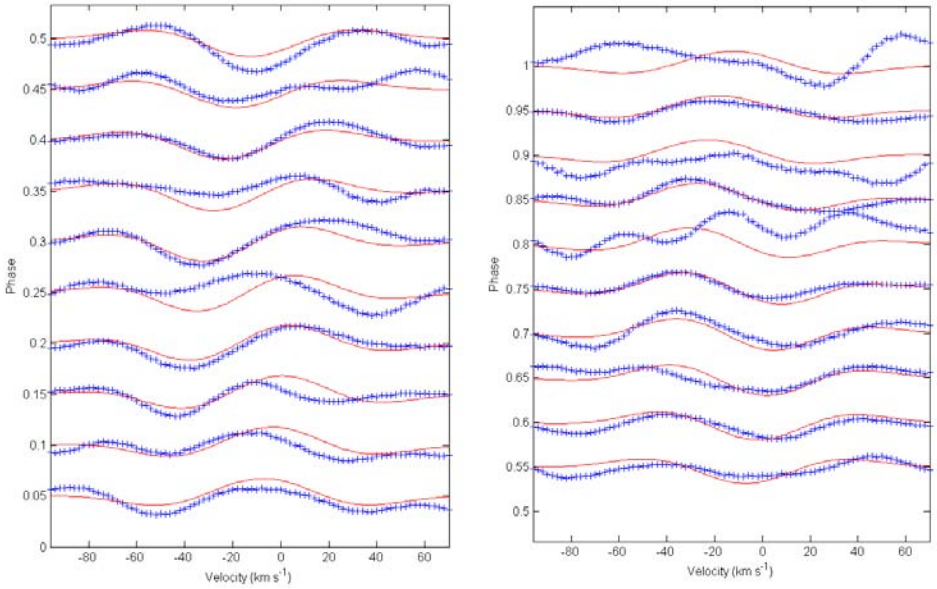

Figure 5-33: Same as Figure 5-29 but phased to f_4.

Table 5-6: Summary of the results of the FPF method.

	IPS		**FPF**	
	f_1	f_4	f_1	f_4
Degree l	1±1	4±1	1±1	4±2
Order m	N/A	N/A	0±0	3±2
Inclination (^{o})	N/A	N/A	N/A(l=0)	<70^o
$V_{rot}\sin i$ (km s^{-1})	N/A	N/A	61.4	62.5
Amplitude (fraction of radius)	N/A	N/A	N/A(l=0)	0.001±0.001

5.7 Conclusions

V2052 Oph shows clear variation in its line profiles. The frequencies 7.145 cd^{-1} (f_1) and 6.827 cd^{-1} (f_4) were previously identified as pulsational frequencies present in the spectral line profiles. The frequencies 0.2748 cd^{-1}

(f_3, f_{rot}) and 0.5496 cd^{-1} (f_2, $2f_{rot}$) were also present and were identified as being a result of the rotation of V2052 Oph. All of these frequencies were detected in the data studied in this thesis. Because all of the frequencies except f_4 were previously identified with higher precision than was able to be obtained from the available data, the previous works' frequencies were adopted. f_4 was determined from the data set analysed in this thesis.

Neiner et al. (2003) had observed evidence of modulation of the pulsation frequency with the rotation frequency, which implies the pulsation axis may not coincide with the rotation axis. That these two axes coincide is a basic assumption of both of the mode identification methods used in this analysis. As there are no mode identification methods currently available that include the ability for a non-aligned pulsation axis, a normal application of the IPS and FPF methods were completed.

The results of the IPS mode identification were $l = 1 \pm 1$ for f_1 and $l = 4 \pm 1$ for f_4. Both phase changes were able to be measured easily and the result for f_1 agreed with previous photometry and spectroscopy indicating $l = 0$. The result for f_4 agreed with previous spectroscopy which indicated $l = 3$ or 4.

The results from the FPF analysis on the pulsational frequencies f_1 and f_4 were encouraging. The 95% confidence limit for the reduced χ^2 is 1.35 was not reached for any of the three lines analysed but all three obtained best fit reduced χ^2 values less than 4.

The genetic optimisation graphs provided some limitations for various pulsational and stellar parameters. Of significance in these results was the stellar parameter $V_{rot} \sin i = 62 \pm 1$ km s^{-1}, and the pulsational parameters $l = 1 \pm 1$,

m=0, and amplitude=0.0043±0.001 R_{star} for f_1, and l =4±1, m=3±1, and amplitude=0.0008±0.001 R_{star} for f_4. It is not possible to draw conclusions about the inclination from the optimisations. The ambiguity may be because the pulsation axis is not aligned with the rotation axis. Little other information could be obtained from the optimisations because of the insensitivity of the other parameters.

The fits of the synthetic line profiles generated using the optimum parameters from the FPF analysis were good for both pulsational frequencies.

Because of these convincing fits to the observed line profiles, it is thought that if the pulsation axis is not aligned with the rotation axis, as has been suggested, then the effects of this are not sufficient to disrupt mode identification for the two identified pulsation frequencies.

Chapter 6
QW Puppis

The γ Doradus object QW Puppis (QW Pup, HD5589, HR2740) was first discovered to be variable by Hensberge (1981), who had used it as a comparison star. It was determined to be a 'mild Ap star' based on 20 *ubvy* data collected over 41 days from which they derived a period of 0.9363±0.0050 days. Hensberge (1981) noted that QW Pup did not have any continuum depression near 5200Å, which would be expected for Ap stars, and that additional photometry was required to confirm their period and classification. Poretti (1997) determined that QW Pup was a γ Dor star based on the line profile variation (LPVs) observed in its spectrum and the frequencies determined from photometry. They determined four independent frequencies 1.0434±0.0004 cd^{-1}, 0.9951±0.0010 cd^{-1}, 1.1088±0.0017 cd^{-1} and 0.9019±0.0020 cd^{-1} from multi-site photometry which almost completely explained the variability observed.

6.1 Observations

For this thesis, 179 spectroscopic observations were obtained over the time interval JD 2453409-2453464 (see Table 6-1). This implies a theoretical frequency resolution of 0.027 cd^{-1} (Loumos and Deeming 1978). However, based on experience it is unlikely that this resolution was achieved due to the large gaps in the dataset over this time (see Figure 6-1). The observations were

~15 minute integrations. By requiring a maximum of one tenth of a pulsation cycle to be sampled for a well defined frequency an upper limit of 9.6 cd^{-1} can be placed on the well defined frequency range.

Two sets of profile data were extracted from the spectra. One consisted of the addition, in velocity space, of a few spectral lines. The other was the scaled CCF. The datasets were analysed in similar ways so that a comparison between the two methods of defining a spectral line could be carried out. The analysis of the data begins with the determination of the individual spectral line profiles to be combined for use in this study.

6.2 Line selection for combined profile

To be able to combine spectral lines together the lines should be isolated, with easily definable continuum on either side of the line profile, and the lines should show identical temporal behaviour.

Because of the reasonably broad lines of QW Pup and the extreme crowding of spectral lines in early F type stars, few spectral lines were identified in the available wavelength range that have definable continuum on either side as is necessary for this investigation of their variability.

Table 6-1: Observations obtained of QW Puppis

Date	**Julian date (-2453000)**	**Site**	**Instrument**	**# of obs.**
7 - 9 Feb 2004	409-411	MJUO	HERCULES	18
28 Feb – 4 Mar 2004	430-434	MJUO	HERCULES	12
29 Mar – 3 Apr	460-464	MJUO	HERCULES	27

2004				
23 Mar – 3 Apr 2004	452-464	SAAO	GIRAFFE	122

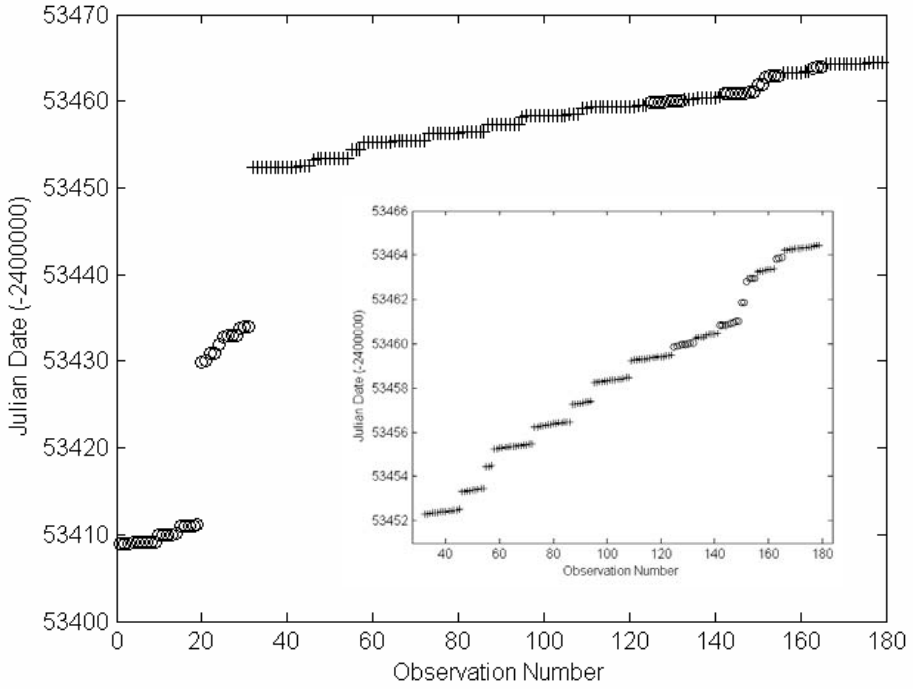

Figure 6-1: Observations of QW Pup taken at MJUO (circles) and SAAO (pluses) over the period 2453409 - 2453464 JD. The smaller graph is an enlargement of the main campaign period.

The search for isolated lines resulted in the twelve lines listed in Table 6-2. Some of these lines had considerably different excitation potentials though all lines were observed to vary in similar ways (see examples in Figure 6-2).

Thorough testing was done to examine the results of combining the lines in Table 6-2. During the addition of the different line profiles it was observed

that inclusion of the weaker lines (see Table 6-2) increased the noise in the combined profile for the more noisy SAAO observations. Though all of the line profiles visually varied similarly (see Figure 6-2 for the four strongest line profiles), some of the weaker lines that were not included in the combination had some observations which were clearly in error. This was found to be linked to a random and rare occurrence in the reduction of the SAAO data. This software error caused some parts of a few of the red spectral orders in an observation to have zero intensity. For these reasons the most simple and reliable data set was made from combining only the four strongest lines of those listed in Table 6-2. The lines were the Ca I 6122Å, Fe I 5302Å, Fe I 5367Å, and Fe I 5570Å lines.

Table 6-2: Information on the lines used for the analysis of QW Puppis from Moore (1966). Weaker lines are marked with an asterisk.

Wavelength (Å)	**Species**	**Lower excitation Potential (eV)**
5090.78 *	Fe I	4.26
5115.40 *	Ni I	3.83
5302.31	Fe I	3.28
5313.59 *	Cr II	4.07
5367.48	Fe I	4.42
5569.63	Fe I	3.42
5576.10	Fe I	3.43
5581.98 *	Ca I	2.52
5853.69	Ba II	0.60
5862.37 *	Fe I	4.55

6122.23	Ca I	1.89
6393.61	Fe I	2.43

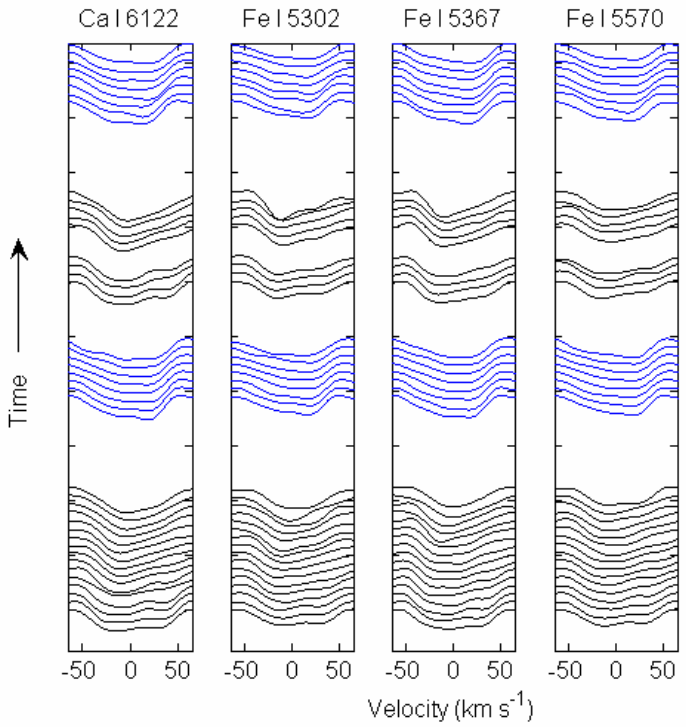

Figure 6-2: Stacked line profiles for the Ca I 6122Å, Fe I 5302Å, Fe I 5367Å and Fe I 5570Å lines demonstrating the similar distortion of each line. SAAO observations are in black and MJUO observations are in blue. The observations are approximately spaced to represent the time between the observations with the gap between each site's observations reduced for display purposes.

In order to combine the data from different observing sites the different spectrographs' instrumental profiles (or response functions) had to be removed. The spectrographs' instrumental profiles change from night to night (Zima 2005), so they were measured by using a selection of thorium lines from one of the wavelength calibration spectra for each night's observation and for

each site. The procedure used to measure and remove the instrumental profile is outlined in Section 2.4.2.

Once the data were homogeneous between both sites, the radial velocities were measured and the mean profile for all observations was determined for each line. By visually examining the mean of all the observations for each of the four selected lines shown in Figure 6-3, it can be seen that the lines can be combined without fear of broadening because of poorly known rest wavelengths or due to the lines having different mean velocities. The amplitudes and phases for the different spectral lines are similar as seen in Figure 6-4.

The mean profile of the four spectral lines was determined for each of the observations after converting them into velocity space and projecting each line onto the same velocity axis. Each observation was then represented by a single line profile. These combined line profiles are now ready for frequency analysis.

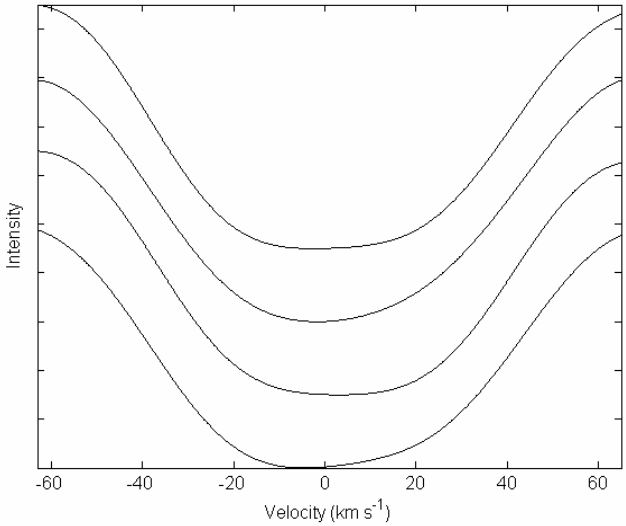

Figure 6-3: Mean line profiles for the Ca I 6122Å, Fe I 5302Å, Fe I 5367Å and Fe I 5570Å lines bottom to top respectively. The lines have been normalised so that their depth is the same and then offset from each other so as to show the similar extent in velocity space of the lines and the small differences in the mean profiles.

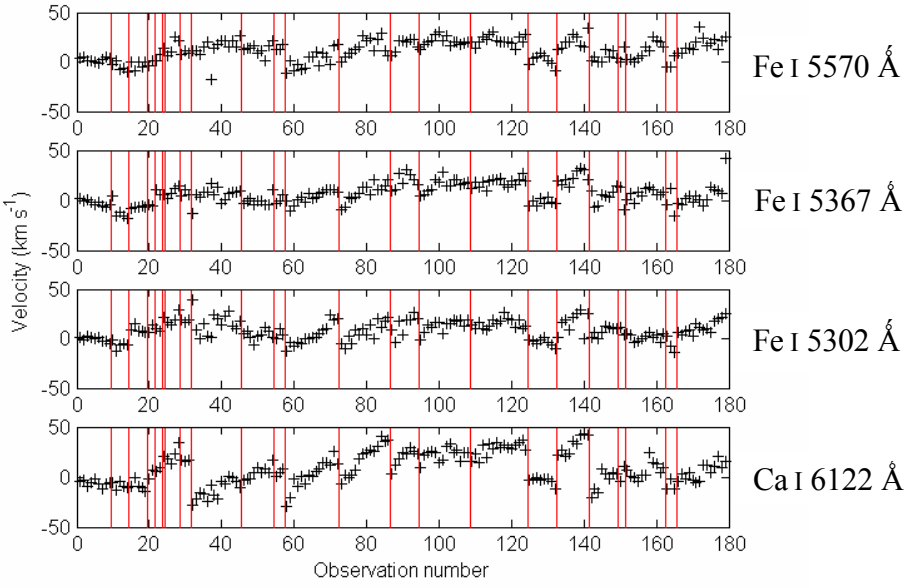

Figure 6-4: Velocities of the Ca I 6122Å, Fe I 5302Å, Fe I 5367Å and Fe I 5570Å lines bottom to top respectively. The velocity is plotted versus observation number to show

the variations in a given night. The vertical red lines show the end of a night. The length of time between nights varies.

6.3 Scaled delta-function cross-correlation profiles

The scaled delta function CCF method of line profile determination was applied to the spectra of QW Pup. Because of the quality of some of the SAAO observation's red orders, the wavelength range of the delta function template used in the cross-correlation was limited to 4507-5819Å. With the interorder gaps in the HERCULES spectrum removed, this contained 1078 spectral lines.

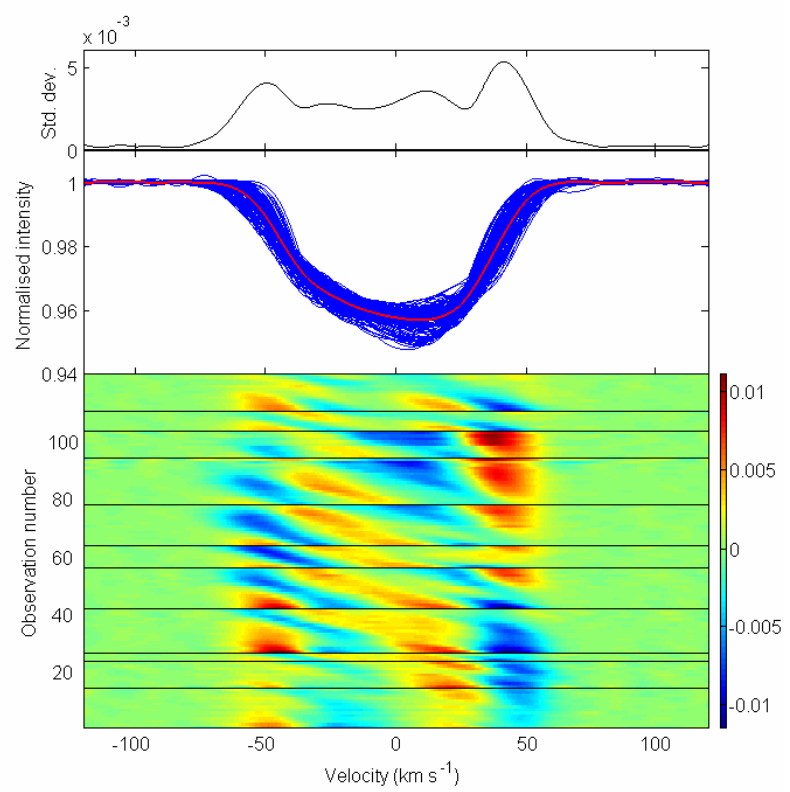

Figure 6-5: Top: Standard deviation of the cross-correlation profiles for the SAAO observations. Middle: All of the CCFs overplotted in blue with the mean profile in red. Bottom: Coloured surface plot of the CCFs. Black lines indicate the end of a night. The length of time between nights varies.

In Figure 6-5 the SAAO observations scaled CCFs are shown overplotted on each other along with a colour-mapped surface of the residuals after subtraction of the mean CCF profile. At the top of the figure is the standard deviation observed across the CCF profile. In this figure, clear non-radial pulsation-like (NRP-like) variations can be seen to be present in the dataset.

The two different observatory's datasets were homogenised into one dataset by removal of the instrumental profile using the same Gaussian representations of

the instrumental profile as was used for combining the line profile. Because of the very high S/N of the CCF profiles the choice of the parameter α_0 for the filtering of the profiles was not difficult (see Section 2.4.2). The smoothing for the scaled CCFs was carried out in velocity space using the value $\alpha_0 = 40$ (equivalent to $\alpha_0 = 0.35$ in wavelength space). The CCF profiles are now ready for frequency analysis.

6.4 $V_{rot}sin$ i measurements

The V_{rot}sin *i* of QW Pup was measured with both of the methods described in Section 4.1.2 and was applied to both the mean of the combined line profiles and the mean of the scaled CCF profiles.

The combined line profiles gave 52.2±2 km s^{-1} for the fitting method (see Figure 6-6) and 50.8±2 km s^{-1} for the Fourier method (see Figure 6-7). The CCF profiles gave 51.5±1 km s^{-1} for the fitting method (see Figure 6-8) and 51.4±1 km s^{-1} for the Fourier method (see Figure 6-9).

Using this information a decision was reached about which mode identification methods could be used to analyse the star. A NRP star with a V_{rot}sin *i* ~50 km s^{-1} can be analysed with both the FPF and the IPS methods of mode identification. The moment method is not appropriate (see Section 4.2.3.1).

6.5 Frequency analysis

Typical γ Dor frequencies range from ~0.3-3 cd^{-1}. In this frequency range it is particularly difficult to identify any frequencies present in the data because a

full pulsation cycle cannot be sampled in one night's observations, except in the highest frequency cases. Also there is 1 cd^{-1} aliasing present in the data despite its multi-site nature (see Figure 6-10).

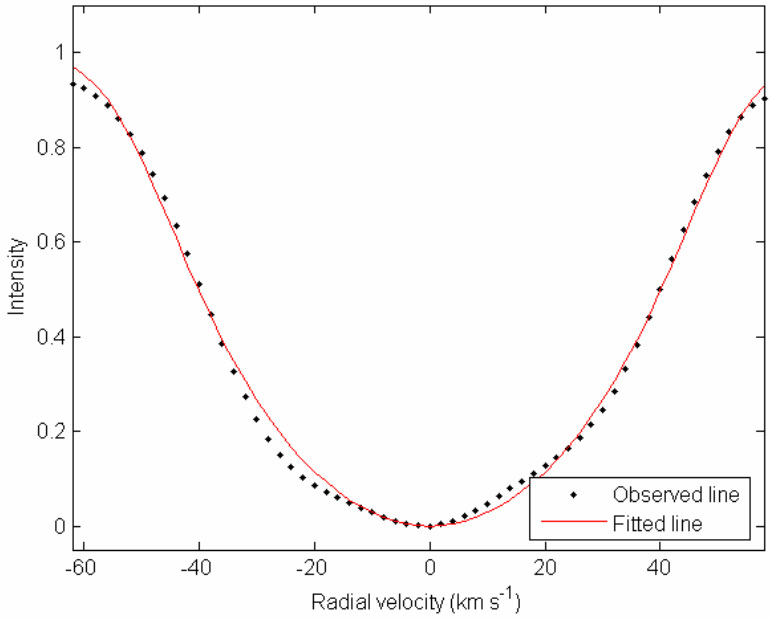

Figure 6-6: Fitting profile analysis of the mean of the combined line profiles gives $V_{rot}\sin i = 52.2\pm2$ km s^{-1}.

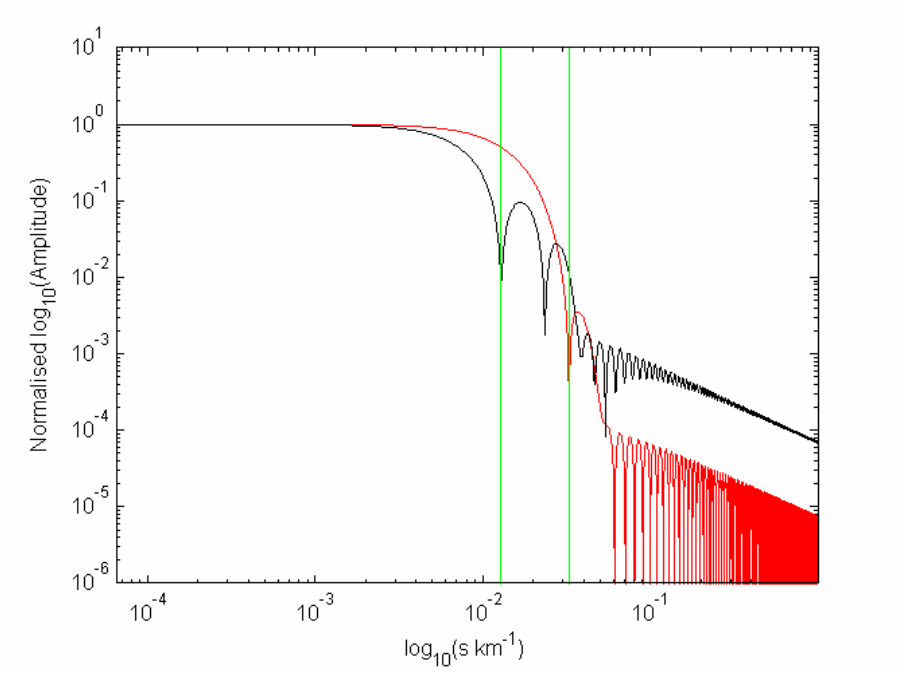

Figure 6-7:Fourier profile analysis of the mean of the combined line profiles gives $V_{rot}\sin i = 50.8\pm2$ km s^{-1}.

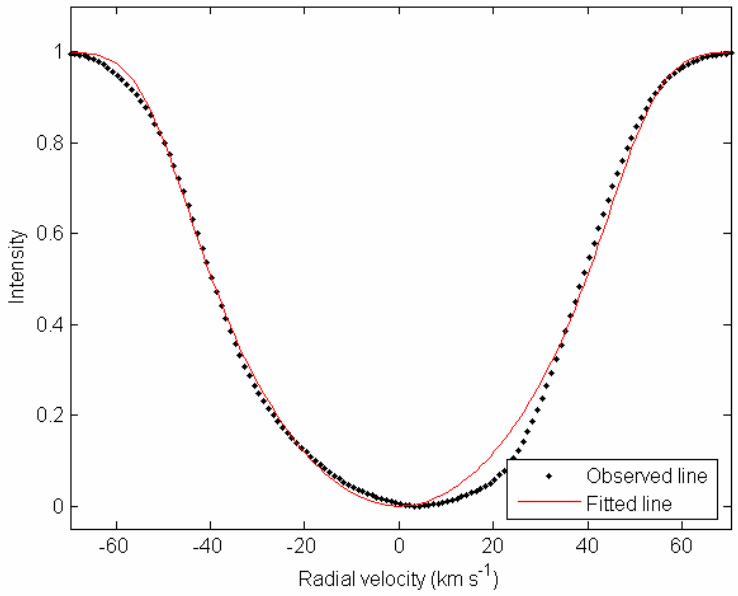

Figure 6-8: Fitting profile analysis of the mean of the scaled CCFs gives $V_{rot}\sin i = 51.5\pm1$ km s^{-1}.

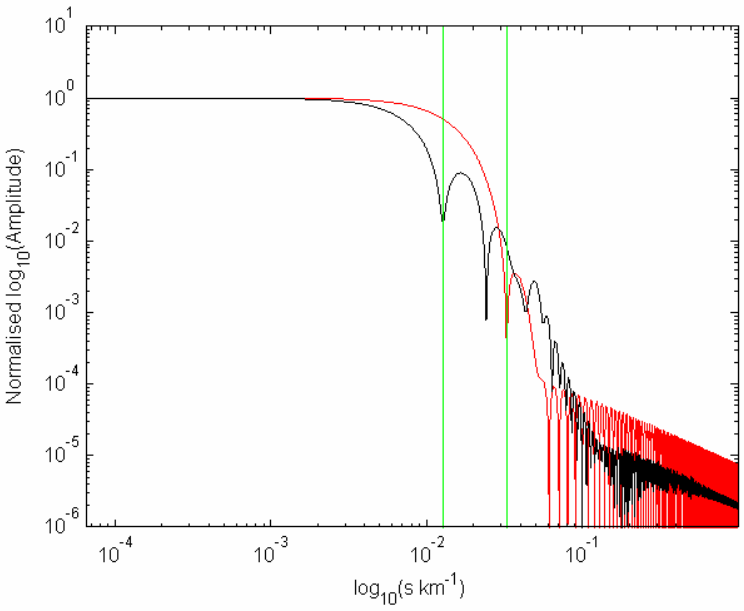

Figure 6-9: Fourier profile analysis of the mean of the scaled CCFs gives $V_{rot}\sin i$ = 51.4±1 km s^{-1}.

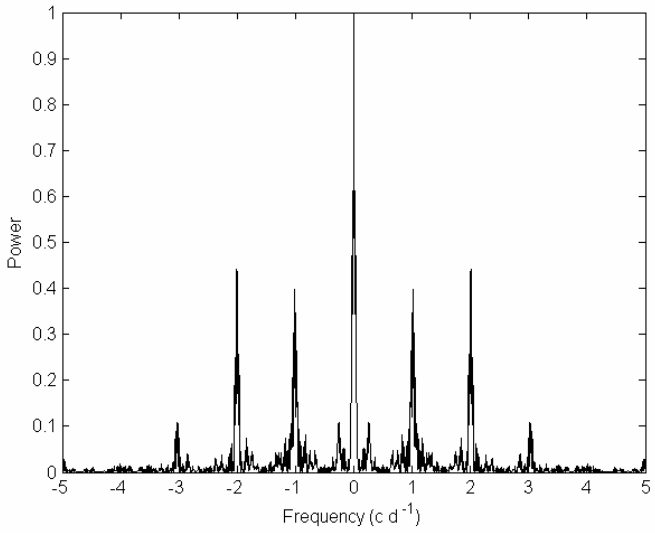

Figure 6-10: The window function for the complete QW Pup dataset. Despite the multi-site nature of the observations the 1 cd^{-1} and 2 cd^{-1} aliases are still around 45% of the height of the main peak.

It has been stated that a frequency resolution of 0.027 d^{-1} is expected for these data with an upper frequency limit of 9.6 cd^{-1} for well determined frequencies.. These values are appropriate for the detection of typical γ Dor type frequencies.

Table 6-3: Forced fits to Poretti (1997) photometric frequencies. Because the frequencies are fitted simultaneously there is only one residual value for each fit.

	Combined profiles		**Scaled CCF profiles**	
Freq (cd^{-1})	**Amp (km s^{-1})**	**Residual**	**Amp (km s^{-1})**	**Residual**
1.0434	1.321		1.116	
0.9951	1.139		1.034	
1.1088	1.265		1.378	
0.9019	0.7427	0.842	0.6932	0.843

QW Pup has four frequencies identified in a previous photometric study (Poretti et al. 1997). To determine whether these photometric frequencies are observed as spectroscopic line profile variations, a forced frequency extraction was carried out on the velocity variations in both the combined line profiles and the CCF profiles. To do this, a multi-frequency fit using the precise frequencies from Poretti (1997) was made and the Fourier transform of the residual of the data was examined for remaining frequencies.

For both datasets the photometric frequencies of Poretti (1997) did not satisfactorily explain all of the observed variation. The residual is 47% of the original data variance. For this reason the frequencies extracted

spectroscopically were selected for further analysis rather than the previously identified photometric frequencies.

Throughout all of the frequency analyses the Fourier transform frequency range above 10 cd^{-1} was very low in power. For this reason, and to enhance the appearance of the lower frequency range, the frequency graphs extend only to 10 cd^{-1}.

Table 6-4: Frequency analysis results for equivalent widths of the combined line profiles.

Freq (cd^{-1})	Amp	Residual
1.2912	0.1391	0.2681
5.0738	0.1242	0.2552
1.7807	0.1132	0.2399
1.1204	0.1149	0.2257

Table 6-5:Frequency analysis of the velocity variations for the combined line profiles.

Freq (cd^{-1})	Amp	Residual
0.2234	1.7607	1.349
0.7083	0.8971	1.183
3.5030	0.7617	1.099
2.0573	0.7407	1.027
0.9283	0.5386	0.970
4.8837	0.5382	0.905
6.2745	0.5006	0.855
9.0105	0.4802	0.807
2.4356	0.4150	0.755
9.6677	0.3357	0.720

6.5.1 Combined line profiles

6.5.1.1 Velocity and equivalent width frequency analysis

Table 6-4 shows the results of the equivalent width frequency extraction. The final residual for the multi-periodic fits is still a substantial fraction of the residuals in the case where no periodic fit has been made (~77%). This implies that the variations observed in the equivalent width consist of either a large number of frequencies, all of which contribute evenly to the variation, or the simpler and more likely explanation, that the variation observed is primarily caused by noise in the data. The latter explanation is further supported by the fact that many of the frequencies extracted are not detected in any other analysis of either the combination line profiles or scaled CCF profiles. In the situation where the amplitudes obtained from the fit are real, it is useful to note that the largest amplitude single frequency is approximately 3.5% of the mean equivalent width for the combined line profiles. This is a small equivalent width variation.

The results from the frequency extraction of the velocity data are shown in

Table 6-5. Only two of the frequencies present in the extraction are similar to the four previous photometric frequencies. They are the 0.9283 cd^{-1} frequency which may correspond to the photometric 0.9019 cd^{-1} frequency, and the 2.0573 cd^{-1} frequency which may be a 1 cd^{-1} alias of the photometric 1.0434 cd^{-1} frequency. It appears from

Table 6-5 that the velocity variation for the combined line profiles is not easily explained with just a few frequencies.

6.5.1.2 Pixel-by-pixel frequency analysis

The pixel-by-pixel frequency extraction of the combined line profile data followed the procedure outlined in Section 4.2.2.

For each frequency selected, a least squares fit to each velocity bin's variation was made and the result subtracted. From this subtraction process the amplitude and phase across the profile at that frequency was obtained. In Figure 6-11 (Top) the 2-dimensional Fourier transform of the line profile variation before subtraction of any frequencies is shown with the mean of the frequency spectrum across the profile to the right, and the mean profile and standard deviation across the profile on top.

Five frequencies were obtained from the pixel-by-pixel method, they are 1.043 cd^{-1}, 1.242 cd^{-1}, 2.778 cd^{-1}, 1.112 cd^{-1} and 0.734 cd^{-1}. Two of these frequencies are likely to be associated with the photometric frequencies of Poretti (1997). The pixel-by-pixel frequencies 1.043 cd^{-1} and 1.112 cd^{-1} are probably the photometric 1.0434 cd^{-1} and 1.1088 cd^{-1} frequencies. The other frequencies do not correspond to frequencies obtained from the velocities or equivalent widths.

For the two strongest frequencies, the line profile residuals phased to the frequency, and the amplitude and phase across the profile obtained from the least squares fit (e.g. Figure 6-11 bottom) are also shown.

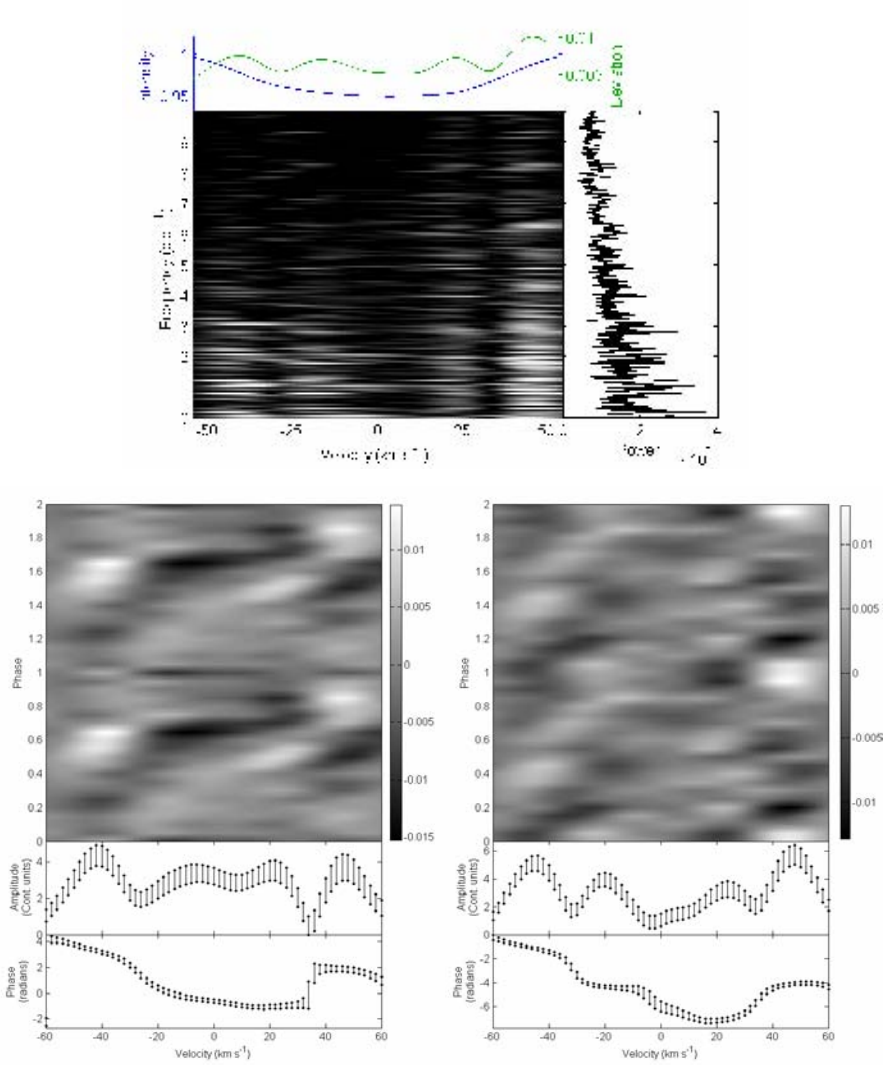

Figure 6-11: Top: The pixel-by-pixel frequency analysis 2-D plot. Bottom: The phased surface plots and extracted amplitude and phase across the profile for the two strongest frequencies 1.043 cd^{-1} and 1.242 cd^{-1} left to right respectively.

The two phased surface plots (Figure 6-11 bottom) correspond to the strongest frequencies. These frequencies also show the most NRP-like variation in their phased surface plots with some visible left-to-right movement through the profile with time. Despite this, the amplitude and phase across the profile for

those frequencies is not typical of NRP and the movement in the phased surface plots is not so well defined as to be easily identified as due to NRP.

From the phased surface plots created from both the velocity frequency analysis and the pixel-by-pixel frequency analysis, it is clear that the combined line profile data is insufficient to clearly resolve the frequencies present in the data, and whether or not there are NRPs.

6.5.2 Scaled CCF profiles

6.5.2.1 Equivalent width and velocity frequency analysis

In Figure 6-12 the extraction of frequencies from the equivalent width data using the approach outlined in Section 4.2.1 was carried out. The frequencies extracted, and their amplitudes, are shown in Table 6-6. The strongest three frequencies extracted only reduce the residual to 85% of what it is when no fit has been made. This implies that the variations in the equivalent widths cannot easily be explained by fitting a few frequencies. Of the three frequencies selected only the 1.105 cd^{-1} frequency corresponds to those frequencies extracted from the velocity and pixel-by-pixel frequencies. For these reasons it is thought that the equivalent width variation observed other than due to the 1.105 cd^{-1} frequency is primarily caused by noise.

The frequencies obtained from the velocity variations of the scaled CCFs are outlined in Table 6-7. The frequency 2.1530 cd^{-1} is possibly an harmonic of the 1.0628 cd^{-1} frequency.

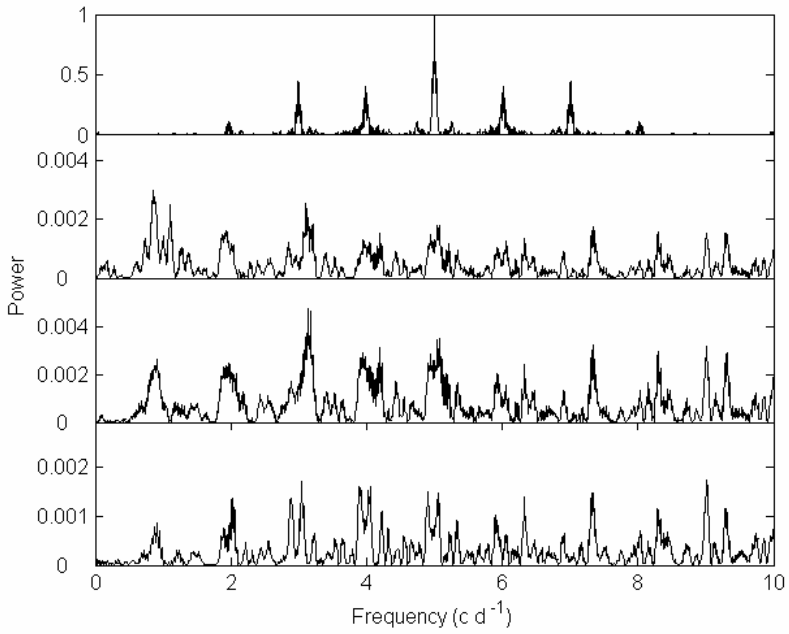

Figure 6-12: The frequency extraction for the equivalent widths of the scaled CCF profiles. The second, third and fourth panels show the Fourier transform of the equivalent width data after extraction of the strongest frequency from the previous panel. The top panel is the window function of the data.

Table 6-6: Frequency analysis results for the equivalent widths of the scaled CCFs. The three strongest frequencies do not explain much of the variance in the data as can be seen in the residual column.

Freq (cd^{-1})	Amp (kms^{-1})	Residual
1.105	0.0858	0.1077
3.137	0.0722	0.09950
9.019	0.0414	0.09506

Table 6-7:The frequency analysis for the velocities of the scaled CCFs

Freq (cd^{-1})	Amp ($km\ s^{-1}$)	Residual
1.063	2.334	1.145
2.235	1.016	0.904
2.153	0.647	0.805
3.126	0.674	0.715
1.808	0.599	0.602

6.5.2.2 Pixel-by-pixel frequency analysis

The pixel-by-pixel frequency analysis for the scaled CCFs was carried out as explained in Section 4.2.2.

Figure 6-13 shows the pixel-by-pixel 2-D Fourier transform for the scaled CCFs. Strong peaks are present in the mean frequency spectrum at 1 cd^{-1}, although the peaks at 2 cd^{-1} are stronger. The peak frequency is 2.122 cd^{-1} which demonstrates strong NRP-like behaviour in its phased surface plot (Figure 6-14). This frequency was expected to be a 1 cd^{-1} alias of the photometrically identified 1.109 cd^{-1} frequency but, on extraction of this photometric frequency, the phased surface plot does not show convincing NRP-like variation. As a result the 2.122 cd^{-1} frequency is interpreted as the actual variation frequency, and the 1.109 cd^{-1} frequency is treated as the 1 cd^{-1} alias.

Table 6-8 lists the frequencies extracted from the data using the pixel-by-pixel frequency detection method. Figure 6-14 displays the phased surface plots obtained from the frequencies detected using the pixel-by-pixel technique and which showed NRP-like variation. These phased surface plots all indicate LPVs that will not distort the line profile enough to be easily detected in the velocity measurement of the line. An example of a phased surface plot that does produce easily detectable velocity variations is V2052 Oph's 7.145 cd^{-1} frequency (Section 5.6.2, Figure 5-28). The side-to-side motion of the profiles in that case makes that frequency's variation clearly present in the velocity measurements. It was for this reason that the frequencies detected using the pixel-by-pixel method of frequency determination were used in the mode identifications of the variability of QW Pup.

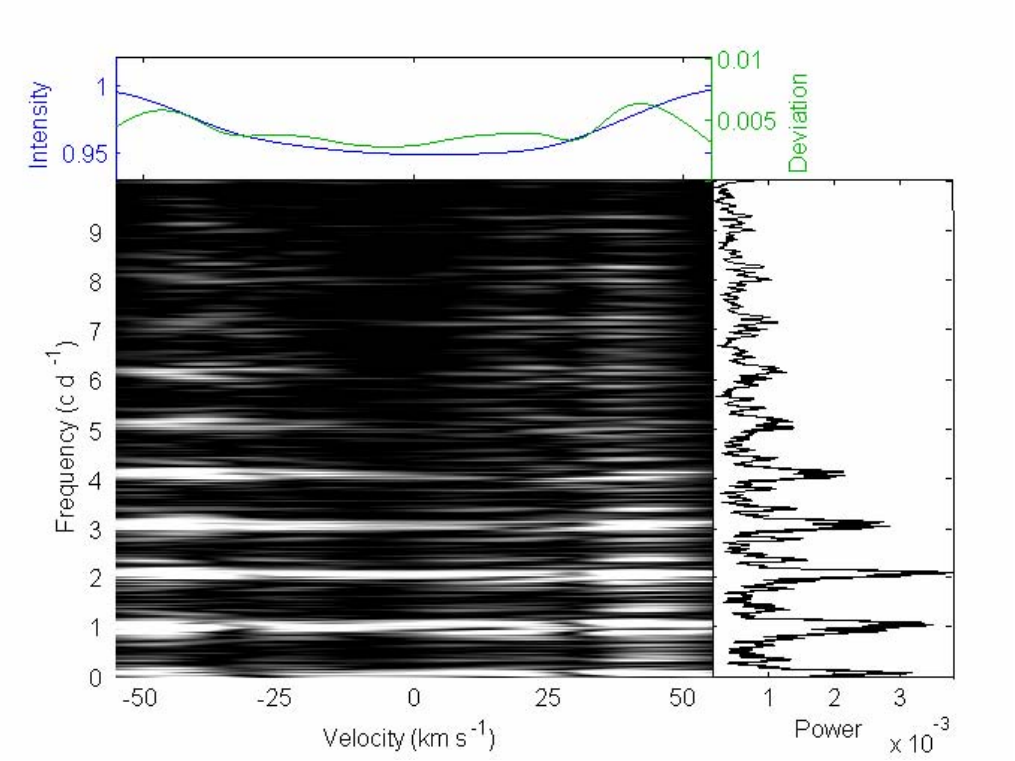

Figure 6-13: Pixel-by-pixel frequency analysis of the scaled CCFs. The 2-D Fourier transform is of the residuals of the scaled CCFs after the subtraction of the mean profile.

Table 6-8: Frequency determination of the pixel-by-pixel method for the scaled CCFs. Amplitudes are calculated from the integral of the amplitude across the profile.

Freq (cd^{-1})	Amp (km s^{-1})	Residual
2.122	2.334	1.145
2.039	1.016	0.904
6.229	0.647	0.805
0.9249	0.674	0.715
2.998	0.599	0.602
5.108	0.452	0.557
2.218	0.235	0.524

6.023	0.221	0.498

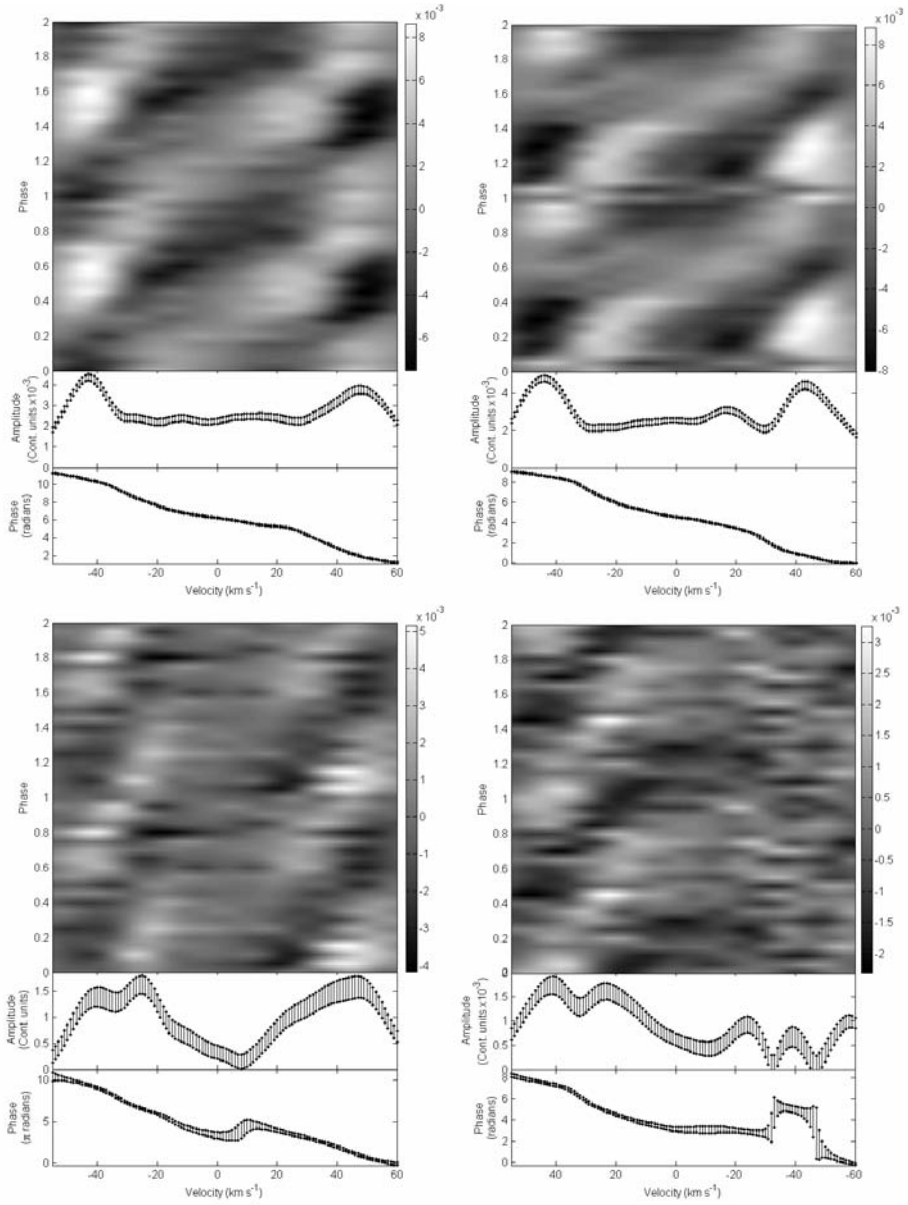

Figure 6-14: The phased surface plots and amplitude and phase across the profile for the four frequencies observed to show NRP-like behaviour. The frequencies are, from top left to bottom right, 2.122 cd^{-1}, 2.038 cd^{-1}, 6.229 cd^{-1} and 5.108 cd^{-1} as extracted from pixel-by-pixel frequency detection method.

6.6 Comparison of variation between profile datasets

The two datasets, combined line profiles and scaled CCF profiles, are expected to show similar temporal variation. The CCF profiles should be a higher S/N version of the combined line profiles, although there is still the as-yet-untested factor of how any temperature variations may affect the scaled CCFs. This is because different spectral lines can respond differently to changes in temperature.

A comparison of the frequencies extracted from the two profile datasets could lead one to believe that the two datasets show considerably different behaviour. To confirm or deny a this, a nights spectroscopic observations from the two data sets were shown side by side in a stack plot (Figure 6-15). It is clear that the two different datasets demonstrate very similar gross changes to their profile whilst not agreeing precisely with each other. Given this situation, and the fact that the scaled CCF profiles were able to provide more convincing NRP-like phased surface plots, it appears that the scaled CCF profiles produce better S/N profile variations for spectra of γ Dor stars that cover a large wavelength range.

6.7 Mode identification

The IPS and FPF spectroscopic mode identification methods were applied only to the frequencies determined from the scaled CCF profiles that showed clear NRP-like variability (f_1, f_2, f_3 and f_6). This was because the frequencies

obtained from the combined line profiles appeared insufficiently well defined for such a detailed analysis.

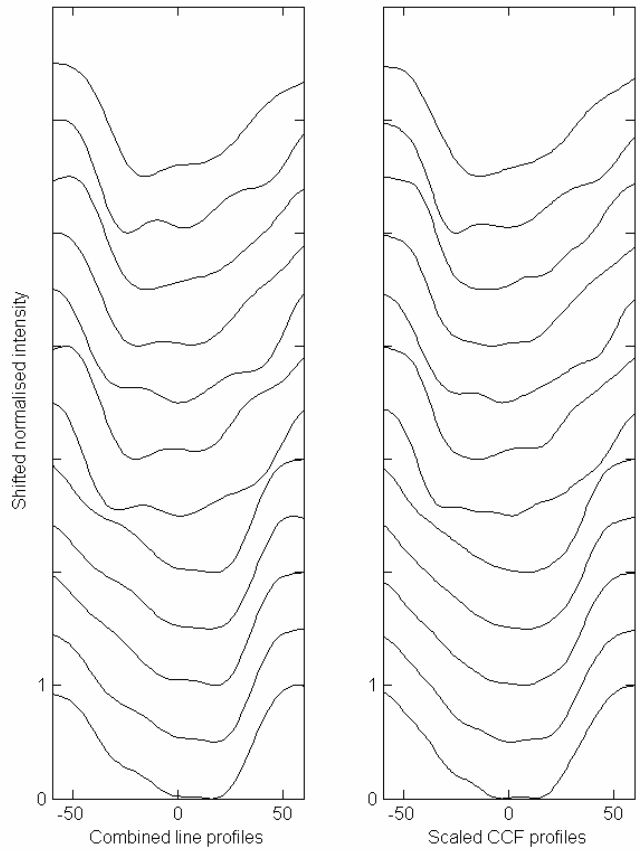

Figure 6-15: A side-by-side comparison of some combined line profiles and scaled CCFs. The lines were resized to be depth one and each consecutive observation is shifted up another 0.5. These observations were some of the highest S/N spectra obtained.

6.7.1 IPS method

The intensity period search mode identification method is described in Telting (1997) and Schrijvers (1999). The relationships for the phase change across the profile ($\Delta\Psi_0$) and *l*, and $\Delta\Psi_1$ and *m* are given in these papers. The specific case examined in the IPS papers, and considered most appropriate to QW Pup, is the situation when little or no temperature variations are taken into account (Telting and Schrijvers 1997b). The selection of this relationship can be justified by considering that only small equivalent width variations are seen. However, if the equivalent width response to temperature α_w is less than 3 the effects of the brightness variation and the equivalent width variation due to temperature can cancel each other out (Schrijvers and Telting 1999). Hence the only way significant temperature variation could be occurring without affecting the equivalent width is if $\alpha_w < 3$.

Further justification for the selection of this relationship is that the amplitudes across the profile for all the extracted frequencies are reasonably symmetric. It is known that asymmetric amplitude diagrams appear only if both the surface velocities and temperature effects of a non-adiabatic mode contribute significantly (Schrijvers and Telting 1999). Therefore, significant temperature variations would give an asymmetric amplitude diagram if a NRP was non-adiabatic, with a phase lag greater than 10^o. Hence, to observe very little equivalent width variation and symmetric amplitude across the profile diagrams, as has been done for QW Pup's NRPs, they must be either:

- modes with little or no temperature variation (the assumption for this star);
- adiabatic modes with temperature variations and a $\alpha_w \leq 3$
- non-adiabatic modes with a small non-adiabatic phase lag.

The relationship developed for Doppler velocity field pulsations with no temperature effects considered is

$$\lambda \approx 0.089 + 1.096 \cdot \left|\Delta\Psi_0\right| / \pi \tag{6.1}$$

Table 6-9: IPS results for the frequencies determined for the scaled CCFs of QW Pup that show clear NRP-like variation.

Freq #	Frequency (c d^{-1})	$\lvert\Delta\Psi_0\rvert$	l (±1)
f_1	2.122	10.07	4
f_2	2.038	8.882	3
f_3	6.229	10.19	4
f_6	5.108	11.20	4

The relation for m was not used because no harmonics were found for the frequencies exhibiting NRP-like variation.

The results from the application of the IPS relations for each of the scaled CCF frequencies are shown in Table 6-9.

6.7.2 The FPF method

The FPF mode identification was applied to the frequencies detected in the pixel-by-pixel frequency detection method that displayed variation consistent with NRP. These are f_1, f_2, f_3 and f_6. Only small equivalent width variations were observed in the CCFs, hence it is believed that QW Pup's LPVs are caused primarily by velocity field effects with little or no contribution from temperature effects. For this reason the FPF method was applied to the CCF

profiles without considering temperature variations. This means that the equivalent width response to temperature (α_w), the ratio of the stellar flux to radius variation (f), and the phase lag between the radius and flux variations (ψ) are fixed at zero. This considerably reduced the computation time for the FPF application. This also allowed an examination of the possible high degree modes, since each increase in the l parameter space adds 2 (l +1) m modes to be tested which can quickly increase the computation time to many days. The parameter space examined for each of the four frequencies is outlined in Table 6-10. The equivalent width parameter was fixed at the mean value for all the CCFs of 3.92 km s^{-1} and after some preliminary trials the $V_{rot}\sin i$ was fixed at 50.26 km s^{-1}. In the figures of the optimisation process the degree l, azimuthal order m, inclination (^{o}), pulsation amplitude (as a fraction of the radius) and pulsation phase are shown.

The FPF optimisation for f_1 was not successful (see Figure 6-16). A minimum χ^2 of 50.17 was obtained. This frequency is strong in the velocity and pixel-by-pixel data. Its phased surface plot is clearly indicative of NRP so it is surprising that the best fit χ^2 is so high. It can be seen in Figure 6-17 that the reason the χ^2 value is not very good is because the amplitude across the profile was unable to be fitted well.

A similar situation was found for f_2 (see Figure 6-18). The optimisation was not successful with a minimum χ^2 of 24.06. The phased surface plot for this frequency is also clearly NRP-like but again the amplitude across the profile was not fitted well (see Figure 6-19).

Table 6-10: FPF parameters for the genetic optimisation for all four frequencies examined.

Variable	All frequencies parameter range [range] (step)
Degree *l*	[0, 8] (1)
Azimuthal order *m*	[-8, 8] (1)
Inclination (^{o})	[5, 90] (5)
Amplitude (frac. of radius)	[0.00005, 0.006] (0.00005)
Phase	[0, 1] (0.01)
Intrinsic line width	[3.5, 8 0] (1)

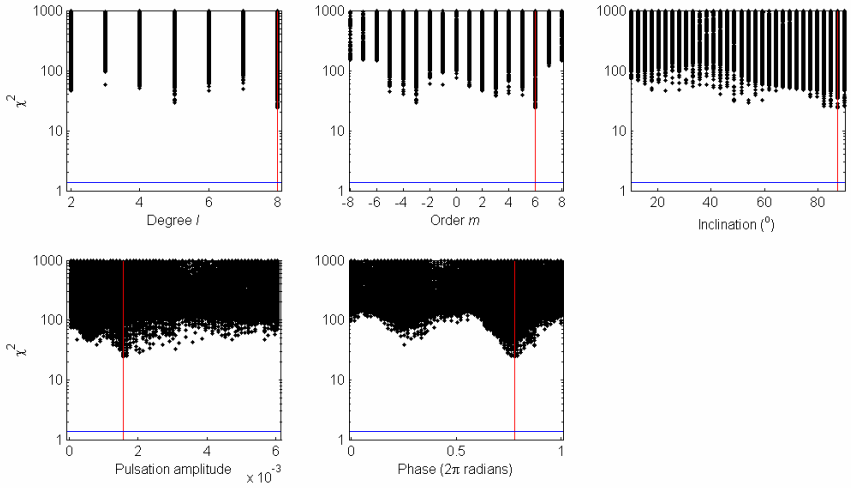

Figure 6-16:Genetic optimisation for the frequency f_1=2.122 cd^{-1}. The subplots are for the degree (*l*), the azimuthal order (*m*), the stellar rotational axis inclination in degrees, the pulsational amplitude as a fraction of the stellar radius and the phase of the pulsation. The red lines indicate the minimum χ^2 positions and the blue line indicates the 95% confidence level.

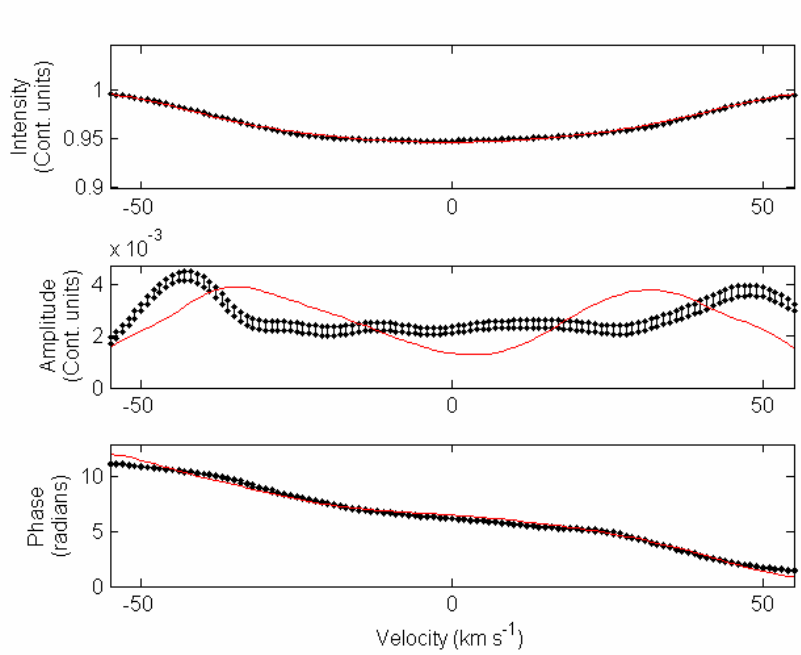

Figure 6-17: Fit to the zero point amplitude and phase for f_1 using the best parameters from the optimisation.

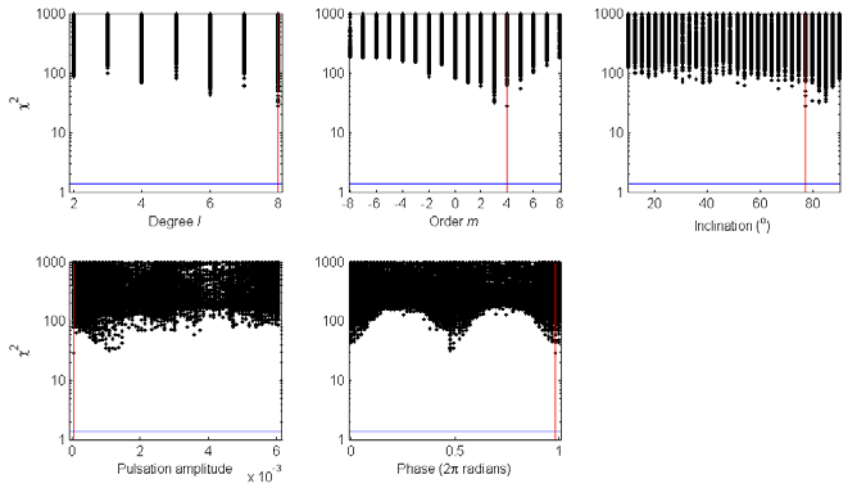

Figure 6-18: The genetic optimisation graphs for the frequency f_2=2.038 cd^{-1}.

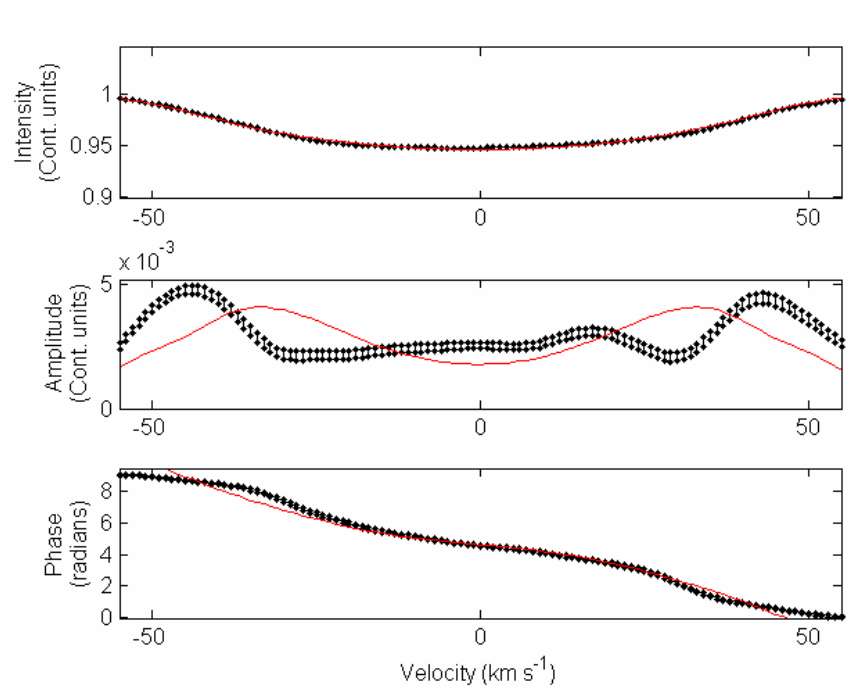

Figure 6-19: Best fit to the zero point profile and amplitude and phase across the profile for the frequency f_2. The fit is a l=5 m=5 non-radial pulsation.

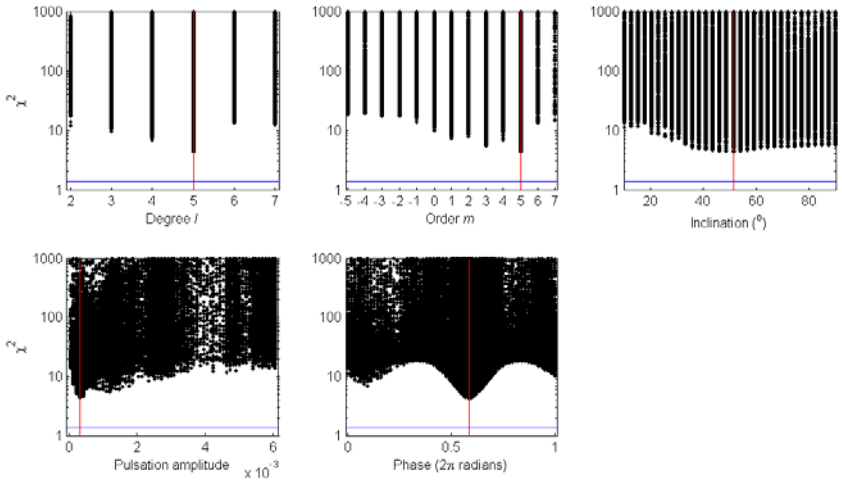

Figure 6-20:The genetic optimisation graphs for the frequency f_3 (6.229 cd^{-1}).

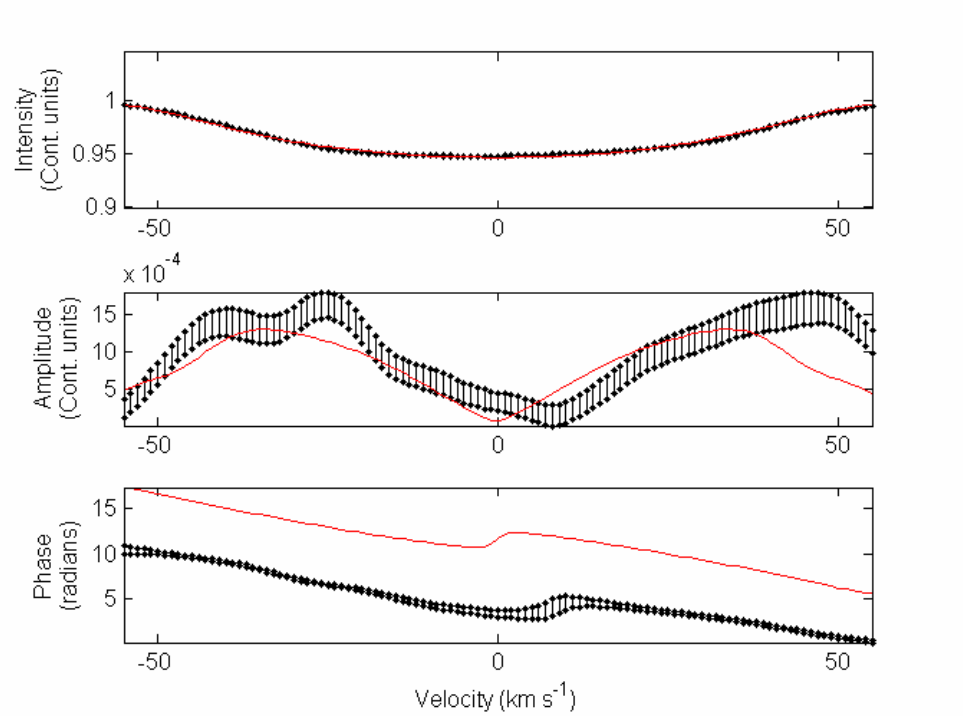

Figure 6-21: Best fit to the zero point profile and amplitude and phase across the profile for the frequency f_3. The fit is a l=5 m=5 non-radial pulsation.

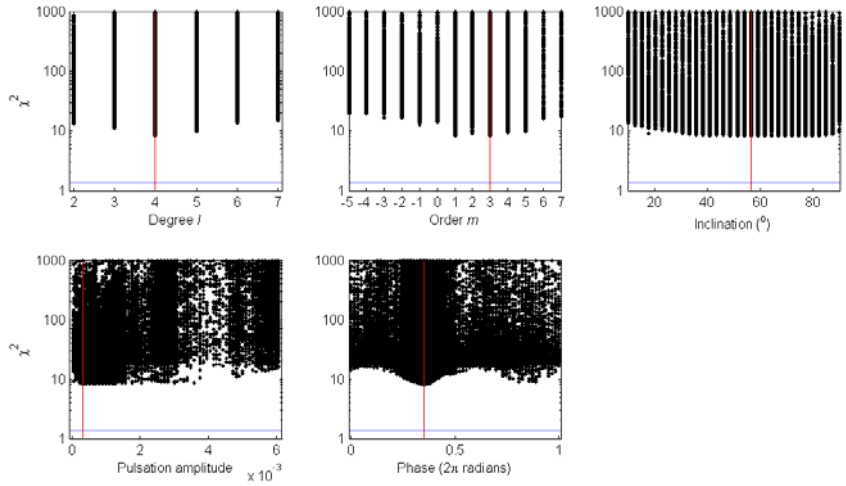

Figure 6-22: The genetic optimisation graphs for the frequency f_6 (5.108 cd^{-1}).

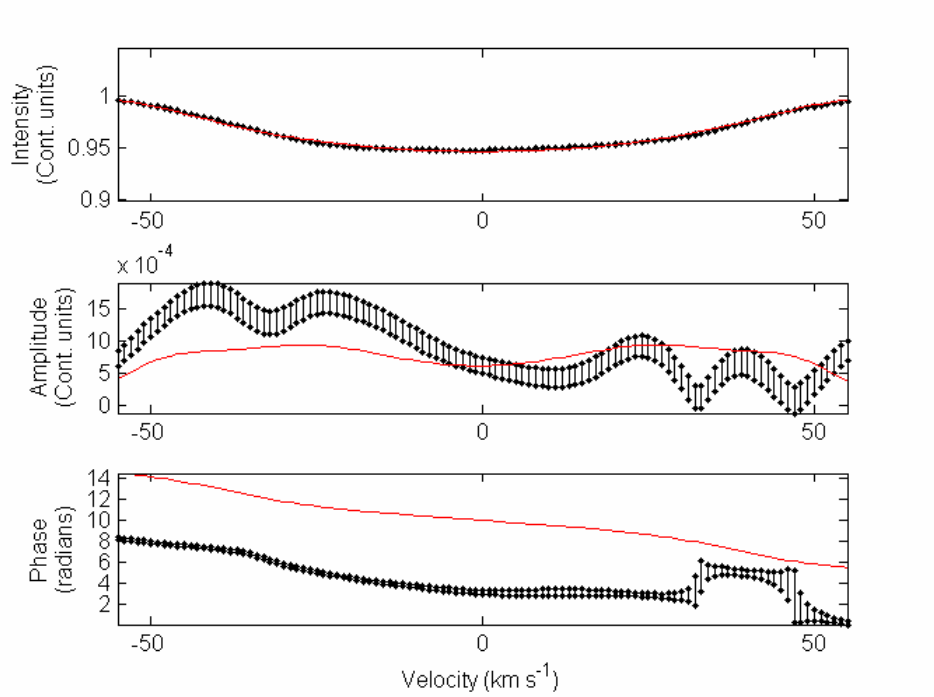

Figure 6-23: Best fit to the zero point profile and amplitude and phase across the profile for the frequency f_2. The fit is a l=4 m=3 non-radial pulsation.

Table 6-11:: FPF results for the four frequencies determined for the scaled CCFs of QW Pup that show clear NRP-like variation.

Frequency	l	m
f_1=2.122 cd^{-1}	5±3	4±2
f_2=2.038 cd^{-1}	6±2	4±2
f_3=6.229 cd^{-1}	4±2	4±2
f_6=5.108 cd^{-1}	4±3	3±2

For f_3 and f_6 the minimum χ^2 values were 4.37 and 8.19 respectively. Though these indicate much better fits than for f_1 and f_2, the poor definition of the l and m minima in Figure 6-20 and Figure 6-22 prevent any definite identifications for the modes of pulsation. The reason for the improvement in the fits for f_3

and f_6 is because of the larger uncertainties in the phase and amplitude diagrams as shown in Figure 6-21 and Figure 6-23.

Despite identifying frequencies demonstrating LPVs consistent with that expected for NRP the FPF results do not allow any definite conclusions of the modes of pulsations to be made. The results for the FPF are shown in Table 6-11. The uncertainties in the table are based on the shape of the minima in the optimisation graphs.

6.8 Conclusions

Clear line profile variability has been observed for QW Pup. Both combined line profiles and scaled CCFs were examined for periodic profile variations. Both groups of profile data appeared to vary similarly.

Very little equivalent width variability was observed and from this, and the symmetrical shape of the amplitude across the profile, the LPVs are expected to be caused primarily by the velocity field due to the NRPs rather than by temperature and brightness effects.

The frequencies obtained from the pixel-by-pixel frequency detection (2.122 cd^{-1}, 2.038 cd^{-1}, 6.229 cd^{-1} and 5.108 cd^{-1}) method were considered the most reliable given the type of line profile variability. Of the frequencies obtained from this method only the 0.9248 cd^{-1} could correspond to any of four photometrically determined frequencies of Poretti (1997). The frequencies 1.043 cd^{-1} and 1.1088 cd^{-1} of Poretti (1997) were obtained as 2.038 cd^{-1} and 2.122 cd^{-1}, their 1 cd^{-1} aliases. These values for the frequencies were determined based on the appearance of the phased surface plots (Figure 6-14).

The IPS method indicated NRP modes of degree l=3 or 4 for each of the four modes detected.

The FPF method indicated that the modes were of moderate degree ($2< l <6$) and that that all had $m>0$.

One of the frequencies (6.228 cd^{-1}) had a large region of no variation in the core of the CCF profiles (see Figure 6-14). A similar effect is observed in one of the synthetic profile datasets of Schrijvers (1997) where they use a model of a l=8, m=8 mode in a line with a small intrinsic width and large ratio of horizontal to vertical motion, that is typical of *g*-modes.

Chapter 7
HD139095

The γ Doradus candidate HD139095 was observed during a campaign for which QW Puppis was the primary target. The object was selected primarily because of its right ascention (RA) which allowed it to be observed in the latter part of the night when QW Pup had set.

It has a magnitude of V= 7.91 and was identified as a candidate γ Dor variable by Handler (1999) from an investigation of HIPPARCOS data looking for γ Dor type periodicity. It was excluded from being a prime candidate γ Dor star because it was suspected of having δ Scuti type pulsations.

Henry (2002) determined the period for the largest photometric amplitude as 0.634 d, and derived the values M_v = 2.53, L=7.5 L_{sun} , R=1.9 R_{sun} from the HIPPARCOS data.

Handler and Shobbrook (2002) found evidence for multiperiodicity in the light curves of the HIPPARCOS observations as well as in their ground based multicolour photometry. A *B/V* colour amplitude ratio of 1.23±0.02 was observed, which is typical for pulsational variability in this spectral type. There was no evidence for δ Scuti frequency variations within a limit of

1.1mmag in their amplitude spectrum. Based on these results HD139095 was confirmed as a bona fide γ Dor star (Handler and Shobbrook 2002).

7.1 Observations

Fifty-seven spectroscopic observations were obtained of HD139095 at SAAO during the QW Pup campaign from 20 March - 4 April 2005. This implies a theoretical frequency resolution of 0.11537 cd^{-1} (Loumos and Deeming 1978). The observations were 30 minute integrations. By requiring a maximum of one tenth of a pulsation cycle to be sampled for a well defined frequency, an upper limit of 4.8 cd^{-1} can be placed on the well defined frequency range.

Figure 7-1 shows a selection of stacked line profiles for the 6122.2ÅCa I line and the 6393.6Å Fe I line. There appear to be changes in the line profile over time but because of the low S/N of the individual observations, no conclusions can be made about definitive periodic line profile variations.

In Figure 7-2 is the Fourier transform of the equivalent widths, the velocities, the second moment and the third moment extracted from the observations of these two lines. There are no frequencies that are above the required S/N of 4 for extraction. The low S/N of the line profiles and the strong aliasing due to the small number of observations causes the frequency determination to be very difficult and a more detailed analysis of the line profile is not possible. For this reason only the scaled CCF profiles were used for analysis of HD139095 rather than individual or combined line profiles.

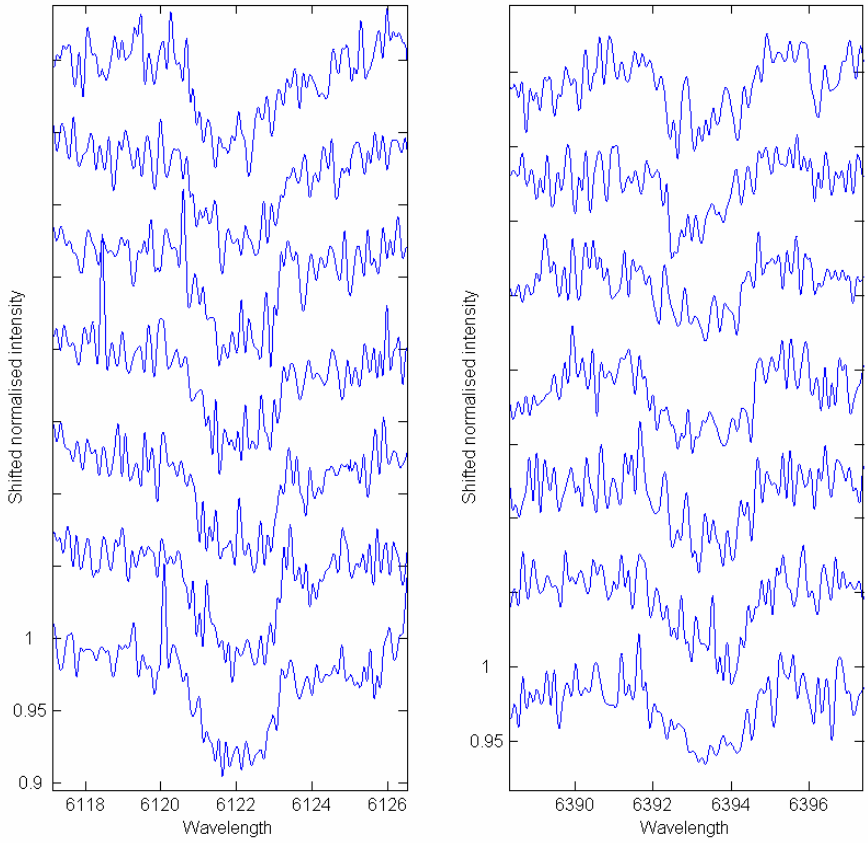

Figure 7-1: Stacked line profiles for the 6122.2Å Ca I line (left) and 6393.6Å Fe I line (right).

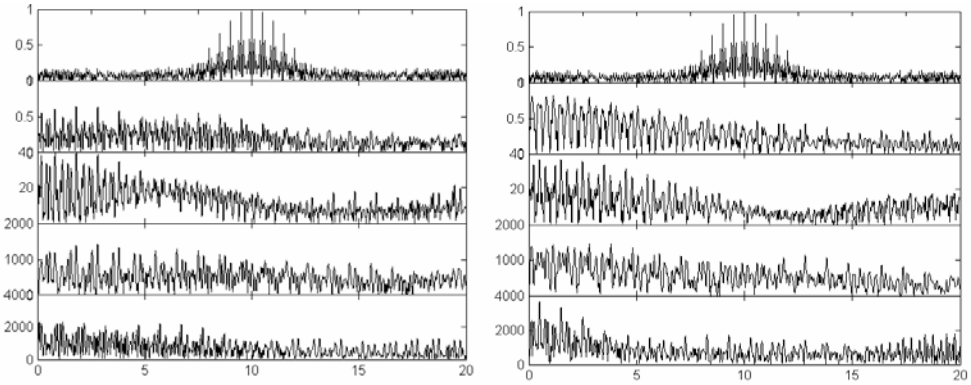

Figure 7-2:). The Fourier transform of the equivalent widths, the velocities, the second moment and the third moment extracted from the complete set of observations of the 6122.2Å Ca I line (left) and 6393.6Å Fe I line (right). The top panels are the window function.

7.2 Cross-correlation function profiles

The cross-correlation function profiles (CCF) obtained from the spectrum show strong profile variations. These variations are visible in the stacked plot of the CCFs in Figure 7-3 and in the bottom panel surface plot of the CCFs in Figure 7-4. The type of variability observed indicates multiple frequencies with at least one strong non-radial pulsation (NRP). The size of the variations in the line profile can be seen in the middle panel of Figure 7-4 in which all the CCF profiles are shown with the mean profile in red. It is clear that the variation is occurring across the whole profile, both in the wings and in the line centre, which indicates the likely presence of at least one *g*-mode pulsation.

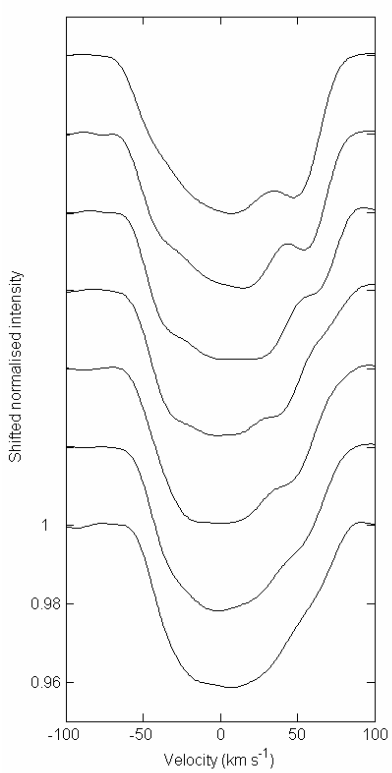

Figure 7-3: Stacked plot of the scaled CCFs for observations from a single night. The observations are shifted vertically to allow examination of the changes. Time is increasing upwards.

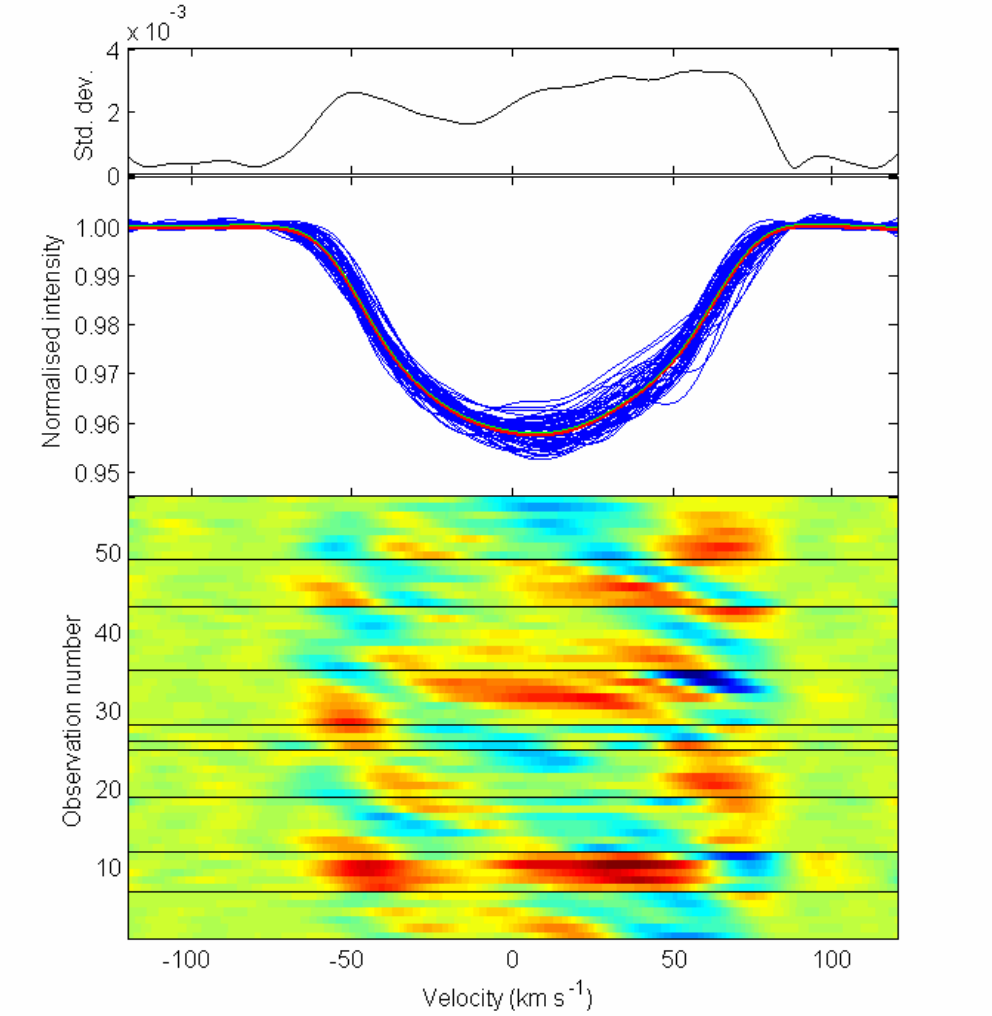

Figure 7-4: Middle: each CCF profile is plotted in blue with the mean profile in red. Bottom: coloured surface of the residuals from each profile after subtracting the mean profile. Blue indicates higher values and red lower values. The black lines indicate the end of a night's observing. Top: the standard deviation for each pixel across the profile.

7.3 V_{rot}sin i *measurements*

The V_{rot}sin *i* of HD139095 was measured with both methods described in Chapter 4.1.2. The direct fitting method gave V_{rot}sin *i* = 64.5±0.3 km s^{-1} and the Fourier method gave V_{rot}sin *i* = 64.4±0.3 km s^{-1} (see Figure 7-5 and Figure

7-6). The direct fit to the mean profile was very good and a small change in the $V_{rot}\sin i$ significantly increased the residuals. The value of the direct fit was used in defining the $V_{rot}\sin i$ range to be tested in the FPF method application.

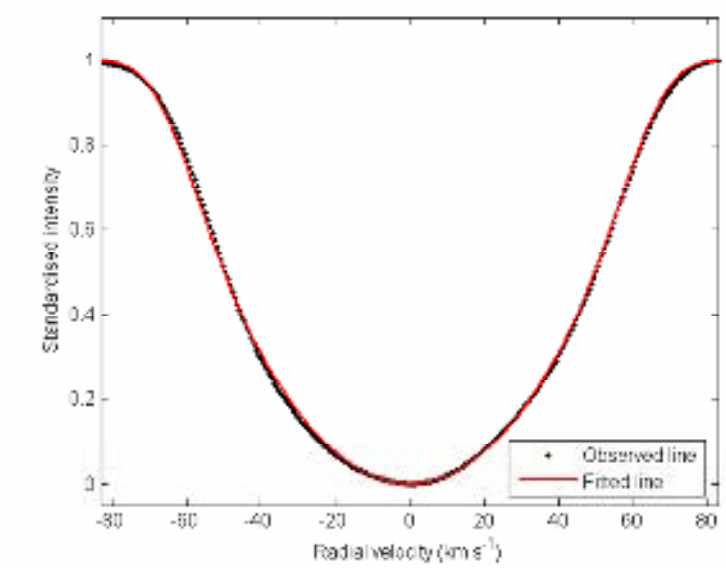

Figure 7-5: Fitting profile analysis of the mean profile of the scaled CCFs gives $V_{rot}\sin i$ = 64.5±0.3 km s^{-1}.

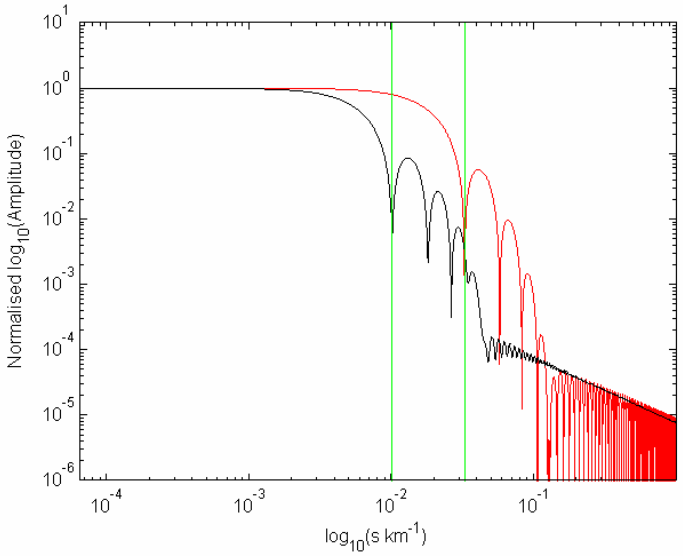

Figure 7-6: Fourier profile analysis of the mean profile of the scaled CCFs gives $V_{rot}\sin i$ = 64.4±0.3 km s^{-1}.

7.4 Frequency Analysis

A frequency analysis of the equivalent width and the velocity measurements for the scaled CCF profiles was carried out following the procedure outlined in Section 4.2.1. A pixel-by-pixel analysis was completed following the description in Section 4.2.2.

It has been stated that a frequency resolution of 0.1154 cd^{-1} is expected for these data and an upper frequency limit of 4.8 cd^{-1} for well determined frequencies was calculated. Because these numbers are marginal for reliable frequency extraction, each frequency detected is examined carefully and confirmed based on the appearance of the phased observations.

7.4.1 Equivalent width and velocity variations

The Fourier transform of the equivalent width values measured from the CCF profiles is shown in Figure 7-7. It shows a number of peaks. However, on extraction, none of the peak frequencies show convincing sinusoidal phase plots, and none of the frequencies correlate with those extracted from either the velocity or pixel-by-pixel variations. The peak frequencies extracted are 0.3570 cd^{-1}, 3.234 cd^{-1} and 7.526 cd^{-1}.

To estimate the maximum percentage change in the equivalent widths of the CCF profiles due to NRP, the frequency with the largest amplitude was examined regardless of whether it coincided with frequencies determined from other data. The 0.3570 cd^{-1} frequency had an amplitude of ~0.15 km s^{-1} which is ~3.7% of the CCF profiles mean equivalent width. This is a small percentage equivalent width variation, hence surface temparature and

brightness effects are not considered as strongly contributing to the LPVs in HD139095.

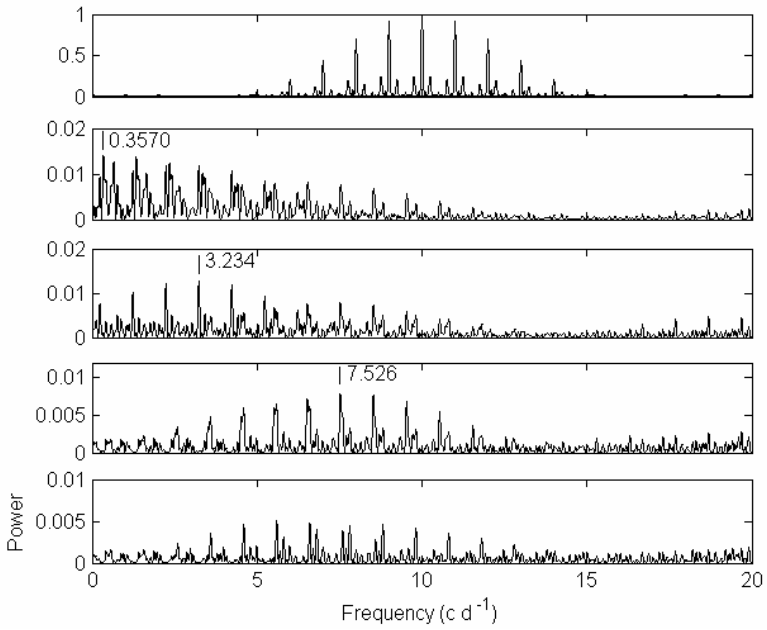

Figure 7-7: Fourier transform of the equivalent width measurements. Top: The window function for the data set. The lower four panels show the frequency extraction. None of the frequencies extracted (shown next to the vertical lines) coincided with those extracted from the velocity measurements or the pixel-by-pixel methods.

The frequency extraction for the velocity measurements of the CCF profiles is shown in Figure 7-8. The peak frequency does not demonstrate well defined NRP-like variation when the CCF profiles are phased, therefore other peaks were investigated. The fourth highest peak (2.381 cd^{-1}) produced a phased profile graph that appeared similar to a NRP, and also produced the similar variance in the residuals to that obtained from a fit using the peak frequency so this frequency was selected. None of the peaks in the Fourier transform of the residuals after removal of the 2.381 cd^{-1} frequency produced a NRP-like phased surface plot. Hence, the peak frequency at 0.4392 cd^{-1} was removed so

that further extracted frequencies could be examined for possible NRP behaviour. The next peak frequency was 7.710 cd^{-1} which is well above the frequency limit that was stated for well defined frequencies. When the profiles are phased to this frequency there is no apparent NRP behaviour observed in the CCFs. After extraction of this frequency there still appears to be variability in the residuals, though further extraction does not provide frequencies consistent with those obtained in the pixel-by-pixel analysis. The frequency determination from the velocities is stopped at this point.

It appears that either there are too few observations to clearly identify the frequencies responsible for the LPVs that are visible in a single nights CCFs, or the variability in the CCF profiles produces variations in the velocities too small to extract. If the latter is the case then this may indicate that higher degree modes are present to which the centroid velocity is known to be insensitive.

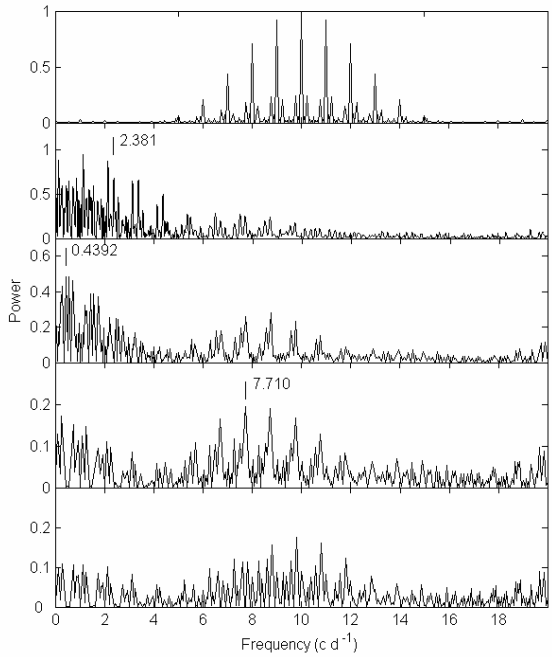

Figure 7-8: The frequency extraction procedure for the velocities of the CCFs for HD139095. Top: Window function for the observations. Second panel: Fourier transform of the velocity data. Third, fourth and fifth panels show the Fourier transforms of the residuals after prewhitening of any prior frequencies. The selected frequencies are shown next to the vertical line above the peak.

7.4.2 Pixel-by-pixel frequency analysis

Pixel-by-pixel frequency extraction of this data consisted of examining the highest few peaks from a Fourier transform of each velocity bin to determine the highest peak that demonstrated NRP-like behaviour. In the case where one of the highest peaks was an harmonic or combination frequency within a tolerance level of ±0.05 cd^{-1}, that peak frequency was selected above any others.

After a frequency was selected, a least squares fit to each velocity bin's variation was made and the result subtracted. From this subtraction process the amplitude and phase across the profile at that frequency was obtained.

In Figure 7-9 the 2-dimensional Fourier transform of the line profile variation is shown, with the mean of the frequency spectrum across the profile to the right, and the mean profile and standard deviation across the profile on top. The strongest frequency in the mean Fourier spectrum was 2.353 cd^{-1}. This frequency was extracted from the data. The line profile residuals phased to this frequency and the amplitude and phase across the profile obtained from the least squares fit are shown in Figure 7-10.

In Figure 7-10 clear red-to-blue movement can be seen occurring with increasing phase. The movement is similar to that expected from NRP, though not as clearly defined. The amplitude and phase across the profile are not indicative of NRP. This may be because the frequency selected is not precise due to the limited number of observations. Because it is the amplitude and phase across the profile that are fitted in the Fourier parameter fit method of mode identification, it is likely that the mode will not be well identified.

Frequency extraction using the pixel-by-pixel analysis method continued as per Section 4.2.2 and the list of frequencies extracted from the data is shown in Table 7.1.

Of the seven independent frequencies extracted only f_1, f_4, f_8 and f_9 demonstrate clearly moving bumps in their phased surface plots (see Figure 7-11). In all of these cases the NRP-like variability is much stronger on the blue side of the phased surface plots, between -40 and -80 km s^{-1}.

Four of the extracted frequencies were associated with the frequency f_2. This is surprising because f_2 does not appear to have a particularly large amplitude variation and does not show clearly moving bumps in the phased surface plot (see Figure 7-12).

The frequency f_2 (0.4461 cd^{-1}) was initially suspected of being the rotational frequency and this can be examined by determining the equatorial velocity for this rotation frequency using the derived stellar parameters of Henry (2002). $V_{rot} \approx 42.8$ km s^{-1} is obtained which is considerably lower than the measured $V_{rot}\sin i$ of 64.5±0.3 km s^{-1}. R_{star} would have to be greater than 2.84 R_{sun} for this frequency to be the rotation frequency and this is considered unlikely given R_{star}=1.9 R_{sun} from Henry (2002). It is concluded therefore that the f_2 frequency is not the rotation frequency.

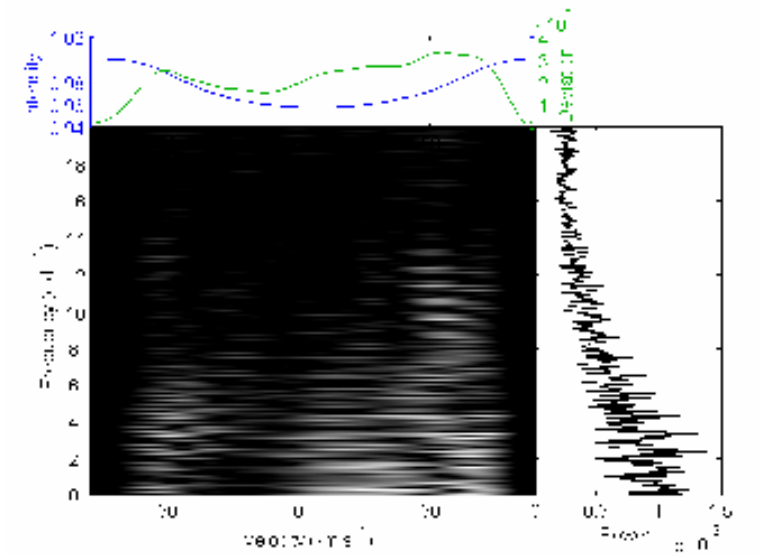

Figure 7-9: Pixel-by-pixel Fourier transform analysis of the scaled CCFs of HD139095. The peak in the mean frequency spectrum (right side) is 2.353 cd^{-1}. This frequency was extracted from the data.

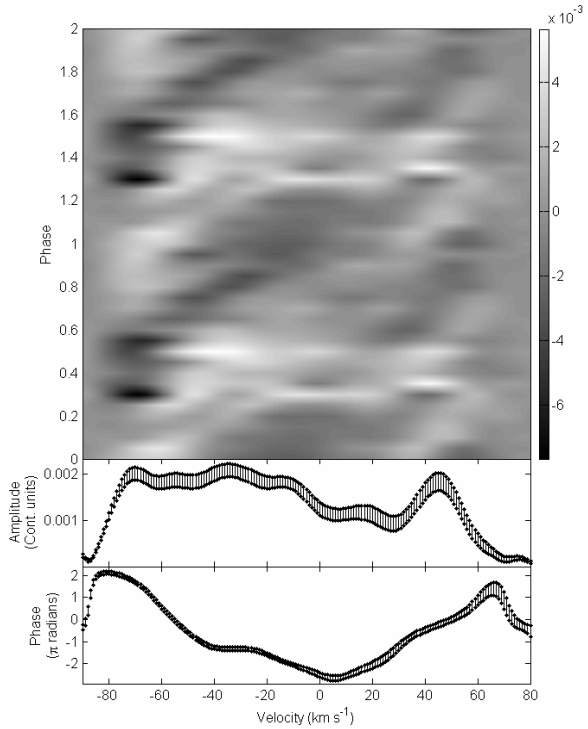

Figure 7-10: Grayscale plot of the observations phased to the 2.353 cd^{-1} frequency (f_1). The scale of the colouring is shown on the right. blue (negative velocity) to Red (positive velocity) movement within the profile is evident.

Table 7-1: Frequencies as extracted from the pixel-by-pixel method. Combinations were determined with a tolerance of 0.05 cd^{-1}. *Q* is the pulsation constant and was determined only for those frequencies believed to correspond to pulsation frequencies.

Label	Frequency	Combinations	Possible *m*	*Q*
f_1	2.353		*m*>0	0.188
f_2	0.4461			
f_3	3.238	f1+2*f2		
f_4	9.560		*m*>0	0.046
f_5	0.8769	2*f2		
f_6	2.776	f1+f2		
f_7	4.707	2*f1		
f_8	8.638		*m*>0	0.051
f_9	10.14		*m*>0	0.044
f_{10}	2.600			
f_{11}	1.938			

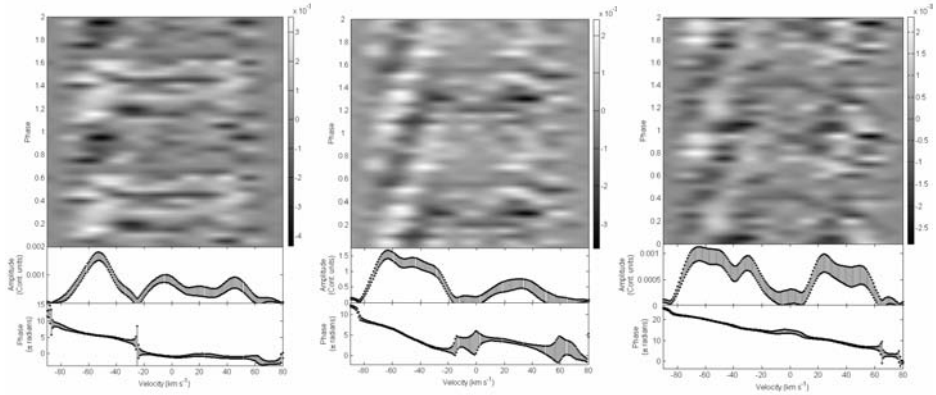

Figure 7-11: Surface phased plots of the observations phased to the 9.560 cd^{-1} frequency (f_4), the 8.637 cd^{-1} frequency (f_8) and the 10.14 cd^{-1} frequency (f_9) left to right respectively.

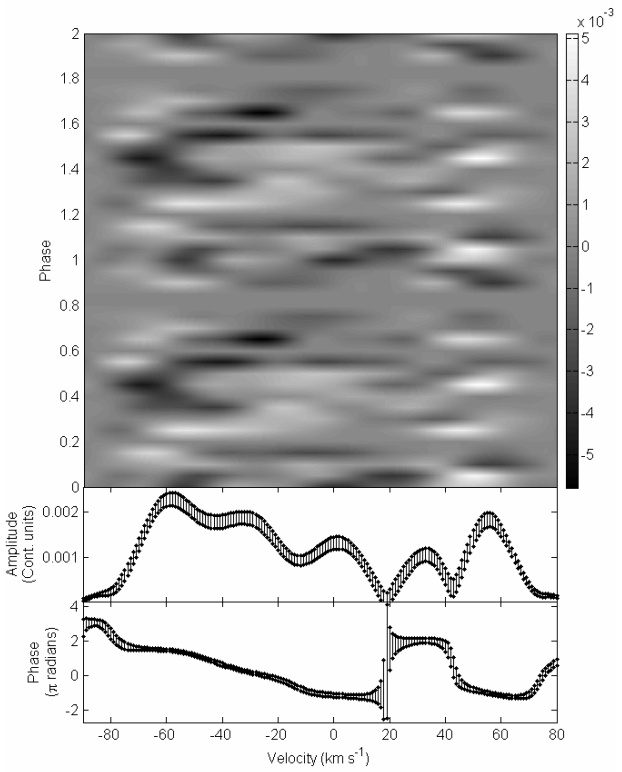

Figure 7-12: Top: Surface phased plot of the observations phased to the frequency f_2=0.4461 cd^{-1}. Bottom: Amplitude and phase across the profile at this frequency.

7.4.3 Examining the frequencies

As explained in Section 6.5, the pulsation frequency range for γ Dor stars is similar to the rotational frequency range expected for this spectral type. This means that either ellipsoidal variations or star spots can be confused with NRP.

Based on the frequencies and variations observed, HD139095 cannot be a simple ellipsoidal variable because multiple frequencies were extracted that were not harmonically related. Only two frequencies, f_1 and f_2, have observable harmonic frequencies. f_1 can be ruled out as being caused by ellipsoidal variations because of the red-to-blue bumps observed in the

frequency's phased surface plots. f_2 cannot be easily ruled out as being caused by ellipsoidal variations, although this frequency will not be investigated as a possible NRP mode because its phased surface plot is not as expected for a NRP.

Using

$$V_{rot} = 2\pi R_{star} f_{rot} \tag{7.1}$$

and the derived parameters from Henry (2002) it can be shown that star spots are not a reasonable explanation for the higher frequencies detected.

The highest frequency for which clear profile variations are observed is 10.14 cd^{-1} which would give a value for the equatorial rotational velocity $V_{rot} \approx 974$ km s^{-1} much higher than the break-up velocity of ~400kms^{-1} for a main sequence F0V star (Allen 1976). In fact any frequency greater than 4.2 cd^{-1} will give a $V_{rot} > 400$ km s^{-1} so f_4, f_8 and f_9 cannot be star spot variations. Because of this it seems likely that the other frequency, f_1, that displays NRP-like variation is also not caused by star spot variations.

Each frequency exhibiting NRP-like behaviour was determined to be a *p*- or *g*-mode pulsations based on the pulsational constant Q_i as defined in Handler (2002),

$$\log Q_i = -6.456 + 0.5 \log g + 0.1 M_{bol} + \log T_{eff} + \log P_i, \tag{7.2}$$

where P_i is the pulsation frequency.

For HD139095 the values to be substituted into Equation 0-2 are log g = 4.0, log T_{eff} = 3.8460, M_{bol} = 2.561. The M_v value of Henry (2002) was used to calculate the bolometric magnitude with a bolometric correction of 0.031 obtained from Flower (1996).

A pulsational constant <0.04 d is expected for *p*-mode pulsations (considered to be δ Scuti pulsations in this type of star). This limit comes from the fundamental radial mode having Q_i <0.033 d. An error of ~18% in the determination of Q_i arising from the uncertainties in the substituted physical parameters is included to form the pulsation type limit of 0.04 d (Handler and Shobbrook 2002). The Q values were obtained only for the independent frequencies. These are listed in Table 7-1. They ranged from clear *g*-mode pulsation constants for f_1, f_2, f_{10} and f_{11} to borderline *p*- or *g*-mode pulsation constants for f_4, f_8 and f_9. One piece of evidence that supports f_4, f_8 and f_9 being *g*-mode type pulsations is the position in which the variation in the CCF profiles occurs. There is a higher ratio of horizontal to vertical velocities for *g*-mode pulsations than *p*-modes. This causes the profile variations due to *g*-modes to occur more in the wings of the profiles. The limb-darkening effect counteracts this somewhat and the variation becomes relatively evenly spread across the entire line profile. *p*-mode pulsation occurs primarily in the core of the line profile. The region of the largest variation observed in the profiles for the f_4, f_8 and f_9 frequencies is clearly located in the blue wing of the CCF profiles, hence these are unlikley to be *p*-mode frequencies.

The lack of the HIPPARCOS frequency 1.58 cd^{-1} (Handler 1999) in the extracted frequency list is noted.

7.5 Mode identification

Mode identification using the intensity period search (IPS) and Fourier parameter fit (FPF) methods was attempted for the frequencies f_1, f_4, f_8 and f_9. The moment analysis method was not appropriate for such a fast rotator.

Table 7-2: IPS results for the frequencies f_1, f_4, f_8 and f_9 and the harmonic frequency f_7.

Frequency (cd^{-1})	$\lvert\Delta\Psi_0\rvert$	l (±1)	Harmonic (cd^{-1})	$\lvert\Delta\Psi_1\rvert$	$\lvert m\rvert$(±2)
f_1=2.353	4.94	2	f_7=4.707	12.18	1
f_4=9.560	13.63	5	Not present		
f_8=8.638	13.24	5	Not present		
f_9=10.14	23.48	8	Not present		

7.5.1 IPS method

The frequency f_1 had a negative slope for the blue half of the phase across the profile and a positive slope for the red half of the phase across the profile (see Figure 7-10). This is unexpected in a NRP and may indicate that this frequency is not well determined.

This situation is termed a slope reversal and Telting (1997) outline the process used to obtain $\Delta\Psi_0$ or $\Delta\Psi_1$ in this circumstance. The approach is to define $\Delta\Psi_0$ or $\Delta\Psi_1$ as the maximum of the phase across the profile minus the minimum of the phase across the profile, regardless of the position of the maximum and minimum phase.

The values of $\Delta\Psi_0$ and $\Delta\Psi_1$ were determined only for the frequencies showing NRP-like behaviour in their phased surface plots (f_1, f_4, f_8 and f_9) and

the one harmonic frequency (f_7). The relationships between l and $\Delta\Psi_0$, and m and $\Delta\Psi_1$, were selected from Schrijvers (1999). The specific relationship used was valid for variations caused primarily by velocity field effects (little or no temperature effects are considered). This relationship was selected due to the small equivalent width variations observed and the lack of correspondence between the equivalent width frequencies and the pixel-by-pixel frequencies. The relations are

$$\lambda \approx 0.065 + 1.098\left|\Delta\Psi_0\right|/\pi \tag{7.3}$$

and

$$m \approx -1.001 + 0.549\left|\Delta\Psi_1\right|/\pi\,, \tag{7.4}$$

where $\Delta\Psi_0$ and $\Delta\Psi_1$ are defined as above.

The results for each of the frequencies investigated are listed in Table 7-2

7.5.2 The FPF method

The FPF method was applied to the independent frequencies that displayed variations consistent with NRP. Only small equivalent width variations were observed for the CCFs of HD139095. As a result, the temperature-variation-related parameters are given zero values in the optimisations.

The adopted confidence interval for the optimisation process was 95% which corresponded to a reduced χ^2 of 1.31.

The pulsation parameter space optimised in the fit is outlined in Table 7-3. The equivalent width of the CCF profiles is well defined from the observations. A fixed value of 3.98 km s^{-1} is used, obtained from the mean value of the CCFs. The degree (l) and order (m) of the pulsation were adapted to the frequency based on the IPS information. Table 7-3 outlines the selected l and m values for each frequency.

Table 7-3:FPF mode identification parameters for all the frequencies tested.

Variable	**All frequencies parameter range [range] (step)**
Degree l	[0, 8] (1)
Azimuthal order m	[-8, 8] (1)
Inclination (^{o})	[5, 90] (5)
Amplitude (frac. of radius)	[0.00005, 0.006] (0.00005)
Phase	[0, 1] (0.01)
$V_{rot}\sin i$	[62, 66] (0.1)
Intrinsic width	[3.5, 8] (0.1)

Figure 7-13 shows the FPF optimisation for frequency f_1. The sub-figures are the reduced χ^2 for each parameter optimised: degree (l), order (m), inclination of the rotational axis, pulsation amplitude and pulsation phase. The minimum χ^2 is 26.10. This is a very poor fit.. In Figure 7-13 there are no well defined minima for any of the parameters. In Figure 7-14 the fits to the phase and amplitude across the profile are shown. No limits can be placed on the mode parameters l and m, or any of the other parameters in the optimisation. This result may indicate a misidentification of the pulsation frequency.

In Figure 7-15 the optimisation for the frequency f_4=9.560 cd^{-1} is shown. The minimum χ^2 is 10.52. The fit to the amplitude and phase across the profile is shown in Figure 7-16. This is a poor fit. Each of the parameter's optimisation

graphs have no pronounced minima so no conclusions can be drawn for the *l* and *m* of the frequency.

The optimisation for the frequency f_8=8.638 cd^{-1} is in Figure 7-17. The minimum χ^2 is 4.931. This is an average-quality fit. The best fit to the amplitude and phase across the profile is a *l*=7 *m*=5 non-radial pulsation mode shown in Figure 7-18. Due to a lack of pronounced minima little can be said about the pulsation parameters at this frequency. *m*>0 is expected for this mode based on Figure 7-18.

Figure 7-19 shows the results of the optimisation process for the frequency f_9=10.14 cd^{-1}. The minimum χ^2 is 1.995. This is a reasonable fit, though it is possible that this is because of the large uncertainty bars on the amplitude across the profile (see Figure 7-20). To further examine the best fit to this frequency a set of synthetic profiles is produced from the optimum fit parameters and is compared with the phased surface plot for f_9. The synthetic profiles surface plot does not appear to be an especially great match to the phased surface plot variation.

None of the applications of the FPF method to the frequencies gave a reduced χ^2 value of less than 1.35 which is the adopted confidence interval of 95% so no conclusive statements can be made on the pulsational variability in HD139095. The results for the four frequencies are summarised in Table 7-4

It appears likely that all four of the frequencies are *m*>0 modes based on the phase change across the profile, though in general little can be said about the parameters examined due to the poorly defined minima in the optimisation plots and low quality fits. The low quality of the fits may have been a result of

imprecise frequency determination because of the small sample size of the dataset.

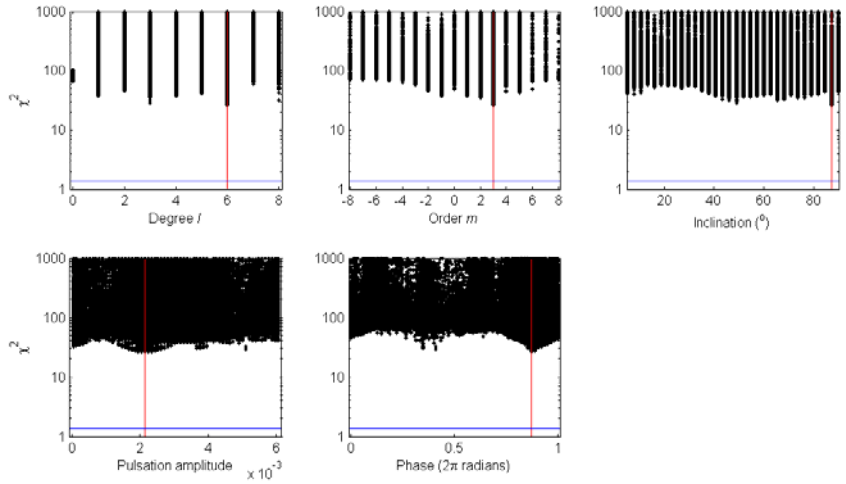

Figure 7-13: Genetic optimisation for the frequency f_1=2.353 cd^{-1} of the parameters degree *l*, order *m*, inclination, pulsation amplitude, pulsation phase. The minimum χ^2 is 26.10. This is a very poor fit.

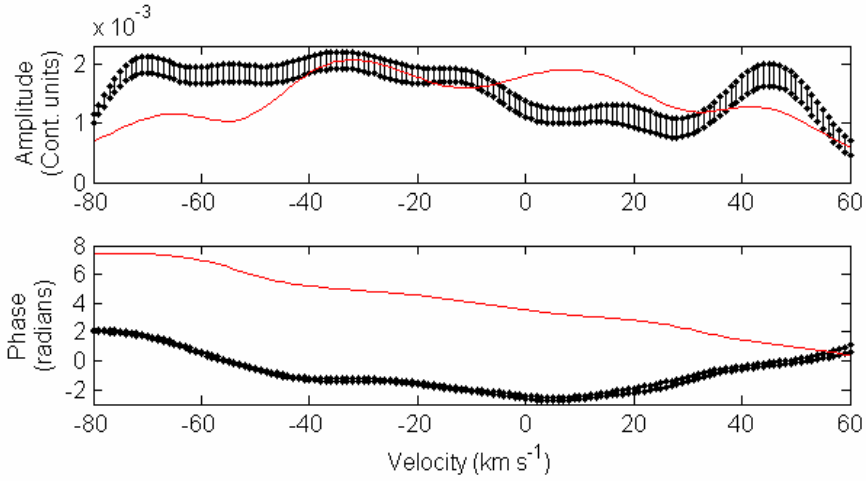

Figure 7-14: Best fit to the amplitude and phase across the profile for the frequency f_1=2.353 cd^{-1}. The fit is a *l*=6 *m*=3 non-radial pulsation mode

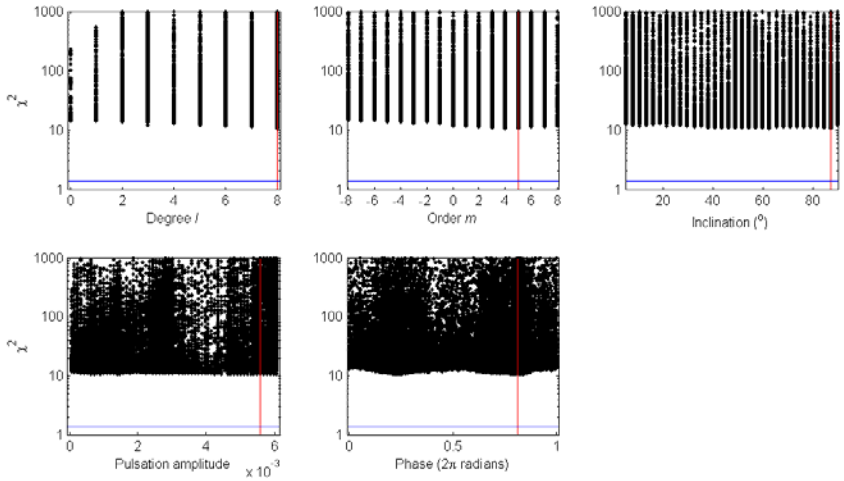

Figure 7-15: Genetic optimisation for the frequency f_4=9.560 cd^{-1}. The minimum χ^2 is 10.52. This is a poor fit.

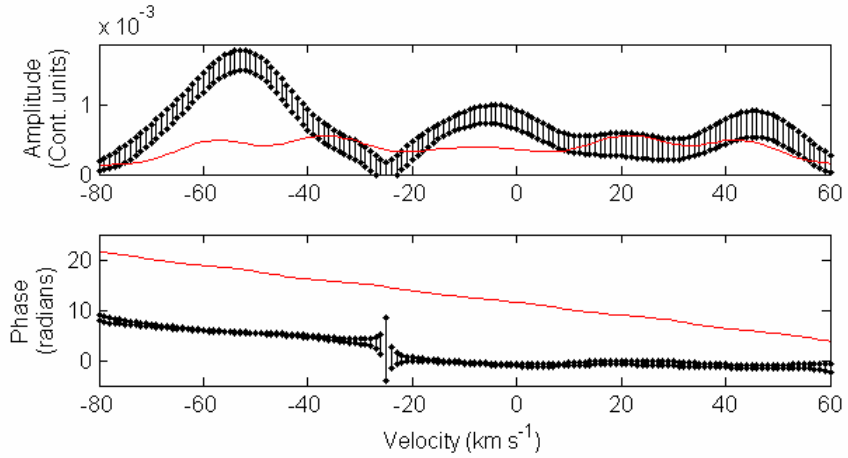

Figure 7-16: Best fit to the amplitude and phase across the profile for the frequency f_4=9.560 cd^{-1}. The fit is a l=8 m=5 mode.

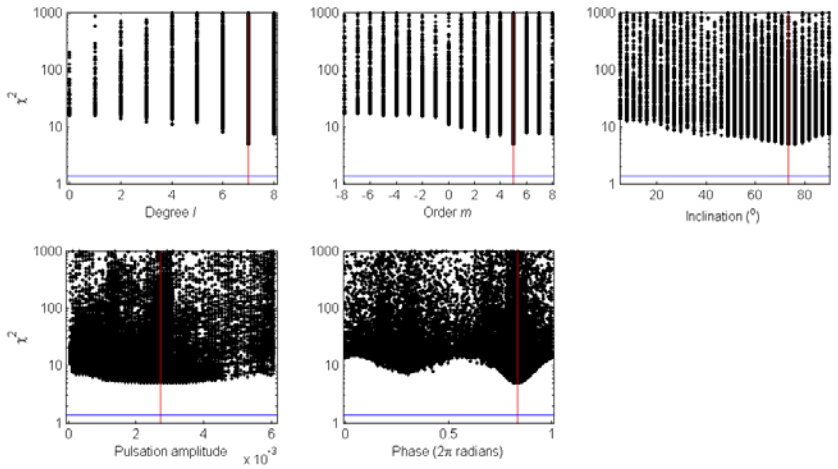

Figure 7-17: Genetic optimisation for the frequency f_8=8.638 cd^{-1}. The minimum χ^2 is 4.931. This is an average-quality fit.

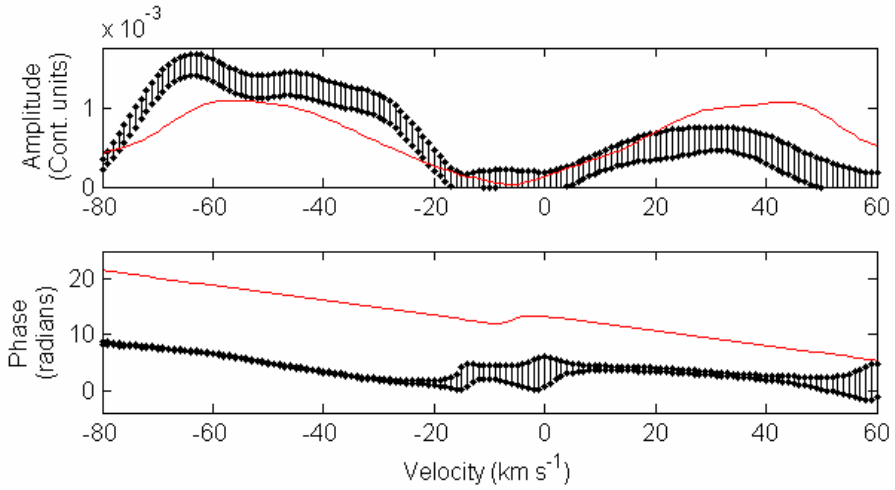

Figure 7-18: Best fit to the amplitude and phase across the profile for the frequency f_8=8.638 cd^{-1}. The fit is a l=7 m=5 non-radial pulsation

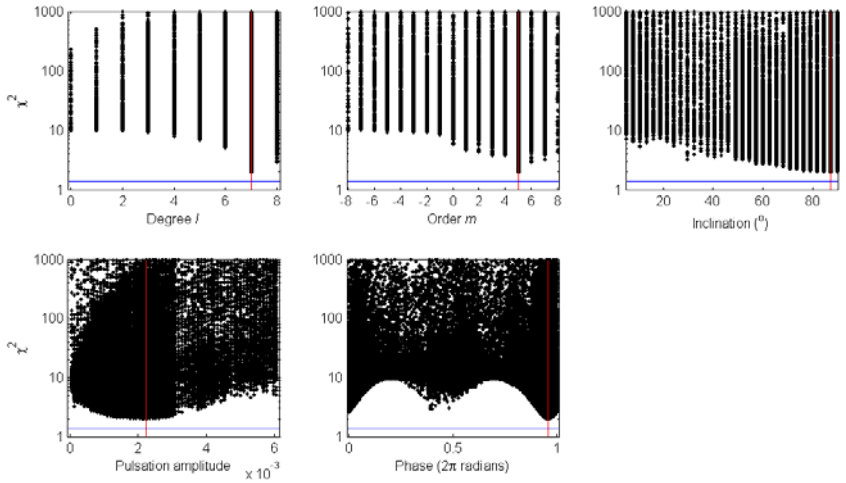

Figure 7-19: Genetic optimisation for the frequency f_9=10.14 cd^{-1}. The minimum χ^2 is 1.995. This is a good fit.

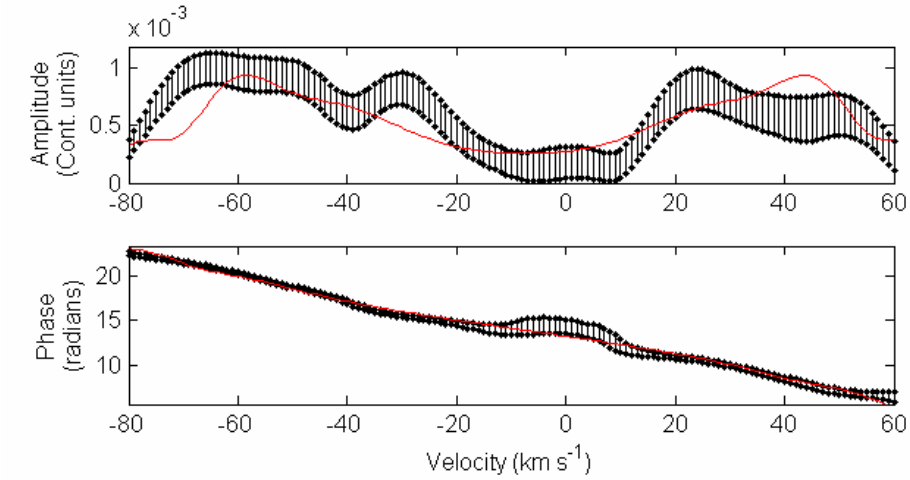

Figure 7-20: Best fit to the amplitude and phase across the profile for the frequency f_9=10.14 cd^{-1}. The fit is a l=7 m=5 non-radial pulsation.

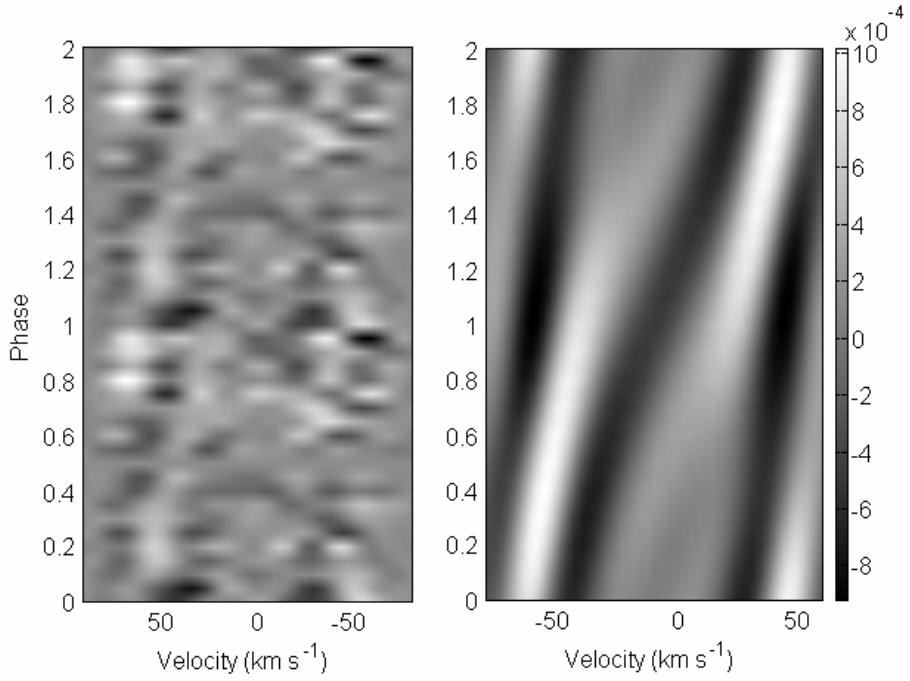

Figure 7-21: The phased surface plot of the residuals to the frequency f_9=10.14 cd^{-1} (left) and the synthetic profile surface plot produced from the best fit paramters determined in the optimisation (right).

Table 7-4: Summary of results for the FPF analysis.

Frequency (cd^{-1})	l	m	inclination	Pulsation amplitude
f_1=2.353	none	none	none	none
f_4=9.560	none	none	none	none
f_8=8.638	none	>0	none	none
f_9=10.14	7±3	5±3	none	(2±1)x10^{-3}

7.6 Conclusions

HD139095 is a multiperiodic γ Dor star with some clear LPVs. The line profile data of HD139095 were combined to produce scaled CCF profiles which were analysed. The resulting CCFs showed considerable periodic variation.

HD139095 has a $V_{rot}\sin i = 64.5\pm0.3$ km s^{-1} obtained using the direct fitting and the Fourier methods. The $V_{rot}\sin i$ fitting within the application of the FPF mode identification method gave $V_{rot}\sin i = 64.1\pm0.3$ km s^{-1}.

The small amount of equivalent width variation observed in the CCF profiles was unable to be explained by frequencies detected in the velocity or pixel-by-pixel variations. The frequencies extracted from the data are listed in Table 7-1. Ellipsoidal variations and star spots were ruled out as an explanation of the observed profile variability for the frequencies under consideration as NRPs. These frequencies were determined to be γ Dor frequencies by examining the pulsational constant described in Handler (2002) for each frequency.

The four frequencies were examined with the IPS and FPF mode identification methods. The results for the two methods are summarised in Table 7-4. None of the modes were uniquely identified, although the FPF method indicated that all four frequencies were likely to be $m>0$.

Chapter 8
Other γ Doradus Candidates

A small number of observations were obtained for a few other candidate γ Dor stars. These observations were an endeavour to increase the number of γ Dor stars and to enable better characterisation of the group. These observations were used to measure the $V_{rot}\sin i$ of each star and to discern whether LPVs are present. This information will help astronomers select targets for future observing campaigns given their available instrumentation and observing period.

All of the observations used in this chapter were obtained at MJUO. A list of the stars and number of observations for each object is shown in Table 8-1. Each observation was cross-correlated with the same template used for QW Pup, but with the inclusion of the red wavelengths. The template covered the wavelength range 4505-6865Å and contained 1211 spectral lines. The scaled CCF profiles resulting from the cross-correlations were used in the analysis.

8.1 Line profile variations and $V_{rot}\sin i$ measurements

LPVs is considered to be present if there are significant differences between the line profiles for each observation of a star. The scaled CCF profiles are high S/N since they combine information from many spectral lines. Because of

this a small deviation in the scaled CCF is considered significant. The measure of the variation in the profiles was defined to be the mean of the standard deviation across the profile. If this measure was larger than 0.0015 then the profiles were considered to show LPVs for the star. This definition was based on examining the mean of the standard deviation of different selections of scaled CCF profiles for HD139095. It is by no means a perfect discriminator between the presence or lack of LPVs but, based on the testing undertaken, only a few high S/N profiles should be required to identify whether LPVs are present. The binaries are not examined for LPVs since there are not enough observations to determine orbits for them, so the CCF profiles cannot be easily compared. For comparison, QW Pup has a mean standard deviation of the profile of 0.0042 and HD139095 has a value of 0.0025.

Table 8-1: LPVs and $V_{rot}\sin i$ results for a selection of γ Dor candidates. Binarity can be Single, SB1 (single-lined spectroscopic binary) or SB2 (double-lined spectroscopic binary).

Target (HD #)	Binarity	$V_{rot}\sin i$ (km s^{-1})	# obs	Deviation
10167	SB2	0±3, 2±3	2	N/A
14940	Single	42±3	2	0.00215
17310	SB1	1±3	2	N/A
20313	Single	32±4	2	0.00088
40745	Single	40±3	2	0.00230
41448	Single	107±10	2	0.00093
166114	unknown	unknown	12	unknown
172416	SB2	54±5, 32±5	8	N/A
187028	Single	85±4	1	N/A
189631	Single	44±3	5	0.00457

206481	Single	96±4	1	N/A
216910	Single	95±2	9	0.00083

The $V_{rot}\sin i$ of a candidate for a spectroscopic campaign is useful because certain mode identification methods have $V_{rot}\sin i$ limitations. More noise is expected for high $V_{rot}\sin i$ objects since the line profile is spread over more pixels. The $V_{rot}\sin i$ also places a lower limit on the inclination for a star if the equatorial break-up velocity can be estimated.

The $V_{rot}\sin i$ for each star is measured with the Fourier profile comparison method. It was applied to the mean of the scaled CCF profiles available for each star. This method was used because only a few observations are available for each object, so many of the mean CCF profiles are asymmetric and the direct fitting method does not perform well for asymmetric lines. There are a few cases of very low $V_{rot}\sin i$ where the Fourier profile comparison method does not function well ($V_{rot}\sin i$ <15 km s^{-1}) for the reasons explained in Section 4.1.2.2. In these cases the direct fitting method is used because, although it does not deal well with asymmetric profiles, it can distinguish between Gaussian, and rotationally broadened Gaussian profile shapes at low $V_{rot}\sin i$. Each binary star's components are analysed separately using the most separated observation available for that star. The errors on the $V_{rot}\sin i$ measurements are estimated based on the number of observations. The results for all the stars are in Table 8-1.

Figure 8-1 shows a spectrum and the $V_{rot}\sin i$ results for HD10167. It is a double-lined spectroscopic binary. Both components have low $V_{rot}\sin i$. The Fourier profile comparison method gave values for both lines of ~5 km s^{-1} but the direct fitting method gave values of 0 and 2 km s^{-1}. de Cat (2006) obtained

values of 4.5 and 4.9 km s^{-1} for the two components using the direct fitting technique. The differences in the results may be due to the inclusion of the wings of the line profile for the calculations of de Cat (2006) or because of the broadening introduced by de Cat (2006) by cross-correlating the observed spectrum with a synthetic spectrum instead of delta-functions. For this thesis, the direct fitting method values were accepted. During the fit, the wings of the scaled CCF profile were not considered because the program was unable to fit them well. This is probably because the CCF profiles are better described as rotationally-broadened Voigt profiles but are being fitted with rotationally-broadened Gaussians. The largest deviation between these two profiles is in the wings. Because no orbital solution is known, the measurement of the standard deviation across the profile based on the two observations available was not made for either component.

In Figure 8-2 the two scaled CCFs available for HD14940 show differences that lead to a mean standard deviation across the profile of 0.00215, which is considered indicative of profile variations. The Fourier profile comparison of the average profile gives $V_{rot}\sin i$ =42±3 km s^{-1} which agrees with the value $V_{rot}\sin i$ =39±4 km s^{-1} of de Cat (2006).

HD17310 is a single-lined spectroscopic binary (Henry et al. 2005). It has a low $V_{rot}\sin i$ measured by the direct fitting method as 2±2 km s^{-1} (see Figure 8-3). During the direct fitting the CCF profile's wings were not fitted. The binarity of HD17310 prevented the measurement of the mean standard deviation across the profile.

HD20313 has $V_{rot}\sin i$ =32±4 km s^{-1} and a mean standard deviation of 0.00088, not enough to indicate LPVs (see Figure 8-4).

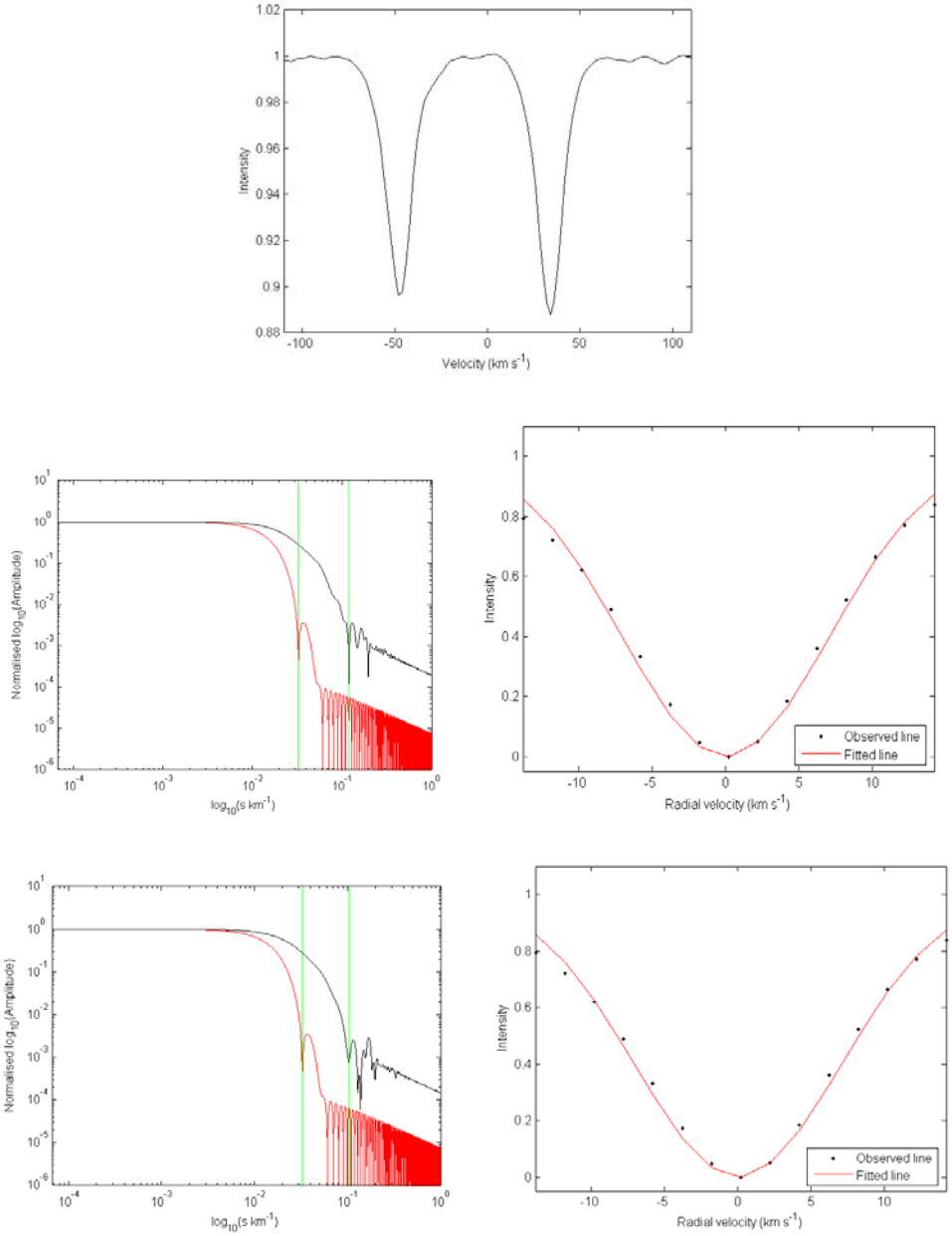

Figure 8-1: The results of the CCF for both of the components of HD10167. Top: the scaled CCF used for the measurements of $V_{rot}\sin i$. Middle: the Fourier profile comparison figure (left) and the direct fitting result (right) for the left component shown in the top sub-figure. Bottom: the Fourier profile comparison figure (left) and the direct fitting result (right) for the right component shown in the top sub-figure.

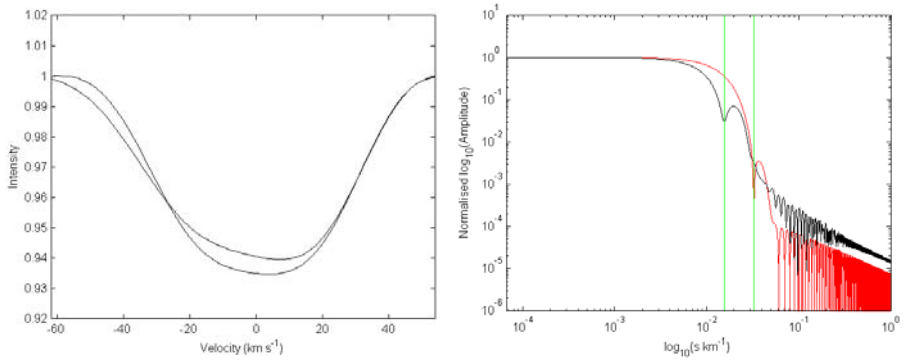

Figure 8-2: The results of the CCF for HD14940. Left: The two CCF profiles available. Right: The Fourier profile comparison figure of the mean CCF.

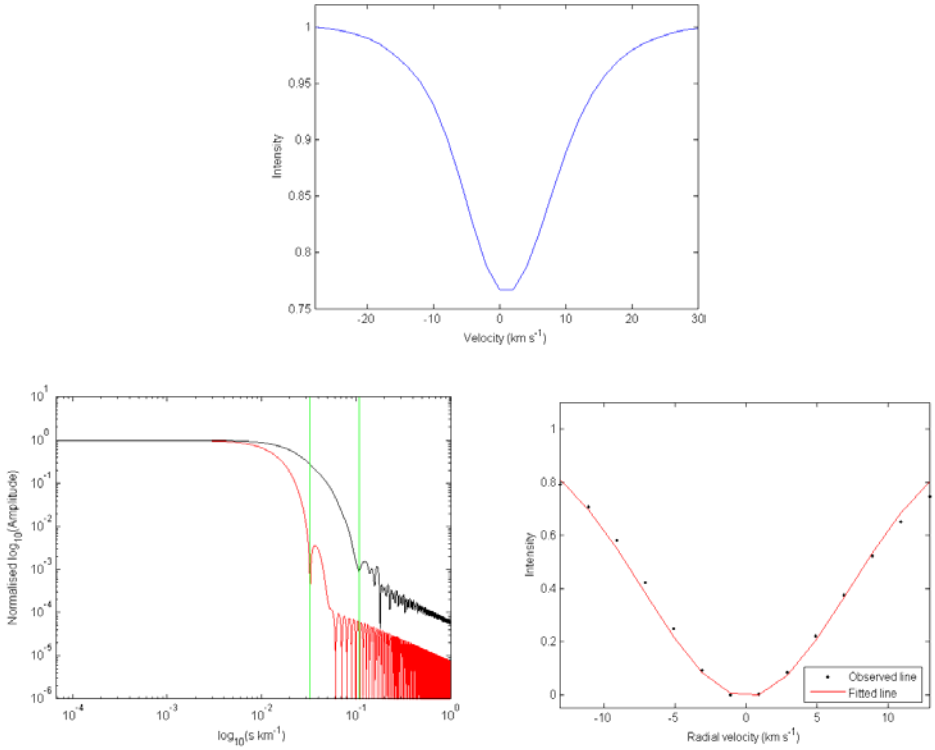

Figure 8-3: The results of the CCF for HD17310. Top: the scaled CCF used for the measurement of $V_{rot}\sin i$. Bottom left: The Fourier profile comparison figure. Bottom right: The direct fitting result. Note that the wings of the profile were not considered in the fit.

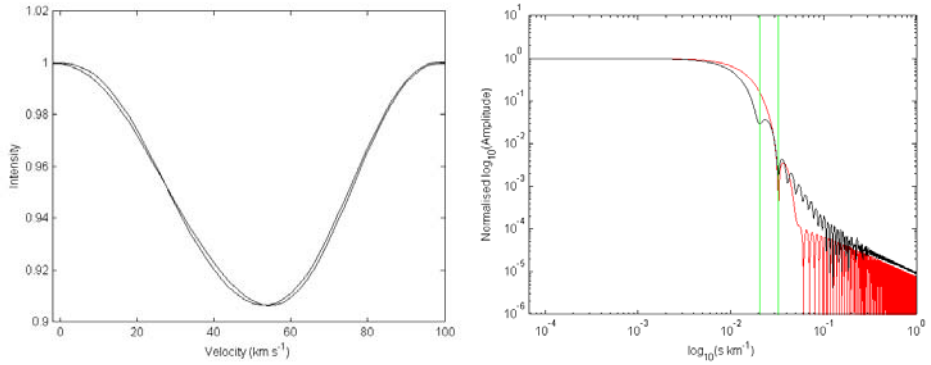

Figure 8-4: Results for HD20313. Left: The two CCF profiles available. Right: The Fourier profile comparison figure of the mean CCF.

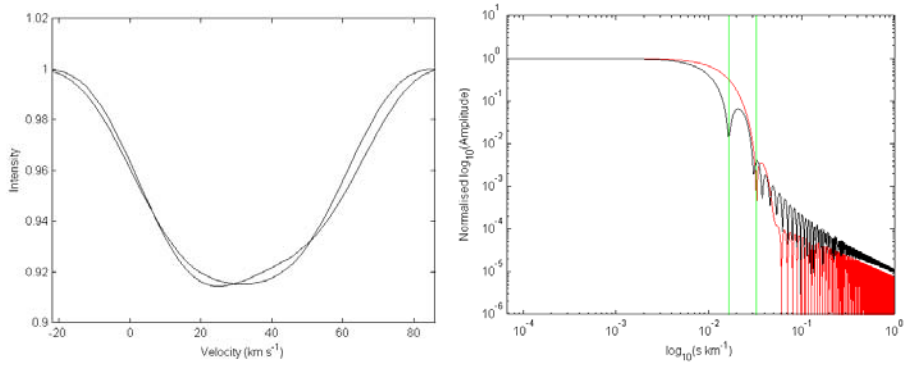

Figure 8-5: Results for HD40745. Left: The two CCF profiles available. Right: The Fourier profile comparison figure of the mean CCF.

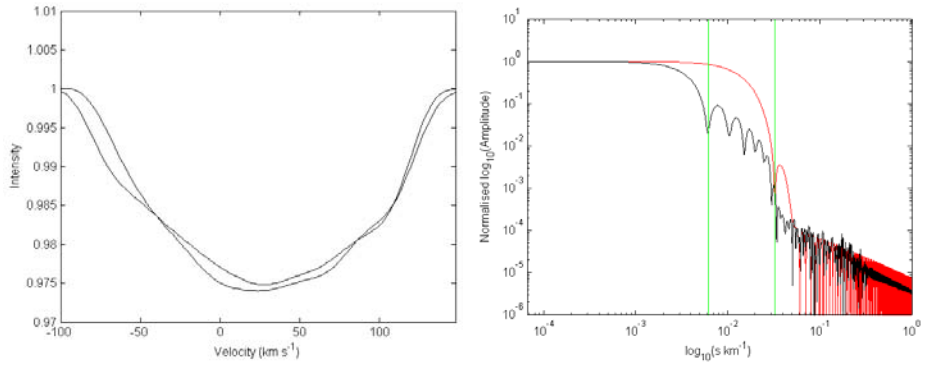

Figure 8-6: Results for HD41448. Left: The two CCF profiles available. Right: The Fourier profile comparison figure of the mean CCF.

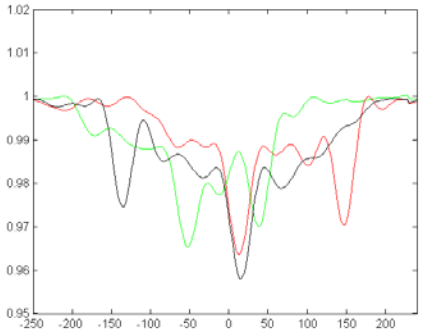

Figure 8-7: A few scaled CCF profiles for HD166114. It is difficult to draw any definite conclusions on the state of this star.

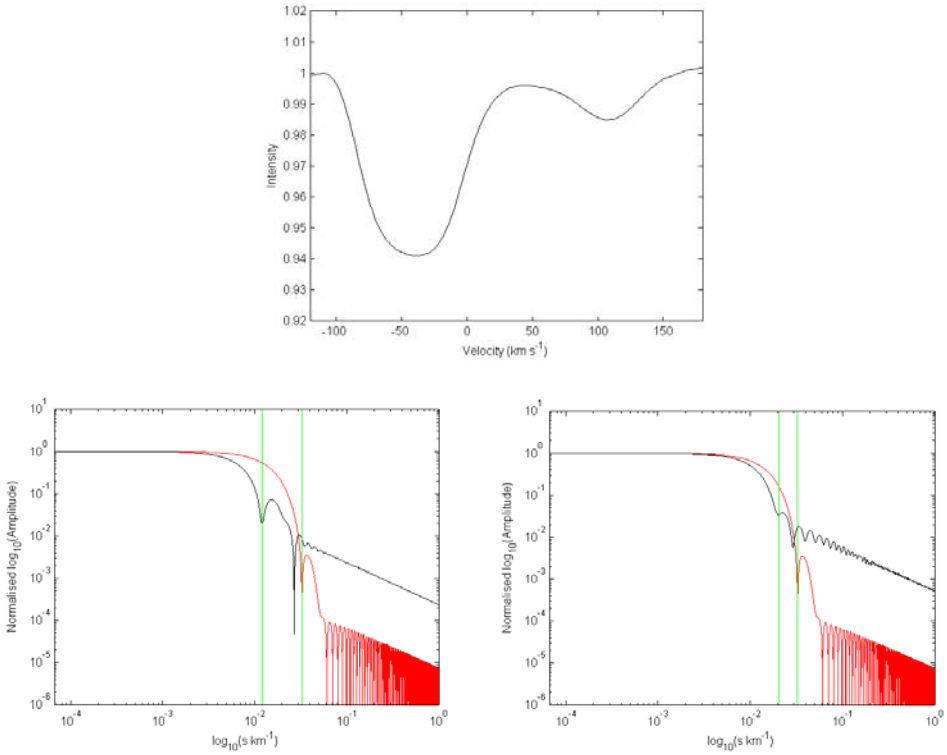

Figure 8-8: Top: The most separated observation of HD172416. Bottom left: The Fourier profile comparison figure for the deeper profile component. Bottom right: The Fourier profile comparison figure for the shallower profile component.

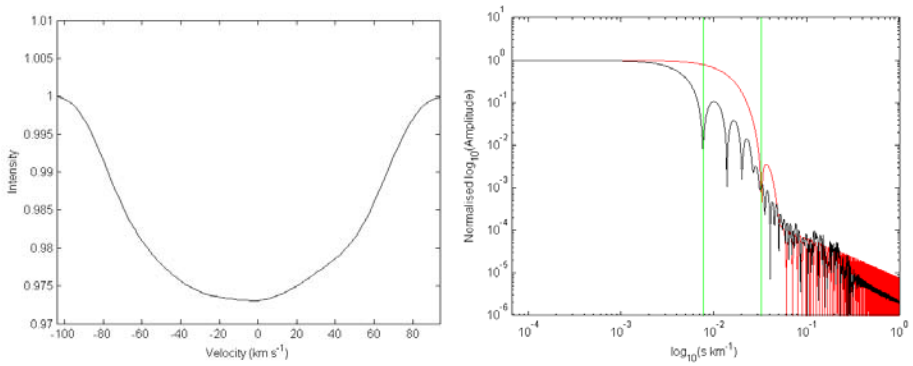

Figure 8-9: Results for HD187028. Left: The only CCF profile available. Right: The Fourier profile comparison figure.

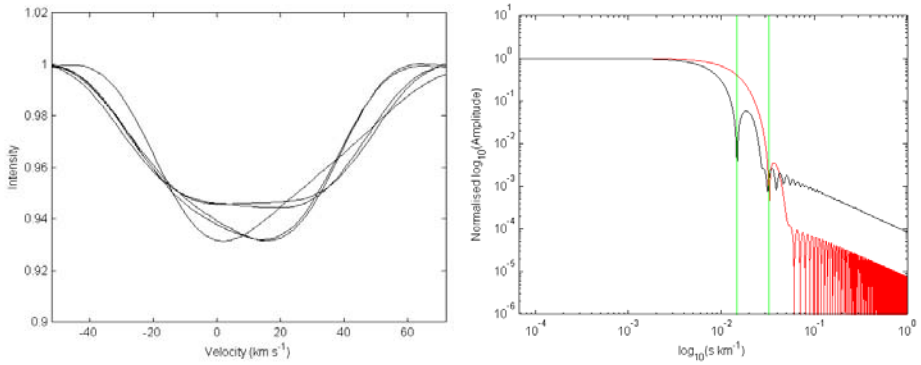

Figure 8-10: Results for HD189631. Left: All of the CCF profiles available. Right: The Fourier profile comparison figure of the mean CCF.

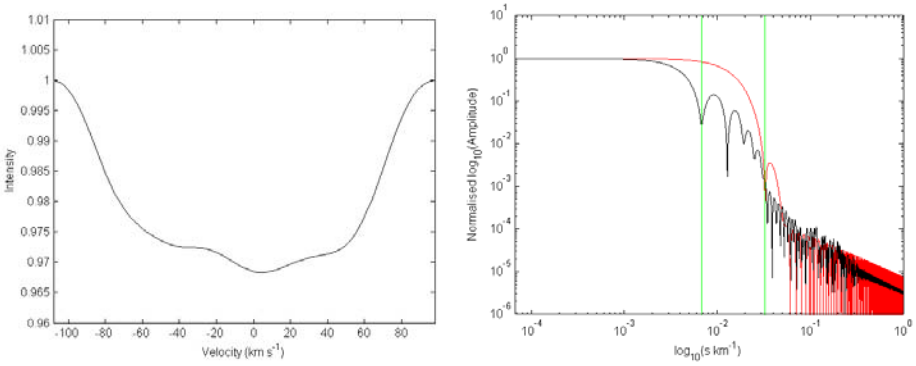

Figure 8-11: Results for HD206481. Left: The only CCF profile available. Right: The Fourier profile comparison figure.

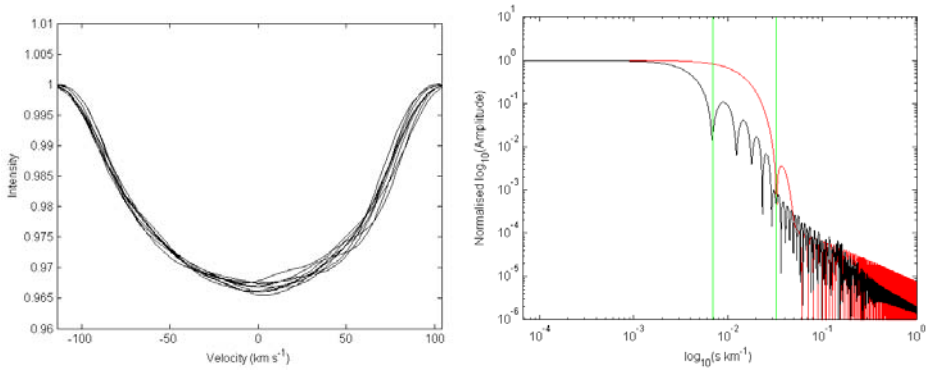

Figure 8-12: Results for HD216910. Left: All of the CCF profiles available. Right: The Fourier profile comparison figure of the mean CCF.

Figure 8-5 shows the two CCF profiles available for HD40745 and the $V_{rot}\sin i$ measurement. The mean standard deviation is 0.00230 which is indicative of profile variations. The $V_{rot}\sin i$ =40±3 km s^{-1} which agrees with the value of 39±2 km s^{-1} from de Cat (2006).

HD41448 is a broad-lined star with $V_{rot}\sin i$ =107±10 km s^{-1} (see Figure 8-6) which agrees with $V_{rot}\sin i$ =106±3 km s^{-1} obtained by de Cat (2006). The mean of the standard deviation across the profile for the two observations was 0.00093 which does not indicate the presence of LPVs, although de Cat (2006) identify LPVs based on variations in their velocity measurements.

HD166114 is a very unusual star. In Figure 8-7 a selection of the scaled CCFs are plotted. It can be seen that there is a broad depression feature, which may be a spectral line for a very fast rotator, with two sharp absorption features within it. It could be that this is a triple system where two stars are in a close binary (since the two sharp lines change rapidly relative to each other) and the third component (the broad feature) is in a wider orbit around them. One of the difficulties found with this interpretation is the very uneven broad feature.

These wobbles are unlikely to be noise since the CCF is produced from so many spectral lines. Therefore it cannot be ruled out that sharp features may be variations occurring in a single broad spectral line where any apparent movement of the spectral line could be explained by a poorly defined continuum.

HD172416 is a double-lined spectroscopic binary (see Figure 8-8). For the deeper profile $V_{rot}\sin i$ =54±5 km s^{-1} is obtained and for the shallower profile $V_{rot}\sin i$ =32±5 km s^{-1}. No measure of the standard deviation across the profile was possible due to the binary nature of the star.

Only one observation was available for HD187028 and its $V_{rot}\sin i$ was found to be 85±4 km s^{-1} (Figure 8-9).

The CCFs of HD189631 show large variations (see Figure 8-10). The $V_{rot}\sin i$ was determined as 44±3 km s^{-1} which is a good value for the application of the FPF mode identification method. This is an excellent candidate for future multi-site campaigns, though the variability should be further examined to ensure it is not caused by ellipsoidal variation.

Only one observation was available for HD206481, shown in Figure 8-11, and its $V_{rot}\sin i$ was found to be 96±4 km s^{-1}.

HD216910 is a broad-lined star with $V_{rot}\sin i$ =95±2 km s^{-1}. This agrees with de Cat (2006) who obtained 92±3 km s^{-1} from 11 observations. Although small variations are observed in the CCFs they are not sufficient to indicate LPVs. de Cat (2006) identify the presence of LPVs in their data based their velocity measurements.

8.2 Good candidates for observational campaigns

Based on the results in Table 8-1 three of the γ Dor candidates can be chosen as good targets for an observational campaign.

The strongest LPVs are observed in HD189631. This star has $V_{rot}\sin i$ =44±3 km s^{-1} which is good for analysis with the FPF mode identification method. A small single-site dataset should be obtained to check that the LPVs is not due to ellipsoidal varation before a large multi-site campaign is undertaken.

HD14940 has been identified as a bona fide γ Dor star by de Cat (2006) based on 63 high resolution spectroscopic observations. The two observations obtained for this thesis indicated LPVs and a medium $V_{rot}\sin i$ =42±3 km s^{-1} which agrees with the value $V_{rot}\sin i$ =39±4 km s^{-1} of de Cat (2006). A campaign is planned for this object in the next couple of years.

The two observations of HD40745 indicated LPVs and a medium $V_{rot}\sin i$ of 40±3 km s^{-1}. This $V_{rot}\sin i$ value agrees with the measurement of $V_{rot}\sin i$ = 39±2 km s^{-1} of de Cat (2006). de Cat (2006) also indicate this as a bona fide γ Dor star based on eight observations.

It is worth noting that the individual components of the binary stars observed were not able to be examined for LPVs, so there may be some good campaign candidates in those stars. This is especially true for the double-lined spectroscopic binaries since determination of the orbit can provide additional constraints on some fundamental stellar parameters.

Finally, the spectra obtained of star HD166114 were confusing. This object warrants further investigation though it is not considered a good multi-site candidate at this stage.

Chapter 9

Summary and future work

This thesis has analysed spectroscopic data for three stars in detail, one β Cephei star and two γ Doradus stars. Twelve other candidate γ Doradus stars have had their $V_{rot}\sin i$, binary status and, where possible, the presence of line profile variation (LPVs) determined.

A new technique utilising scaled delta functions has been developed to allow the extraction of a single, high S/N line profile from a high resolution and large wavelength range spectrum. This procedure is applicable to γ Doradus stars.

The application of the new mode identification technique the Fourier Parameter Fit (FPF) method to the three stars examined in detail has been very successful. For all stars constraints have been placed on the degree (l) and the azimuthal order (m) of the non-radial pulsation (NRP) modes detected.

9.1 Spectral line profile recovery

In this thesis a method of cross-correlation to produce a single very high S/N line profile was tested. This method cross-correlated a complete normalised and continuum fitted spectrum with a template of delta-functions positioned at the rest wavelengths of all the significant lines in the spectrum. The delta

functions were scaled to the depth of the lines in the spectrum. In this way a high S/N single profile was obtained that represented all of the spectral lines observed in the star.

The temporal behaviour of the scaled CCFs obtained from the QW Pup observations was compared with the behaviour of a profile made from the same spectra by combining four strong spectral lines together. The two profiles vary quite similarly which indicates that the technique is providing a scaled CCF which is representitive of the line profiles in the spectrum.

Further theoretical testing is required to investigate the ability of the technique to retrieve pulsationally-distorted profiles in a spectrum.

Further observational testing is required to compare the scaled CCF profile with individual and combined line profiles in stars where multiple modes have already been precisely identified (e.g. FG Virginis). The effects on the quality of the CCF profile when a star's mode is known to have considerable temperature variations needs to be explored to better understand the limitations of this technique.

9.2 V2052 Oph

V2052 Oph shows clear variation in its line profiles. The frequencies 7.145 cd^{-1} (f_1) and 6.827 cd^{-1} (f_4) were previously identified as pulsational frequencies present in the spectral line profiles. The frequencies 0.2748 cd^{-1} (f_3, f_{rot}) and 0.5496 cd^{-1} (f_2, $2f_{rot}$) were also present and were identified as being a result of the rotation of V2052 Oph. All of these frequencies were detected in the data obtained for this thesis.

The results of the intensity period search (IPS) mode identification were l =1±1 for f_1 and l =4±1 for f_4. The result for f_1 agreed with previous photometry and spectroscopy indicating l =0. The value for f_4 agreed with previous spectroscopy which indicated l =3 or 4.

The results from the Fourier parameter fit (FPF) analysis on the pulsational frequencies f_1 and f_4 were encouraging. The 95% confidence limit for the reduced χ^2 of 1.35 was not reached for any of the lines analysed but all three obtained best fit reduced χ^2 values less than 4. From the optimisation graphs values for various pulsational and stellar parameters can be estimated. Of significance in these results was the stellar parameter $V_{rot}\sin i$ =42±1 km s^{-1}, and the pulsational parameters l=1±1, m=0, and amplitude=0.004±0.001 R_{star} for f_1, and for $f4$ l=4±1, m=3±1, and amplitude=0.001±0.001 R_{star}. The inclination was determined as ~40^o in both optimisations but this value is taken with caution because of the possibility of the pulsational axis not being aligned with the rotational axis which had been suggested by Neiner (2003). Little other information could be obtained from the optimisations because of the insensitivity of the other parameters.

The fits of the synthetic line profiles generated using the optimal parameters from the FPF analysis were good for both pulsational frequencies, which further supports the modes suggested in the FPF application.

Because of the convincing fits to the observed line profiles, it is thought that if the pulsational axis is not aligned with the rotational axis, then the effects of this are not sufficient to disrupt mode identification for the two identified pulsational frequencies.

9.3 QW Puppis

QW Pup demonstrates clear LPVs in the spectra obtained. The spectral line variations were examined using a profile made from combining four carefully selected, isolated and strong spectral lines and also using the scaled CCF profile obtained from the method outlined in Chapter 3. During the frequency analysis it was decided that, although the two sets of profiles' temporal variability was somewhat similar, the scaled CCF profiles produced the most convincing NRP-like phased surface plots. For this reason only the scaled CCF profiles were examined in detail with the IPS and FPF mode identification techniques.

A previous multi-site photometric study had determined that four pulsations frequencies around 1 cd^{-1} explained the light variations well (Poretti et al. 1997). The variations observed in the scaled CCFs studied in this thesis were not well explained by these frequencies. Two of the previous photometrically determined frequencies (1.043 cd^{-1} and 1.109 cd^{-1}) were found to be 1 cd^{-1} aliases of the two strongest frequencies present in the CCFs variations (2.038 cd^{-1} and 2.122 cd^{-1}). A third frequency (0.9249 cd^{-1}) was found in the CCF variation that was close to another of the photometric frequencies (0.9019 cd^{-1}).

Four frequencies were found that had a phased surface plot that appeared NRP-like, with clear bumps moving from blue to red through the CCF profile with time (2.1220 cd^{-1}, 2.038 cd^{-1}, 6.229 cd^{-1} and 5.108 cd^{-1}). These

frequencies were investigated with the IPS and FPF mode identification methods.

The IPS results indicated l=4±1, l=3±1, l=4±1 and l=4±1 for each of the four frequencies respectively. The FPF were not well constrained with reduced χ^2 values of 50.17, 24.06, 4.37 and 8.19. Many of the fits also showed poorly defined minima. This was surprising given the quality of the dataset and it may indicate that, despite the best efforts, the frequencies may have been incorrectly identified. From the FPF results the best fitting modes were l=5±3, m=4±2; l=6±2, m=4±2; l=4±2, m=4±2; l>0, m=3±2; for the four frequencies respectively. The uncertainties for these values were determined from the shape and clarity of the minima in the optimisation plots.

This star needs further investigation with multi-site observations to better determine the frequencies of the spectroscopic line profile variation.

9.4 HD139095

The observations of HD139095 contained clear line profile variability. Scaled CCFs were created from the spectra for a detailed analysis of the varations. The equivalent width measurements show some variation but no frequencies were able to satisfactorily describe it.

The frequencies were poorly determined because of the few observations avaliable, the relatively low S/N of the spectra and the effect of single-site sampling. Despite this, four frequencies were found to show NRP-like behaviour (2.353 cd^{-1}, 9.560 cd^{-1}, 8.637 cd^{-1} and 10.14 cd^{-1}).

These frequencies were examined with the IPS and FPF mode identification methods. Both of these methods are based on an analysis of the phase across the profile, the FPF method additionally utilises the amplitude across the profile. For all of the frequencies examined the phase and amplitude across the profile had considerable uncertainty. This was likely the result of the poorly determined frequencies.

For the IPS method an uncertainty of ±1 is assumed for the determination of l, for the case of well defined frequencies. The uncertainty is likely to be more because the frequencies were not well defined. The values obtained were l=2, m=1 for the 2.353 cd^{-1} frequency, l=5 for the 9.560 cd^{-1} frequency, l=5 for the 8.638 cd^{-1} frequency and l=8 for the 10.14 cd^{-1} frequency.

The resulting χ^2 values were 26.10 for f_1, 10.52 for f_4, 4.931 for f_8 and 1.995 for f_9. The bad fit for f_1, the strongest and most well defined frequency, and the poorly defined minima for the other frequencies led to the conclusion that the better χ^2 values for f_8 and f_9 are likely due to the increasing uncertainties encountered due to lower amplitudes. The results from the analysis are simply that the four frequencies appear to be $m>0$ and that f_9 has l=7±3 and m=5±3.

In conclusion this star is a multiperiodic variable with clear line profile variations. Further investigation with a dedicated multi-site campaign will allow a better determination of the frequencies and modes of the oscillations present in this star.

9.5 Other candidates

A few observations were obtained for twelve candidate γ Dor stars. The scaled CCFs were examined for LPVs using a value of 0.0015 for the mean standard deviation across the profile to discriminate between the presence or lack of LPVs. The $V_{rot}\sin i$ of the mean CCF was measured with the Fourier profile comparison method and in the case of $V_{rot}\sin i$ <15 km s^{-1} the direct fitting method was applied as well.

Based on the results three γ Dor candidate stars, HD14940, HD40745 and HD189631 are noted as good campaign targets due to their moderate $V_{rot}\sin i$ (all around 40 km s^{-1}) and clear profile variations.

Acknowledgements

I would like to thank my wife Sarah for her incredible patience with me when Jonathan needed attention and I was out in the office. I could not have completed this project with out your understanding and consideration.

I thank my mum and dad for helping Sarah with Jonathan when I couldn't be there, it was a great comfort to know you were there to help us when we needed it.

I thank Dan, Glen and Orlon for their shell scripts which put me on the path to better programming. I also thank my office mates and Ben and Alex for entertaining off topic conversations and lunch breaks.

I'd like to thank the Physics and Astronomy department for giving me many observing runs at MJUO and also for assistance with travel for observing and conferences. I also thank SAAO for the telescope time allocated to me during my PhD.

I thank Wolfgang Zima for his FPF programs and the time he took to explain them to me and Peter De Cat for helping me and offering me the opportunity for a future in astronomy.

Finally I thank my supervisors Karen Pollard and Peter Cottrell. Karen has helped me immensely through my PhD and for that I am extremely grateful to her. Peter got me interested in this topic in my fourth year and has helped me with it since for which I cannot thank him enough.

References

Aerts, C., et al. (2004). "Asteroseismology of the beta; Cephei star nu; Eridani - II. Spectroscopic observations and pulsational frequency analysis." Monthly Notices of the Royal Astronomical Society **347**: 463-470.

Aerts, C., M. de Pauw and C. Waelkens (1992). "Mode identification of pulsating stars from line profile variations with the moment method. an example - The Beta Cephei star Delta Ceti." Astronomy and Astrophysics **266**: 294-306.

Aerts, C., H. Lehmann, M. Briquet, R. Scuflaire, M. A. Dupret, J. De Ridder and A. Thoul (2003). "Spectroscopic mode identification for the beta Cephei star EN (16) Lacertae." Astronomy and Astrophysics **399**: 639-645.

Aerts, C., et al. (2003). "Asteroseismology of HD 129929: Core Overshooting and Nonrigid Rotation." Science **300**: 1926-1928.

Aerts, C., et al. (2004). "Asteroseismology of the beta Cep star HD 129929. I. Observations, oscillation frequencies and stellar parameters." Astronomy and Astrophysics **415**: 241-249.

Allen, C. W. (1976). Astrophysical Quantities.

Balona, L. A. (1986). "Mode identification from line profile variations." Monthly Notices of the Royal Astronomical Society **219**: 111-129.

Balona, L. A. (1986). "Mode identification from line profile variations. II - A quantitative least-squares algorithm." Monthly Notices of the Royal Astronomical Society **220**: 647-656.

Balona, L. A. (1987). "Mode identification from line profile variations. III - Temperature variation and toroidal modes." Monthly Notices of the Royal Astronomical Society **224**: 41-52.

Balona, L. A. (2003). "Mode Identification from Line Profiles using the Direct Fitting Technique." Astrophysics and Space Science **284**: 121-124.

Baudrand, J. and T. Bohm (1992). "MUSICOS - A fiber-fed spectrograph for multi-site observations." Astronomy and Astrophysics **259**: 711-719.

Berdyugina, S. V., J. H. Telting and H. Korhonen (2003). "Surface imaging of stellar non-radial pulsations. I. Inversions of simulated data." Astronomy and Astrophysics **406**: 273-280.

Briquet, M. and C. Aerts (2003). "A new version of the moment method, optimized for mode identification in multiperiodic stars." Astronomy and Astrophysics **398**: 687-696.

Briquet, M., T. Morel, A. Thoul, R. Scuflaire, A. Miglio, J. Montalbán, M.-A. Dupret and C. Aerts (2007). "An asteroseismic study of the beta Cephei star theta Ophiuchi: constraints on global stellar parameters and core overshooting." Monthly Notices of the Royal Astronomical Society **381**: 1482-1488.

Casas, R., J. C. Suárez, A. Moya and R. Garrido (2006). "A comprehensive asteroseismic modelling of the high-amplitude delta Scuti star RV Arietis." Astronomy and Astrophysics **455**: 1019-1029.

Cugier, H., W. A. Dziembowski and A. A. Pamyatnykh (1994). "Nonadiabatic observables in beta Cephei models." Astronomy and Astrophysics **291**: 143-154.

Daszynska-Daszkiewicz, J., W. A. Dziembowski and A. A. Pamyatnykh (2003). "Constraints on stellar convection from multi-colour photometry of delta Scuti stars." Astronomy and Astrophysics **407**: 999-1006.

de Cat, P., et al. (2006). "A spectroscopic study of southern (candidate) gamma Doradus stars. I. Time series analysis." Astronomy and Astrophysics **449**: 281-292.

De Ridder, J., M.-A. Dupret, C. Neuforge and C. Aerts (2002). "Influence of non-adiabatic temperature variations on line profile variations of slowly rotating beta Cephei stars and SPBs. II. Simulations of line profile time series." Astronomy and Astrophysics **385**: 572-584.

Dupret, M.-A., J. De Ridder, P. De Cat, C. Aerts, R. Scuflaire, A. Noels and A. Thoul (2003). "A photometric mode identification method, including an improved non-adiabatic treatment of the atmosphere." Astronomy and Astrophysics **398**: 677-685.

Dupret, M.-A., et al. (2004). "Asteroseismology of the beta Cep star HD 129929. II. Seismic constraints on core overshooting, internal rotation and stellar parameters." Astronomy and Astrophysics **415**: 251-257.

Flower, P. J. (1996). "Transformations from Theoretical Hertzsprung-Russell Diagrams to Color-Magnitude Diagrams: Effective Temperatures, B-V Colors, and Bolometric Corrections." Astrophysical Journal **469**: 355.

Gautschy, A. and H. Saio (1995). "Stellar Pulsations Across The HR Diagram: Part 1." Annual Review of Astronomy and Astrophysics **33**: 75-114.

Gies, D. R. and A. Kullavanijaya (1988). "The line profile variations of Epsilon Persei. I - Evidence for multimode nonradial pulsations." Astrophysical Journal **326**: 813-831.

Gray, D. F. (1992). The observation and analysis of stellar photospheres.

Guzik, J. A., A. B. Kaye, P. A. Bradley, A. N. Cox and C. Neuforge (2000). "Driving the Gravity-Mode Pulsations in gamma Doradus Variables." Astrophysical Journal **542**: L57-L60.

Handler, G. (1999). "The domain of gamma; Doradus variables in the Hertzsprung-Russell diagram." Monthly Notices of the Royal Astronomical Society **309**: L19-L23.

Handler, G. and R. R. Shobbrook (2002). "On the relationship between the delta Scuti and gamma Doradus pulsators." Monthly Notices of the Royal Astronomical Society **333**: 251-262.

Handler, G., R. R. Shobbrook, F. F. Vuthela, L. A. Balona, F. Rodler and T. Tshenye (2003). "Asteroseismological studies of three beta Cephei stars: IL Vel, V433 Car and KZ Mus." Monthly Notices of the Royal Astronomical Society **341**: 1005-1019.

Hearnshaw, J. B., S. I. Barnes, N. Frost, G. M. Kershaw, G. Graham and G. R. Nankivell (2003). HERCULES: A High-resolution Spectrograph for Small to Medium-sized Telescopes. The Proceedings of the IAU 8th Asian-Pacific Regional Meeting, Volume I.

Henry, G. W. and F. C. Fekel (2002). "Six New gamma Doradus Stars." Publications of the Astronomical Society of the Pacific **114**: 988-998.

Henry, G. W. and F. C. Fekel (2003). "A Dozen New gamma Doradus Stars." Astronomical Journal **126**: 3058-3075.

Henry, G. W., F. C. Fekel and S. M. Henry (2005). "Eleven New gamma Doradus Stars." Astronomical Journal **129**: 2815-2830.

Hensberge, H., et al. (1981). "A photoelectric investigation of light variability in AP stars." Astronomy and Astrophysics Supplement Series **46**: 151-170.

Heynderickx, D. (1992). "A photometric study of Beta Cephei stars. I - Frequency analyses." Astronomy and Astrophysics Supplement Series **96**: 207-254.

Heynderickx, D., C. Waelkens and P. Smeyers (1994). "A photometric study of beta Cephei stars. II. Determination of the degrees L of pulsation modes." Astronomy and Astrophysics Supplement Series **105**: 447-480.

Hubeny, I. and T. Lanz (1995). "Non-LTE line-blanketed model atmospheres of hot stars. 1: Hybrid complete linearization/accelerated lambda iteration method." Astrophysical Journal **439**: 875-904.

Jerzykiewicz, M. (1972). "HR 6684: A New Beta Cephei Type Variable Star." Publications of the Astronomical Society of the Pacific **84**: 718.

Kanaan, A., et al. (2005). "Whole Earth Telescope observations of BPM 37093: A seismological test of crystallization theory in white dwarfs." Astronomy and Astrophysics **432**: 219-224.

Kaye, A. B., G. Handler, K. Krisciunas, E. Poretti and F. M. Zerbi (1999). "Gamma Doradus Stars: Defining a New Class of Pulsating

Variables." Publications of the Astronomical Society of the Pacific **111**: 840-844.
Lenz, P. and M. Breger (2004). Period04: A software package to extract multiple frequencies from real data. The A-Star Puzzle.
Lenz, P., A. A. Pamyatnykh, M. Breger and V. Antoci (2008). "An asteroseismic study of the delta Scuti star 44 Tauri." Astronomy and Astrophysics **478**: 855-863.
Loumos, G. L. and T. J. Deeming (1978). "Spurious results from Fourier analysis of data with closely spaced frequencies." Astrophysics and Space Science **56**: 285-291.
Mantegazza, L. (2000). Mode Detection from Line-Profile Variations. Delta Scuti and Related Stars.
Mantegazza, L. and E. Poretti (2002). "Line profile variations in the delta Scuti star FG Virginis: A high number of axisymmetric modes." Astronomy and Astrophysics **396**: 911-916.
Mantegazza, L., F. M. Zerbi and A. Sacchi (2000). "Simultaneous intensive photometry and high resolution spectroscopy of delta Scuti stars. IV. An improved picture of the pulsational behaviour of X Caeli." Astronomy and Astrophysics **354**: 112-124.
Mazumdar, A., M. Briquet, M. Desmet and C. Aerts (2006). "An asteroseismic study of the beta Cephei star beta Canis Majoris." Astronomy and Astrophysics **459**: 589-596.
Merryfield, W. J. and E. J. Kennelly (1993). Fourier Analysis of Variable Line Profiles - Towards Stellar M-V Diagrams. GONG 1992. Seismic Investigation of the Sun and Stars.
Morton, A. E. and H. K. Hansen (1974). "Temperature Variations in HR 6684." Publications of the Astronomical Society of the Pacific **86**: 943.
Neiner, C., et al. (2003). "Rotation, pulsations and magnetic field in V 2052 Ophiuchi: A new He-strong star." Astronomy and Astrophysics **411**: 565-579.
Papaj, J., J. Krelowski and W. Wegner (1991). "Atlas of extinction curves derived from ultraviolet spectra of the TD-1 satellite." Monthly Notices of the Royal Astronomical Society **252**: 403-407.
Perryman, M. A. C., et al. (1997). "The HIPPARCOS Catalogue." Astronomy and Astrophysics **323**: L49-L52.
Pike, C. D. (1974). "Radial Velocity Variations of HR 6684." Publications of the Astronomical Society of the Pacific **86**: 681.
Poretti, E., C. Koen, P. Martinez, F. Breuer, H. Haupt and D. de Alwis (1997). "Discovery and analysis of Gamma Doradus type pulsations in the F0 IV star HR 2740=QW PUP." Monthly Notices of the Royal Astronomical Society **292**: 621.

Rodríguez, E., et al. (2006). "Asteroseismology of the new multiperiodic gamma Dor variable HD 239276." Astronomy and Astrophysics **456**: 261-268.

Schaller, G., D. Schaerer, G. Meynet and A. Maeder (1992). "New grids of stellar models from 0.8 to 120 solar masses at Z = 0.020 and Z = 0.001." Astronomy and Astrophysics Supplement Series **96**: 269-331.

Schrijvers, C. and J. H. Telting (1999). "Line-profile variations due to adiabatic non-radial pulsations in rotating stars. IV. The effects of intrinsic profile variations on the IPS diagnostics." Astronomy and Astrophysics **342**: 453-463.

Schrijvers, C., J. H. Telting, C. Aerts, E. Ruymaekers and H. F. Henrichs (1997). "Line-profile variations due to adiabatic non-radial pulsations in rotating stars. I. Observable characteristics of spheroidal modes." Astronomy and Astrophysics Supplement Series **121**: 343-368.

Skuljan, J. (2004). HRSP - A dedicated echelle reduction software package for Hercules. IAU Colloq. 193: Variable Stars in the Local Group.

Skuljan, J., J. B. Hearnshaw and P. L. Cottrell (1999). Absolute Radial Velocities by Cross-Correlation with Synthetic Spectra. IAU Colloq. 170: Precise Stellar Radial Velocities.

Skuljan, J., J. B. Hearnshaw and P. L. Cottrell (2000). "High-Precision Radial Velocity Measurements of Some Southern Stars." Publications of the Astronomical Society of the Pacific **112**: 966-976.

Sneden, C. A. (1973). Carbon and Nitrogen Abundances in Metal-Poor Stars. Ph.D. Thesis**:** 180.

Telting, J. H. and C. Schrijvers (1997). "Line-profile variations of non-radial adiabatic pulsations of rotating stars. II. The diagnostic value of amplitude and phase diagrams derived from time series of spectra." Astronomy and Astrophysics **317**: 723-741.

Telting, J. H. and C. Schrijvers (1997). "Line-profile variations of non-radial adiabatic pulsations of rotating stars. III. On the alleged misidentification of tesseral modes." Astronomy and Astrophysics **317**: 742-748.

Wright, D. (2003). A spectroscopic study of two non-radially pulsating stars: HD160641 and FG Virginis. Department of Physics and Astronomy, University of Canterbury.

Zima, W. (2005). A new spectroscopic mode identification method. Vienna, Vienna University.

Zima, W. (2006). "A new method for the spectroscopic identification of stellar non-radial pulsation modes. I. The method and numerical tests." Astronomy and Astrophysics **455**: 227-234.

Zima, W., et al. (2006). "A new method for the spectroscopic identification of stellar non-radial pulsation modes. II. Mode identification of the delta Scuti star FG Virginis." Astronomy and Astrophysics **455**: 235-246.

Appendix A

A copy of the entire γ Doradus star list used for target selection. The list has been made primarily from the papers Handler 1999 and Henry and Fekel 2003.

HD #	alpha (2000.0)	delta (2000.0)	Sp. Type	V	v sin i
2842	0:31:50	+04:50:46.2	F0	7.99	----
7169	1:12:54	+51:36:08.5	A5	7.3	----
9365	1:33:45	+60:37:23.2	F0	8.21	----
10167	1:38:31	-42:55:40.4	F0 V	6.67	5
11443	1:53:05	+29:34:43.8	F6 IV	3.42	112
14940	2:24:10	-16:15:15.5	F0 IV-V	6.68	39
17310	2:46:34	-06:42:06.8	F0	7.77	----
19655	3:11:41	+48:03:14.8	F2Vn	8.61	----
21788	3:30:48	+05:09:09.5	F0	7.46	----
22702	3:39:51	+25:11:42.4	A2	8.81	----
23005	3:46:01	+67:12:05.8	F0 IV	5.78	----
23585	3:47:04	+23:59:43.0	A9 V	8.37	105
23874	3:48:52	+11:42:31.7	F0	8.2	----
26298	4:09:08	-16:23:58.0	F0/F2V	8.16	----
27377	4:17:51	-34:11:11.6	F0 V	7.48	----
27397	4:19:58	+14:02:06.7	F0 IV	5.58	100
33204	5:09:45	+28:01:49.7	A5m	5.93	45
34025	5:11:59	-47:16:26.4	F2 IV	7.87	----
35187	5:24:01	+24:57:37.6	A2	7.79	----
40745	6:00:18	-12:54:00.1	F2 IV	6.21	40
41448	6:04:35	-14:01:57.4	A9 V	7.6	----
48271	6:44:12	+36:59:38.4	F0	7.49	----
49434	6:48:19	-01:19:08.1	F1 V	5.75	82
62863	7:45:29	-14:41:10.2	A8 V	6.89	----
63436	7:48:58	+00:39:43.0	F2	7.46	----
66853	8:05:32	+02:09:31.7	F2	9.24	76
69715	8:19:32	+35:02:44.4	A5	7.18	----
70645	8:27:40	+67:58:26.8	F0	8.15	----
73854	8:41:11	+19:49:46.4	F5 V	9.04	126
75202	8:46:23	-52:50:37.4	A3 IV	7.7	----

80731	9:24:03	+61:46:22.9	F0 V	8.46	----	
81421	9:25:27	-06:24:16.3	A3	7.01		19
85693	9:52:56	-26:45:20.2	F0 V	7.71		17
85964	9:54:29	-37:17:24.4	F3 IV-V	7.52	----	
86358	9:58:26	+27:45:32.4	F3 V	6.64		25
91201	10:29:59	-62:42:45.2	F0/F2IV-V	8.1	----	
99267	11:25:38	+29:59:14.4	F1 V	6.88		93
100215	11:32:13	+38:55:33.0	Am	7.99	----	
103257	11:53:17	-36:34:38.5	F2 V	6.63	----	
104860	12:04:34	+66:20:11.7	F8	7.92	----	
105085	12:06:01	+23:12:16.8	F5	7.49	----	
106103	12:12:25	+27:22:48.5	F4 V	8.07		20
107192	12:15:20	+87:42:00.4	F2 V	6.27		75
109032	12:31:39	+12:07:40.3	F0	8.09	----	
109799	12:37:42	-27:08:20.0	F1 IV	5.42	----	
109838	12:37:33	+45:15:13.6	F2 V	8		25
110606	12:43:40	-35:24:50.5	F2 V	7.88	----	
111829	12:53:41	-74:53:47.8	A1 IV-V	9.46	----	
112429	12:55:28	+65:26:18.5	A5n	5.23		130
112685	12:59:07	-45:57:43.8	F0 V	7.85	----	
112934	13:00:33	-33:03:04.8	A9 V	6.59		83
113357	13:03:37	-38:58:06.4	F0 V	7.89	----	
113867	13:06:23	+22:16:47.6	F0	6.84	----	
115466	13:17:27	-10:32:46.6	F0	6.89	----	
117777	13:32:03	+28:35:04.9	F2 V	9.24		74
118388	13:34:50	+65:15:18.1	F2	7.95	----	
122300	13:59:41	+52:09:30.0	F5	8.18		13
124248	14:12:34	-09:54:00.3	F0	7.15	----	
126516	14:26:03	-00:41:30.3	F3 V	8.29	----	
130173	14:44:04	+61:05:53.8	F2	6.88	----	
133803	15:07:15	-29:30:16.1	A9 V	8.16	----	
135825	15:17:32	-10:30:02.2	F0	7.31	----	
137785	15:29:19	-38:38:06.0	F2 V	6.44		105
144451	16:06:51	-21:51:49.8	F0 V	7.84		54
147787	16:27:57	-64:03:28.6	F4 IV	5.28		50
149989	16:40:44	-51:28:41.7	A9 V	6.3		136
152896	16:55:01	+29:02:19.9	A5	7.55		50
153580	17:03:09	-53:14:13.3	F6 V	5.29		58
155854	17:15:40	-34:21:08.1	F0 V	7.88	----	

160295	17:38:58	+02:39:30.3	F0	7.72		61
165645	18:05:01	+41:56:46.6	F0 Vn	6.38		135
166114	18:11:06	-41:21:32.8	F2 V	5.86	----	
169577	18:25:06	+05:59:54.6	F0	8.65	----	
171244	18:32:48	+24:40:45.3	F0	7.74		49
172416	18:42:22	-47:45:39.5	F5 V	6.6	----	
173977	18:44:53	+57:05:17.2	F2	8.3	----	
175337	18:54:54	+01:07:17.7	F5	7.38	----	
182640	19:25:30	+03:06:53.2	F0 IV	3.4		85
182640	19:25:30	+03:06:53.2	F0 IV	3.4		85
187028	19:50:08	-50:36:09.1	F0 V	7.6	----	
187353	19:49:51	-10:43:30.2	F0	7.59	----	
187615	19:50:25	+14:30:49.9	A3	7.98	----	
188032	19:55:20	-48:16:56.2	A9/F0 V	8.14	----	
189631	20:02:41	-41:25:03.9	F0 V	7.53	----	
197187	20:42:40	-18:06:34.8	F2 IV-V	7.35	----	
197451	20:43:57	-05:35:24.8	F0 IV-V	7.19	----	
199143	20:55:48	-17:06:51.0	F8 V	7.27	----	
201985	21:13:14	-04:16:00.2	A3	7.95	----	
202444	21:14:48	+38:02:43.1	F0 IV	3.74		94
206481	21:45:44	-69:21:49.4	F0 V	7.88	----	
207651	21:50:08	+19:25:26.4	A5	7.22	----	
211699	22:18:51	+04:08:35.3	F0	9.13	----	
213617	22:32:36	+20:13:48.1	F1 V	6.42		83
214291	22:37:48	-39:51:25.6	F7 V	6.54	----	
216108	22:49:28	+43:50:36.7	A0	8	----	
216910	22:57:59	-59:05:22.2	F2 IV	6.7	----	
218225	23:06:48	-38:47:38.8	F3 IV	8.71	-----	
219843	23:18:42	+36:05:24.8	F0	7.35	----	
224288	23:56:35	-55:29:00.4	F0 IV	8.02	----	

Appendix B

A collection of MATLAB codes used in this thesis. I wrote these codes with a focus on function rather than speed. Some attempts for vectorising the codes, particularly the ones that operate on large data sets, have been made to optimise computing speed in MATLAB. There is some basic commenting in the programs to allow for updating by one who is somewhat familiar with the code. The toolboxes that are regularly used are: the statistics toolbox, curve fitting toolbox and the optimisation toolbox.

They are in the following order:

Contbyresid – The automatic continuum fitting code that discards points based on residuals to polynomial fits.

Splinecontinfit – The manual continuum fitting code. It uses a spline defined by points specified by the user to remove the pseudo continuum shape from a spectral order.

Deconvobs – the program used for smoothing (filtering) and removing the instrumental profile by deconvolution.

Vsinidirectfit – This is the code to determine the $V_{rot}\sin i$ of a line profile from directly fitting a rotationally broadened Gaussian in a least-squares manner.

Vsinifittingfn – This is the function that is minimised in the computation of the direct fit to the line profile in the $V_{rot}\sin i$ determination.

fourvsinimeasure – This is the Fourier technique used to measure $V_{rot}\sin i$.

checkfreqlistforcombos – This is a program that checks a supplied list of frequencies to see if any members can be made up from twice another member or from the addition of two other members. This is to identify basic harmonics or combination frequencies.

contbyresid

```
function [newwave,newint]=contbyresid(wave,int)

if nargin ~= 2
    disp('[newwave,newint]=contbyresid(wave,int)')
    disp('two inputs required')
    return
end
warning off
newwave = wave; %no smoothing
newint = int; %no smoothing

%must be vectors
szwave=size(newwave);
szint=size(newint);
if szwave(2) > 1
    newwave = newwave';
end
if szint(2) > 1
    newint = newint';
end

tempwave=newwave;
tempint=newint;
[fresult,gof,residuals]=fit(newwave,newint,'poly5');
inds=find(abs(residuals.residuals)>2*std(residuals.residuals))
tempwave(inds)=[];
tempint(inds)=[];
[fresult,gof,residuals]=fit(tempwave,tempint,'poly5');
inds=find(abs(residuals.residuals)>2*std(residuals.residuals))
tempwave(inds)=[];
tempint(inds)=[];
[fresult,gof,residuals]=fit(tempwave,tempint,'poly5');
inds=find(residuals.residuals<-1*std(residuals.residuals));
tempwave(inds)=[];
tempint(inds)=[];
[fresult,gof,residuals]=fit(tempwave,tempint,'poly5');
inds=find(residuals.residuals<-1*std(residuals.residuals));
tempwave(inds)=[];
tempint(inds)=[];
```

```
[fresult,gof,residuals]=fit(tempwave,tempint,'poly5');
inds=find(residuals.residuals<-1*std(residuals.residuals));
tempwave(inds)=[];
tempint(inds)=[];
continfit=fresult.p1*newwave.^5+fresult.p2*newwave.^4+fresult.
p3*newwave.^3+fresult.p4*newwave.^2+fresult.p5*newwave+fresult
.p6+std(residuals.residuals);
newint=newint./continfit;
```

testprofilerecovery

```
function [tstatunit,tstatscaled,tstatbestline] =
testprofilerecovery(linex,liney,specmaxsize,numlines,noise,dis
ppos,cerramp,dep)

%future work: Add the random fractional variation in the
scaled delta
%functions, option to emulate errors in the depths of the
scaled
%delta functions

%[wave,int,actualpositions,depths,delfn,ccf,tstat,linedens,tst
atbestline,tbestline] =
makespecfromprofileunit(linex,liney,specmaxsize,numlines,noise
)
%liney should be a row vector I think
%inputs should be odd lengths
if (numel(linex)/2 == round(numel(linex)/2)) %then even
    linex(end)=[];
    liney(end)=[];
end

%invert and normalise liney for use
liney=1-liney;
liney=liney/max(liney);

%define line centre as an indice (size of half of line)
linecentre=round(numel(liney)/2);

%make vector of random positions including numlines of lines
over the range
%1:specmaxsize in terms of indices of linex (which is assumed
to be
%linear) don't accept lines too near edge else get edge
effects!
step=roundn(linex(2)-linex(1),-3);
wave=0:step:specmaxsize;
%wave should be odd
if (numel(wave)/2 == round(numel(wave)/2)) %then even
```

```
    wave(end)=[];
end
position=round(rand(numlines,1)*(numel(wave)-
(round(1.2*numel(liney))+1))+round(1.2*linecentre));
actualpositions=wave(position);

%make vector of random depths of lines ranging from mindeep
(0.02) to maxdeep (0.5) deep (in
%continuum units
mindeep=0.02;
maxdeep=dep;
depths=rand(numlines,1)*(maxdeep-mindeep)+mindeep;


%build the inverted spectrum by adding lines at positions to a
zero vector
int=zeros(size(wave));
for lineno=1:numlines
    templine=liney*depths(lineno);
    if (position(lineno)+linecentre > numel(int)) %line needs
to be chopped
        templine(end-(position(lineno)+linecentre-numel(int)-
2):end)=[];
        templine(1:numel(templine))=0;
        int(end-numel(templine)+1:end)=int(end-
numel(templine)+1:end)+templine;
    elseif (position(lineno)-linecentre < 1) %line needs to be
chopped
        templine(1:-1*(position(lineno)-linecentre))=[];
        templine(1:numel(templine))=0;

int(1:numel(templine))=int(1:numel(templine))+templine;
    else
        %define the range of int for adding and then add
        int(position(lineno)-linecentre+1:position(lineno)-
linecentre+numel(templine))=int(position(lineno)-
linecentre+1:position(lineno)-
linecentre+numel(templine))+templine;
    end
end

%make built spectrum upright
int=1-int;

%add (normal distribution) noise to the built spectrum
int=int+randn(size(int))/2*noise;

%add continuum fitting errors
if cerramp ~= 0
    div=rand(1)*0.2+0.4;
```

```
    %two random wavelengths ranging from 2/3 to 1/2 and 1/3 to
1/4 of the
    %length of wave vector
    f1=1/((2/(rand(1)+3))*(max(wave)-min(wave)));
    f2=1/((1/(rand(1)+2))*(max(wave)-min(wave)));
    cfiterror=div*cerramp*sin(2*pi*f1*wave+rand(1)*2*pi)+(1-
div)*cerramp*sin(2*pi*f2*wave+rand(1)*2*pi);
    int=int+cfiterror;
end

%fourier smooth spectrum
%wave and int must be columns
szwave=size(wave);
szint=size(int);
if szwave(2) > 1
    wave=wave';
end
if szint(2) > 1
    int=int';
end
[wave,int] = Fourierfiltering(wave,int); %noise is available
as an output
%now back to rows
wave=wave';
int=int';

%notification of line density
%blendingparam=(max(linex)-min(linex))*numlines/specmaxsize;
%fprintf('Line density = %.2f lines/x-axis unit\n',linedens)


%add normally distributed displacement to positions in terms
of pixels
%where each pixel is 0.01 units
if disppos ~= 0
    displace=round(randn(size(position))*disppos);
    position=position+displace;
end

%testing ccf delfn vector
delfnsc=zeros(size(wave));
delfnun=zeros(size(wave));
depthssc=depths;
depths2sc=depthssc;
depthsun(1:numel(depthssc))=1;
depths2un=depthsun;
% numdoubles=numel(position)-numel(unique(position));
qq=sort(position);
ss=diff(qq);
tt=find(ss==0);
```

```
for i=1:numel(tt)
    v=find(position==qq(tt(i)));
    depths2sc(v(end))=sum(depthssc(v));
    depths2un(v(end))=sum(depthsun(v));
end
delfnun(position)=depths2un;
delfnsc(position)=depths2sc;

%testing and normalising ccf
type='unbiased';
ccf=xcorr(int,delfnun,floor(numel(linex)/2),type); %output
could be [ccf,lags]
ccf=ccf-min(ccf);
ccf=ccf/max(ccf);
ccfsc=xcorr(int,delfnsc,floor(numel(linex)/2),type); %output
could be [ccfsc,lags]
ccfsc=ccfsc-min(ccfsc);
ccfsc=ccfsc/max(ccfsc);

%fraction of line depth  of input line to define what gets cut
off each end
%for measuring sameness
minlinedepth=0.20;
ind1=[];
ind2=[];
while (isempty(ind1) || isnan(ind1))
ind1=ceil(round(mean(find(roundn(liney(1:round(numel(liney)/2)
),-2)==minlinedepth))));
if isnan(ind1)
    minlinedepth=roundn(minlinedepth+0.01,-2);
end
end
if minlinedepth > 0.3
    disp('problem finding minlinedepth ind1')
end
minlinedepth=0.2;
while (isempty(ind2) || isnan(ind2))
ind2=floor(mean(find(roundn(liney(end-
round(numel(liney)/2):end),-2)==minlinedepth)))+linecentre-1;
if isnan(ind2)
    minlinedepth=roundn(minlinedepth+0.01,-2);
end
end
if minlinedepth > 0.3
    disp('problem finding minlinedepth ind2')
end

%UNIT
%chop off parts of lines and then compare using tstat=(Summed
RMS difference)/(sum of line input)
```

```
tccf=ccf(ind1:ind2);
tliney=liney(ind1:ind2);
tstatunit=sum(sqrt(((1-tliney)-tccf).^2))/numel(tliney);
%fprintf('(Summed RMS difference)/(sum of line input) =
%.3f\n',tstat)

%SCALED
%chop off parts of lines and then compare using tstat=(Summed
RMS difference)/(sum of line input)
tccfsc=ccfsc(ind1:ind2);
tstatscaled=sum(sqrt(((1-tliney)-tccfsc).^2))/numel(tliney);
%fprintf('(Summed RMS difference)/(sum of line input) =
%.3f\n',tstat)


%find single isolated line for comparison
%define two things to find 'best line'
[spos,ix]=sort(position);
%rearrage depths to match
sdep=depths(ix);
difference=diff(spos);
linedif=zeros(size(position));
linedif(1)=difference(1);
linedif(end)=difference(end);
szdiff=size(difference);
if szdiff(1) > 1      %make a row vector
    difference=difference';
end
difference2=padarray(difference,[0 1],'pre');
difference2(end)=[];
difference(2,:)=difference2;
difference=min(difference);
linedif(2:end-1)=difference(2:end);
%isolated-ness
iso=linedif/linecentre;
%depths already defined
%the line with the highest linedif^1.5*depth is the best line
for comparison
%we choose to weight isolation ahead of depth
bestlineind=find((iso.^2).*sdep==max((iso.^2).*sdep));
bestline=int(position(ix(bestlineind))-
(linecentre):position(ix(bestlineind))+linecentre);
whi=1;
while numel(bestline)~=numel(linex)
    if whi==1
        bestline(1)=[];
    else
        bestline(end)=[];
    end
    whi=whi*-1;
```

```
end
bestline=bestline-min(bestline);
bestline=bestline/max(bestline);
tbestline=bestline(ind1:ind2);
tstatbestline=sum(sqrt(((1-tliney)-
tbestline).^2))/numel(tliney);

%testing plots
% figure
% subplot(2,1,1);plot(wave,int)
% subplot(2,1,1);hold on
% subplot(2,1,1);plot(actualpositions,1-depths,'r+')
% subplot(2,1,1);plot(wave,delfnun,'c')
% subplot(2,1,1);plot(wave,delfnsc,'k')
%
subplot(2,1,1);plot(wave(position(ix(bestlineind))),0.4,'*k')
% subplot(2,1,2);plot(linex,1-liney)
% subplot(2,1,2);hold on
% subplot(2,1,2);plot(linex,ccf,'r')
% subplot(2,1,2);plot(linex,ccfsc,'m')
% subplot(2,1,2);plot([linex(ind1) linex(ind1)],[0 1],'g')
% subplot(2,1,2);plot([linex(ind2) linex(ind2)],[0 1],'g')
% title(['Unit CCF {\it t} statistic='
num2str(roundn(tstatunit,-2)) ', Scaled CCF {\it t}
statistic=' num2str(roundn(tstatscaled,-2))])
% legend('Input profile','Unit CCF function','Scaled CCF
function','Boundaries','Location','North')
%
% figure
% plot(linex,1-liney,'k','LineWidth',1.0)
% hold on
% plot(linex,ccf,'r--')
% plot(linex,ccfsc,'m--')
% plot(linex,bestline,'b--')
% plot([linex(ind1) linex(ind1)],[0 1],'g');plot([linex(ind2)
linex(ind2)],[0 1],'g')
% title(['Unit CCF {\it t} statistic='
num2str(roundn(tstatunit,-2)) ', Scaled CCF {\it t}
statistic=' num2str(roundn(tstatunit,-2)) ', Best line {\it t}
statistic=' num2str(roundn(tstatbestline,-2))])
% legend('Input profile','Unit CCF function','Scaled CCF
function','Best line','Boundaries','Location','North')
% xlabel('''Wavelength''');ylabel('Normalised line intensity')
```

splinecontinfit

```
function [wavelength,intensity] = splinecontinfit(wave,int);

% Continuum fit a spectrum
figure(100)
```

```
clf reset

plot(wave,int)
axis([-inf inf min(int)-0.1*(max(int)-min(int))
max(int)+0.1*(max(int)-min(int))])
hold on
while 1
    figure(100)
    [a,b]=contline;     % get continuum fit line to use
    pp=spline(a,b);
    contin=ppval(pp,wave);
    intensity=int./contin;
    wavelength=wave;
    figure(200)
    clf reset
    plot(wavelength,intensity)
    hold on
    plot(wavelength,1)
    hold off
    axis([-inf inf min(intensity)-0.1*(max(intensity)-
min(intensity)) max(intensity)+0.1*(max(intensity)-
min(intensity))])
    happy=input('Are you happy with this continuum fitted
spectrum? (y/n) [y] ->','s');
    if isempty(happy)
        happy='y';
    end
    if (happy == 'y')
        break
    else
        close(200)
    end
end
%%%%%%%%%%%%%%%%%%%%%%%%% Sub-function %%%%%%%%%%%%%%%%%%%%%%%%
function [X,Y] = contline();

% Make a line based on mose presses to be able to make a
spline and divide
% it out.
% There must be a plot already
hold on
i=1;
X=[];
Y=[];
while 1
    disp('press LMB at point to include for continuum
definition')
    eval(strcat('[x',num2str(i),',y',num2str(i),'] =
ginput(1);'))
```

```
eval(strcat('plot(x',num2str(i),',y',num2str(i),','r+')'))
    %axis([-inf inf 0.8*max(int) 1.05*max(int)])
    eval(strcat('X(i)=x',num2str(i),';'))
    eval(strcat('Y(i)=y',num2str(i),';'))
    fin=input('press x then enter to finish adding points just
enter key to continue ->','s');
    if (fin == 'x')
        break
    end
    i=i+1;
end
```

deconvobs

```
function[velocity,reconlinedeconv]=deconvobs(vel,int,respfn,no
ise,alpha0);
%deconvolve observed RLP by that instruments that nights
spectrograph response function
c=299792.458; %speed of light (km/s)
%convert alpha0 into velocity units
alpha0=alpha0/4000*c;

%make the number of points in the int vector odd
if (round(numel(int)/2) == numel(int)/2)
    vel(1)=[];
    int(1)=[];
end

%test if profile needs inverting
if (round(int(1)) == 1)
    int=1-int;
    invertneed=1;
else
    invertneed=0;
end

stepsizevel=vel(end)-vel(end-1);

%take fft of CCF
z=fft(int);
Z=sqrt(z.*conj(z));   %for plotting fft(CCF)
xaxvel=1/stepsizevel*(0:numel(vel)-1)/numel(vel);  %make x-
axis for plotting
xaxvelhalf=xaxvel(1:round(numel(xaxvel)/2));

%make filter
deconvfilt=real(1./(1+(noise/Z(1))^2*10.^(alpha0^2*xaxvelhalf.
^2)));
deconvfiltbak=deconvfilt;
```

```
for u=1:numel(deconvfilt)
    if isnan(deconvfilt(u))
        deconvfilt(u)=0;
    end
end
%filter must be symmetric like fft(int)
deconvfiltcopy=deconvfilt;
deconvfiltcopy(1)=[];
deconvfiltcopy=fliplr(deconvfiltcopy);
deconvfilt=cat(1,deconvfilt',deconvfiltcopy');
deconvfilt=deconvfilt';

%apply filter
if(size(z)==size(deconvfilt))
    x=z.*deconvfilt;
else
    x=z.*deconvfilt';
end
X=sqrt(x.*conj(x));

%make gaussian representing spectrograph resopnse function on
same axis for deconvolving
gaussian=0.01*exp(-(vel/respfn).^2);
u=fft(gaussian);
U=sqrt(u.*conj(u));
U=U/max(U); %this is the deconvolving variable used

%apply deconvolution (division in Fourier space)
deconv=x./real(U);
DECONV=sqrt(deconv.*conj(deconv));  %for plotting

%check for inf's and nan's both should be set to zero
for uu=1:numel(deconv)
    if isnan(deconv(uu))
        deconv(uu)=0;
    end
end
for uu=1:numel(deconv)
    if isinf(deconv(uu))
        deconv(uu)=0;
    end
end
%reconstruct line
reconlinedeconv=ifft(deconv,'symmetric');
%put back the way they started
if (invertneed == 1)
    reconlinedeconv=1-reconlinedeconv;
    int=1-int;
end
velocity=vel;
```

Vsinidirectfit

```
function [FWHMgauss,Vsini,fittedint]=Vsinidirectfit(vel,int);

if nargin~=2
    fprintf('wrong number of inputs!\n - 2 required (Velocity
vector, Intensity vector)\n')
    return
end
format long g
global lamda0 epsx


warning off

% Fit the line profile by optimizing an unconstrained FWHM
Gaussian convolved with the rotational broadening curve of
Gray 1992 for the specified wavelength (usually the weighted
centre wavelength of the ccf-function). Note that the input
spectrum is in velocity space.

c=299792.458; % Speed of light

%invert line profile and normalise
int=1-int;
int=int/max(int);

%function parameters
x0=[20 10]; %defaults
a1=input('input line centre (in km/s), this will be subtracted
from the velocities to centre the line [0] ->');
if isempty(a1)
    a1=0;
end
vel=vel-a1;
a2=input('input starting FWHM for pre-rotationally broadened
line (in km/s, a range will be tested) [20] ->');
a3=input('input starting V sin(i) (in km/s, a range will be
tested) [10] ->');
if (isempty(a2) ~= 1)
    x0(1)=a2;
end
if (isempty(a3) ~= 1)
    x0(2)=a3;
end
lamda0=input('input lambda0 (use centre wavelength of ccf if a
ccf) [5500] ->');
```

```
lb=[0 0];
ub=[200 1000];
if isempty(lamda0)
    lamda0=5500;
end
%respfnwidth=input('input spectrograph response width
parameter or leave empty to fit Thar lines (telwave and
telint); -> ');

epsx=input('input limb darkening coefficient [0.555] ->');
if isempty(epsx)
    epsx = 0.555; %limb darkening coefficient
end

%convert FWHM to wavelength
x0(1)=x0(1)*lamda0/c;

%fit line data with a broadened Gaussian
disp(' ')
disp('beginning V sin(i) determination ...')
disp(' ')
[x] = lsqcurvefit(@vsinifittingfn,x0,vel,int,lb,ub);
disp(' ')
disp('V sin(i) determination complete')
disp(' ')
results=x;
x(1)=x(1)/lamda0*c;
results1=x;
width=x(1); % for use later
FWHMgauss=x(1);
clear x0 x
Vsini=results1(2);
fittedint=vsinifittingfn(results,vel);
figure
plot(vel,1-int,'.k')
hold on
plot(vel,1-fittedint,'r')
hold off
xlabel('Radial velocity (km/s)')
ylabel('Intensity')
legend('Observed line','Fitted line','Location','SouthEast')
axis([-inf inf -0.05 1.1])
disp(' ')
fprintf('\nResults:\nFWHM for line and spectrograph response
fn = %.2f km/s\nV sin(i) = %.2f
km/s\n\n',results1(1),results1(2));
warning on
```

vsinifittingfn

```
function V = vsinifittingfn(x,xdata);

%works out broadened line profile in lamda space and converts
to velocity
%space

if nargin~=2
    fprintf('wrong number of inputs!\n - 2 required (Start
points vector, Intensity vector)\n')
    return
end
warning off
% x(1)=FWHM gaussian
% x(2)=V sin(i)
global lamda0 epsx
c=299792.458; %speed of light (km/s)

deltalamda=-10:0.001:10;   %make a fine wavelength grid on
which to construct
deltalamda1=-10:0.001:10;   %our broadening curve

indices=find(real( (2*(1-epsx)*((1-
((deltalamda*c/lamda0)/(x(2))) .^2).^0.5)+0.5*pi*epsx*(1-
((deltalamda*c/lamda0)/(x(2)))  .^2))  / (pi*lamda0*x(2)/c*(1-
epsx/3))  ) > 0);
start=indices(1);
finish=indices(end);
deltalamda=deltalamda(start:finish);

    K=real(conv(real((2*(1-epsx)*((1-
((deltalamda*c/lamda0)/(x(2))).^2).^0.5)+0.5*pi*epsx*(1-
((deltalamda*c/lamda0)/(x(2))).^2))/(pi*lamda0*x(2)/c*(1-
epsx/3))),exp(-(2*sqrt(log(2))*deltalamda1/x(1)).^2)));
    centre1=find(deltalamda==0);
    centre2=find(deltalamda1==0);
    centre=centre1+centre2-1;
    %convert width parameter to velocity units

%make an x-axis for the convolution
newxax=-(centre-1)*0.001:0.001:0;
t=numel(K)-numel(newxax);
newxax=-(centre-1)*0.001:0.001:t*0.001;
%convert the x-axis to velocity space
newxax=newxax/lamda0*c;
%project it on to the required axis
V=spline(newxax,K,xdata);
V=V/max(V);  %normalise
warning on
```

fourvsinimeasure

```
function Vsini = fourvsinimeasure(vel,int,epsx,lamda);

%fourier transform vsini method

if nargin~=4
    disp('function [Vsini] =
fourvsinimeasure(vel,int,epsx,lamda);')
    disp('wrong number of inputs!\n - 5 required -Velocity
vector, Intensity vector,')
    disp('limbdarkening coeff, and rest wavelength')
    return
end
%standardise int
int=int-min(int);
int=int/max(int);

%make reference line
refvsini=20;
FWHM=25;
ref = Linemakerspecial(refvsini,FWHM,epsx,lamda);
step=mean(diff(ref(:,1)));
xax=min(vel):step:max(vel);
int=spline(vel,int,xax);
refline=zeros(size(xax));refline=refline+1;
refline(1:numel(ref(:,2)))=ref(:,2);
% numel(xax)
% figure
% plot(xax,refline,'r')
% hold on
% plot(xax,int,'k')
%take forier transforms padded to high numbers for resolution
at low
%frequencies
x=fft(int-1,262144);
X=sqrt(x.*conj(x));
y=fft(refline-1,262144);
Y=sqrt(y.*conj(y));
fax=1/step*(0:numel(x)-1)/numel(x);
%remove excess info from vectors
ind=linearfindnearest(fax,1);
fax(ind:end)=[];x(ind:end)=[];X(ind:end)=[];y(ind:end)=[];Y(in
d:end)=[];

figure
loglog(fax,Y/max(Y),'r')
```

```
hold on
loglog(fax,X/max(X),'k')

%%%%Now find 1st minima points
grdx=gradient(X);
grdy=gradient(Y);
ind1=find(grdx<0);
ind2=find(grdx>=0);
if grdx(1)<0
    ind2(1); %first indice after first crossover;
    dataminima=mean([fax(ind2(1)) fax(ind2(1)-1)]);
else
    ind1(1); %first indice after first crossover;
    dataminima=mean([fax(ind1(1)) fax(ind1(1)-1)]);
end
ind1=find(grdy<0);
ind2=find(grdy>=0);
if grdy(1)<0
    ind2(1); %first indice after first crossover;
    refminima=mean([fax(ind2(1)) fax(ind2(1)-1)]);
else
    ind1(1); %first indice after first crossover;
    refminima=mean([fax(ind1(1)) fax(ind1(1)-1)]);
end
Vsini=roundn(refvsini*refminima/dataminima,-2);
plot([refminima refminima],[1e-8 1e5],'g')
plot([dataminima dataminima],[1e-8 1e5],'g')
axis([min(fax) max(fax) 1e-6 10])
xlabel('log_10(s/km)')
ylabel('Normalised log_10(Amplitude)')

%%%%%%%%%%%%The following is a subfunction%%%%%%%%%%%%%%%%%%
function result = Linemakerspecial(vsiniest,FWHM,epsx,lamda);
%Make a broadened line profile

format long g
vsini=vsiniest;
c=299792.458; %speed of light (km/s)
% Define rotational broadening curve
deltalamda=-10:0.001:10;
lam=deltalamda/lamda;
lamgrp=lam/(vsini/c);
%rotational broadening fn from Gray 1992
G=real((2*(1-epsx)*((1-lamgrp.^2).^0.5)+0.5*pi*epsx*(1-
lamgrp.^2))/(pi*lamda*vsini/c*(1-epsx/3)));
indices=find(G > 0);  %indices to the positive part of G
D=deltalamda(min(indices):max(indices));  %select the right
parts of G and deltalamda
D(2,:)=G(min(indices):max(indices));
D=D';
```

```
broadcurve=D(:,2);
clear lam lamgrp indices
% make gaussian curve to be broadened in same wavelength space
as broadening profile
a1=0.6;
b1=0;
%convert FWHM (velocity to wavelength)
FWHM=FWHM*lamda/c;
gaussiancurve=a1*exp(-(2*sqrt(log(2))*(deltalamda-
b1)/FWHM).^2);
% convolve the gaussian line and the broadening curve to
produce the
% broadened curve
res=real(conv(broadcurve,gaussiancurve));
% scale to height 1
res=res/max(res);
%invert
res=1-res;
% make x axis for result
newax=-(round(numel(res)/2)-
1)*0.001:0.001:(round(numel(res)/2)-1)*0.001;
%convert axis to velocity
newax=newax/lamda*c;
result=newax;
result(2,:)=res;
result=result';
d=find(roundn(result(:,2),-3)==0.999);
dd=find(diff(d)>10);
ind1=round(mean(d(1:dd)));
ind2=round(mean(d(dd+1:end)));
result=result(ind1:ind2,:);
```

checkfreqlistforcombos

```
function [tests]=checkfreqlistforcombos(freqs,tol)

%freqs is the frequency list
%tol is the +/-tolerance in frequency units when deciding if
other frequencies are combos.
tests=zeros(numel(freqs));
for s=1:numel(freqs)
    eval(['f' num2str(s) '=freqs(' num2str(s) ');'])
    for r=s:numel(freqs)
        tests(s,r)=freqs(s)+freqs(r);
    end
end
%now check to see if they're the same as other freqs
for q=1:numel(freqs)
```

```
    %num2str(q)
    %check for combos
    [inds,indr]=find(tests > freqs(q)-tol & tests <
freqs(q)+tol);
    if ~isempty(inds) && ~isempty(indr)
        for b=1:numel(inds)
            fprintf(['The frequency f' num2str(q) '=%f is f'
num2str(inds(b)) '=%f + f' num2str(indr(b)) '=%f
difference=%f\n'],freqs(q),freqs(inds(b)),freqs(indr(b)),freqs
(q)-(freqs(inds(b))+freqs(indr(b))))
        end
    end
    %Now check for 1c/d aliases or aliases of combos
    [inds,indr]=find(tests > freqs(q)-tol+1 & tests <
freqs(q)+tol+1);
    if ~isempty(inds) && ~isempty(indr)
        for b=1:numel(inds)
            fprintf(['The frequency f' num2str(q) '=%f is a
1c/d alias of f' num2str(inds(b)) '=%f + f' num2str(indr(b))
'=%f which totals ' num2str(tests(inds(b),indr(b))) '
difference=%f\n'],freqs(q),freqs(inds(b)),freqs(indr(b)),freqs
(q)-(freqs(inds(b))+freqs(indr(b))))
        end
    end
    [inds,indr]=find(tests > freqs(q)-tol-1 & tests <
freqs(q)+tol-1);
    if ~isempty(inds) && ~isempty(indr)
        for b=1:numel(inds)
            fprintf(['The frequency f' num2str(q) '=%f is a
1c/d alias of f' num2str(inds(b)) '=%f + f' num2str(indr(b))
'=%f which totals ' num2str(tests(inds(b),indr(b))) '
difference=%f\n'],freqs(q),freqs(inds(b)),freqs(indr(b)),freqs
(q)-(freqs(inds(b))+freqs(indr(b))))
        end
    end

end
disp(' ')
fprintf('All statements are true to within the supplied
tolerance limit of +/-%f\n',tol)
disp(' ')
```

Appendix C

A complete list of wavelengths and depths used in the application of the scaled delta function CCF method. This template was based on matching the spectrum of HD17310, chosen because it is a sharp lined γ Dor star, using the SYNTH and EWFIND drivers in the MOOG (Sneden 1973) program and a Kurucz stellar model with the parameters T_{eff} = 7000 K, log g = 4.0, [Fe/H] = 0.0 relative to the sun and microturbulence = 2.0 km s^{-1}. The depths for each line were then determined by a linear relationship between the EW and the synthetic spectral line depth. These depths were scaled to match the depths of HD17310.

Not all of this list was used for each application of the scaled delta function CCF as some spectra contained inter-order spaces which had to be removed from the template etc. Note that the regions around the Hydrogen lines and regions where telluric lines are present have been removed from this template and that only lines with a depth sufficient to be seen in the spectrum of HD17310 observed have been included (practically this means lines with a minimum depth of ~0.02 in continuum units in this template).

Wavelength	Depth	EP	logGF	Atom	Abund	EW(mA)
4400.39	0.284	0.6	-0.51	Sc II	3.1	108.6
4400.57	0.028	0.26	-0.41	V I	4	10.8
4400.86	0.033	3.65	-1.182	Ni I	6.25	12.7
4401.29	0.19	3.6	-0.92	Fe I	7.52	72.7
4401.44	0.174	2.83	-1.65	Fe I	7.52	66.3
4401.54	0.24	3.19	0.04	Ni I	6.25	91.6
4403.34	0.027	4.58	-1.472	Fe I	7.52	10.3
4403.35	0.021	1.18	-1.203	Zr II	2.67.9	

4404.75	0.597	1.56	-0.142	Fe I	7.52	227.9
4404.85	0.03	4.58	-1.413	Fe I	7.52	11.6
4405.02	0.02	0.05	-5.221	Fe I	7.52	7.8
4406.63	0.042	0.3	-0.19	V I	4 16	
4407.64	0.062	0.29	0.01	V I	4 23.7	
4407.66	0.038	3.02	-2.523	Fe I	7.52	14.6
4407.68	0.139	1.22	-2.47	Ti II	4.99	53.2
4407.71	0.211	2.17	-1.92	Fe I	7.52	80.5
4408.19	0.064	0.28	0.02	V I	4 24.5	
4408.41	0.237	2.2	-1.71	Fe I	7.52	90.4
4408.5	0.036	0.26	-0.29	V I	4 13.9	
4408.51	0.049	0.27	-0.13	V I	4 18.8	
4409.12	0.044	3.3	-2.23	Fe I	7.52	16.8
4409.24	0.109	1.24	-2.638	Ti II	4.99	41.6
4409.52	0.122	1.23	-2.569	Ti II	4.99	46.6
4410.51	0.068	3.3	-1.08	Ni I	6.25	26
4411.07	0.122	3.09	-1.06	Ti II	4.99	46.7
4411.09	0.026	3.01	-0.72	Cr I	5.67	9.9
4411.93	0.15	1.22	-2.406	Ti II	4.99	57.3
4413.38	0.039	4.16	-0.712	Ni I	6.25	14.8
4413.4	0.052	4.07	-1.53	Fe I	7.52	20
4413.6	0.144	2.67	-3.87	Fe II	7.52	54.9
4413.85	0.021	3.55	-0.4	Cr I	5.67	8
4414.23	0.049	3.07	-2.353	Fe I	7.52	18.8
4414.46	0.024	4.17	-1.848	Fe I	7.52	9.1
4414.54	0.02	1.24	-1.171	Zr II	2.67.8	
4414.89	0.105	2.89	-0.29	Mn I	5.39	40.1
4415.12	0.453	1.61	-0.615	Fe I	7.52	173.1
4415.47	0.027	4.95	-2.35	Si I	7.55	10.4
4415.56	0.269	0.59	-0.64	Sc II	3.1102.6	
4416.83	0.304	2.78	-2.6	Fe II	7.52	116.2
4417.27	0.034	1.89	-0.02	Ti I	4.99	12.8
4417.72	0.298	1.16	-1.43	Ti II	4.99	114
4418.33	0.139	1.24	-2.46	Ti II	4.99	53.2
4420.67	0.045	0.62	-2.14	Sc II	3.1117.3	
4421.94	0.142	2.06	-1.77	Ti II	4.99	54.4
4422.57	0.247	2.84	-1.11	Fe I	7.52	94.3
4422.59	0.116	0.1	-1.27	Y II	2.24	44.4
4422.69	0.021	3.55	-0.4	Cr I	5.67	8
4423.14	0.041	2.99	-2.51	Fe I	7.52	15.8
4423.24	0.106	1.23	-2.672	Ti II	4.99	40.4
4423.84	0.081	3.65	-1.61	Fe I	7.52	31.1
4424.07	0.028	3.64	-2.185	Fe I	7.52	10.8
4424.19	0.093	3.54	-1.61	Fe I	7.52	35.6
4424.28	0.053	3.01	-0.37	Cr I	5.67	20.1
4425.44	0.286	1.88	-0.385	Ca I	6.36	109.2
4426.92	0.021	6.86	-2	S I	7.21	8.2
4427.1	0.093	1.5	0.23	Ti I	4.99	35.6

4427.3	0.136	3.65	-1.246	Fe I	7.52	51.8
4427.31	0.291	0.05	-3.044	Fe I	7.52	111.3
4427.88	0.047	1.24	-3.13	Ti II	4.99	17.9
4429.14	0.026	6.86	-1.9	S I	7.21	10.1
4429.19	0.023	3.93	-2.053	Fe I	7.52	8.9
4429.9	0.039	0.23	-0.49	La II	1.22	14.8
4430.19	0.102	3.02	-1.97	Fe I	7.52	38.9
4430.48	0.079	4.95	-1.81	Si I	7.55	30
4430.61	0.24	2.22	-1.659	Fe I	7.52	91.7
4431.35	0.075	0.6	-1.88	Sc II	3.128.6	
4431.44	0.026	6.86	-1.9	S I	7.21	10
4432.11	0.199	1.24	-2.1	Ti II	4.99	75.9
4432.17	0.027	2.87	-0.8	Cr I	5.67	10.5
4432.57	0.091	3.57	-1.6	Fe I	7.52	34.8
4433.22	0.216	3.65	-0.7	Fe I	7.52	82.6
4433.78	0.137	3.6	-1.27	Fe I	7.52	52.5
4433.99	0.034	9.99	-0.91	Mg II	7.58	12.8
4434.96	0.335	1.88	-0.029	Ca I	6.36	127.9
4435.15	0.096	0.09	-4.379	Fe I	7.52	36.7
4435.58	0.037	0.21	-0.092	Eu II	0.51	14
4435.68	0.268	1.88	-0.5	Ca I	6.36	102.5
4436.36	0.102	2.92	-0.288	Mn I	5.39	38.8
4436.92	0.079	3.04	-2.11	Fe I	7.52	30
4436.97	0.026	3.5	-1.42	Ni I	6.25	10.1
4437.56	0.029	3.68	-1.24	Ni I	6.25	10.9
4438.34	0.075	3.68	-1.63	Fe I	7.52	28.8
4438.52	0.031	3.88	-1.956	Fe I	7.52	11.7
4439.88	0.047	2.28	-3.002	Fe I	7.52	18.1
4440.34	0.023	1.87	-0.22	Ti I	4.99	8.6
4440.45	0.024	1.21	-1.127	Zr II	2.69	
4440.48	0.038	3.6	-2.07	Fe I	7.52	14.5
4440.82	0.055	3.96	-1.6	Fe I	7.52	20.9
4440.97	0.051	3.3	-2.155	Fe I	7.52	19.4
4441.55	0.034	3.88	-1.899	Fe I	7.52	13.1
4441.73	0.156	1.18	-2.41	Ti II	4.99	59.5
4442.34	0.293	2.2	-1.255	Fe I	7.52	111.8
4442.42	0.054	3.5	-1.061	Ni I	6.25	20.6
4442.83	0.08	2.17	-2.792	Fe I	7.52	30.7
4443.01	0.071	1.49	-0.33	Zr II	2.627.3	
4443.19	0.257	2.86	-1.02	Fe I	7.52	98
4443.79	0.402	1.08	-0.7	Ti II	4.99	153.7
4444.12	0.052	4.95	-2.03	Si I	7.55	20
4444.56	0.226	1.11	-2.03	Ti II	4.99	86.2
4446.24	0.023	5.95	-2.439	Fe II	7.52	8.6
4446.27	0.053	4.55	-1.154	Fe I	7.52	20.3
4446.83	0.118	3.68	-1.33	Fe I	7.52	45.2
4446.9	0.026	3.3	-2.501	Fe I	7.52	9.8
4447.13	0.107	2.2	-2.59	Fe I	7.52	40.9

4447.72	0.28	2.22	-1.342	Fe I	7.52	107.1
4449.14	0.088	1.89	0.5	Ti I	4.99	33.5
4449.42	0.032	4.55	-1.404	Fe I	7.52	12.4
4449.93	0.13	4.95	-1.5	Si I	7.55	49.7
4450.32	0.08	3.11	-2.05	Fe I	7.52	30.6
4450.48	0.306	1.08	-1.45	Ti II	4.99	116.7
4450.89	0.076	1.88	0.41	Ti I	4.99	29.2
4451.55	0.055	6.13	-1.844	Fe II	7.52	21.1
4451.56	0.03	0.38	-0.04	Nd II	1.511.5	
4451.59	0.193	2.89	0.278	Mn I	5.39	73.6
4452.61	0.03	3.94	-1.93	Fe I	7.52	11.3
4453.01	0.072	2.94	-0.49	Mn I	5.39	27.6
4453.31	0.064	1.43	-0.051	Ti I	4.99	24.4
4453.32	0.029	3.96	-1.933	Fe I	7.52	10.9
4453.7	0.035	1.87	-0.01	Ti I	4.99	13.5
4454.38	0.231	2.83	-1.25	Fe I	7.52	88.3
4454.78	0.379	1.9	0.252	Ca I	6.36	144.9
4455.01	0.071	3.07	-0.393	Mn I	5.39	27.3
4455.03	0.132	3.88	-1.09	Fe I	7.52	50.5
4455.27	0.027	6.22	-2.143	Fe II	7.52	10.5
4455.31	0.091	3.07	-0.246	Mn I	5.39	34.8
4455.32	0.069	1.44	0	Ti I	4.99	26.2
4455.62	0.029	4.55	-1.463	Fe I	7.52	11
4455.81	0.058	3.07	-0.51	Mn I	5.39	22.2
4455.89	0.267	1.9	-0.51	Ca I	6.36	102
4456.33	0.071	3.04	-2.17	Fe I	7.52	27.3
4456.62	0.09	1.9	-1.66	Ca I	6.36	34.4
4456.63	0.053	3.88	-1.68	Fe I	7.52	20.3
4456.65	0.07	3.12	-1.408	Ti II	4.99	26.7
4457.04	0.053	3.07	-0.555	Mn I	5.39	20.4
4457.43	0.091	1.46	0.18	Ti I	4.99	34.7
4457.43	0.048	1.18	-0.8	Zr II	2.618.3	
4457.55	0.109	3.07	-0.117	Mn I	5.39	41.8
4458.08	0.125	3.88	-1.136	Fe I	7.52	47.8
4458.25	0.135	3.07	0.042	Mn I	5.39	51.4
4458.51	0.044	3.55	-0.05	Cr I	5.67	16.7
4458.54	0.052	3.01	-0.38	Cr I	5.67	19.7
4459.03	0.201	3.3	-0.18	Ni I	6.25	76.7
4459.12	0.293	2.17	-1.279	Fe I	7.52	112
4459.35	0.059	4.17	-1.395	Fe I	7.52	22.4
4459.73	0.03	3.01	-0.65	Cr I	5.67	11.6
4459.75	0.023	0.29	-0.5	V I	4 8.7	
4460.21	0.035	0.48	0.171	Ce II	1.55	13.2
4460.29	0.046	0.3	-0.15	V I	4 17.4	
4460.37	0.021	3.07	-1.006	Mn I	5.39	8.2
4460.68	0.023	4.6	-1.538	Fe I	7.52	8.8
4461.08	0.073	3.07	-0.38	Mn I	5.39	27.9
4461.2	0.106	3.02	-1.944	Fe I	7.52	40.6

4461.25	0.03	1.01	-1.176	Zr II	2.611.5	
4461.37	0.02	3.41	-2.523	Fe I	7.52	7.8
4461.44	0.118	2.58	-4.114	Fe II	7.52	45.1
4461.65	0.27	0.09	-3.21	Fe I	7.52	103
4461.71	0.034	6.22	-2.046	Fe II	7.52	12.8
4461.97	0.149	3.6	-1.207	Fe I	7.52	56.9
4461.99	0.108	3.07	-1.889	Fe I	7.52	41.3
4462.03	0.178	3.07	0.32	Mn I	5.39	67.8
4462.45	0.126	3.46	-0.55	Ni I	6.25	48.2
4462.98	0.028	0.56	0.07	Nd II	1.510.7	
4463.4	0.022	4.25	-1.821	Fe I	7.52	8.5
4463.53	0.02	1.89	-0.27	Ti I	4.99	7.7
4464.45	0.214	1.16	-2.08	Ti II	4.99	81.6
4464.68	0.131	2.92	-0.104	Mn I	5.39	50
4464.77	0.132	3.02	-1.78	Fe I	7.52	50.3
4465.81	0.032	1.74	-0.163	Ti I	4.99	12.2
4466.55	0.313	2.83	-0.59	Fe I	7.52	119.6
4466.57	0.082	0.11	-4.464	Fe I	7.52	31.2
4466.94	0.087	3.93	-1.35	Fe I	7.52	33.4
4468.51	0.412	1.13	-0.6	Ti II	4.99	157.3
4469.14	0.22	1.08	-2.099	Ti II	4.99	83.9
4469.38	0.275	3.65	-0.26	Fe I	7.52	104.9
4469.54	0.025	2.96	-0.335	Co I	4.92	9.4
4469.69	0.034	4.55	-1.386	Fe I	7.52	12.9
4470.14	0.078	2.94	-0.444	Mn I	5.39	29.8
4470.47	0.17	3.4	-0.31	Ni I	6.25	65
4470.86	0.18	1.16	-2.28	Ti II	4.99	68.7
4471.24	0.037	1.73	-0.103	Ti I	4.99	14
4471.24	0.023	0.7	0.149	Ce II	1.55	8.7
4471.7	0.046	4.6	-1.197	Fe I	7.52	17.4
4472.7	0.027	3.64	-2.211	Fe I	7.52	10.3
4472.81	0.06	2.95	-0.583	Mn I	5.39	23
4472.93	0.192	2.84	-3.43	Fe II	7.52	73.2
4476.02	0.315	2.84	-0.57	Fe I	7.52	120.2
4476.08	0.267	3.68	-0.292	Fe I	7.52	102.1
4479.6	0.063	3.63	-1.78	Fe I	7.52	24
4479.61	0.079	3.68	-1.609	Fe I	7.52	30.1
4479.96	0.062	3.98	-1.52	Fe I	7.52	23.5
4480.14	0.089	3.04	-2.04	Fe I	7.52	33.9
4481.13	0.452	8.86	0.74	Mg II	7.58	172.6
4481.15	0.17	8.86	-0.56	Mg II	7.58	65.1
4481.26	0.051	1.75	0.08	Ti I	4.99	19.4
4481.32	0.407	8.86	0.59	Mg II	7.58	155.6
4481.61	0.105	3.68	-1.42	Fe I	7.52	40.1
4482.17	0.23	0.11	-3.501	Fe I	7.52	87.8
4482.25	0.264	2.22	-1.482	Fe I	7.52	100.7
4482.74	0.12	3.65	-1.35	Fe I	7.52	45.7
4483.91	0.02	4.58	-1.614	Fe I	7.52	7.7

4484.22	0.22	3.6	-0.72	Fe I	7.52	84
4485.03	0.021	4.58	-1.605	Fe I	7.52	7.9
4485.68	0.167	3.68	-1.02	Fe I	7.52	63.8
4485.72	0.045	4.58	-1.22	Fe I	7.52	17.3
4487.25	0.041	4.54	-1.298	Fe I	7.52	15.7
4487.69	0.036	4.95	-2.22	Si I	7.55	13.7
4488.05	0.022	4.2	0.12	Cr I	5.67	8.4
4488.13	0.073	3.6	-1.72	Fe I	7.52	28
4488.33	0.159	3.12	-0.82	Ti II	4.99	60.6
4488.91	0.056	3.65	-1.831	Fe I	7.52	21.4
4489.09	0.036	1.74	-0.106	Ti I	4.99	13.8
4489.18	0.025	8.43	-0.726	Ca II	6.36	9.7
4489.18	0.033	8.43	-0.613	Ca II	6.36	12.5
4489.18	0.256	2.83	-2.97	Fe II	7.52	97.7
4489.46	0.034	3.55	-0.173	Cr I	5.67	12.9
4489.74	0.159	0.12	-3.966	Fe I	7.52	60.8
4490.08	0.163	3.02	-1.58	Fe I	7.52	62.2
4490.09	0.068	2.95	-0.522	Mn I	5.39	25.8
4490.54	0.025	3.89	-0.08	Cr I	5.67	9.4
4490.76	0.141	3.94	-0.99	Fe I	7.52	53.8
4490.81	0.042	3.94	-1.752	Fe I	7.52	16.2
4491.4	0.287	2.85	-2.7	Fe II	7.52	109.6
4492.31	0.029	3.37	-0.392	Cr I	5.67	11
4492.68	0.049	3.98	-1.65	Fe I	7.52	18.6
4493.51	0.117	1.08	-2.73	Ti II	4.99	44.8
4494.05	0.036	3.98	-1.81	Fe I	7.52	13.6
4494.18	0.025	2.1	-1.82	Na I	6.33	9.6
4494.56	0.309	2.2	-1.136	Fe I	7.52	118.2
4495.43	0.084	3.88	-1.422	Fe I	7.52	31.9
4495.45	0.023	1.18	-3.544	Ti II	4.99	8.6
4495.45	0.021	1.21	-1.2	Zr II	2.67.9	
4495.57	0.035	3.6	-2.12	Fe I	7.52	13.3
4495.95	0.069	3.65	-1.72	Fe I	7.52	26.2
4496.15	0.031	1.75	-0.18	Ti I	4.99	11.7
4496.85	0.179	0.94	-1.15	Cr I	5.67	68.3
4496.98	0.086	0.71	-0.86	Zr II	2.632.8	
4497.66	0.043	2.1	-1.56	Na I	6.33	16.5
4498.54	0.081	3.88	-1.442	Fe I	7.52	30.8
4498.72	0.02	2.91	-0.92	Cr I	5.67	7.7
4498.9	0.092	2.94	-0.343	Mn I	5.39	35.2
4499.4	0.03	4.59	-1.416	Fe I	7.52	11.6
4500.28	0.05	3.08	-0.35	Cr I	5.67	19
4500.35	0.065	1.08	-3.093	Ti II	4.99	24.9
4501.08	0.024	3.55	-0.335	Cr I	5.67	9.3
4501.27	0.395	1.11	-0.75	Ti II	4.99	150.9
4502.21	0.094	2.92	-0.345	Mn I	5.39	35.8
4502.59	0.023	3.57	-2.35	Fe I	7.52	8.6
4504.83	0.043	3.26	-2.27	Fe I	7.52	16.6

4505.93	0.041	4.95	-2.15	Si I	7.55	15.8
4506.74	0.039	1.13	-3.32	Ti II	4.99	14.8
4507.22	0.037	3.11	-2.469	Fe I	7.52	14.2
4508.29	0.347	2.85	-2.21	Fe II	7.52	132.6
4509.73	0.031	4.22	-1.69	Fe I	7.52	11.9
4511.05	0.023	3.94	-2.051	Fe I	7.52	8.8
4511.89	0.049	3.08	-0.343	Cr I	5.67	18.9
4512.39	0.043	4.55	-1.268	Fe I	7.52	16.4
4512.73	0.07	0.83	-0.48	Ti I	4.99	26.6
4514.18	0.087	3.04	-2.05	Fe I	7.52	33.4
4514.41	0.056	4.54	-1.131	Fe I	7.52	21.5
4515.34	0.315	2.84	-2.48	Fe II	7.52	120.2
4516.45	0.037	3.65	-2.051	Fe I	7.52	14
4517.52	0.115	3.07	-1.84	Fe I	7.52	44.1
4518.02	0.092	0.82	-0.325	Ti I	4.99	35
4518.33	0.147	1.08	-2.555	Ti II	4.99	56.3
4519.98	0.026	1.68	-2.88	Ni I	6.25	10
4520.22	0.304	2.81	-2.6	Fe II	7.52	116.1
4520.24	0.037	3.07	-2.5	Fe I	7.52	14.3
4521.32	0.021	4.23	-0.949	Ni I	6.25	8.2
4522.37	0.093	0	-0.2	La II	1.22	35.4
4522.63	0.373	2.84	-2.03	Fe II	7.52	142.3
4522.8	0.084	0.82	-0.39	Ti I	4.99	31.9
4523.4	0.042	3.65	-1.99	Fe I	7.52	15.9
4524.69	0.162	1.23	-2.343	Ti II	4.99	62
4524.93	0.034	2.51	-0.36	Ba II	2.13	13
4525.14	0.271	3.6	-0.34	Fe I	7.52	103.4
4525.24	0.027	1.08	-3.544	Ti II	4.99	10.2
4526.36	0.05	1.5	-0.134	Ti I	4.99	19
4526.45	0.132	2.54	-0.156	Cr I	5.67	50.4
4526.93	0.19	2.71	-0.43	Ca I	6.36	72.5
4527.3	0.074	0.81	-0.47	Ti I	4.99	28.1
4527.35	0.027	2.54	-1.07	Cr I	5.67	10.4
4528.5	0.053	2.27	-1.31	V II	4 20.3	
4528.61	0.353	2.17	-0.822	Fe I	7.52	134.8
4528.76	0.069	3.3	-1.991	Fe I	7.52	26.5
4528.82	0.043	3.02	-2.48	Fe I	7.52	16.3
4529.21	0.031	4.6	-1.395	Fe I	7.52	11.8
4529.47	0.167	1.57	-2.03	Ti II	4.99	63.9
4530.68	0.038	2.54	-0.91	Cr I	5.67	14.4
4530.74	0.113	2.54	-0.272	Cr I	5.67	43.3
4530.95	0.067	2.92	0.152	Co I	4.92	25.6
4531.15	0.257	1.48	-2.155	Fe I	7.52	98.1
4531.63	0.029	3.21	-2.511	Fe I	7.52	11.2
4531.64	0.031	3.63	-2.16	Fe I	7.52	11.7
4533.13	0.079	3.27	-1.94	Fe I	7.52	30.1
4533.24	0.215	0.85	0.476	Ti I	4.99	82.2
4533.97	0.38	1.24	-0.77	Ti II	4.99	145

4534.17	0.186	2.85	-3.47	Fe II	7.52	71
4534.78	0.188	0.83	0.28	Ti I	4.99	71.9
4535.14	0.033	2.54	-0.98	Cr I	5.67	12.6
4535.57	0.164	0.82	0.12	Ti I	4.99	62.5
4535.63	0.043	4.6	-1.235	Fe I	7.52	16.4
4535.7	0.097	2.54	-0.383	Cr I	5.67	36.9
4535.75	0.023	2.54	-1.16	Cr I	5.67	8.6
4535.92	0.133	0.82	-0.07	Ti I	4.99	50.9
4536.04	0.113	0.81	-0.2	Ti I	4.99	43.3
4539.6	0.038	4.04	-2.53	Cr II	5.67	14.4
4539.78	0.023	2.54	-1.15	Cr I	5.67	8.9
4540.5	0.083	2.54	-0.487	Cr I	5.67	31.6
4540.7	0.093	3.1	0.028	Cr I	5.67	35.5
4541.06	0.024	2.54	-1.14	Cr I	5.67	9
4541.52	0.243	2.85	-3.05	Fe II	7.52	92.9
4542.41	0.038	3.64	-2.05	Fe I	7.52	14.4
4544.03	0.151	1.24	-2.4	Ti II	4.99	57.5
4544.61	0.07	2.54	-0.582	Cr I	5.67	26.7
4544.69	0.067	0.82	-0.52	Ti I	4.99	25.5
4545.13	0.248	1.13	-1.869	Ti II	4.99	94.7
4545.75	0.022	3.23	-2.637	Fe I	7.52	8.3
4545.95	0.143	0.94	-1.37	Cr I	5.67	54.8
4546.92	0.087	4.16	-0.271	Ni I	6.25	33.2
4547.02	0.036	1.56	-3.73	Fe I	7.52	13.8
4547.22	0.034	3.63	-1.202	Ni I	6.25	12.9
4547.85	0.218	3.54	-0.78	Fe I	7.52	83.4
4548.76	0.088	0.82	-0.354	Ti I	4.99	33.6
4549.19	0.07	5.91	-1.87	Fe II	7.52	26.8
4549.47	0.051	3.88	-1.705	Fe I	7.52	19.5
4549.47	0.417	2.83	-1.75	Fe II	7.52	159.2
4549.62	0.384	1.58	-0.45	Ti II	4.99	146.7
4549.65	0.021	3.06	-0.328	Co I	4.92	8
4549.81	0.173	1.18	-2.321	Ti II	4.99	66
4551.22	0.028	4.16	-0.88	Ni I	6.25	10.7
4551.65	0.023	3.94	-2.06	Fe I	7.52	8.7
4552.29	0.034	1.11	-3.4	Ti II	4.99	13
4552.45	0.088	0.83	-0.34	Ti I	4.99	33.8
4554.03	0.358	0	0.17	Ba II	2.13	136.8
4554.99	0.188	4.07	-1.38	Cr II	5.67	71.9
4555.08	0.025	3.1	-0.667	Cr I	5.67	9.7
4555.48	0.068	0.85	-0.488	Ti I	4.99	26.1
4555.89	0.341	2.83	-2.29	Fe II	7.52	130.3
4556.13	0.211	3.6	-0.787	Fe I	7.52	80.7
4558.65	0.284	4.07	-0.66	Cr II	5.67	108.4
4558.78	0.041	4.07	-2.462	Cr II	5.67	15.6
4560.09	0.051	3.6	-1.92	Fe I	7.52	19.6
4561.39	0.023	4.34	-3.02	Mg I	7.58	8.6
4562.36	0.029	0.48	0.081	Ce II	1.55	11.2

4563.76	0.357	1.22	-0.96	Ti II	4.99	136.4
4564.59	0.041	2.27	-1.45	V II	4 15.8	
4565.31	0.027	3.27	-2.51	Fe I	7.52	10.2
4565.5	0.047	0.98	-2.05	Cr I	5.67	17.9
4565.58	0.029	3.01	-0.22	Co I	4.92	11
4565.66	0.047	3.24	-2.25	Fe I	7.52	18.1
4565.74	0.081	4.04	-2.11	Cr II	5.67	30.9
4566.52	0.043	3.3	-2.25	Fe I	7.52	16.6
4566.99	0.05	3.41	-2.08	Fe I	7.52	19.2
4568.31	0.112	1.22	-2.65	Ti II	4.99	42.8
4568.76	0.025	3.26	-2.558	Fe I	7.52	9.4
4569.61	0.026	3.12	-0.64	Cr I	5.67	10
4571.1	0.103	0	-5.691	Mg I	7.58	39.4
4571.67	0.05	2.54	-0.77	Cr I	5.67	19.2
4571.97	0.376	1.57	-0.53	Ti II	4.99	143.6
4572.04	0.048	4.26	-0.536	Ni I	6.25	18.3
4574.22	0.03	3.21	-2.5	Fe I	7.52	11.6
4574.72	0.052	2.28	-2.97	Fe I	7.52	19.8
4576.34	0.247	2.84	-3.04	Fe II	7.52	94.5
4578.55	0.191	2.52	-0.56	Ca I	6.36	73.1
4580.05	0.1	0.94	-1.65	Cr I	5.67	38.2
4580.06	0.181	2.58	-3.725	Fe II	7.52	69.3
4580.45	0.09	1.23	-2.79	Ti II	4.99	34.3
4580.58	0.034	3.65	-2.09	Fe I	7.52	13.1
4581.4	0.227	2.52	-0.337	Ca I	6.36	86.7
4581.47	0.079	2.52	-1.26	Ca I	6.36	30.1
4581.51	0.098	3.24	-1.83	Fe I	7.52	37.5
4581.59	0.036	2.96	-0.152	Co I	4.92	13.9
4582.84	0.239	2.84	-3.1	Fe II	7.52	91.2
4583.41	0.108	1.16	-2.72	Ti II	4.99	41.4
4583.72	0.027	3.11	-2.632	Fe I	7.52	10.3
4583.84	0.38	2.81	-2.02	Fe II	7.52	145.2
4584	0.089	2.7	-4.216	Fe II	7.52	33.9
4584.6	0.158	4.54	-0.427	Fe I	7.52	60.4
4584.72	0.055	3.6	-1.888	Fe I	7.52	20.9
4585.34	0.082	4.6	-0.871	Fe I	7.52	31.5
4585.86	0.248	2.52	-0.186	Ca I	6.36	94.9
4585.96	0.078	2.52	-1.26	Ca I	6.36	29.8
4587.13	0.069	3.57	-1.78	Fe I	7.52	26.4
4588.2	0.289	4.07	-0.63	Cr II	5.67	110.2
4588.41	0.042	4.08	-0.745	Ni I	6.25	15.9
4589.9	0.027	4.07	-2.66	Cr II	5.67	10.5
4589.96	0.248	1.24	-1.79	Ti II	4.99	94.8
4591.39	0.084	0.97	-1.74	Cr I	5.67	31.9
4592.05	0.211	4.07	-1.22	Cr II	5.67	80.6
4592.52	0.145	3.54	-0.37	Ni I	6.25	55.2
4592.65	0.211	1.56	-2.449	Fe I	7.52	80.5
4593.37	0.02	4.6	-1.595	Fe I	7.52	7.8

4593.52	0.023	3.94	-2.06	Fe I	7.52	8.7
4594.12	0.024	0.07	-0.67	V I	4 9	
4595.36	0.107	3.3	-1.72	Fe I	7.52	40.7
4595.59	0.032	4.18	0.29	Cr I	5.67	12.4
4595.68	0.068	2.85	-4.255	Fe II	7.52	26
4596.02	0.049	6.22	-1.837	Fe II	7.52	18.9
4596.06	0.084	3.6	-1.64	Fe I	7.52	32.2
4596.38	0.045	4.09	-0.704	Ni I	6.25	17.2
4596.41	0.021	3.65	-2.32	Fe I	7.52	8.1
4597.38	0.031	4.55	-1.441	Fe I	7.52	11.7
4598.12	0.132	3.28	-1.57	Fe I	7.52	50.6
4598.32	0.041	0.96	-4.155	Fe I	7.52	15.8
4598.73	0.021	4.58	-1.606	Fe I	7.52	7.9
4600.1	0.022	2.54	-1.18	Cr I	5.67	8.3
4600.35	0.102	3.59	-0.61	Ni I	6.25	38.9
4600.75	0.154	1	-1.26	Cr I	5.67	59
4600.93	0.025	3.23	-2.57	Fe I	7.52	9.6
4601.02	0.02	2.54	-1.21	Cr I	5.67	7.8
4601.26	0.036	5.08	-2.12	Si I	7.55	13.9
4601.31	0.069	3.3	-2.003	Fe I	7.52	26.2
4601.38	0.047	2.89	-4.428	Fe II	7.52	18.1
4602	0.096	1.61	-3.154	Fe I	7.52	36.6
4602.94	0.284	1.48	-1.95	Fe I	7.52	108.4
4603.95	0.021	2.99	-2.84	Fe I	7.52	8.2
4604.78	0.023	4.23	-0.922	Ni I	6.25	8.8
4604.98	0.171	3.48	-0.25	Ni I	6.25	65.5
4606.22	0.053	3.59	-1	Ni I	6.25	20.4
4607.65	0.122	3.26	-1.652	Fe I	7.52	46.6
4609.26	0.041	1.18	-3.26	Ti II	4.99	15.8
4609.9	0.057	4.08	-0.58	Ni I	6.25	21.8
4611.28	0.223	3.65	-0.67	Fe I	7.52	85.3
4611.35	0.079	0.91	-3.837	Fe I	7.52	30.3
4613.2	0.116	3.29	-1.67	Fe I	7.52	44.4
4613.36	0.093	0.96	-1.68	Cr I	5.67	35.7
4614.2	0.02	3.3	-2.62	Fe I	7.52	7.8
4615.56	0.038	4.58	-1.319	Fe I	7.52	14.5
4615.73	0.026	4.59	-1.498	Fe I	7.52	9.9
4616.12	0.17	0.98	-1.19	Cr I	5.67	64.8
4616.6	0.069	4.59	-0.991	Fe I	7.52	26.4
4616.63	0.202	4.07	-1.29	Cr II	5.67	77.2
4617.27	0.09	1.75	0.389	Ti I	4.99	34.2
4617.86	0.062	4.1	-0.525	Ni I	6.25	23.6
4618.76	0.062	2.95	-2.34	Fe I	7.52	23.7
4618.8	0.229	4.07	-1.11	Cr II	5.67	87.3
4619.29	0.164	3.6	-1.12	Fe I	7.52	62.8
4619.53	0.036	2.98	-0.59	Cr I	5.67	13.9
4620.52	0.218	2.83	-3.28	Fe II	7.52	83.2
4621.96	0.034	2.54	-0.966	Cr I	5.67	13.1

4622.45	0.045	3.55	-0.04	Cr I	5.67	17.1
4623.1	0.056	1.74	0.11	Ti I	4.99	21.2
4625.05	0.174	3.24	-1.34	Fe I	7.52	66.5
4625.89	0.036	5.95	-2.202	Fe II	7.52	13.9
4626.17	0.149	0.97	-1.32	Cr I	5.67	56.9
4627.38	0.11	5.08	-1.52	Si I	7.55	42.2
4628.16	0.024	0.52	0.008	Ce II	1.55	9.1
4629.28	0.188	1.18	-2.24	Ti II	4.99	71.8
4629.34	0.029	1.73	-0.23	Ti I	4.99	11
4629.34	0.336	2.81	-2.37	Fe II	7.52	128.3
4629.36	0.029	3.05	-0.187	Co I	4.92	11.1
4630.12	0.098	2.28	-2.6	Fe I	7.52	37.4
4631.02	0.026	4.1	-0.957	Ni I	6.25	10.1
4632.82	0.041	3.65	-2	Fe I	7.52	15.8
4632.91	0.134	1.61	-2.913	Fe I	7.52	51.3
4634.07	0.209	4.07	-1.24	Cr II	5.67	79.8
4635.32	0.093	5.95	-1.65	Fe II	7.52	35.6
4635.85	0.062	2.84	-2.42	Fe I	7.52	23.7
4636.32	0.088	1.16	-2.855	Ti II	4.99	33.8
4637.5	0.161	3.28	-1.39	Fe I	7.52	61.4
4637.76	0.021	2.54	-1.208	Cr I	5.67	7.9
4638.01	0.163	3.6	-1.12	Fe I	7.52	62.4
4639.36	0.044	1.74	-0.015	Ti I	4.99	16.8
4639.51	0.025	3.11	-0.67	Cr I	5.67	9.6
4639.66	0.036	1.75	-0.112	Ti I	4.99	13.6
4639.94	0.031	1.73	-0.192	Ti I	4.99	11.9
4641.83	0.059	4.79	-0.924	Fe I	7.52	22.7
4643.46	0.131	3.65	-1.29	Fe I	7.52	49.9
4646.16	0.236	1.03	-0.7	Cr I	5.67	90
4647.18	0.036	4.63	-1.303	Fe I	7.52	13.7
4647.43	0.213	2.95	-1.31	Fe I	7.52	81.4
4648.23	0.021	2.84	-4.853	Fe II	7.52	8.2
4648.65	0.202	3.42	-0.1	Ni I	6.25	77
4648.94	0.079	2.58	-4.389	Fe II	7.52	30.2
4649.47	0.029	3.55	-0.257	Cr I	5.67	11.1
4651.28	0.125	0.98	-1.46	Cr I	5.67	47.9
4652.16	0.192	1	-1.03	Cr I	5.67	73.4
4653.49	0.021	0.99	-4.457	Fe I	7.52	8.1
4654.5	0.162	1.56	-2.783	Fe I	7.52	62
4654.61	0.171	3.6	-1.077	Fe I	7.52	65.2
4654.63	0.117	3.21	-1.73	Fe I	7.52	44.7
4655.77	0.068	1.16	-3.014	Ti II	4.99	26.1
4656.47	0.051	0	-1.345	Ti I	4.99	19.3
4656.98	0.158	2.89	-3.63	Fe II	7.52	60.3
4657.21	0.196	1.24	-2.15	Ti II	4.99	74.7
4657.59	0.024	2.84	-2.9	Fe I	7.52	9.3
4661.53	0.044	4.55	-1.27	Fe I	7.52	16.7
4661.97	0.047	2.99	-2.46	Fe I	7.52	18

4662.74	0.03	1.16	-3.429	Ti II	4.99	11.6
4663.18	0.021	3.54	-2.42	Fe I	7.52	8
4663.31	0.024	3.1	-0.71	Cr I	5.67	9
4663.4	0.023	3.13	-0.25	Co I	4.92	8.6
4663.71	0.064	2.89	-4.265	Fe II	7.52	24.6
4663.82	0.033	3.11	-0.543	Cr I	5.67	12.6
4664.78	0.036	3.12	-0.478	Cr I	5.67	13.9
4664.81	0.044	2.1	-1.55	Na I	6.33	16.9
4665.81	0.024	2.7	-4.918	Fe II	7.52	9.1
4666.48	0.034	3.14	-0.505	Cr I	5.67	12.8
4666.76	0.211	2.83	-3.33	Fe II	7.52	80.4
4666.98	0.04	3.79	-0.99	Ni I	6.25	15.4
4667.45	0.218	3.6	-0.751	Fe I	7.52	83.2
4667.59	0.065	0.02	-1.194	Ti I	4.99	24.8
4667.76	0.045	3.7	-1.008	Ni I	6.25	17.1
4668.06	0.077	3.68	-1.63	Fe I	7.52	29.5
4668.13	0.159	3.26	-1.416	Fe I	7.52	60.8
4668.56	0.071	2.1	-1.3	Na I	6.33	27.2
4669.17	0.112	3.65	-1.41	Fe I	7.52	42.8
4669.32	0.034	3.17	-0.486	Cr I	5.67	12.8
4670.18	0.122	2.58	-4.1	Fe II	7.52	46.7
4670.41	0.223	1.36	-0.37	Sc II	3.185.3	
4673.16	0.179	3.65	-0.98	Fe I	7.52	68.4
4673.27	0.137	3.65	-1.25	Fe I	7.52	52.5
4675.09	0.03	4.1	-1.811	Fe I	7.52	11.4
4678.85	0.231	3.6	-0.66	Fe I	7.52	88.2
4679.22	0.058	4.55	-1.115	Fe I	7.52	22.2
4679.23	0.049	3.37	-2.14	Fe I	7.52	18.6
4680.13	0.101	4	-0.815	Zn I	4.638.7	
4680.3	0.031	1.61	-3.774	Fe I	7.52	11.9
4680.47	0.034	2.86	-2.728	Fe I	7.52	13
4681.47	0.051	4.6	-1.147	Fe I	7.52	19.5
4681.91	0.078	0.05	-1.071	Ti I	4.99	29.6
4682.11	0.067	4.55	-1.035	Fe I	7.52	25.6
4682.32	0.054	0.41	-1.51	Y II	2.24	20.6
4683.56	0.052	2.83	-2.53	Fe I	7.52	20
4685.27	0.088	2.93	-0.88	Ca I	6.36	33.7
4686.1	0.035	3.65	-1.174	Ni I	6.25	13.3
4686.21	0.107	3.59	-0.58	Ni I	6.25	40.8
4687.3	0.03	0.96	-4.317	Fe I	7.52	11.5
4687.39	0.03	2.83	-2.81	Fe I	7.52	11.5
4688.18	0.073	4.6	-0.951	Fe I	7.52	27.8
4689.36	0.041	3.12	-0.42	Cr I	5.67	15.7
4690.14	0.071	3.68	-1.68	Fe I	7.52	27.2
4690.68	0.074	7.94	-2.09	C I	8.56	28.2
4691.33	0.025	1.07	-0.84	Ti I	4.99	9.4
4691.41	0.189	2.99	-1.45	Fe I	7.52	72.3
4691.57	0.026	7.94	-2.62	C I	8.56	9.8

4694.11	0.057	6.52	-1.77	S I	7.21	21.6
4695.44	0.043	6.52	-1.92	S I	7.21	16.3
4696.25	0.027	6.52	-2.14	S I	7.21	10.4
4697.05	0.022	2.71	-1.06	Cr I	5.67	8.3
4698.39	0.035	4.08	-0.84	Ni I	6.25	13.4
4698.46	0.052	3.14	-0.29	Cr I	5.67	19.7
4698.76	0.03	1.05	-0.76	Ti I	4.99	11.4
4700.16	0.027	4.32	-1.695	Fe I	7.52	10.3
4700.19	0.071	3.69	-1.68	Fe I	7.52	27
4701.05	0.043	3.68	-1.96	Fe I	7.52	16.3
4701.35	0.042	3.48	-1.22	Ni I	6.25	16.1
4701.53	0.08	4.08	-0.39	Ni I	6.25	30.6
4702.24	0.041	4.15	-0.715	Ni I	6.25	15.5
4702.91	0.041	3.23	-2.331	Fe I	7.52	15.8
4702.99	0.408	4.34	-0.666	Mg I	7.58	155.7
4703.8	0.079	3.65	-0.735	Ni I	6.25	30.1
4704.95	0.086	3.68	-1.57	Fe I	7.52	32.9
4705.46	0.026	3.54	-2.31	Fe I	7.52	10.1
4705.92	0.023	3.65	-1.387	Ni I	6.25	8.7
4706.76	0.024	5.08	-2.33	Si I	7.55	9
4707.27	0.214	3.24	-1.08	Fe I	7.52	81.7
4707.49	0.073	2.84	-2.34	Fe I	7.52	27.7
4708.01	0.099	3.17	0.11	Cr I	5.67	37.9
4708.66	0.187	1.24	-2.21	Ti II	4.99	71.6
4708.97	0.04	3.64	-2.033	Fe I	7.52	15.2
4709.09	0.171	3.65	-1.038	Fe I	7.52	65.4
4709.71	0.1	2.89	-0.34	Mn I	5.39	38.3
4710.18	0.024	2.17	0.028	Ti I	4.99	9.1
4710.28	0.16	3.02	-1.612	Fe I	7.52	61.3
4711.33	0.051	4.83	-0.982	Fe I	7.52	19.3
4713.19	0.02	2.78	-4.932	Fe II	7.52	7.8
4713.98	0.027	4.18	0.207	Cr I	5.67	10.5
4714.07	0.025	4.55	-1.54	Fe I	7.52	9.6
4714.36	0.021	4.6	-1.596	Fe I	7.52	7.9
4714.41	0.255	3.38	0.26	Ni I	6.25	97.4
4715.76	0.154	3.54	-0.32	Ni I	6.25	58.8
4715.89	0.025	4.15	-0.941	Ni I	6.25	9.7
4716.74	0.101	7.04	-0.938	Ca II	6.36	38.6
4718.42	0.093	3.19	0.09	Cr I	5.67	35.4
4719.52	0.041	1.24	-3.22	Ti II	4.99	15.7
4721	0.024	2.99	-2.801	Fe I	7.52	9
4721.02	0.125	7.04	-0.783	Ca II	6.36	47.8
4721.57	0.057	4.92	-2.02	Si I	7.55	21.7
4722.15	0.173	4.03	-0.338	Zn I	4.666	
4723	0.022	4.15	-1.006	Ni I	6.25	8.5
4723.1	0.027	3.08	-0.66	Cr I	5.67	10.4
4723.34	0.022	4.17	-2.705	Cr II	5.67	8.3
4724.12	0.025	4.16	-0.945	Ni I	6.25	9.4

4724.41	0.023	3.08	-0.733	Cr I	5.67	8.8
4727.15	0.031	3	-0.66	Cr I	5.67	11.8
4727.4	0.148	3.68	-1.162	Fe I	7.52	56.4
4727.46	0.079	2.92	-0.47	Mn I	5.39	30.1
4728.46	0.037	4.79	-1.172	Fe I	7.52	14.1
4728.55	0.133	3.65	-1.28	Fe I	7.52	50.8
4729.02	0.042	4.07	-1.66	Fe I	7.52	16.2
4729.68	0.024	3.39	-2.47	Fe I	7.52	9.2
4729.84	0.022	3.09	-0.76	Cr I	5.67	8.3
4730.03	0.063	4.34	-2.523	Mg I	7.58	23.9
4730.71	0.068	3.08	-0.192	Cr I	5.67	25.8
4731.45	0.201	2.89	-3.36	Fe II	7.52	76.7
4731.6	0.058	3.68	-1.794	Fe I	7.52	22.3
4731.79	0.051	3.83	-0.85	Ni I	6.25	19.3
4732.26	0.025	4.6	-1.502	Fe I	7.52	9.7
4732.46	0.059	4.1	-0.55	Ni I	6.25	22.6
4733.59	0.184	1.48	-2.71	Fe I	7.52	70.4
4734.1	0.036	4.29	-1.58	Fe I	7.52	13.6
4734.26	0.074	7.94	-2.09	C I	8.56	28.1
4735.84	0.092	4.07	-1.22	Fe I	7.52	35.1
4736.77	0.262	3.21	-0.74	Fe I	7.52	100.2
4737.35	0.078	3.08	-0.099	Cr I	5.67	29.9
4737.64	0.026	3.27	-2.54	Fe I	7.52	9.9
4738.46	0.044	7.94	-2.36	C I	8.56	16.8
4738.83	0.077	4.93	-1.85	Si I	7.55	29.3
4739.09	0.074	2.94	-0.49	Mn I	5.39	28.4
4740.34	0.029	3.02	-2.68	Fe I	7.52	11.2
4741.53	0.123	2.83	-2	Fe I	7.52	47
4742.56	0.021	7.94	-2.72	C I	8.56	7.9
4742.79	0.032	2.23	0.21	Ti I	4.99	12.2
4744.94	0.035	3.27	-2.388	Fe I	7.52	13.5
4745.8	0.135	3.65	-1.27	Fe I	7.52	51.7
4747.99	0.091	4.93	-1.75	Si I	7.55	34.8
4749.65	0.027	4.15	-1.831	Fe I	7.52	10.2
4749.67	0.023	3.05	-0.321	Co I	4.92	8.6
4749.95	0.038	4.55	-1.34	Fe I	7.52	14.6
4752.09	0.045	4.18	0.44	Cr I	5.67	17
4752.41	0.084	3.65	-0.7	Ni I	6.25	31.9
4754.04	0.214	2.28	-0.086	Mn I	5.39	81.8
4754.76	0.054	3.63	-0.97	Ni I	6.25	20.6
4755.73	0.036	5.39	-1.242	Mn II	5.39	13.6
4756.11	0.103	3.1	0.09	Cr I	5.67	39.4
4756.51	0.17	3.48	-0.27	Ni I	6.25	64.8
4757.58	0.023	3.27	-2.585	Fe I	7.52	8.9
4758.12	0.048	2.25	0.425	Ti I	4.99	18.2
4758.98	0.024	4.95	-2.43	Si I	7.55	9
4759.27	0.056	2.25	0.514	Ti I	4.99	21.3
4761.51	0.124	2.95	-0.138	Mn I	5.39	47.3

4762.31	0.061	7.47	-2.53	C I	8.56	23.2
4762.37	0.218	2.89	0.425	Mn I	5.39	83.2
4762.53	0.071	7.48	-2.445	C I	8.56	27.1
4762.63	0.045	1.93	-2.42	Ni I	6.25	17.2
4762.78	0.124	1.08	-2.71	Ti II	4.99	47.3
4763.88	0.15	1.22	-2.447	Ti II	4.99	57.2
4763.94	0.066	3.65	-0.842	Ni I	6.25	25.3
4764.29	0.028	3.55	-0.28	Cr I	5.67	10.7
4764.53	0.094	1.24	-2.77	Ti II	4.99	35.8
4764.73	0.029	5.39	-1.351	Mn II	5.39	10.9
4765.85	0.135	2.94	-0.08	Mn I	5.39	51.4
4766.42	0.165	2.92	0.1	Mn I	5.39	63.2
4766.67	0.09	7.48	-2.309	C I	8.56	34.3
4766.87	0.033	3.41	-2.31	Fe I	7.52	12.5
4768.32	0.156	3.68	-1.115	Fe I	7.52	59.5
4768.4	0.05	2.94	-2.471	Fe I	7.52	19.1
4770.03	0.042	7.48	-2.722	C I	8.56	15.9
4771.74	0.121	7.48	-2.12	C I	8.56	46.3
4772.8	0.145	1.56	-2.897	Fe I	7.52	55.5
4772.83	0.074	3.02	-2.192	Fe I	7.52	28.3
4772.86	0.024	3.7	-1.333	Ni I	6.25	9
4775.9	0.114	7.48	-2.163	C I	8.56	43.4
4776.38	0.062	4.55	-1.083	Fe I	7.52	23.7
4779.44	0.033	3.41	-2.31	Fe I	7.52	12.5
4779.98	0.216	2.05	-1.37	Ti II	4.99	82.4
4782.99	0.022	4.95	-2.47	Si I	7.55	8.3
4783.43	0.231	2.3	0.042	Mn I	5.39	88.2
4783.8	0.029	7.94	-2.56	C I	8.56	11.1
4785.96	0.022	4.14	-1.93	Fe I	7.52	8.5
4786.53	0.195	3.42	-0.16	Ni I	6.25	74.4
4786.58	0.031	1.03	-1.29	Y II	2.24	11.8
4786.81	0.165	3.02	-1.59	Fe I	7.52	63.1
4787.83	0.025	3	-2.77	Fe I	7.52	9.6
4788.76	0.103	3.23	-1.81	Fe I	7.52	39.4
4789.34	0.102	2.54	-0.366	Cr I	5.67	38.8
4789.58	0.086	4.47	-0.958	Fe I	7.52	32.9
4789.65	0.214	3.54	-0.84	Fe I	7.52	81.7
4791.25	0.027	3.27	-2.51	Fe I	7.52	10.5
4792.21	0.029	4.93	-2.35	Si I	7.55	11.2
4792.32	0.103	4.95	-1.66	Si I	7.55	39.2
4792.43	0.034	1.24	-3.328	Ti II	4.99	12.9
4792.51	0.049	3.11	-0.35	Cr I	5.67	18.7
4792.85	0.027	3.25	-0.067	Co I	4.92	10.5
4798.27	0.045	4.18	-1.55	Fe I	7.52	17.1
4798.52	0.173	1.08	-2.43	Ti II	4.99	66
4799.41	0.027	3.64	-2.23	Fe I	7.52	10.3
4799.97	0.034	8.43	-0.582	Ca II	6.36	12.9
4799.97	0.043	8.43	-0.469	Ca II	6.36	16.5

4800.13	0.025	3.04	-2.74	Fe I	7.52	9.6
4800.55	0.126	3.3	-1.606	Fe I	7.52	48.2
4800.65	0.08	4.14	-1.26	Fe I	7.52	30.4
4801.02	0.071	3.12	-0.131	Cr I	5.67	27.3
4801.77	0.025	4.83	-1.343	Fe I	7.52	9.4
4802.88	0.023	3.69	-2.27	Fe I	7.52	8.6
4802.88	0.099	3.64	-1.514	Fe I	7.52	38
4805.09	0.253	2.06	-1.1	Ti II	4.99	96.6
4805.32	0.045	4.73	-1.118	Fe I	7.52	17.3
4805.41	0.024	2.34	0.15	Ti I	4.99	9
4806.98	0.09	3.68	-0.64	Ni I	6.25	34.3
4807.71	0.044	3.37	-2.2	Fe I	7.52	16.8
4808.87	0.02	3.7	-1.41	Ni I	6.25	7.7
4809.14	0.02	3.69	-2.325	Fe I	7.52	7.7
4810.53	0.196	4.08	-0.137	Zn I	4.675	
4812.34	0.151	3.86	-1.8	Cr II	5.67	57.8
4813.47	0.037	3.21	0.05	Co I	4.92	14.1
4815.22	0.068	7.94	-2.13	C I	8.56	26
4815.48	0.039	7.94	-2.42	C I	8.56	14.8
4817.58	0.067	4.95	-1.91	Si I	7.55	25.5
4817.81	0.036	4.15	-0.77	Ni I	6.25	13.9
4818.05	0.151	4.95	-1.38	Si I	7.55	57.7
4820.41	0.028	1.5	-0.441	Ti I	4.99	10.6
4821.12	0.031	4.15	-0.85	Ni I	6.25	11.9
4822.33	0.027	4.73	-1.383	Fe I	7.52	10.2
4823.3	0.047	0.99	-1.11	Y II	2.24	18
4823.52	0.243	2.32	0.144	Mn I	5.39	92.8
4824.13	0.238	3.87	-1.22	Cr II	5.67	90.9
4824.16	0.022	3.63	-2.329	Fe I	7.52	8.5
4825.74	0.033	2.63	-4.829	Fe II	7.52	12.5
4826.8	0.024	7.48	-2.98	C I	8.56	9.3
4829.02	0.154	3.54	-0.33	Ni I	6.25	58.9
4829.37	0.048	2.54	-0.81	Cr I	5.67	18.2
4831.17	0.148	3.6	-0.32	Ni I	6.25	56.4
4832.68	0.026	4.3	-1.733	Fe I	7.52	9.9
4832.69	0.042	3.79	-0.979	Ni I	6.25	16.2
4832.73	0.052	3.64	-1.897	Fe I	7.52	20
4833.2	0.035	2.65	-4.78	Fe II	7.52	13.4
4835.87	0.056	4.1	-1.5	Fe I	7.52	21.4
4836.23	0.084	3.85	-2.25	Cr II	5.67	32
4838.51	0.066	3.41	-1.95	Fe I	7.52	25.1
4838.64	0.089	4.16	-0.27	Ni I	6.25	34
4839.54	0.099	3.27	-1.82	Fe I	7.52	37.8
4839.89	0.024	4.73	-1.446	Fe I	7.52	9
4840	0.026	2.67	-4.9	Fe II	7.52	10.1
4880.52	0.033	4.07	-1.796	Fe I	7.52	12.6
4881.56	0.025	0.07	-0.66	V I	4 9.7	
4881.72	0.101	3.3	-1.781	Fe I	7.52	38.5

4882.14	0.108	3.41	-1.64	Fe I	7.52	41.4
4883.68	0.205	1.08	0.07	Y II	2.24	78.2
4884.61	0.109	3.85	-2.08	Cr II	5.67	41.6
4885.08	0.073	1.89	0.358	Ti I	4.99	27.8
4885.43	0.135	3.88	-1.095	Fe I	7.52	51.5
4885.77	0.029	2.54	-1.055	Cr I	5.67	11.2
4886.33	0.166	4.15	-0.685	Fe I	7.52	63.4
4886.98	0.041	3.63	-1.12	Ni I	6.25	15.6
4887.01	0.108	3.08	0.1	Cr I	5.67	41.1
4887.19	0.117	4.19	-0.964	Fe I	7.52	44.8
4888.52	0.025	2.54	-1.127	Cr I	5.67	9.6
4888.64	0.023	4.1	-1.938	Fe I	7.52	8.9
4888.94	0.028	7.48	-2.91	C I	8.56	10.7
4889	0.119	2.2	-2.548	Fe I	7.52	45.4
4889.1	0.104	3.88	-1.292	Fe I	7.52	39.7
4890.65	0.053	7.48	-2.59	C I	8.56	20.4
4890.76	0.341	2.87	-0.43	Fe I	7.52	130.2
4891.05	0.051	4.07	-1.571	Fe I	7.52	19.5
4891.15	0.097	4.14	-1.135	Fe I	7.52	37.2
4891.49	0.387	2.85	-0.14	Fe I	7.52	147.9
4892.86	0.069	4.21	-1.29	Fe I	7.52	26.5
4893.82	0.051	2.83	-4.45	Fe II	7.52	19.6
4894.56	0.05	4.14	-1.529	Fe I	7.52	19.1
4896.44	0.026	3.88	-2.05	Fe I	7.52	10.1
4899.91	0.062	1.88	0.26	Ti I	4.99	23.6
4899.91	0.025	0	-0.94	La II	1.22	9.6
4899.93	0.045	2.72	-0.08	Ba II	2.13	17
4900.12	0.188	1.03	-0.09	Y II	2.24	71.8
4901.62	0.027	6.48	-0.826	Cr II	5.67	10.5
4902.23	0.04	4.55	-1.319	Fe I	7.52	15.4
4903.23	0.027	2.54	-1.1	Cr I	5.67	10.2
4903.31	0.254	2.88	-1.08	Fe I	7.52	97.2
4904.41	0.179	3.54	-0.17	Ni I	6.25	68.3
4905.13	0.025	3.93	-2.05	Fe I	7.52	9.4
4907.32	0.038	4.14	-1.666	Fe I	7.52	14.6
4907.73	0.078	3.43	-1.84	Fe I	7.52	29.8
4907.97	0.045	4.18	-1.547	Fe I	7.52	17.3
4908.03	0.057	4.21	-1.396	Fe I	7.52	21.9
4909.38	0.094	3.93	-1.327	Fe I	7.52	35.9
4910.01	0.02	4.14	-1.972	Fe I	7.52	7.8
4910.02	0.109	3.39	-1.647	Fe I	7.52	41.6
4910.32	0.195	4.19	-0.465	Fe I	7.52	74.6
4910.56	0.197	4.21	-0.435	Fe I	7.52	75.2
4911.19	0.239	3.12	-0.34	Ti II	4.99	91.2
4911.78	0.042	3.93	-1.79	Fe I	7.52	16
4912.02	0.062	3.77	-0.8	Ni I	6.25	23.6
4912.46	0.021	6.48	-0.948	Cr II	5.67	8.2
4913.61	0.052	1.87	0.16	Ti I	4.99	19.7

4913.97	0.085	3.74	-0.63	Ni I	6.25	32.5
4915.85	0.039	4.14	-1.663	Fe I	7.52	14.8
4917.23	0.086	4.19	-1.18	Fe I	7.52	32.9
4918.01	0.06	4.23	-1.36	Fe I	7.52	23.1
4918.36	0.132	3.84	-0.24	Ni I	6.25	50.4
4918.71	0.064	3.77	-0.78	Ni I	6.25	24.5
4918.95	0.218	4.15	-0.342	Fe I	7.52	83.3
4918.99	0.352	2.86	-0.37	Fe I	7.52	134.4
4920.23	0.053	3.88	-2.488	Cr II	5.67	20.4
4920.5	0.426	2.83	0.06	Fe I	7.52	162.8
4920.98	0.031	0.13	-0.73	La II	1.22	12
4921.76	0.023	2.17	-0.01	Ti I	4.99	8.7
4921.78	0.028	0.24	-0.68	La II	1.22	10.8
4922.27	0.133	3.1	0.27	Cr I	5.67	50.7
4923.93	0.508	2.89	-1.32	Fe II	7.52	194.2
4924.3	0.021	4.79	-1.46	Fe I	7.52	7.9
4924.77	0.162	2.28	-2.22	Fe I	7.52	61.8
4924.92	0.028	2.84	-4.749	Fe II	7.52	10.6
4925.56	0.076	3.65	-0.77	Ni I	6.25	29.1
4926.43	0.043	8.53	-1.974	C I	8.56	16.3
4927.42	0.049	3.57	-1.99	Fe I	7.52	18.7
4928.34	0.027	2.15	0.05	Ti I	4.99	10.2
4930.27	0.02	4.18	-1.948	Fe I	7.52	7.7
4930.31	0.088	3.96	-1.35	Fe I	7.52	33.6
4932.05	0.139	7.68	-1.884	C I	8.56	52.9
4933.29	0.037	3.3	-2.345	Fe I	7.52	14.2
4933.34	0.17	4.23	-0.597	Fe I	7.52	65.1
4934.01	0.177	4.15	-0.614	Fe I	7.52	67.6
4934.08	0.333	0	-0.15	Ba II	2.13	127.2
4934.08	0.041	3.3	-2.3	Fe I	7.52	15.5
4935.83	0.103	3.94	-0.35	Ni I	6.25	39.2
4936.34	0.05	3.11	-0.34	Cr I	5.67	19.1
4937.29	0.042	4.14	-1.617	Fe I	7.52	16.1
4937.34	0.137	3.6	-0.39	Ni I	6.25	52.5
4938.17	0.14	3.94	-1.018	Fe I	7.52	53.4
4938.81	0.256	2.87	-1.077	Fe I	7.52	97.9
4939.24	0.046	4.21	-1.51	Fe I	7.52	17.7
4939.24	0.097	4.15	-1.13	Fe I	7.52	37.1
4939.69	0.17	0.86	-3.34	Fe I	7.52	64.8
4942.46	0.056	4.22	-1.409	Fe I	7.52	21.4
4942.5	0.032	0.94	-2.294	Cr I	5.67	12.4
4945.44	0.057	3.79	-0.82	Ni I	6.25	21.9
4945.64	0.047	4.21	-1.51	Fe I	7.52	18
4946.03	0.023	3.79	-1.29	Ni I	6.25	8.6
4946.39	0.188	3.37	-1.17	Fe I	7.52	71.7
4947.61	0.067	5.08	-1.82	Si I	7.55	25.4
4950.11	0.104	3.41	-1.67	Fe I	7.52	39.6
4953.2	0.092	3.74	-0.58	Ni I	6.25	35.2

4953.99	0.021	5.57	-2.757	Fe II	7.52	8.1
4954.81	0.053	3.12	-0.3	Cr I	5.67	20.3
4957.3	0.358	2.85	-0.342	Fe I	7.52	136.6
4957.6	0.443	2.81	0.127	Fe I	7.52	169.3
4957.68	0.216	4.19	-0.327	Fe I	7.52	82.4
4961.91	0.024	3.63	-2.29	Fe I	7.52	9.3
4961.96	0.034	4.18	-1.698	Fe I	7.52	12.9
4962.57	0.073	4.17	-1.29	Fe I	7.52	27.9
4965.17	0.065	3.79	-0.753	Ni I	6.25	24.8
4966.09	0.233	3.33	-0.89	Fe I	7.52	88.8
4967.9	0.185	4.19	-0.534	Fe I	7.52	70.8
4968.39	0.061	4.22	-1.362	Fe I	7.52	23.3
4968.7	0.066	3.64	-1.78	Fe I	7.52	25.1
4969.92	0.155	4.21	-0.71	Fe I	7.52	59.3
4970.5	0.076	3.63	-1.7	Fe I	7.52	29
4970.65	0.027	3.96	-1.976	Fe I	7.52	10.5
4973.1	0.15	3.96	-0.95	Fe I	7.52	57.1
4975.34	0.02	2.5	0.2	Ti I	4.99	7.8
4976.13	0.034	3.6	-1.25	Ni I	6.25	12.8
4978.54	0.086	2.1	-1.21	Na I	6.33	32.7
4978.6	0.15	3.98	-0.93	Fe I	7.52	57.3
4978.69	0.211	4.07	-0.455	Fe I	7.52	80.7
4980.17	0.208	3.6	0.07	Ni I	6.25	79.6
4980.28	0.051	4.17	-1.498	Fe I	7.52	19.4
4980.54	0.078	4.18	-1.249	Fe I	7.52	29.9
4981.35	0.028	1.56	-3.16	Ti II	4.99	10.8
4981.73	0.227	0.85	0.504	Ti I	4.99	86.8
4982.13	0.031	1.03	-1.29	Y II	2.24	12
4982.5	0.295	4.1	0.164	Fe I	7.52	112.7
4982.81	0.021	2.1	-1.91	Na I	6.33	8.1
4982.81	0.127	2.1	-0.95	Na I	6.33	48.6
4983.25	0.251	4.15	-0.111	Fe I	7.52	95.7
4983.85	0.265	4.1	-0.05	Fe I	7.52	101.1
4984.11	0.226	3.79	0.35	Ni I	6.25	86.3
4985.25	0.212	3.93	-0.56	Fe I	7.52	80.8
4985.55	0.223	2.86	-1.331	Fe I	7.52	85.3
4986.22	0.058	4.21	-1.39	Fe I	7.52	22.3
4988.95	0.134	4.15	-0.89	Fe I	7.52	51.2
4989.14	0.02	1.98	-0.217	Ti I	4.99	7.8
4991.06	0.211	0.83	0.38	Ti I	4.99	80.4
4991.13	0.065	2.78	-4.365	Fe II	7.52	24.8
4991.27	0.165	4.19	-0.67	Fe I	7.52	62.9
4991.87	0.021	4.22	-1.91	Fe I	7.52	7.9
4993.36	0.17	2.81	-3.65	Fe II	7.52	64.8
4993.68	0.051	4.21	-1.47	Fe I	7.52	19.5
4993.75	0.043	4.18	-1.573	Fe I	7.52	16.6
4994.13	0.204	0.91	-3.08	Fe I	7.52	78
4995.41	0.02	4.26	-1.89	Fe I	7.52	7.7

4996.37	0.045	1.58	-2.915	Ti II	4.99	17.2
4996.84	0.054	3.63	-0.98	Ni I	6.25	20.7
4998.22	0.092	3.6	-0.69	Ni I	6.25	35.2
4999.11	0.031	4.18	-1.74	Fe I	7.52	11.9
4999.5	0.191	0.82	0.25	Ti I	4.99	73.1
5000.34	0.128	3.63	-0.43	Ni I	6.25	49
5000.74	0.032	2.78	-4.74	Fe II	7.52	12.2
5001.48	0.116	7.5	-0.517	Ca II	6.36	44.3
5001.86	0.297	3.88	0.01	Fe I	7.52	113.6
5002.58	0.141	4.18	-0.826	Fe I	7.52	53.8
5002.79	0.12	3.39	-1.58	Fe I	7.52	46
5003.73	0.033	1.68	-2.8	Ni I	6.25	12.6
5004.04	0.058	4.21	-1.4	Fe I	7.52	22.1
5004.63	0.06	4.14	-1.428	Fe I	7.52	23.1
5005.16	0.089	1.56	-2.55	Ti II	4.99	34
5005.71	0.275	3.88	-0.142	Fe I	7.52	105
5006.06	0.143	5.08	-1.33	Si I	7.55	54.6
5006.12	0.323	2.83	-0.615	Fe I	7.52	123.2
5007.21	0.169	0.82	0.112	Ti I	4.99	64.7
5007.27	0.244	4.1	-0.196	Fe I	7.52	93.3
5007.73	0.041	4.29	-1.519	Fe I	7.52	15.6
5010.02	0.044	3.77	-0.98	Ni I	6.25	16.9
5010.21	0.086	3.09	-1.336	Ti II	4.99	32.9
5010.93	0.066	3.63	-0.87	Ni I	6.25	25.2
5012.07	0.271	0.86	-2.642	Fe I	7.52	103.6
5012.16	0.122	4.19	-0.939	Fe I	7.52	46.7
5012.44	0.105	3.7	-0.53	Ni I	6.25	40
5012.44	0.169	4.14	-0.678	Fe I	7.52	64.6
5012.69	0.024	4.28	-1.79	Fe I	7.52	9.2
5013.28	0.025	2.02	-0.095	Ti I	4.99	9.5
5013.31	0.03	2.71	-0.92	Cr I	5.67	11.5
5013.33	0.021	3.09	-2.063	Ti II	4.99	8.1
5013.68	0.19	1.58	-1.935	Ti II	4.99	72.4
5014.19	0.067	0	-1.22	Ti I	4.99	25.6
5014.21	0.047	4.42	-0.441	Ni I	6.25	18
5014.28	0.17	0.81	0.11	Ti I	4.99	64.9
5014.94	0.254	3.94	-0.25	Fe I	7.52	97.1
5015.31	0.086	4.07	-1.272	Fe I	7.52	32.9
5016.03	0.058	4.91	-0.861	Fe I	7.52	22
5016.16	0.062	0.85	-0.574	Ti I	4.99	23.7
5016.48	0.031	4.25	-1.69	Fe I	7.52	11.8
5017.09	0.033	7.94	-2.5	C I	8.56	12.5
5017.57	0.203	3.54	-0.02	Ni I	6.25	77.7
5017.76	0.021	7.94	-2.7	C I	8.56	8.2
5018.1	0.085	7.94	-2	C I	8.56	32.5
5018.28	0.067	3.83	-0.703	Ni I	6.25	25.7
5018.44	0.538	2.89	-1.22	Fe II	7.52	205.3
5019.46	0.024	5.57	-2.697	Fe II	7.52	9.3

5019.97	0.16	7.51	-0.257	Ca II	6.36	61.1
5020.03	0.083	0.83	-0.414	Ti I	4.99	31.7
5021.14	0.034	7.51	-1.217	Ca II	6.36	12.8
5021.51	0.05	4.95	-0.901	Fe I	7.52	19.2
5021.59	0.156	4.25	-0.677	Fe I	7.52	59.5
5021.68	0.052	4.21	-1.461	Fe I	7.52	19.7
5021.94	0.059	3.27	-2.13	Fe I	7.52	22.6
5022.24	0.211	3.98	-0.53	Fe I	7.52	80.5
5022.79	0.078	2.99	-2.196	Fe I	7.52	29.9
5022.87	0.081	0.82	-0.434	Ti I	4.99	31.1
5023.19	0.036	4.28	-1.6	Fe I	7.52	13.6
5023.5	0.027	4.31	-1.71	Fe I	7.52	10.4
5023.85	0.04	7.94	-2.4	C I	8.56	15.3
5024.84	0.062	0.82	-0.602	Ti I	4.99	23.6
5024.92	0.021	7.94	-2.7	C I	8.56	8.2
5025.57	0.031	2.04	0.025	Ti I	4.99	11.8
5027.12	0.191	4.15	-0.53	Fe I	7.52	73
5027.23	0.054	3.64	-1.885	Fe I	7.52	20.8
5027.76	0.076	4.21	-1.25	Fe I	7.52	28.9
5028.13	0.171	3.57	-1.123	Fe I	7.52	65.5
5029.62	0.056	3.41	-2.05	Fe I	7.52	21.4
5031.02	0.247	1.36	-0.26	Sc II	3.194.4	
5031.91	0.027	4.37	-1.67	Fe I	7.52	10.3
5032.72	0.02	3.9	-1.27	Ni I	6.25	7.7
5035.36	0.236	3.63	0.29	Ni I	6.25	90
5035.9	0.108	1.46	0.26	Ti I	4.99	41.3
5035.97	0.157	3.65	-0.234	Ni I	6.25	59.8
5036.46	0.091	1.44	0.13	Ti I	4.99	34.6
5036.92	0.046	2.83	-4.52	Fe II	7.52	17.4
5038.4	0.076	1.43	0.013	Ti I	4.99	29
5038.59	0.136	3.83	-0.22	Ni I	6.25	52
5039.06	0.085	7.94	-2	C I	8.56	32.4
5039.1	0.05	7.94	-2.286	C I	8.56	19.1
5039.25	0.125	3.37	-1.573	Fe I	7.52	47.8
5039.35	0.039	3.63	-1.15	Ni I	6.25	14.9
5039.96	0.076	0.02	-1.13	Ti I	4.99	29
5040.13	0.032	7.94	-2.5	C I	8.56	12.4
5040.25	0.026	4.22	-1.791	Fe I	7.52	10.1
5040.77	0.026	7.94	-2.6	C I	8.56	10.1
5040.85	0.147	4.25	-0.731	Fe I	7.52	56.2
5040.91	0.18	4.28	-0.5	Fe I	7.52	68.8
5041.01	0.041	3.83	-0.973	Ni I	6.25	15.6
5041.07	0.198	0.96	-3.087	Fe I	7.52	75.6
5041.48	0.136	7.94	-1.7	C I	8.56	51.8
5041.62	0.193	2.71	-0.42	Ca I	6.36	73.8
5041.76	0.261	1.48	-2.203	Fe I	7.52	99.5
5041.8	0.032	7.94	-2.5	C I	8.56	12.4
5041.85	0.121	4.28	-0.872	Fe I	7.52	46.3

5042.18	0.102	3.65	-0.58	Ni I	6.25	39
5044.21	0.101	2.85	-2.15	Fe I	7.52	38.4
5048.06	0.037	3.83	-1.022	Ni I	6.25	14.2
5048.18	0.033	4.23	-1.674	Fe I	7.52	12.7
5048.23	0.029	3.84	-1.137	Ni I	6.25	11
5048.44	0.101	3.96	-1.26	Fe I	7.52	38.7
5048.84	0.11	3.84	-0.38	Ni I	6.25	42.1
5049.82	0.278	2.28	-1.42	Fe I	7.52	106
5051.28	0.09	4.22	-1.135	Fe I	7.52	34.3
5051.51	0.069	3.65	-0.836	Ni I	6.25	26.2
5051.64	0.246	0.91	-2.795	Fe I	7.52	93.9
5052.17	0.185	7.68	-1.648	C I	8.56	70.7
5054.64	0.033	3.64	-2.14	Fe I	7.52	12.7
5057.48	0.022	4.19	-1.905	Fe I	7.52	8.4
5057.98	0.029	3.63	-1.3	Ni I	6.25	11
5060.04	0.032	4.3	-1.643	Fe I	7.52	12.1
5064.65	0.093	0.05	-0.991	Ti I	4.99	35.4
5064.95	0.036	4.25	-1.618	Fe I	7.52	13.7
5065.02	0.236	4.25	-0.147	Fe I	7.52	90
5065.19	0.101	3.64	-1.513	Fe I	7.52	38.6
5067.15	0.114	4.22	-0.97	Fe I	7.52	43.7
5067.71	0.02	2.71	-1.114	Cr I	5.67	7.7
5068.77	0.23	2.94	-1.23	Fe I	7.52	88
5069.09	0.076	3.12	-1.39	Ti II	4.99	29.1
5069.42	0.042	4.29	-1.511	Fe I	7.52	16
5072.08	0.137	4.28	-0.774	Fe I	7.52	52.5
5072.28	0.176	3.12	-0.75	Ti II	4.99	67.4
5072.67	0.096	4.22	-1.091	Fe I	7.52	36.8
5074.75	0.233	4.22	-0.2	Fe I	7.52	88.8
5075.17	0.115	4.17	-0.998	Fe I	7.52	44.1
5076.26	0.145	4.3	-0.712	Fe I	7.52	55.5
5076.33	0.024	3.65	-1.38	Ni I	6.25	9.1
5078.98	0.197	4.3	-0.381	Fe I	7.52	75.2
5079.22	0.199	2.2	-2.067	Fe I	7.52	75.9
5079.74	0.174	0.99	-3.22	Fe I	7.52	66.5
5079.95	0.029	1.82	-2.75	Ni I	6.25	11
5080.53	0.241	3.65	0.33	Ni I	6.25	91.9
5081.11	0.215	3.84	0.3	Ni I	6.25	82.2
5082.34	0.109	3.65	-0.54	Ni I	6.25	41.6
5083.34	0.218	0.96	-2.958	Fe I	7.52	83.3
5084.09	0.195	3.68	0.03	Ni I	6.25	74.6
5084.51	0.024	4.53	-0.691	Ni I	6.25	9.1
5087.42	0.171	1.08	-0.17	Y II	2.24	65.4
5088.15	0.03	4.15	-1.78	Fe I	7.52	11.6
5088.53	0.04	3.84	-0.98	Ni I	6.25	15.1
5088.95	0.025	3.68	-1.34	Ni I	6.25	9.5
5090.77	0.198	4.25	-0.4	Fe I	7.52	75.8
5093.97	0.042	4.91	-1.027	Fe I	7.52	16.1

5094.41	0.033	3.83	-1.08	Ni I	6.25	12.7
5096.85	0.054	3.74	-0.9	Ni I	6.25	20.8
5097	0.226	4.28	-0.196	Fe I	7.52	86.2
5097.31	0.052	3.71	-2.64	Cr II	5.67	20
5098.1	0.033	4.91	-1.148	Fe I	7.52	12.6
5098.57	0.152	3.93	-0.957	Fe I	7.52	58.2
5098.7	0.206	2.17	-2.026	Fe I	7.52	78.8
5099.08	0.064	3.98	-1.53	Fe I	7.52	24.4
5099.32	0.125	3.65	-0.44	Ni I	6.25	47.7
5099.93	0.175	3.68	-0.1	Ni I	6.25	66.8
5100.66	0.063	2.81	-4.37	Fe II	7.52	23.9
5100.85	0.082	5.91	-1.778	Fe II	7.52	31.5
5102.65	0.041	4.18	-1.612	Fe I	7.52	15.5
5102.96	0.048	1.68	-2.62	Ni I	6.25	18.2
5104.03	0.02	3.02	-2.87	Fe I	7.52	7.8
5104.44	0.03	4.28	-1.69	Fe I	7.52	11.4
5105.54	0.097	1.39	-1.516	Cu I	4.21	36.9
5106.24	0.06	4.91	-0.838	Fe I	7.52	23
5107.45	0.195	0.99	-3.087	Fe I	7.52	74.5
5107.64	0.224	1.56	-2.418	Fe I	7.52	85.7
5109.65	0.104	4.3	-0.98	Fe I	7.52	39.6
5110.27	0.046	4.95	-0.951	Fe I	7.52	17.6
5110.36	0.133	3.57	-1.366	Fe I	7.52	50.8
5111.85	0.082	4.91	-0.661	Fe I	7.52	31.2
5112.3	0.036	1.66	-0.59	Zr II	2.613.9	
5115.16	0.023	4.95	-1.292	Fe I	7.52	8.7
5115.39	0.154	3.83	-0.11	Ni I	6.25	58.7
5116.04	0.033	4.14	-1.749	Fe I	7.52	12.6
5119.11	0.03	0.99	-1.36	Y II	2.24	11.4
5120.35	0.08	2.83	-4.214	Fe II	7.52	30.4
5120.41	0.027	2.58	0.38	Ti I	4.99	10.2
5121.56	0.033	3.94	-1.005	Ni I	6.25	12.5
5121.64	0.131	4.28	-0.81	Fe I	7.52	50.2
5123.21	0.081	0.99	-0.83	Y II	2.24	30.9
5123.72	0.195	1.01	-3.068	Fe I	7.52	74.6
5124.07	0.058	1.5	-0.082	Ti I	4.99	22.3
5124.72	0.042	4.91	-1.024	Fe I	7.52	16.2
5125.12	0.241	4.22	-0.14	Fe I	7.52	92.1
5125.23	0.09	3.68	-0.65	Ni I	6.25	34.5
5125.6	0.026	5.08	-2.29	Si I	7.55	10
5125.84	0.201	4.14	-0.478	Fe I	7.52	76.6
5126.19	0.094	4.25	-1.08	Fe I	7.52	35.9
5126.82	0.081	3.7	-0.702	Ni I	6.25	31
5127.36	0.17	0.91	-3.307	Fe I	7.52	64.8
5127.87	0.034	5.57	-2.535	Fe II	7.52	13
5129.15	0.237	1.89	-1.39	Ti II	4.99	90.6
5129.37	0.093	3.68	-0.63	Ni I	6.25	35.7
5129.63	0.037	3.94	-1.85	Fe I	7.52	14.1

5130.36	0.023	3.84	-1.25	Ni I	6.25	8.9
5130.59	0.024	1.3	0.57	Nd II	1.59.3	
5131.31	0.022	1.89	-3.015	Ti II	4.99	8.5
5131.47	0.117	2.22	-2.56	Fe I	7.52	44.5
5131.77	0.024	3.7	-1.351	Ni I	6.25	9.1
5132.67	0.087	2.81	-4.18	Fe II	7.52	33.2
5133.69	0.286	4.17	0.14	Fe I	7.52	109.4
5136.8	0.048	2.84	-4.49	Fe II	7.52	18.2
5137.07	0.132	1.68	-1.99	Ni I	6.25	50.6
5137.38	0.209	4.17	-0.4	Fe I	7.52	79.7
5139.25	0.288	3	-0.767	Fe I	7.52	110
5139.26	0.043	3.65	-1.097	Ni I	6.25	16.3
5139.46	0.321	2.94	-0.57	Fe I	7.52	122.6
5139.65	0.025	3.42	-0.46	Cr I	5.67	9.4
5141.74	0.156	2.42	-2.15	Fe I	7.52	59.4
5142.49	0.126	4.3	-0.831	Fe I	7.52	48
5142.54	0.236	4.25	-0.143	Fe I	7.52	90.3
5142.77	0.151	3.7	-0.231	Ni I	6.25	57.6
5142.93	0.077	3.7	-0.732	Ni I	6.25	29.4
5142.93	0.202	0.96	-3.067	Fe I	7.52	77.3
5145.09	0.038	2.2	-3.23	Fe I	7.52	14.5
5145.46	0.024	1.46	-0.574	Ti I	4.99	9
5146.13	0.124	2.83	-3.913	Fe II	7.52	47.5
5146.48	0.204	3.7	0.12	Ni I	6.25	78.1
5148.04	0.156	4.28	-0.657	Fe I	7.52	59.5
5148.23	0.215	4.25	-0.29	Fe I	7.52	82.2
5150.84	0.198	0.99	-3.07	Fe I	7.52	75.7
5150.94	0.05	2.85	-4.452	Fe II	7.52	19.2
5151.91	0.154	1.01	-3.322	Fe I	7.52	58.8
5153.23	0.071	3.78	0.217	Cu I	4.21	27.1
5153.4	0.03	2.1	-1.76	Na I	6.33	11.3
5153.5	0.044	3.75	-2.696	Cr II	5.67	16.9
5154.07	0.197	1.56	-1.92	Ti II	4.99	75.1
5154.1	0.053	3.88	-1.712	Fe I	7.52	20.3
5154.41	0.089	2.84	-4.136	Fe II	7.52	34
5155.1	0.049	8.64	-1.82	C I	8.56	18.8
5155.12	0.068	3.9	-0.65	Ni I	6.25	26.1
5155.76	0.15	3.9	-0.09	Ni I	6.25	57.1
5159.06	0.13	4.28	-0.82	Fe I	7.52	49.8
5159.92	0.024	8.64	-2.15	C I	8.56	9.2
5160.84	0.027	5.57	-2.641	Fe II	7.52	10.5
5161.18	0.048	2.85	-4.483	Fe II	7.52	18.2
5162.27	0.269	4.17	0.02	Fe I	7.52	102.8
5163.98	0.026	4.98	-1.213	Fe I	7.52	9.9
5164.55	0.046	4.43	-1.36	Fe I	7.52	17.4
5164.91	0.021	4.14	-1.976	Fe I	7.52	7.9
5165.41	0.257	4.22	-0.026	Fe I	7.52	98.2
5166.22	0.021	3.43	-0.518	Cr I	5.67	8.1

5166.28	0.149	0	-4.195	Fe I	7.52	56.8
5167.32	0.55	2.71	-1.03	Mg I	7.58	209.9
5167.49	0.389	1.48	-1.26	Fe I	7.52	148.6
5168.66	0.121	3.7	-0.43	Ni I	6.25	46.2
5168.9	0.18	0.05	-3.969	Fe I	7.52	68.6
5169.03	0.663	2.89	-0.87	Fe II	7.52	253.1
5169.3	0.23	4.07	-0.324	Fe I	7.52	88
5171.6	0.316	1.48	-1.793	Fe I	7.52	120.8
5171.64	0.063	2.81	-4.372	Fe II	7.52	23.9
5171.67	0.052	3.64	-1.912	Fe I	7.52	19.9
5172.68	0.791	2.71	-0.402	Mg I	7.58	302.3
5172.87	0.036	3.7	-1.147	Ni I	6.25	13.7
5172.99	0.023	5.91	-2.463	Fe II	7.52	8.9
5173.74	0.081	0	-1.118	Ti I	4.99	31
5176.56	0.096	3.9	-0.44	Ni I	6.25	36.6
5177.96	0.023	4.98	-1.275	Fe I	7.52	8.6
5180.06	0.052	4.47	-1.26	Fe I	7.52	19.9
5180.17	0.025	4.99	-1.228	Fe I	7.52	9.5
5183.41	0.022	0.4	-0.69	La II	1.22	8.4
5183.6	0.939	2.71	-0.18	Mg I	7.58	358.5
5183.71	0.037	1.89	-2.78	Ti II	4.99	14
5184.25	0.03	4.99	-1.146	Fe I	7.52	11.3
5184.27	0.103	4.28	-1	Fe I	7.52	39.3
5184.56	0.028	3.41	-0.41	Cr I	5.67	10.7
5184.56	0.065	3.7	-0.833	Ni I	6.25	24.8
5184.86	0.034	4.95	-1.104	Fe I	7.52	13
5185.91	0.245	1.89	-1.35	Ti II	4.99	93.6
5187.91	0.082	4.14	-1.26	Fe I	7.52	31.4
5188.68	0.303	1.58	-1.21	Ti II	4.99	115.9
5188.84	0.222	2.93	-0.09	Ca I	6.36	84.7
5191.45	0.313	3.04	-0.551	Fe I	7.52	119.7
5191.59	0.025	1.75	-0.712	Zr II	2.69.5	
5191.99	0.03	3.39	-0.39	Cr I	5.67	11.4
5192.34	0.336	3	-0.421	Fe I	7.52	128.3
5192.49	0.027	3.7	-1.29	Ni I	6.25	10.3
5192.97	0.095	0.02	-1.006	Ti I	4.99	36.4
5194.94	0.271	1.56	-2.09	Fe I	7.52	103.5
5195.47	0.263	4.22	0.018	Fe I	7.52	100.6
5196.06	0.18	4.25	-0.524	Fe I	7.52	68.8
5196.42	0.023	1.75	-0.88	Y II	2.24	8.6
5196.45	0.035	3.45	-0.27	Cr I	5.67	13.3
5196.56	0.029	3.45	-0.36	Cr I	5.67	11.1
5196.59	0.025	3.13	-0.93	Mn I	5.39	9.4
5197.16	0.024	3.9	-1.19	Ni I	6.25	9.1
5197.58	0.34	3.23	-2.1	Fe II	7.52	129.9
5197.94	0.032	4.3	-1.64	Fe I	7.52	12.2
5198.71	0.185	2.22	-2.135	Fe I	7.52	70.7
5200.41	0.121	0.99	-0.57	Y II	2.24	46.1

5202.26	0.021	4.25	-1.871	Fe I	7.52	8.2
5202.34	0.235	2.17	-1.838	Fe I	7.52	89.8
5204.51	0.32	0.94	-0.208	Cr I	5.67	122.3
5204.58	0.114	0.09	-4.332	Fe I	7.52	43.4
5205.72	0.153	1.03	-0.34	Y II	2.24	58.4
5206.04	0.351	0.94	0.019	Cr I	5.67	134.1
5206.09	0.108	2.49	1.07	Ti I	4.99	41.1
5208.43	0.371	0.94	0.158	Cr I	5.67	141.7
5208.59	0.233	3.24	-0.98	Fe I	7.52	88.8
5210.39	0.111	0.05	-0.884	Ti I	4.99	42.3
5210.86	0.027	3.75	-2.945	Cr II	5.67	10.3
5211.54	0.149	2.59	-1.356	Ti II	4.99	57
5214.61	0.023	4.29	-1.821	Fe I	7.52	8.6
5215.18	0.232	3.26	-0.967	Fe I	7.52	88.6
5216.27	0.257	1.61	-2.15	Fe I	7.52	98.3
5216.47	0.059	3.74	-0.86	Ni I	6.25	22.5
5217.39	0.211	3.21	-1.162	Fe I	7.52	80.5
5217.92	0.074	3.64	-1.719	Fe I	7.52	28.4
5218.2	0.103	3.81	0.476	Cu I	4.21	39.3
5220.21	0.083	4.18	-1.215	Fe I	7.52	31.7
5220.28	0.024	3.74	-1.31	Ni I	6.25	9.2
5223.18	0.02	3.63	-2.39	Fe I	7.52	7.7
5224.31	0.039	2.13	0.21	Ti I	4.99	15
5224.93	0.049	3.45	-0.096	Cr I	5.67	18.7
5225.02	0.025	3.43	-0.441	Cr I	5.67	9.7
5225.53	0.051	0.11	-4.789	Fe I	7.52	19.4
5226.54	0.292	1.56	-1.3	Ti II	4.99	111.4
5226.86	0.313	3.04	-0.555	Fe I	7.52	119.4
5226.9	0.069	4.29	-1.246	Fe I	7.52	26.2
5227.15	0.273	2.42	-1.355	Fe I	7.52	104.1
5227.19	0.387	1.56	-1.228	Fe I	7.52	147.8
5227.5	0.042	5.03	-0.935	Fe I	7.52	16.2
5228.38	0.07	4.22	-1.29	Fe I	7.52	26.8
5229.85	0.206	3.28	-1.136	Fe I	7.52	78.5
5229.87	0.227	4.22	-0.241	Fe I	7.52	86.7
5232.5	0.084	4.07	-2.093	Cr II	5.67	32.1
5232.94	0.377	2.94	-0.19	Fe I	7.52	144
5234.62	0.35	3.22	-2.05	Fe II	7.52	133.5
5235.39	0.133	4.07	-0.967	Fe I	7.52	50.9
5235.49	0.033	3.9	-1.032	Ni I	6.25	12.7
5236.2	0.033	4.18	-1.72	Fe I	7.52	12.6
5237.33	0.228	4.07	-1.16	Cr II	5.67	87
5239.81	0.151	1.45	-0.77	Sc II	3.157.8	
5241.91	0.025	4.41	-1.67	Fe I	7.52	9.7
5242.49	0.208	3.63	-0.84	Fe I	7.52	79.5
5243.35	0.021	3.39	-0.567	Cr I	5.67	7.9
5243.78	0.085	4.25	-1.15	Fe I	7.52	32.4
5245.63	0.076	4.31	-1.171	Fe I	7.52	29.2

5245.72	0.065	5.08	-0.673	Fe I	7.52	24.7
5246.77	0.075	3.71	-2.45	Cr II	5.67	28.5
5247.05	0.039	0.09	-4.946	Fe I	7.52	14.9
5247.56	0.106	0.96	-1.64	Cr I	5.67	40.5
5249.1	0.034	4.47	-1.48	Fe I	7.52	12.9
5249.44	0.073	3.75	-2.426	Cr II	5.67	27.8
5249.58	0.02	0.97	0.21	Nd II	1.57.8	
5250.21	0.037	0.12	-4.938	Fe I	7.52	14.3
5250.65	0.202	2.2	-2.05	Fe I	7.52	77.2
5251.61	0.049	5.06	-0.831	Fe I	7.52	18.9
5252.02	0.02	2.59	-2.502	Ti II	4.99	7.7
5253.46	0.122	3.28	-1.67	Fe I	7.52	46.6
5254.9	0.021	3.41	-0.551	Cr I	5.67	7.9
5254.93	0.184	3.23	-3.227	Fe II	7.52	70.2
5254.95	0.054	0.11	-4.764	Fe I	7.52	20.5
5254.98	0.027	4.29	-1.724	Fe I	7.52	10.5
5255.11	0.027	3.46	-0.386	Cr I	5.67	10.3
5255.33	0.035	3.13	-0.763	Mn I	5.39	13.4
5255.66	0.025	4.22	-1.824	Fe I	7.52	9.6
5255.74	0.057	4.28	-1.361	Fe I	7.52	21.8
5256.94	0.069	2.89	-4.25	Fe II	7.52	26.5
5258.84	0.464	5.61	-0.18	Si I	7.55	177.1
5259.09	0.038	4.37	-1.506	Fe I	7.52	14.4
5260.39	0.024	2.52	-1.9	Ca I	6.36	9.2
5260.66	0.176	5.61	-0.92	Si I	7.55	67.3
5261.7	0.167	2.52	-0.73	Ca I	6.36	63.9
5261.75	0.021	3.69	-0.32	Cr I	5.67	8
5262.14	0.163	1.58	-2.106	Ti II	4.99	62.4
5262.24	0.189	2.52	-0.6	Ca I	6.36	72.1
5262.25	0.068	5.1	-0.633	Fe I	7.52	26
5262.88	0.022	3.25	-2.66	Fe I	7.52	8.3
5263.31	0.232	3.26	-0.97	Fe I	7.52	88.5
5263.39	0.023	3.64	-2.336	Fe I	7.52	8.6
5263.86	0.038	3.57	-2.13	Fe I	7.52	14.6
5264.15	0.162	0.97	-1.29	Cr I	5.67	62
5264.24	0.169	2.52	-0.72	Ca I	6.36	64.5
5264.81	0.19	3.23	-3.19	Fe II	7.52	72.7
5265.15	0.021	3.43	-0.529	Cr I	5.67	8.1
5265.56	0.243	2.52	-0.26	Ca I	6.36	92.7
5265.72	0.088	0.97	-1.75	Cr I	5.67	33.8
5266.56	0.327	3	-0.49	Fe I	7.52	124.9
5266.66	0.152	5.62	-1.01	Si I	7.55	58
5267.27	0.022	4.37	-1.77	Fe I	7.52	8.4
5267.65	0.022	5.06	-1.238	Fe I	7.52	8.3
5268.32	0.022	4.53	-0.726	Ni I	6.25	8.5
5268.39	0.288	5.62	-0.58	Si I	7.55	109.9
5268.61	0.105	2.6	-1.62	Ti II	4.99	40.2
5268.95	0.021	8.53	-2.28	C I	8.56	8

5269.54	0.468	0.86	-1.321	Fe I	7.52	178.9
5270.27	0.285	2.52	0.02	Ca I	6.36	109
5270.36	0.343	1.61	-1.51	Fe I	7.52	131.1
5272	0.026	3.45	-0.422	Cr I	5.67	9.8
5272.27	0.063	5.03	-0.725	Fe I	7.52	24.1
5272.4	0.051	5.95	-2.03	Fe II	7.52	19.5
5273.16	0.219	3.29	-1.037	Fe I	7.52	83.7
5273.37	0.144	2.48	-2.18	Fe I	7.52	55
5274.96	0.209	4.07	-1.29	Cr II	5.67	79.9
5275.17	0.034	3.37	-0.347	Cr I	5.67	12.8
5275.28	0.079	2.89	-0.276	Cr I	5.67	30
5275.75	0.11	2.89	-0.054	Cr I	5.67	42
5276	0.368	3.2	-1.94	Fe II	7.52	140.4
5276.07	0.103	2.89	-0.1	Cr I	5.67	39.4
5277.31	0.037	4.41	-1.477	Fe I	7.52	14.3
5278.81	0.067	5.03	-0.686	Fe I	7.52	25.7
5278.94	0.026	5.91	-2.408	Fe II	7.52	9.9
5278.99	0.027	6.86	-1.9	S I	7.21	10.3
5279.88	0.083	4.07	-2.1	Cr II	5.67	31.6
5280.05	0.095	4.07	-2.011	Cr II	5.67	36.4
5280.23	0.025	8.53	-2.19	C I	8.56	9.7
5280.36	0.042	3.64	-2.03	Fe I	7.52	16
5281.79	0.251	3.04	-1.02	Fe I	7.52	95.9
5282.43	0.085	4.99	-0.578	Fe I	7.52	32.6
5283.44	0.026	1.88	-0.2	Ti I	4.99	9.8
5283.62	0.281	3.24	-0.63	Fe I	7.52	107.4
5284.11	0.232	2.89	-3.19	Fe II	7.52	88.6
5285.13	0.026	4.43	-1.64	Fe I	7.52	10
5285.27	0.038	7.5	-1.153	Ca II	6.36	14.6
5288.29	0.026	5.1	-1.117	Fe I	7.52	10.1
5288.53	0.075	3.69	-1.67	Fe I	7.52	28.7
5292.6	0.174	4.99	-0.031	Fe I	7.52	66.3
5293.96	0.026	4.14	-1.87	Fe I	7.52	10
5294.09	0.068	5.06	-0.664	Fe I	7.52	25.8
5295.31	0.024	4.41	-1.69	Fe I	7.52	9.3
5296.69	0.142	0.98	-1.4	Cr I	5.67	54.3
5297.23	0.025	1.87	-0.23	Ti I	4.99	9.4
5297.38	0.145	2.9	0.167	Cr I	5.67	55.5
5298.02	0.109	2.9	-0.06	Cr I	5.67	41.5
5298.2	0.059	5.03	-0.759	Fe I	7.52	22.7
5298.27	0.184	0.98	-1.15	Cr I	5.67	70.4
5298.32	0.035	5.08	-0.997	Fe I	7.52	13.3
5298.49	0.069	2.9	-0.35	Cr I	5.67	26.3
5298.54	0.026	5.34	-0.035	Ni I	6.25	9.9
5298.78	0.032	3.64	-2.16	Fe I	7.52	12.4
5298.85	0.037	4.99	-1.044	Fe I	7.52	14
5300.74	0.045	0.98	-2.12	Cr I	5.67	17.1
5302.3	0.244	3.28	-0.88	Fe I	7.52	93.2

5302.87	0.045	8.64	-1.84	C I	8.56	17.3
5305.85	0.075	3.82	-2.357	Cr II	5.67	28.6
5306.31	0.037	8.64	-1.94	C I	8.56	14.1
5307.22	0.066	7.51	-0.853	Ca II	6.36	25.1
5307.36	0.13	1.61	-2.987	Fe I	7.52	49.5
5308.41	0.126	4.07	-1.81	Cr II	5.67	48.2
5310.46	0.029	5.08	-1.085	Fe I	7.52	11
5310.69	0.061	4.07	-2.28	Cr II	5.67	23.3
5313.56	0.152	4.07	-1.65	Cr II	5.67	58.2
5315.07	0.035	4.37	-1.55	Fe I	7.52	13.3
5315.46	0.03	5.06	-1.083	Fe I	7.52	11.4
5316.61	0.388	3.15	-1.85	Fe II	7.52	148.1
5316.78	0.234	3.22	-2.908	Fe II	7.52	89.3
5316.93	0.022	5.08	-1.212	Fe I	7.52	8.5
5317.52	0.084	4.14	-1.244	Fe I	7.52	32.2
5321.11	0.039	4.43	-1.44	Fe I	7.52	15
5322.04	0.05	2.28	-3.03	Fe I	7.52	19.1
5324.18	0.34	3.21	-0.24	Fe I	7.52	129.8
5325.55	0.278	3.22	-2.6	Fe II	7.52	106.3
5326.35	0.025	5.1	-1.133	Fe I	7.52	9.7
5328.04	0.437	0.91	-1.466	Fe I	7.52	166.8
5328.32	0.189	2.91	0.46	Cr I	5.67	72.3
5328.53	0.304	1.56	-1.85	Fe I	7.52	116.1
5329.14	0.106	2.91	-0.064	Cr I	5.67	40.6
5329.78	0.029	2.91	-0.795	Cr I	5.67	10.9
5329.99	0.084	4.07	-1.3	Fe I	7.52	31.9
5332.9	0.144	1.56	-2.94	Fe I	7.52	55.1
5333.24	0.49	5.61	-0.02	Si I	7.55	187
5334.87	0.167	4.07	-1.562	Cr II	5.67	63.6
5336.77	0.234	1.58	-1.7	Ti II	4.99	89.2
5337.73	0.081	3.23	-3.892	Fe II	7.52	30.9
5337.77	0.093	4.07	-2.029	Cr II	5.67	35.5
5337.99	0.49	5.61	-0.02	Si I	7.55	187
5338.21	0.251	5.61	-0.63	Si I	7.55	95.9
5339.42	0.042	4.43	-1.408	Fe I	7.52	16
5339.93	0.273	3.26	-0.68	Fe I	7.52	104.1
5341.02	0.271	1.61	-2.06	Fe I	7.52	103.4
5341.06	0.079	2.11	-1.146	Mn I	5.39	30.1
5342.69	0.039	4.02	0.69	Co I	4.92	14.9
5345.8	0.209	1	-0.98	Cr I	5.67	79.8
5346.04	0.201	5.62	-0.8	Si I	7.55	76.6
5346.07	0.044	3.82	-2.65	Cr II	5.67	16.9
5346.26	0.023	5.62	-1.95	Si I	7.55	8.8
5346.54	0.027	3.75	-2.948	Cr II	5.67	10.4
5347.12	0.04	5.06	-0.942	Fe I	7.52	15.3
5348.31	0.159	1	-1.29	Cr I	5.67	60.6
5348.77	0.045	5.06	-0.89	Fe I	7.52	17
5349.47	0.074	2.71	-1.178	Ca I	6.36	28.4

5349.74	0.055	4.38	-1.3	Fe I	7.52	21.1
5352.05	0.022	3.57	0.06	Co I	4.92	8.5
5353.37	0.151	4.1	-0.84	Fe I	7.52	57.6
5353.39	0.022	1.95	-2.8	Ni I	6.25	8.3
5353.5	0.025	4.14	0.566	Co I	4.92	9.5
5361.62	0.041	4.41	-1.43	Fe I	7.52	15.7
5362.87	0.26	3.2	-2.739	Fe II	7.52	99.4
5364.87	0.27	4.44	0.22	Fe I	7.52	103.3
5365.4	0.189	3.57	-1.02	Fe I	7.52	72
5366.42	0.031	5.06	-1.059	Fe I	7.52	12
5367.47	0.294	4.41	0.35	Fe I	7.52	112.1
5369.36	0.027	3.87	-2.86	Cr II	5.67	10.3
5369.96	0.298	4.37	0.35	Fe I	7.52	113.9
5371.32	0.061	4.42	-0.31	Ni I	6.25	23.4
5371.44	0.057	4.43	-1.244	Fe I	7.52	21.9
5371.49	0.403	0.96	-1.645	Fe I	7.52	154
5371.6	0.134	4.31	-0.78	Fe I	7.52	51.1
5373.71	0.102	4.47	-0.86	Fe I	7.52	39
5377.64	0.043	3.84	-0.109	Mn I	5.39	16.3
5378.23	0.04	5.03	-0.964	Fe I	7.52	15.4
5379.57	0.102	3.69	-1.48	Fe I	7.52	38.8
5380.22	0.022	8.84	-2.03	C I	8.56	8.4
5380.34	0.144	7.68	-1.842	C I	8.56	55.1
5381.02	0.172	1.56	-2.08	Ti II	4.99	65.8
5382.48	0.093	4.37	-1.005	Fe I	7.52	35.5
5383.37	0.329	4.31	0.5	Fe I	7.52	125.7
5386.33	0.032	4.15	-1.77	Fe I	7.52	12.1
5389.48	0.179	4.41	-0.41	Fe I	7.52	68.4
5391.46	0.148	4.15	-0.812	Fe I	7.52	56.7
5393.17	0.244	3.24	-0.91	Fe I	7.52	93.1
5394.68	0.023	0	-3.503	Mn I	5.39	8.9
5394.69	0.041	4.18	-1.62	Fe I	7.52	15.5
5396.23	0.046	1.58	-2.925	Ti II	4.99	17.6
5396.56	0.084	2.6	-1.77	Ti II	4.99	31.9
5397.13	0.359	0.91	-1.993	Fe I	7.52	137.1
5397.2	0.219	4.44	-0.126	Fe I	7.52	83.8
5398.28	0.135	4.44	-0.67	Fe I	7.52	51.5
5399.5	0.029	3.85	-0.287	Mn I	5.39	11.2
5400.5	0.223	4.37	-0.16	Fe I	7.52	85.1
5400.6	0.026	3.37	-0.47	Cr I	5.67	10.1
5402.77	0.042	1.84	-0.51	Y II	2.24	16
5403.35	0.041	5.1	-0.896	Fe I	7.52	15.8
5403.82	0.124	4.07	-1.034	Fe I	7.52	47.2
5404.12	0.335	4.31	0.54	Fe I	7.52	128.1
5404.15	0.319	4.43	0.523	Fe I	7.52	122
5404.66	0.27	5.61	-0.53	Si I	7.55	103
5405.35	0.047	4.38	-1.39	Fe I	7.52	17.9
5405.77	0.372	0.99	-1.844	Fe I	7.52	142

5406.34	0.022	4.07	-2.008	Fe I	7.52	8.4
5406.77	0.025	4.37	-1.72	Fe I	7.52	9.5
5407.42	0.024	2.14	-1.743	Mn I	5.39	9.2
5407.6	0.115	3.82	-2.088	Cr II	5.67	43.8
5408.81	0.025	5.95	-2.393	Fe II	7.52	9.6
5409.13	0.057	4.37	-1.3	Fe I	7.52	21.7
5409.77	0.057	5.61	-1.52	Si I	7.55	21.9
5409.78	0.245	1.03	-0.72	Cr I	5.67	93.5
5409.85	0.223	5.61	-0.69	Si I	7.55	85.3
5410.91	0.278	4.47	0.28	Fe I	7.52	106.1
5413.1	0.218	5.61	-0.71	Si I	7.55	83.1
5414.07	0.097	3.22	-3.79	Fe II	7.52	37
5415.2	0.322	4.38	0.5	Fe I	7.52	122.8
5417.04	0.025	4.41	-1.68	Fe I	7.52	9.6
5418.12	0.065	5.62	-1.45	Si I	7.55	24.8
5418.75	0.184	1.58	-1.999	Ti II	4.99	70.4
5420.35	0.043	2.14	-1.462	Mn I	5.39	16.3
5420.92	0.082	3.75	-2.36	Cr II	5.67	31.4
5421.38	0.061	5.62	-1.48	Si I	7.55	23.4
5424.07	0.331	4.32	0.52	Fe I	7.52	126.3
5424.64	0.023	1.95	-2.77	Ni I	6.25	8.8
5425.26	0.168	3.2	-3.36	Fe II	7.52	64.1
5427.83	0.034	6.72	-1.664	Fe II	7.52	12.9
5429.5	0.122	4.19	-0.952	Fe I	7.52	46.7
5429.7	0.371	0.96	-1.879	Fe I	7.52	141.6
5429.84	0.179	4.47	-0.372	Fe I	7.52	68.2
5432.95	0.08	4.44	-1.04	Fe I	7.52	30.6
5432.97	0.116	3.27	-3.629	Fe II	7.52	44.2
5433.64	0.048	5.06	-0.844	Fe I	7.52	18.5
5434.52	0.332	1.01	-2.122	Fe I	7.52	126.7
5435.03	0.039	5.06	-0.956	Fe I	7.52	14.8
5435.85	0.032	1.98	-2.59	Ni I	6.25	12.2
5436.3	0.035	4.38	-1.54	Fe I	7.52	13.3
5436.59	0.025	2.28	-3.39	Fe I	7.52	9.4
5437.08	0.036	2.45	-3.07	Fe I	7.52	13.6
5441.34	0.027	4.31	-1.73	Fe I	7.52	10.2
5445.04	0.243	4.38	-0.02	Fe I	7.52	92.7
5446.58	0.059	4.41	-1.243	Fe I	7.52	22.5
5446.87	0.111	1.61	-3.109	Fe I	7.52	42.3
5446.92	0.36	0.99	-1.93	Fe I	7.52	137.4
5448.27	0.036	4.14	-1.712	Fe I	7.52	13.9
5455.45	0.296	4.32	0.297	Fe I	7.52	113.1
5455.61	0.336	1.01	-2.091	Fe I	7.52	128.4
5462.48	0.045	3.84	-0.93	Ni I	6.25	17.1
5462.96	0.201	4.47	-0.234	Fe I	7.52	76.6
5463.28	0.256	4.43	0.11	Fe I	7.52	97.8
5464.28	0.036	4.14	-1.72	Fe I	7.52	13.7
5466.4	0.151	4.37	-0.63	Fe I	7.52	57.6

5466.99	0.032	3.57	-2.233	Fe I	7.52	12.1
5470.64	0.025	2.16	-1.702	Mn I	5.39	9.7
5472.71	0.032	4.21	-1.72	Fe I	7.52	12.4
5473.9	0.158	4.15	-0.76	Fe I	7.52	60.3
5476.29	0.131	4.14	-0.935	Fe I	7.52	50
5476.56	0.21	4.1	-0.453	Fe I	7.52	80.3
5476.9	0.28	1.82	-0.89	Ni I	6.25	107.1
5478.36	0.099	4.17	-1.908	Cr II	5.67	37.8
5478.45	0.025	4.19	-1.85	Fe I	7.52	9.7
5480.86	0.075	4.21	-1.26	Fe I	7.52	28.8
5481.24	0.069	4.1	-1.4	Fe I	7.52	26.4
5481.44	0.056	4.19	-1.45	Fe I	7.52	21.3
5483.1	0.046	4.15	-1.58	Fe I	7.52	17.7
5487.15	0.034	4.41	-1.53	Fe I	7.52	13
5487.74	0.2	4.32	-0.352	Fe I	7.52	76.5
5487.77	0.167	4.14	-0.71	Fe I	7.52	63.8
5488.98	0.257	5.61	-0.53	Si I	7.55	98
5490.69	0.079	1.56	-2.65	Ti II	4.99	30.2
5492.86	0.044	1.58	-2.956	Ti II	4.99	16.8
5493.22	0.024	5.08	-2.351	Si I	7.55	9
5493.32	0.081	3.64	-1.677	Fe I	7.52	30.9
5493.5	0.03	4.1	-1.84	Fe I	7.52	11.5
5493.88	0.233	5.61	-0.62	Si I	7.55	88.8
5494.24	0.089	5.61	-1.28	Si I	7.55	34
5494.68	0.048	5.61	-1.6	Si I	7.55	18.5
5497.41	0.043	1.75	-0.58	Y II	2.24	16.4
5497.52	0.233	1.01	-2.849	Fe I	7.52	89
5501.4	0.022	4.53	-0.747	Ni I	6.25	8.3
5501.47	0.225	0.96	-2.95	Fe I	7.52	85.9
5501.56	0.021	7.86	-1.26	S I	7.21	8.2
5502.07	0.089	4.17	-1.99	Cr II	5.67	34
5502.41	0.07	5.62	-1.41	Si I	7.55	26.7
5503.21	0.053	4.14	-2.306	Cr II	5.67	20.3
5505.73	0.021	4.47	-1.713	Fe I	7.52	8.1
5505.88	0.064	4.41	-1.198	Fe I	7.52	24.4
5506.78	0.243	0.99	-2.797	Fe I	7.52	92.7
5507.01	0.03	7.86	-1.11	S I	7.21	11.3
5508.41	0.024	4.95	-1.281	Fe I	7.52	9.1
5508.61	0.074	4.15	-2.11	Cr II	5.67	28.1
5509.6	0.026	5.1	-2.39	Mg I	7.58	10.1
5509.9	0.062	0.99	-1.01	Y II	2.24	23.5
5510	0.047	3.84	-0.9	Ni I	6.25	18.1
5510.7	0.065	3.82	-2.452	Cr II	5.67	24.7
5512.26	0.045	4.37	-1.42	Fe I	7.52	17.3
5512.4	0.03	4.41	-1.587	Fe I	7.52	11.6
5512.52	0.038	1.46	-0.35	Ti I	4.99	14.7
5512.98	0.188	2.93	-0.29	Ca I	6.36	71.8
5514.34	0.041	1.43	-0.35	Ti I	4.99	15.5

5514.53	0.051	1.44	-0.22	Ti I	4.99	19.5
5517.53	0.022	5.08	-2.384	Si I	7.55	8.4
5522.45	0.045	4.21	-1.55	Fe I	7.52	17.3
5525.54	0.066	4.23	-1.33	Fe I	7.52	25.2
5525.85	0.025	5.1	-1.145	Fe I	7.52	9.5
5526.79	0.262	1.77	0.13	Sc II	3.1100.1	
5528.4	0.402	4.34	-0.62	Mg I	7.58	153.5
5529.93	0.022	6.72	-1.875	Fe II	7.52	8.4
5532.75	0.038	3.57	-2.15	Fe I	7.52	14.4
5532.87	0.036	4.44	-1.476	Fe I	7.52	13.9
5534.85	0.231	3.24	-2.93	Fe II	7.52	88.1
5535.42	0.092	4.18	-1.158	Fe I	7.52	35.1
5543.15	0.09	3.69	-1.57	Fe I	7.52	34.2
5543.19	0.029	4.91	-1.221	Fe I	7.52	11.1
5543.94	0.091	4.21	-1.14	Fe I	7.52	34.8
5545.7	0.02	5.07	-1.267	Fe I	7.52	7.8
5546.51	0.056	4.37	-1.31	Fe I	7.52	21.4
5546.99	0.021	4.21	-1.91	Fe I	7.52	8.2
5548.9	0.052	8.64	-1.76	C I	8.56	19.7
5549.55	0.049	4.38	-1.372	Fe I	7.52	18.7
5551.02	0.059	8.64	-1.69	C I	8.56	22.7
5551.58	0.03	8.64	-2.03	C I	8.56	11.4
5553.58	0.042	4.43	-1.41	Fe I	7.52	16.1
5554.89	0.159	4.54	-0.44	Fe I	7.52	60.9
5557.9	0.035	4.47	-1.483	Fe I	7.52	13.2
5557.98	0.051	4.47	-1.28	Fe I	7.52	19.5
5560.21	0.064	4.43	-1.19	Fe I	7.52	24.4
5562.12	0.098	4.38	-0.962	Fe I	7.52	37.5
5562.71	0.151	4.43	-0.58	Fe I	7.52	57.8
5563.6	0.117	4.19	-0.99	Fe I	7.52	44.8
5563.69	0.03	2.42	-3.178	Fe I	7.52	11.6
5565.7	0.149	4.6	-0.458	Fe I	7.52	56.8
5567.27	0.026	4.41	-1.659	Fe I	7.52	10
5567.39	0.047	2.61	-2.8	Fe I	7.52	18.1
5567.84	0.021	6.72	-1.887	Fe II	7.52	8.1
5569.62	0.277	3.41	-0.54	Fe I	7.52	105.8
5569.7	0.031	5.61	-1.82	Si I	7.55	11.7
5572.84	0.312	3.39	-0.31	Fe I	7.52	119
5573.1	0.071	4.19	-1.317	Fe I	7.52	27.2
5575.11	0.093	5.61	-1.25	Si I	7.55	35.4
5576.09	0.211	3.43	-1	Fe I	7.52	80.5
5578.71	0.048	1.68	-2.64	Ni I	6.25	18.3
5581.97	0.172	2.52	-0.71	Ca I	6.36	65.7
5584.77	0.027	3.57	-2.32	Fe I	7.52	10.2
5585.73	0.022	5.03	-1.267	Fe I	7.52	8.3
5586.76	0.33	3.37	-0.21	Fe I	7.52	126.1
5587.57	0.028	4.14	-1.85	Fe I	7.52	10.6
5587.85	0.081	1.93	-2.14	Ni I	6.25	30.9

5588.75	0.317	2.52	0.21	Ca I	6.36	121.2
5589.36	0.027	3.9	-1.14	Ni I	6.25	10.5
5590.11	0.173	2.52	-0.71	Ca I	6.36	65.9
5592.14	0.056	4.23	-0.512	Ni I	6.25	21.3
5592.26	0.036	1.95	-2.57	Ni I	6.25	13.7
5593.73	0.05	3.9	-0.84	Ni I	6.25	19
5594.46	0.278	2.52	-0.05	Ca I	6.36	106
5594.66	0.089	4.54	-0.9	Fe I	7.52	34
5598.29	0.157	4.65	-0.37	Fe I	7.52	60.1
5598.48	0.25	2.52	-0.22	Ca I	6.36	95.6
5600.01	0.057	4.09	-0.609	Ni I	6.25	21.9
5600.1	0.071	5.06	-0.632	Fe I	7.52	27.1
5600.22	0.023	4.26	-1.843	Fe I	7.52	8.8
5601.28	0.175	2.52	-0.69	Ca I	6.36	66.7
5602.77	0.099	4.15	-1.135	Fe I	7.52	37.9
5602.81	0.05	5.06	-0.827	Fe I	7.52	19.1
5602.84	0.173	2.52	-0.7	Ca I	6.36	66.2
5602.88	0.024	4.95	-2.44	Si I	7.55	9.2
5602.94	0.232	3.43	-0.851	Fe I	7.52	88.7
5614.77	0.063	4.15	-0.508	Ni I	6.25	24.1
5615.3	0.123	2.59	-2.248	Fe I	7.52	46.8
5615.64	0.345	3.33	-0.14	Fe I	7.52	131.8
5618.63	0.062	4.21	-1.38	Fe I	7.52	23.8
5619.6	0.025	4.38	-1.7	Fe I	7.52	9.7
5620.03	0.022	4.14	-1.966	Fe I	7.52	8.3
5620.49	0.031	4.15	-1.79	Fe I	7.52	11.8
5624.02	0.04	4.38	-1.48	Fe I	7.52	15.2
5624.54	0.229	3.41	-0.9	Fe I	7.52	87.3
5625.31	0.049	4.09	-0.7	Ni I	6.25	18.7
5627.5	0.027	3.38	-4.36	Fe II	7.52	10.2
5628.34	0.03	4.09	-0.941	Ni I	6.25	11.5
5633.95	0.132	4.99	-0.27	Fe I	7.52	50.4
5635.82	0.021	4.25	-1.89	Fe I	7.52	8.1
5637.11	0.04	3.64	-2.066	Fe I	7.52	15.3
5637.11	0.038	4.09	-0.82	Ni I	6.25	14.7
5638.26	0.132	4.22	-0.87	Fe I	7.52	50.6
5641	0.102	1.5	-1.04	Sc II	3.138.9	
5641.43	0.082	4.25	-1.18	Fe I	7.52	31.5
5641.88	0.023	4.1	-1.07	Ni I	6.25	8.6
5643.93	0.02	4.07	-2.05	Fe I	7.52	7.8
5644.03	0.027	4.55	-1.544	Fe I	7.52	10.2
5644.13	0.023	2.27	0.03	Ti I	4.99	8.6
5645.61	0.047	4.93	-2.14	Si I	7.55	17.8
5649.69	0.035	4.16	-0.807	Ni I	6.25	13.4
5649.99	0.04	5.1	-0.92	Fe I	7.52	15.3
5650.71	0.038	5.08	-0.96	Fe I	7.52	14.4
5653.86	0.029	4.38	-1.64	Fe I	7.52	11
5654.92	0.152	5.61	-0.93	Si I	7.55	58

5655.18	0.071	5.06	-0.64	Fe I	7.52	27.1
5655.49	0.136	5.03	-0.218	Fe I	7.52	52
5655.49	0.109	4.26	-0.989	Fe I	7.52	41.8
5657.9	0.197	1.51	-0.5	Sc II	3.175.3	
5657.94	0.043	3.42	-4.1	Fe II	7.52	16.4
5658.36	0.083	1.5	-1.17	Sc II	3.131.8	
5658.53	0.234	3.43	-0.851	Fe I	7.52	89.3
5658.66	0.069	4.28	-1.269	Fe I	7.52	26.3
5658.82	0.228	3.39	-0.92	Fe I	7.52	87.2
5659.57	0.051	5.08	-0.804	Fe I	7.52	19.4
5659.94	0.04	8.53	-1.96	C I	8.56	15.1
5660.5	0.042	5.61	-1.66	Si I	7.55	16.2
5660.68	0.107	5.61	-1.16	Si I	7.55	40.7
5662.52	0.184	4.17	-0.573	Fe I	7.52	70.4
5662.93	0.115	1.94	0.16	Y II	2.24	43.9
5662.94	0.02	3.69	-2.35	Fe I	7.52	7.8
5663.98	0.042	4.53	-0.43	Ni I	6.25	15.9
5665.56	0.057	4.92	-2.04	Si I	7.55	21.8
5666.68	0.127	5.61	-1.05	Si I	7.55	48.4
5667.15	0.074	1.5	-1.24	Sc II	3.128.1	
5667.52	0.045	4.17	-1.576	Fe I	7.52	17.3
5667.67	0.03	2.61	-3.03	Fe I	7.52	11.6
5669.04	0.09	1.5	-1.12	Sc II	3.134.3	
5669.74	0.078	5.62	-1.34	Si I	7.55	29.9
5669.94	0.021	4.26	-0.964	Ni I	6.25	8.2
5675.42	0.13	5.62	-1.03	Si I	7.55	49.8
5675.76	0.033	5.62	-1.78	Si I	7.55	12.6
5679.02	0.076	4.65	-0.92	Fe I	7.52	28.9
5682.2	0.073	4.1	-0.47	Ni I	6.25	27.7
5682.63	0.178	2.1	-0.7	Na I	6.33	67.8
5684.2	0.1	1.51	-1.05	Sc II	3.138.2	
5684.48	0.107	4.95	-1.65	Si I	7.55	40.7
5686.53	0.13	4.54	-0.63	Fe I	7.52	49.6
5688.19	0.062	2.1	-1.4	Na I	6.33	23.8
5688.2	0.226	2.1	-0.45	Na I	6.33	86.4
5690.43	0.076	4.93	-1.87	Si I	7.55	29.2
5691.5	0.042	4.3	-1.52	Fe I	7.52	16
5693.11	0.049	8.53	-1.85	C I	8.56	18.8
5694.98	0.058	4.09	-0.61	Ni I	6.25	22
5696.97	0.021	7.86	-1.26	S I	7.21	8.1
5698.23	0.021	3.88	-0.191	Cr I	5.67	8
5700.58	0.034	7.86	-1.04	S I	7.21	12.9
5701.1	0.055	4.93	-2.05	Si I	7.55	21.1
5701.51	0.02	4.91	-1.396	Fe I	7.52	7.7
5701.54	0.132	2.56	-2.216	Fe I	7.52	50.4
5704.73	0.034	5.03	-1.056	Fe I	7.52	12.9
5705.46	0.036	4.3	-1.6	Fe I	7.52	13.7
5705.99	0.138	4.6	-0.53	Fe I	7.52	52.6

5706.42	0.041	7.86	-0.95	S I	7.21	15.5
5707.05	0.02	3.64	-2.4	Fe I	7.52	7.7
5708.09	0.031	4.43	-1.57	Fe I	7.52	11.8
5708.4	0.136	4.95	-1.47	Si I	7.55	52.1
5709.38	0.183	3.37	-1.24	Fe I	7.52	70
5709.54	0.108	1.68	-2.17	Ni I	6.25	41.3
5711.09	0.179	4.34	-1.833	Mg I	7.58	68.2
5711.85	0.048	4.28	-1.46	Fe I	7.52	18.5
5711.88	0.065	1.93	-2.27	Ni I	6.25	24.9
5712.13	0.057	3.41	-2.06	Fe I	7.52	21.8
5715.07	0.089	4.08	-0.352	Ni I	6.25	34.1
5717.83	0.087	4.28	-1.13	Fe I	7.52	33.1
5731.76	0.068	4.25	-1.3	Fe I	7.52	25.8
5741.85	0.03	4.25	-1.73	Fe I	7.52	11.4
5744.33	0.053	4.99	-0.858	Fe I	7.52	20.3
5747.67	0.181	5.61	-0.78	Si I	7.55	69.1
5747.95	0.031	4.6	-1.43	Fe I	7.52	11.9
5752.03	0.095	4.54	-0.864	Fe I	7.52	36.1
5753.12	0.145	4.26	-0.76	Fe I	7.52	55.5
5753.44	0.035	5.61	-1.76	Si I	7.55	13.3
5753.62	0.17	5.61	-0.83	Si I	7.55	65
5754.07	0.025	5.61	-1.92	Si I	7.55	9.5
5754.65	0.059	1.93	-2.33	Ni I	6.25	22.6
5755.35	0.025	3.64	-2.298	Fe I	7.52	9.7
5760.83	0.039	4.1	-0.8	Ni I	6.25	15
5762.41	0.026	3.64	-2.28	Fe I	7.52	9.9
5762.98	0.079	5.62	-1.33	Si I	7.55	30.2
5762.98	0.024	5.62	-1.93	Si I	7.55	9.2
5762.99	0.2	4.21	-0.45	Fe I	7.52	76.4
5769.32	0.044	4.6	-1.26	Fe I	7.52	16.7
5772.15	0.077	5.08	-1.75	Si I	7.55	29.4
5775.08	0.071	4.22	-1.298	Fe I	7.52	27.3
5780.38	0.031	4.92	-2.35	Si I	7.55	11.9
5780.6	0.024	3.24	-2.64	Fe I	7.52	9.2
5781.83	0.021	3.32	-0.642	Cr I	5.67	7.9
5782.11	0.021	5.06	-1.268	Fe I	7.52	8
5782.13	0.051	1.64	-1.72	Cu I	4.21	19.3
5783.06	0.028	3.32	-0.5	Cr I	5.67	10.6
5783.85	0.042	3.32	-0.295	Cr I	5.67	16
5784.97	0.036	3.32	-0.38	Cr I	5.67	13.6
5785.31	0.047	5.1	-2.11	Mg I	7.58	18.1
5785.56	0.021	5.1	-2.5	Mg I	7.58	8
5785.73	0.034	3.32	-0.399	Cr I	5.67	13.1
5787.92	0.063	3.32	-0.083	Cr I	5.67	23.9
5790.96	0.058	3.32	-0.124	Cr I	5.67	22.1
5791.02	0.037	3.21	-2.46	Fe I	7.52	14
5791.79	0.067	6.04	-0.691	Cr II	5.67	25.5
5793.07	0.065	4.93	-1.96	Si I	7.55	25

5793.12	0.062	7.94	-2.157	C I	8.56	23.7
5793.91	0.027	4.22	-1.8	Fe I	7.52	10.4
5797.86	0.064	4.95	-1.95	Si I	7.55	24.6
5798.17	0.034	3.93	-1.93	Fe I	7.52	12.8
5800.6	0.036	7.94	-2.44	C I	8.56	13.6
5804.46	0.023	4.28	-1.84	Fe I	7.52	8.7
5805.21	0.045	4.16	-0.69	Ni I	6.25	17
5806.73	0.06	4.6	-1.09	Fe I	7.52	23
5809.22	0.038	3.88	-1.91	Fe I	7.52	14.4
5813.68	0.022	5.57	-2.75	Fe II	7.52	8.4
5816.37	0.086	4.54	-0.93	Fe I	7.52	32.7
5835.49	0.028	5.91	-2.372	Fe II	7.52	10.7
5848.13	0.069	4.6	-1.01	Fe I	7.52	26.5
5852.22	0.042	4.54	-1.33	Fe I	7.52	16.1
5853.67	0.167	0.6	-1	Ba II	2.13	63.6
5856.09	0.034	4.29	-1.64	Fe I	7.52	12.8
5857.45	0.274	2.93	0.23	Ca I	6.36	104.5
5857.75	0.049	4.16	-0.636	Ni I	6.25	18.9
5859.59	0.168	4.54	-0.386	Fe I	7.52	64.3
5862.36	0.22	4.54	-0.051	Fe I	7.52	84.1
5866.45	0.028	1.07	-0.84	Ti I	4.99	10.7
5867.56	0.104	2.93	-0.801	Ca I	6.36	39.8
6001.12	0.026	8.64	-2.07	C I	8.56	10.1
6002.98	0.027	8.64	-2.05	C I	8.56	10.4
6003.01	0.137	3.88	-1.12	Fe I	7.52	52.4
6005.54	0.04	2.59	-2.922	Fe I	7.52	15.4
6007.18	0.021	8.63	-2.18	C I	8.56	8
6007.96	0.069	4.65	-0.978	Fe I	7.52	26.5
6008.56	0.11	3.88	-1.291	Fe I	7.52	42
6010.68	0.03	8.63	-2.02	C I	8.56	11.3
6013.17	0.1	8.64	-1.37	C I	8.56	38.1
6013.21	0.084	8.64	-1.47	C I	8.56	32.2
6013.51	0.1	3.07	-0.251	Mn I	5.39	38.2
6014.83	0.055	8.64	-1.71	C I	8.56	21
6016.45	0.044	8.64	-1.82	C I	8.56	16.9
6016.6	0.074	3.54	-1.82	Fe I	7.52	28.3
6016.67	0.105	3.07	-0.216	Mn I	5.39	40.2
6020.17	0.181	4.6	-0.27	Fe I	7.52	69
6021.82	0.144	3.07	0.034	Mn I	5.39	54.9
6024.06	0.21	4.54	-0.12	Fe I	7.52	80.2
6027.05	0.099	4.07	-1.21	Fe I	7.52	37.8
6029.87	0.299	5.98	-0.42	Si I	7.55	114.2
6045.99	0.022	7.86	-1.24	S I	7.21	8.4
6046.03	0.034	7.86	-1.03	S I	7.21	13
6052.67	0.06	7.86	-0.74	S I	7.21	22.8
6053.47	0.029	4.74	-2.16	Cr II	5.67	10.9
6056.01	0.135	4.73	-0.46	Fe I	7.52	51.4
6065.48	0.236	2.61	-1.53	Fe I	7.52	90.1

6078.49	0.123	4.79	-0.481	Fe I	7.52	47.1
6079.01	0.054	4.65	-1.12	Fe I	7.52	20.7
6084.11	0.1	3.2	-3.808	Fe II	7.52	38.3
6086.28	0.053	4.26	-0.53	Ni I	6.25	20.2
6087.81	0.033	5.87	-1.6	Si I	7.55	12.5
6091.92	0.049	5.87	-1.4	Si I	7.55	18.9
6093.64	0.027	4.6	-1.5	Fe I	7.52	10.5
6096.66	0.031	3.98	-1.93	Fe I	7.52	11.9
6102.17	0.122	4.83	-0.457	Fe I	7.52	46.7
6102.72	0.155	1.88	-1.34	Ca I	6.36	59.3
6103.19	0.066	4.83	-0.864	Fe I	7.52	25.2
6103.29	0.036	4.73	-1.267	Fe I	7.52	13.8
6103.5	0.026	6.21	-2.171	Fe II	7.52	10
6108.11	0.033	1.68	-2.85	Ni I	6.25	12.7
6111.07	0.034	4.08	-0.9	Ni I	6.25	12.9
6113.32	0.049	3.22	-4.208	Fe II	7.52	18.6
6116.17	0.035	4.09	-0.877	Ni I	6.25	13.5
6116.23	0.044	4.26	-0.62	Ni I	6.25	16.9
6122.22	0.226	1.88	-0.909	Ca I	6.36	86.4
6125.02	0.045	5.61	-1.63	Si I	7.55	17.3
6127.91	0.039	4.14	-1.699	Fe I	7.52	14.8
6129.7	0.02	3.2	-4.655	Fe II	7.52	7.8
6131.57	0.036	5.61	-1.75	Si I	7.55	13.6
6131.85	0.036	5.61	-1.74	Si I	7.55	13.9
6136.61	0.184	2.45	-2	Fe I	7.52	70.2
6136.99	0.048	2.2	-3.15	Fe I	7.52	18.4
6137.69	0.165	2.59	-2.003	Fe I	7.52	63.1
6138.52	0.042	5.98	-1.41	Si I	7.55	16
6141.71	0.293	0.7	-0.076	Ba II	2.13	112
6141.73	0.097	3.6	-1.61	Fe I	7.52	36.9
6142.48	0.05	5.62	-1.57	Si I	7.55	19.2
6145.02	0.056	5.61	-1.52	Si I	7.55	21.3
6147.74	0.104	3.89	-3.221	Fe II	7.52	39.9
6147.83	0.029	4.07	-1.9	Fe I	7.52	11
6149.26	0.152	3.89	-2.924	Fe II	7.52	57.9
6151.62	0.02	2.17	-3.599	Fe I	7.52	7.7
6154.23	0.047	2.1	-1.56	Na I	6.33	17.8
6155.13	0.169	5.62	-0.8	Si I	7.55	64.7
6157.73	0.061	4.07	-1.51	Fe I	7.52	23.4
6160.75	0.081	2.1	-1.26	Na I	6.33	30.9
6161.3	0.122	2.52	-1.02	Ca I	6.36	46.7
6162.17	0.384	1.9	0.1	Ca I	6.36	146.5
6163.42	0.051	4.1	-0.682	Ni I	6.25	19.3
6163.76	0.123	2.52	-1.02	Ca I	6.36	46.8
6165.36	0.051	4.14	-1.55	Fe I	7.52	19.6
6166.44	0.142	2.52	-0.9	Ca I	6.36	54.2
6169.04	0.2	2.52	-0.55	Ca I	6.36	76.5
6169.56	0.245	2.52	-0.27	Ca I	6.36	93.6

6170.51	0.13	4.79	-0.44	Fe I	7.52	49.5
6173.33	0.076	2.22	-2.88	Fe I	7.52	28.9
6175.15	0.038	6.22	-1.983	Fe II	7.52	14.4
6175.36	0.068	4.09	-0.53	Ni I	6.25	25.9
6175.85	0.023	8.04	-1.09	S I	7.21	8.7
6176.81	0.104	4.08	-0.26	Ni I	6.25	39.6
6179.38	0.03	5.57	-2.602	Fe II	7.52	11.5
6180.2	0.043	2.73	-2.78	Fe I	7.52	16.5
6186.71	0.029	4.1	-0.96	Ni I	6.25	11.1
6187.99	0.05	3.94	-1.72	Fe I	7.52	19.2
6191.17	0.084	1.68	-2.353	Ni I	6.25	32
6191.56	0.248	2.43	-1.6	Fe I	7.52	94.9
6195.43	0.021	5.87	-1.8	Si I	7.55	8.1
6200.31	0.094	2.61	-2.437	Fe I	7.52	35.8
6204.6	0.023	4.08	-1.1	Ni I	6.25	8.6
6213.43	0.108	2.22	-2.66	Fe I	7.52	41.1
6215.07	0.022	5.96	-1.71	Si I	7.55	8.5
6215.14	0.059	4.18	-1.44	Fe I	7.52	22.6
6216.36	0.024	4.73	-1.475	Fe I	7.52	9
6219.28	0.148	2.2	-2.433	Fe I	7.52	56.5
6219.94	0.028	2.06	-2.819	Ti II	4.99	10.6
6220.21	0.02	5.86	-1.83	Si I	7.55	7.7
6223.98	0.032	4.1	-0.91	Ni I	6.25	12.3
6226.73	0.02	3.88	-2.22	Fe I	7.52	7.8
6229.23	0.024	2.84	-2.97	Fe I	7.52	9.2
6229.35	0.027	2.83	-4.824	Fe II	7.52	10.3
6230.72	0.28	2.56	-1.281	Fe I	7.52	106.8
6232.64	0.155	3.65	-1.2	Fe I	7.52	59.3
6237.32	0.223	5.61	-0.53	Si I	7.55	85.1
6238.29	0.025	5.08	-2.34	Si I	7.55	9.5
6238.39	0.2	3.89	-2.63	Fe II	7.52	76.5
6239.37	0.05	2.81	-4.538	Fe II	7.52	19.1
6239.95	0.075	3.89	-3.439	Fe II	7.52	28.5
6240.31	0.036	4.14	-1.737	Fe I	7.52	13.8
6240.65	0.03	2.22	-3.38	Fe I	7.52	11.3
6243.81	0.174	5.61	-0.77	Si I	7.55	66.5
6244.11	0.042	5.61	-1.67	Si I	7.55	15.9
6244.47	0.19	5.61	-0.69	Si I	7.55	72.5
6245.64	0.115	1.51	-0.98	Sc II	3.144.1	
6246.32	0.199	3.6	-0.96	Fe I	7.52	76
6247.35	0.032	6.2	-2.078	Fe II	7.52	12.2
6247.56	0.245	3.89	-2.329	Fe II	7.52	93.6
6248.9	0.027	5.51	-2.696	Fe II	7.52	10.4
6252.56	0.24	2.4	-1.687	Fe I	7.52	91.5
6254.19	0.207	5.62	-0.6	Si I	7.55	79.2
6254.26	0.13	2.28	-2.48	Fe I	7.52	49.5
6254.84	0.027	5.62	-1.88	Si I	7.55	10.3
6256.35	0.068	1.68	-2.48	Ni I	6.25	25.9

6256.36	0.086	2.45	-2.62	Fe I	7.52	32.8
6258.1	0.042	1.44	-0.355	Ti I	4.99	15.9
6258.71	0.051	1.46	-0.24	Ti I	4.99	19.3
6261.1	0.033	1.43	-0.479	Ti I	4.99	12.6
6265.13	0.132	2.17	-2.55	Fe I	7.52	50.6
6269.97	0.02	3.24	-4.625	Fe II	7.52	7.8
6270.22	0.04	2.86	-2.71	Fe I	7.52	15.4
6271.51	0.034	4.58	-1.415	Fe I	7.52	13
6314.65	0.142	1.93	-1.77	Ni I	6.25	54.4
6314.66	0.03	4.15	-0.921	Ni I	6.25	11.3
6315.31	0.09	4.14	-1.232	Fe I	7.52	34.3
6315.41	0.023	4.14	-1.958	Fe I	7.52	8.8
6315.81	0.042	4.07	-1.71	Fe I	7.52	16.2
6317.39	0.027	6.22	-2.158	Fe II	7.52	10.2
6317.98	0.096	5.51	-1.99	Fe II	7.52	36.7
6318.02	0.148	2.45	-2.228	Fe I	7.52	56.5
6318.11	0.16	4.43	0.699	Ca I	6.36	61.1
6318.72	0.094	5.1	-1.73	Mg I	7.58	36
6319.24	0.064	5.1	-1.95	Mg I	7.58	24.6
6319.49	0.025	5.1	-2.43	Mg I	7.58	9.4
6320.85	0.028	1.5	-1.77	Sc II	3.1	10.6
6322.69	0.099	2.59	-2.426	Fe I	7.52	37.7
6331.95	0.038	6.21	-1.977	Fe II	7.52	14.7
6331.96	0.049	5.08	-2	Si I	7.55	18.9
6335.33	0.183	2.2	-2.23	Fe I	7.52	69.8
6336.82	0.175	3.68	-1.05	Fe I	7.52	67
6338.88	0.049	4.79	-1.06	Fe I	7.52	18.9
6339.11	0.037	4.15	-0.811	Ni I	6.25	14
6342.32	0.032	8.76	-1.88	C I	8.56	12.1
6343.31	0.184	4.44	0.845	Ca I	6.36	70.3
6344.15	0.052	2.43	-2.923	Fe I	7.52	20
6347.11	0.296	8.12	0.297	Si II	7.55	113.2
6355.03	0.071	2.84	-2.42	Fe I	7.52	27
6356.32	0.051	6.09	-1.24	Si I	7.55	19.4
6358.63	0.042	4.14	-1.657	Fe I	7.52	16.2
6358.7	0.032	0.86	-4.468	Fe I	7.52	12.1
6361.79	0.202	4.45	0.954	Ca I	6.36	77.1
6362.34	0.052	5.79	0.15	Zn I	4.6	20
6362.88	0.021	4.18	-1.97	Fe I	7.52	8
6364.36	0.024	4.79	-1.43	Fe I	7.52	9
6366.48	0.021	4.16	-1.064	Ni I	6.25	8.2
6369.46	0.074	2.89	-4.253	Fe II	7.52	28.3
6371.37	0.246	8.12	-0.003	Si II	7.55	93.9
6378.25	0.036	4.15	-0.83	Ni I	6.25	13.6
6380.74	0.064	4.18	-1.4	Fe I	7.52	24.6
6383.72	0.058	5.55	-2.271	Fe II	7.52	22
6385.45	0.03	5.55	-2.618	Fe II	7.52	11.4
6393.6	0.247	2.43	-1.62	Fe I	7.52	94.5

6397.97	0.031	8.76	-1.89	C I	8.56	11.8
6400	0.266	3.6	-0.52	Fe I	7.52	101.6
6400.32	0.039	0.91	-4.318	Fe I	7.52	15
6407.25	0.047	3.89	-3.699	Fe II	7.52	18.1
6407.29	0.04	5.87	-1.5	Si I	7.55	15.4
6408.02	0.188	3.68	-0.97	Fe I	7.52	71.9
6411.65	0.216	3.65	-0.82	Fe I	7.52	82.6
6414.98	0.086	5.87	-1.1	Si I	7.55	32.7
6416.92	0.182	3.89	-2.74	Fe II	7.52	69.6
6416.93	0.048	4.79	-1.074	Fe I	7.52	18.4
6419.95	0.17	4.73	-0.24	Fe I	7.52	64.8
6421.35	0.205	2.28	-2.027	Fe I	7.52	78.4
6430.85	0.222	2.17	-2.006	Fe I	7.52	84.7
6432.68	0.159	2.89	-3.708	Fe II	7.52	60.9
6439.07	0.366	2.52	0.47	Ca I	6.36	139.9
6442.78	0.049	6.12	-1.24	Si I	7.55	18.6
6446.41	0.032	6.22	-2.073	Fe II	7.52	12.1
6449.81	0.202	2.52	-0.55	Ca I	6.36	77.2
6451.52	0.043	5.98	-1.39	Si I	7.55	16.3
6455.6	0.075	2.52	-1.35	Ca I	6.36	28.5
6456.38	0.284	3.9	-2.075	Fe II	7.52	108.3
6456.88	0.04	8.43	-0.426	Ca II	6.36	15.2
6456.88	0.032	8.43	-0.539	Ca II	6.36	12.2
6592.91	0.214	2.73	-1.6	Fe I	7.52	81.8
6593.87	0.121	2.43	-2.422	Fe I	7.52	46.1
6597.56	0.049	4.79	-1.07	Fe I	7.52	18.7
6598.59	0.023	4.23	-0.98	Ni I	6.25	8.8
6604.6	0.064	1.36	-1.48	Sc II	3.124.4	
6605.9	0.031	4.01	-1.206	Ti II	4.99	11.8
6606.95	0.03	2.06	-2.79	Ti II	4.99	11.6
6609.11	0.067	2.56	-2.692	Fe I	7.52	25.7
6627.54	0.023	4.54	-1.64	Fe I	7.52	8.8
6633.41	0.025	4.83	-1.37	Fe I	7.52	9.7
6633.75	0.078	4.55	-1	Fe I	7.52	29.6
6634.11	0.032	4.79	-1.28	Fe I	7.52	12.4
6635.12	0.021	4.42	-0.87	Ni I	6.25	8.2
6639.69	0.021	4.6	-1.637	Fe I	7.52	8.1
6643.62	0.078	1.68	-2.42	Ni I	6.25	29.6
6663.23	0.028	4.55	-1.543	Fe I	7.52	10.7
6663.44	0.07	2.42	-2.779	Fe I	7.52	26.9
6677.98	0.169	2.69	-1.92	Fe I	7.52	64.4
6680.13	0.037	3.09	-1.855	Ti II	4.99	14.2
6696.02	0.068	3.14	-1.347	Al I	6.47	25.9
6698.67	0.038	3.14	-1.647	Al I	6.47	14.6
6705.1	0.03	4.6	-1.47	Fe I	7.52	11.5
6707.77	0.114	0	0.002	Li I	3.31	43.4
6707.9	0.064	0	-0.299	Li I	3.31	24.5
6707.9	0.064	0	-0.299	Li I	3.31	24.5

6707.92	0.114	0	0.002	Li I	3.31	43.4
6707.92	0.114	0	0.002	Li I	3.31	43.4
6708.07	0.064	0	-0.299	Li I	3.31	24.5
6708.07	0.064	0	-0.299	Li I	3.31	24.5
6712.67	0.059	2.59	-2.74	Fe I	7.52	22.6
6713.05	0.027	4.6	-1.51	Fe I	7.52	10.5
6713.59	0.024	8.53	-2.17	C I	8.56	9.3
6715.38	0.021	4.6	-1.64	Fe I	7.52	8
6717.68	0.168	2.71	-0.61	Ca I	6.36	64.2
6717.79	0.039	3.12	-1.804	Ti II	4.99	14.9
6721.85	0.041	5.86	-1.49	Si I	7.55	15.8
6726.28	0.036	9.14	-2	O I	8.93	13.9
6726.54	0.036	9.14	-2	O I	8.93	13.9
6726.67	0.079	4.6	-0.952	Fe I	7.52	30.1
6733.15	0.023	4.63	-1.58	Fe I	7.52	8.7
6743.44	0.02	7.86	-1.27	S I	7.21	7.8
6743.53	0.042	7.86	-0.92	S I	7.21	15.9
6743.64	0.034	7.86	-1.03	S I	7.21	12.8
6748.68	0.052	7.86	-0.8	S I	7.21	19.8
6748.84	0.074	7.86	-0.6	S I	7.21	28.2
6750.15	0.092	2.42	-2.621	Fe I	7.52	35
6752.71	0.036	4.63	-1.36	Fe I	7.52	13.6
6757.01	0.043	7.86	-0.9	S I	7.21	16.4
6757.17	0.115	7.86	-0.31	S I	7.21	44
6765.45	0.067	5.75	-1.49	Mg I	7.58	25.5
6767.77	0.096	1.82	-2.17	Ni I	6.25	36.6
6772.31	0.058	3.65	-0.98	Ni I	6.25	22.1
6782.21	0.025	6.19	-1.5	Si I	7.55	9.4
6783.26	0.033	2.56	-3.071	Fe I	7.52	12.6
6785.21	0.047	3.12	-1.709	Ti II	4.99	18.1
6790.64	0.033	6.07	-1.44	Si I	7.55	12.7
6799	0.056	5.75	-1.56	Mg I	7.58	21.5

Appendix D

Extra figures relating to the analysis of V2052 Ophiuchi. Due to the fact that there were three lines examined for this object some of the figures produced were used in the analysis of the object but were felt not to be necessary to the description of the analysis in the appropriate sections of Chapter 5. A brief description of each group of figures is given as well as appropriate captions.

The following figures relate to the frequency detection for the variations observed in the equivalent width and velocity of the He I 5876Å line.

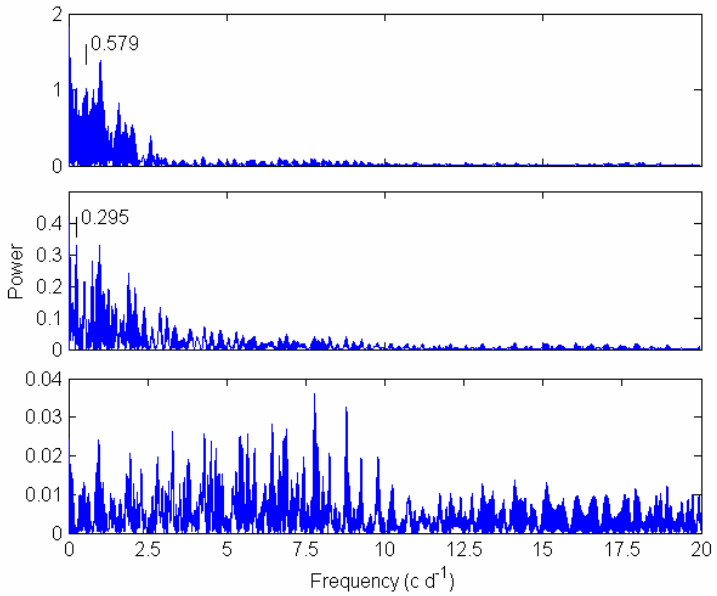

Figure: Frequency extraction for He I 5875Å lines equivalent width variations. Notably lacking is the presence of the 7.145 cd^{-1} frequency. The first frequency was chosen because the highest peak of the graph was likely due to data clumping. Note also that 7 frequencies can be extracted though they are not shown here as they do not coincide with other frequencies extracted and are not used in any further analysis.

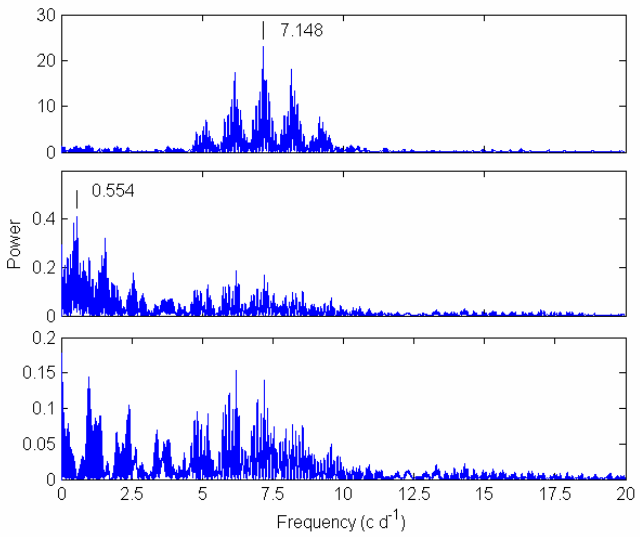

Figure: The extracted frequencies for the velocity variations for the He I 5875Å line.

The following figures relate to the pixel-by-pixel frequency detection for, and the phase and amplitude across the profile for the frequencies detected in the He I 5876Å line.

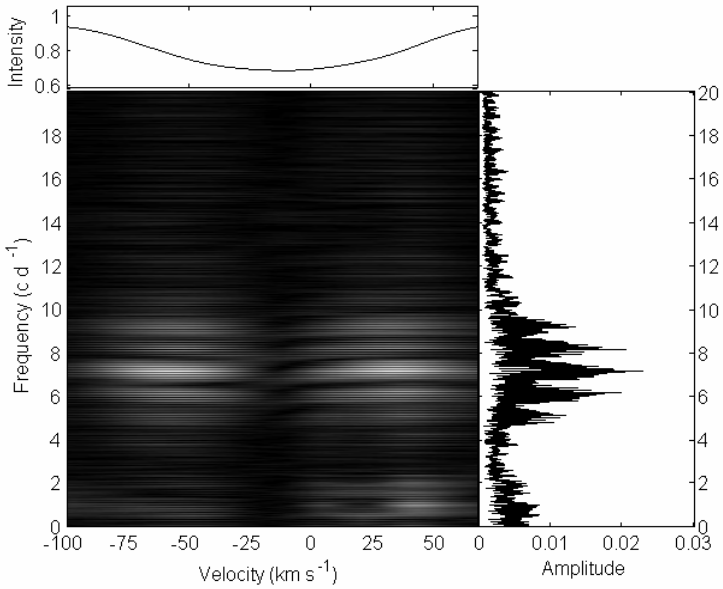

Figure: He I 5876Å line pixel-by-pixel analysis. The peak frequency is at 7.147 cd^{-1}.

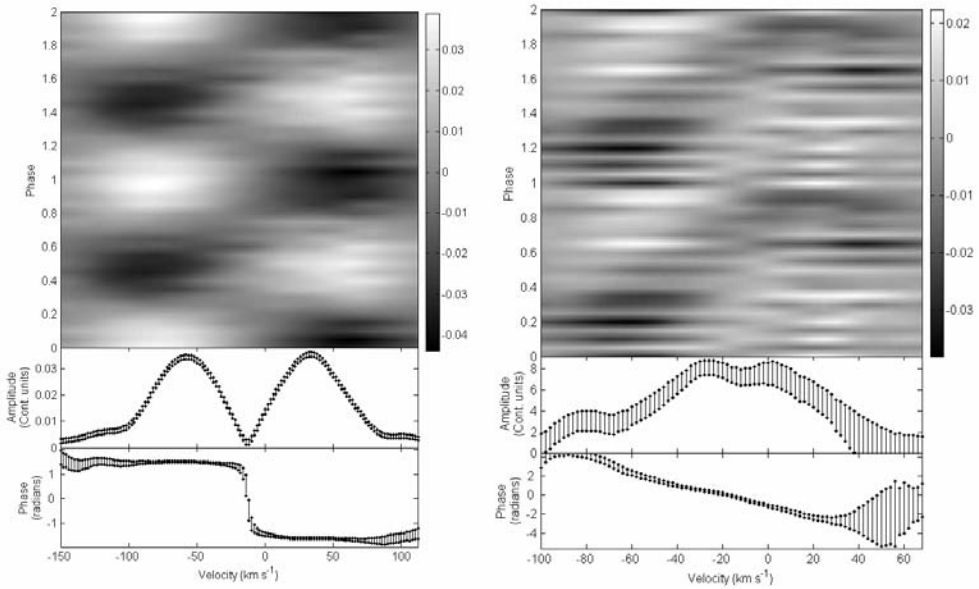

Figure: He I 5876Å line phased surface plot with the amplitude and phase across the profile for the frequencies 7.147 cd^{-1} (left) and 6.825 cd^{-1} (right).

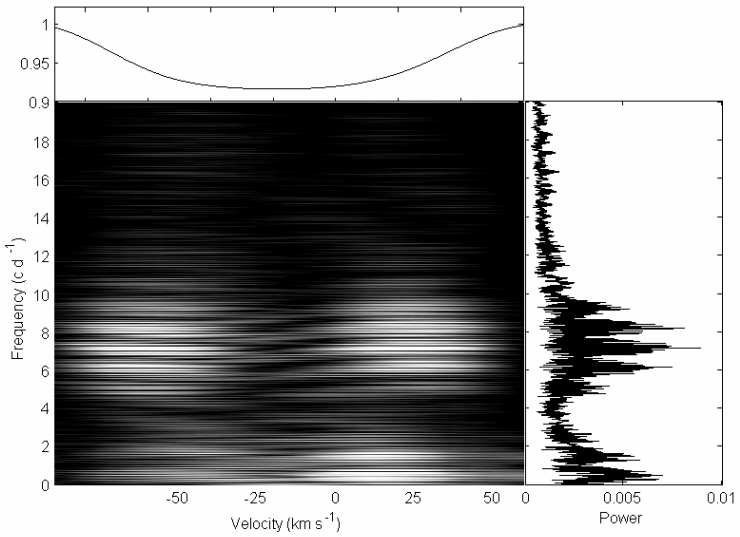

Figure: Si III 4553Å line pixel-by-pixel frequency analysis. The peak frequency is at 7.148 cd^{-1}.

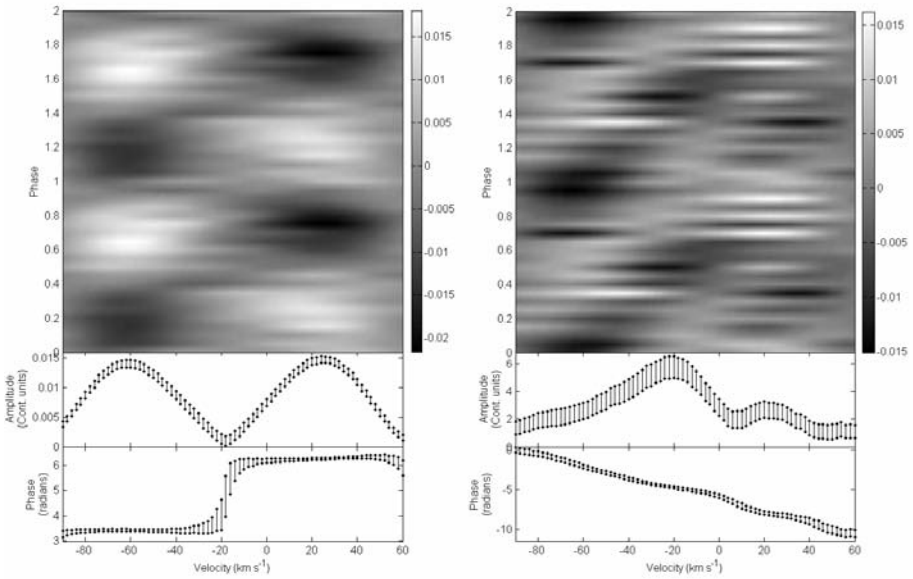

Figure: Si III 4553Å line phased surface plot with the amplitude and phase across the profile for the frequencies 7.148 cd^{-1} (left) and 6.828 cd^{-1} (right).

The following figures relate to the measurement of the projected rotational velocity ($V_{rot}\sin i$) in the He I 5876Å and Si III 4553Å lines.

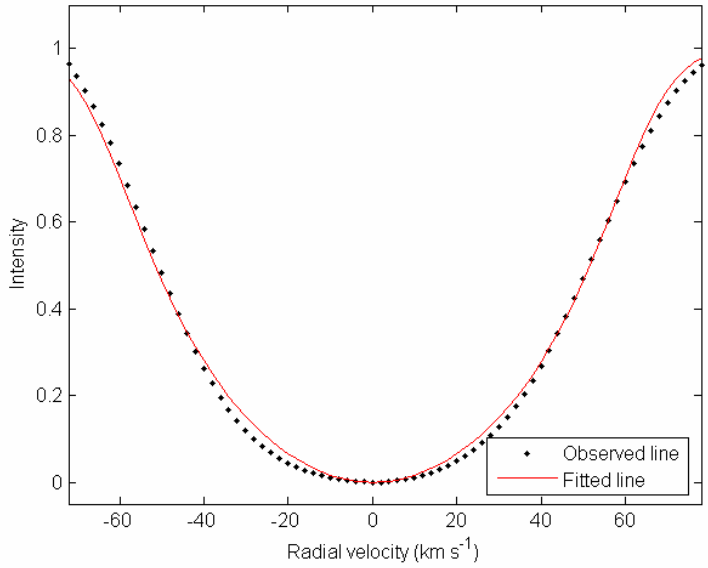

Figure: Si III 4553Å line $V_{rot}\sin i$ fit. $V_{rot}\sin i$ =65.3 km s^{-1}.

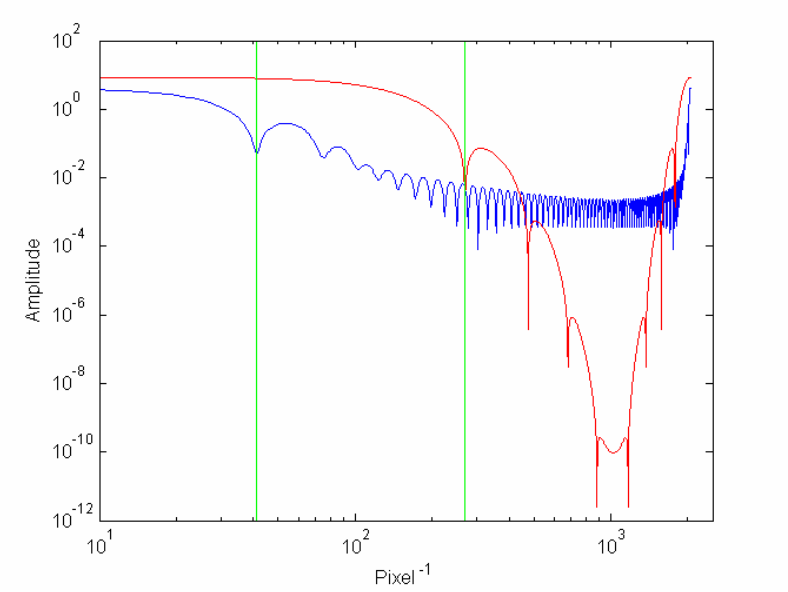

Figure: Si III 4553Å Fourier $V_{rot}\sin i$ measurement. $V_{rot}\sin i$ =65.6 km s^{-1}.

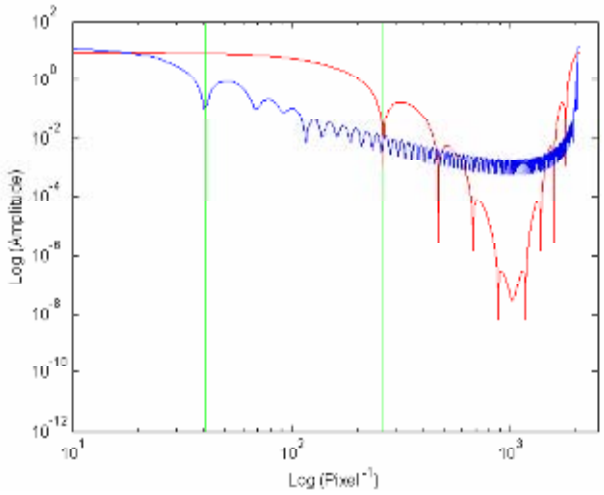

Figure: He I 5876Å Fourier $V_{rot}\sin i$ measurement. $V_{rot}\sin i$ =64.9 km s^{-1}.

The following figures relate to the optimisation of the NRP frequencies detected in the He I 5876Å and Si III 4553Å lines. The He I 5876Å variation was not fitted well, this is probably due to its complex (triplet nature). It is

difficult to differentiate between l=0,1 and 2 for f_1 for this star, as can be seen in the best fits for these modes for f_1 in the Si III 4553Å line.

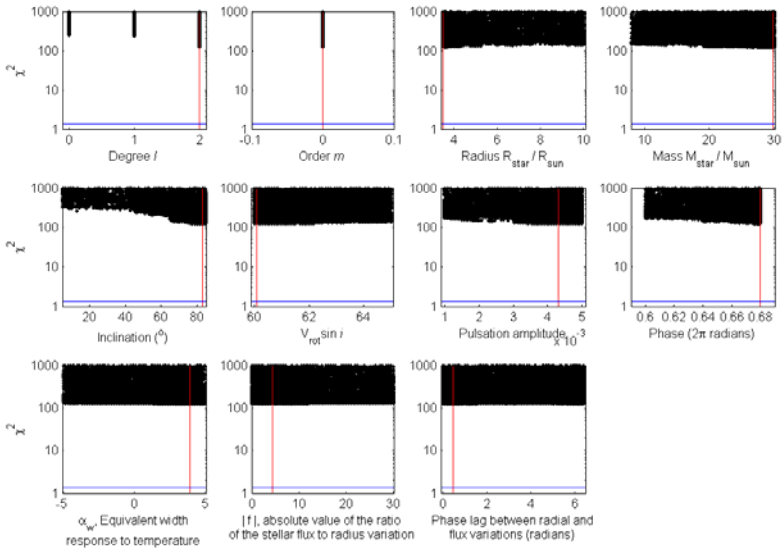

Figure: Optimisations for the 7.147 cd^{-1} frequency for the He I 5876Å line.

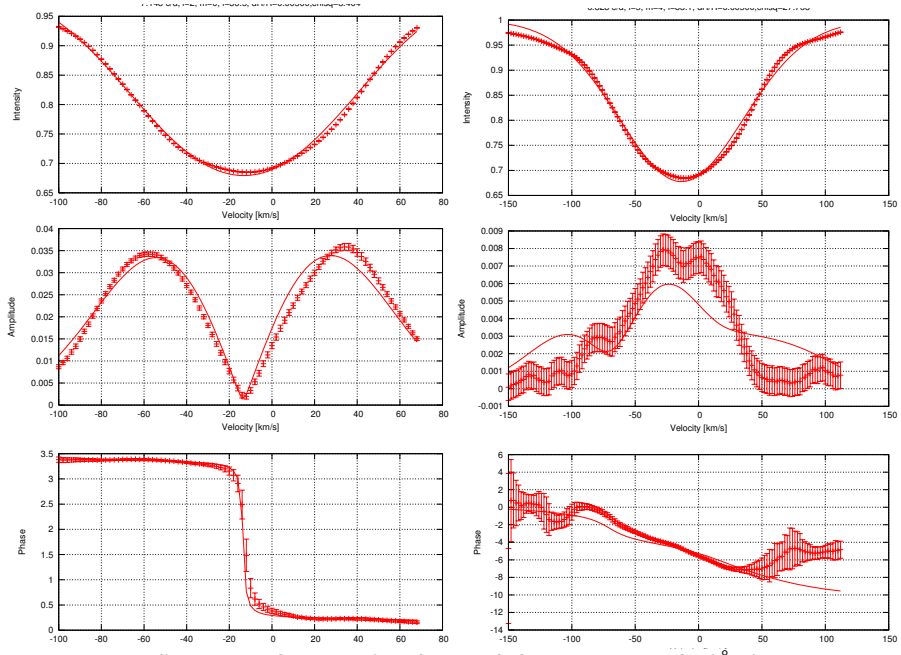

Figure: The best fits to the frequencies f_1 and f_2 for the He I 5876Å line. They are not good fits, probably due to the triplet nature of the He I 5876Å line.

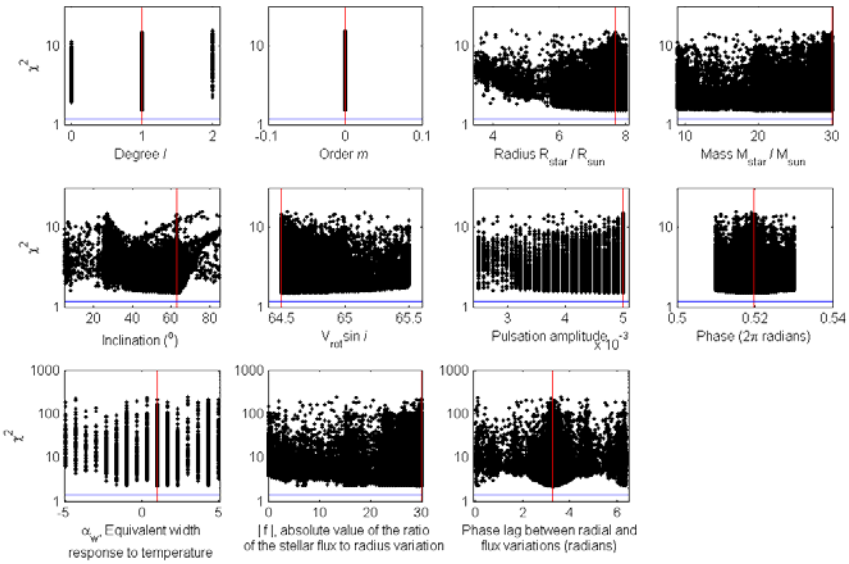

Figure: Optimisations for the 7.148 cd^{-1} frequency for the Si III 4553Å line.

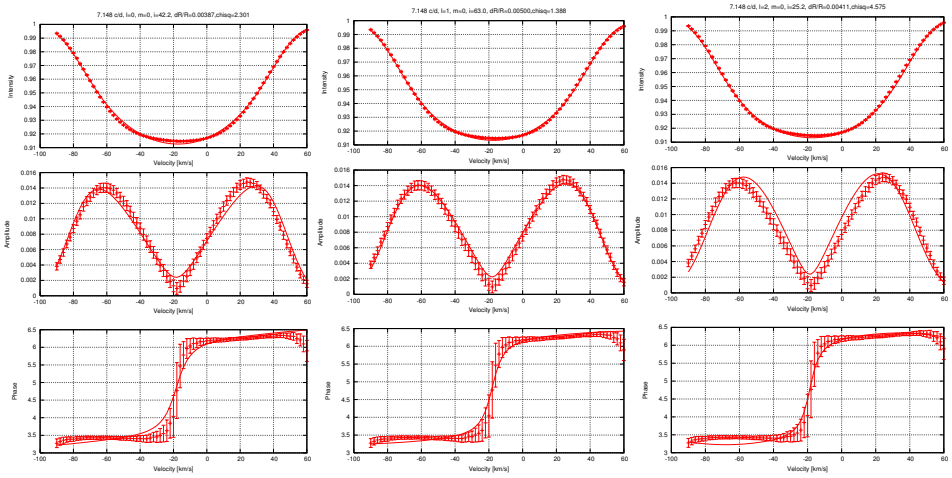

Figure: The best fits of *l*=0 *m*=0 with χ^2=3.805 (left), *l*=1 *m*=0 with χ^2=2.236 (middle) and *l*=2 *m*=0 with χ^2=5.018 (right) to the frequencies f_1 and f_2 for the Si III 4553Å line. This shows why it is difficult for the FPF method to differentiate between the *l* values for this star.